Modeling of a silane-hydrogen plasma discharge including nanoparticle dynamics for photovoltaic applications.

Jean-Maxime Orlac'H

NNT : 2017SACLX023

Thèse de doctorat de l'Université Paris-Saclay préparée à l'École polytechnique

Ecole doctorale n°573
Interfaces
Spécialité de doctorat: Physique

par

M. Jean-Maxime Orlac'h

Modélisation d'un plasma de silane avec dynamique de nanoparticules pour applications photovoltaïques

Thèse présentée et soutenue à Palaiseau, le 2 mai 2017.
Composition du Jury :

M.	L. Boufendi	Professeur Université d'Orléans (GREMI)	Président du jury
M.	T. E. Magin	Professeur Van Karman Institute	Rapporteur
M.	S. L. Girshick	Professeur University of Minnesota	Rapporteur
M.	K. Hassouni	Professeur Université de Villetaneuse (LSPM)	Examinateur
M.	S. Pasquiers	Directeur de recherche CNRS (LPGP)	Examinateur
M.	P. Roca i Cabarrocas	Directeur de recherche CNRS (PICM)	Directeur de thèse
M.	V. Giovangigli	Directeur de recherche CNRS (CMAP)	Directeur de thèse
Mme	T. Novikova	Ingénieur de recherche CNRS (PICM)	Directrice de thèse

Thèse de doctorat de l'Université Paris-Saclay préparée à l'École polytechnique

Ecole doctorale n°573
Interfaces
Spécialité de doctorat: Physique

par

M. Jean-Maxime Orlac'h

Modélisation d'un plasma de silane avec dynamique de nanoparticules pour applications photovoltaïques

Thèse présentée et soutenue à Palaiseau, le 2 mai 2017.
Composition du Jury :

M.	L. Boufendi	Professeur Université d'Orléans (GREMI)	Président du jury
M.	T. E. Magin	Professeur Van Karman Institute	Rapporteur
M.	S. L. Girshick	Professeur University of Minnesota	Rapporteur
M.	K. Hassouni	Professeur Université de Villetaneuse (LSPM)	Examinateur
M.	S. Pasquiers	Directeur de recherche CNRS (LPGP)	Examinateur
M.	P. Roca i Cabarrocas	Directeur de recherche CNRS (PICM)	Directeur de thèse
M.	V. Giovangigli	Directeur de recherche CNRS (CMAP)	Directeur de thèse
Mme	T. Novikova	Ingénieur de recherche CNRS (PICM)	Directrice de thèse

Remerciements

Je tiens à remercier mes trois directeurs de thèse, Pere Roca i Cabarrocas du Laboratoire de Physique des Interfaces et des Couches Minces (LPICM), Vincent Giovangigli du Centre de Mathématiques Appliquées (CMAP), et Tatiana Novikova du LPICM. Merci à Pere, pour m'avoir proposé ce sujet de thèse, et y avoir toujours cru. Pere a toujours été très disponible tout au long de ma thèse, indépendamment de ses nombreuses responsabilités en tant que directeur du LPICM. Il a su me transmettre une part de son immense savoir-faire scientifique, qui est la somme des connaissances accumulées au PICM au cours de sa jeune histoire. Merci à Vincent également, pour m'avoir initié à la théorie cinétique des gaz et à la modélisation des mélanges réactifs gazeux, et pour m'avoir transmis son savoir-faire numérique. Vincent a toujours fait preuve d'une très grande exigence dans le travail et d'une extrême rigueur intellectuelle. Sa grande aisance dans l'analyse théorique et mathématique des modèles va de pair avec une imagination très riche et une connaissance profonde de la physique sous-jacente. Merci enfin à Tatiana, dont la connaissance approfondie des plasmas et de leur modélisation a été indispensable à la bonne conduite de cette thèse. Tatiana a toujours su poser les bonnes questions à chaque étape de la thèse, mais a également toujours su apporter des réponses à chaque difficulté, qu'elle soit d'ordre numérique ou physique, rencontrée.

Je tiens de même à remercier les deux rapporteurs, Steven L. Girshick, et Thierry Magin, pour me faire l'honneur de relire mon manuscrit de thèse. Les travaux de Thierry Magin dans la théorie cinétique des plasmas ont été à la source de l'essentiel de mon travail théorique. Merci à Steven Girshick, pour m'avoir accueilli pendant deux mois à l'Université du Minnesota, où j'ai pu apprendre au contact de son équipe et apprécier l'étendue de ses connaissances physiques. Le modèle développé dans cette thèse doit beaucoup aux travaux précédents du professeur Girshick. Merci aux autres membres du jury, Laïfa Boufendi, Khaled Hassouni et Stéphane Pasquiers, de me faire l'honneur d'assister à ma soutenance.

Je tiens également à remercier Erik Johnson pour ses conseils et nos échanges au sujet de l'étude du potentiel d'autopolarisation, et merci à François Silva, Pavel Bulkin, et Wanghua Chen pour leur aide et leur expertise scientifique.

Merci à TOTAL pour m'avoir accueilli dans ses locaux pendant la durée de ma thèse, et merci aux membres de l'équipe de recherche commune TOTAL/LPICM. Merci aux autres doctorants Rasha, Ronan, Gwenaëlle, Paul, Bastien, Junkang, Farah, Romain, Mutaz, Fatme, Jiang, Linda, Raphaël et merci à tous ceux que j'oublierais encore.

Merci à Laurence et Gabi pour leur travail titanesque au sein de l'équipe administrative du PICM, et pour leur constante bonne humeur en toutes circonstances. Merci aux membres du bureau d'étude que j'ai côtoyé au cours de ma thèse, et notamment à Cyril Jadaud, Jérôme Charliac, Jean-Charles Vanel, et Frédéric Farci.

Je remercie également vivement Eric Paillassa et Frédéric Liège, membres de l'équipe informatique, toujours extrêmement réactifs et qui ont grandement facilité l'exécution des calculs.

Merci à l'équipe de la bibliothèque centrale de l'X, et tout particulièrement à Michel Multan, pour son aide très précieuse dans la recherche de documents.

Je remercie le C'Nano Ile-de-France pour avoir financé cette thèse.

Merci à ma famille : mon père, ma mère, mon frère Pierre, Diane sa femme, et leurs fils Mathieu et Raphaël.

Enfin – et surtout – merci à ma femme Daria et à mon fils Ferdinand : mes deux degrés d'énergie interne.

Résumé de la thèse

Cette thèse porte sur la modélisation des plasmas de silane-hydrogène entretenus par décharge à couplage capacitif radiofréquence. Un tel modèle est requis pour la compréhension et le contrôle de la formation et du transport des nanoparticules (1-10 nm) générées dans les plasmas de silane typiquement utilisés pour la déposition de films minces de silicium pour applications photovoltaïques.

Dans une première partie de la thèse, une dérivation complète des équations fluides pour un plasma réactif bi-température, partiellement ionisé, poly-atomique, magnétisé, est effectuée dans le cadre de la théorie cinétique des gaz. A partir d'une analyse asymptotique de l'équation de Boltzmann, la méthode de Chapman-Enskog a permis d'obtenir les équations d'ordre zéro en le nombre de Knudsen, qui correspondent au régime "Euler", et les équations d'ordre un qui correspondent au régime "Navier-Stokes-Fourier". Le développement asymptotique repose sur l'hypothèse fondamentale selon laquelle la racine carrée du rapport des masses est proportionnelle au nombre de Knudsen. En outre, les temps caractéristiques des collisions inélastiques électrons-lourds ont été supposés grands devant les temps caractéristiques des collisions élastiques, induisant ainsi une thermalisation plus rapide des électrons que des espèces lourdes. Les flux de transport sont exprimés en termes des gradients des variables macroscopiques, pour le cas d'un plasma faiblement magnétisé. Les coefficients de transports associés sont obtenus au moyen de crochets intégraux. De nouveaux couplages entre les degrés d'énergie interne et les forces de diffusion électroniques ont ainsi été mis en évidence dans le cas d'un plasma poly-atomique.

Un logiciel de simulation numérique pour un procédé de dépôt chimique en phase vapeur (CVD) a ensuite été implémenté en langage FORTRAN. Etant donné la configuration axisymétrique du problème, une solution auto-similaire de l'écoulement est recherchée le long de l'axe du réacteur, dans l'hypothèse isobare posée dans la limite d'un faible nombre de Mach. Les équations sont discrétisées à l'aide d'une méthode de différences finies. Une solution stationnaire est obtenue au moyen d'un schéma temporel implicite de Newton. Les propriétés de transport sont calculées grâce à la librairie EGLIB, et les données de chimie du gaz sont implémentées dans Chemkin. Un excellent accord est trouvé avec les résultats du cas test de réacteur CVD.

L'outil de simulation numérique est ensuite étendu du cas d'un gaz composé d'espèces neutres au cas d'un plasma radiofréquence bi-température. Les équations générales obtenues dans le cadre de la théorie cinétique des plasmas bi-température sont simplifiées. L'équation de Poisson pour le potentiel électrique et l'équation d'évolution pour la température électronique ont été couplées aux équations de transport des électrons et des espèces lourdes. Le modèle fluide, couplé à un mécanisme chimique bi-température du gaz, est mis en oeuvre dans les conditions typiques de l'épitaxie par plasma basse température. Les densités des principales espèces sont en accord avec les données expérimentales de la littérature. Une nouvelle condition aux limites pour le potentiel est implémentée, permettant l'étude de la tension d'auto-polarisation apparaissant au niveau de l'électrode RF sous l'effet de formes d'ondes asymétriques sur mesure, pour la première fois pour un plasma de silane.

Le code a ensuite été enrichi à l'aide d'un modèle sectionnel pour la distribution en tailles et en charges des nanoparticules de silicium. La comparaison avec les résultats expérimentaux existants a permis d'étudier l'influence du coefficient d'accommodation du silane sur la croissance surfacique des nanoparticules. L'étude de la phase initiale de développement des nanoparticules a mis en évidence l'accumulation rapide de particules négatives et, dans une moindre mesure, de particules neutres. En

revanche, à ce stade du processus, et pour le mécanisme réactionnel étudié, les particules positives sont en proportion négligeable devant les particules négatives ou neutres, et leur contribution au dépôt est marginale.

Le modèle développé dans cette thèse ouvre ainsi la voie à une étude systématique de l'évolution du plasma en fonction des conditions de dépôt et de l'influence des nanoparticules sur les propriétés physico-chimiques du plasma.

Contents

1 Introduction **1**
Bibliography . . . 7

2 Kinetic Theory of Non-Thermal Reactive Polyatomic Plasmas **11**
2.1 Introduction . . . 11
2.2 Kinetic Framework . . . 13
2.2.1 Species distribution functions . . . 13
2.2.2 Boltzmann equations . . . 14
2.2.3 Heavy-species reference frame . . . 15
2.2.4 Conservation laws and reciprocity relations . . . 17
2.2.5 Collisional invariants of the scattering operator . . . 18
2.2.6 Scattering cross-sections . . . 20
2.3 Asymptotic Expansion of the Boltzmann Equations . . . 20
2.3.1 Choice of scaling . . . 20
2.3.2 Scaled Boltzmann equations . . . 24
2.3.3 Scaled collisional invariants . . . 26
2.3.4 Asymptotic expansion of collision operators . . . 27
2.4 Chapman-Enskog Expansion of the Species Distribution Functions . . . 32
2.4.1 Chapman-Enskog method . . . 33
2.4.2 Electron thermalization . . . 34
2.4.3 Heavy-species thermalization . . . 36
2.4.4 First-order perturbation function for electrons . . . 38
2.4.5 Scaling for inelastic collision cross-sections . . . 40
2.4.6 Zeroth-order macroscopic equations for electrons . . . 43
2.4.7 Zeroth-order macroscopic equations for the heavy species . . . 45
2.4.8 First-order perturbation for the heavy species . . . 46
2.4.9 Second-order perturbation for electrons . . . 47
2.4.10 First-order macroscopic equations for electrons . . . 48
2.4.11 First-order macroscopic equations for the heavy species . . . 49
2.4.12 Chemistry source terms . . . 50
2.5 Transport Fluxes . . . 52
2.5.1 Electron transport coefficients . . . 52
2.5.2 Heavy-species transport coefficients . . . 53
2.5.3 Properties of the heavy-species transport coefficients . . . 57
2.5.4 Electron Kolesnikov transport coefficients . . . 59
2.6 Fluid Equations . . . 63
2.6.1 Conservation of mass, momentum, and energy . . . 63
2.6.2 Transport fluxes . . . 65
2.7 Center-of-Mass Reference Frame . . . 66
2.8 Conclusion . . . 68

Bibliography . . . 70

3 Numerical Simulation of Silicon Chemical Vapor Deposition 73
3.1 Introduction . . . 73
3.2 Chemical Vapor Deposition Reactor . . . 74
3.3 Conservation Equations . . . 74
3.4 Thermodynamics . . . 76
3.4.1 State law and mixture variables . . . 76
3.4.2 Enthalpy and entropy . . . 76
3.4.3 Enthalpy and temperature equations . . . 77
3.4.4 Thermodynamic data . . . 78
3.5 Chemistry . . . 79
3.6 Transport Fluxes . . . 81
3.7 Low Mach Number Flow . . . 83
3.7.1 Momentum equation and pressure splitting . . . 84
3.7.2 Temperature equation . . . 84
3.7.3 Isobaric equations . . . 85
3.8 Strained Flow . . . 85
3.8.1 Self similar solution . . . 85
3.8.2 Traditional variables . . . 87
3.9 Transport Coefficients . . . 87
3.9.1 Molecular parameters and collision integrals . . . 88
3.9.2 Shear viscosity . . . 88
3.9.3 Diffusion coefficients . . . 89
3.9.4 Thermal conductivity and thermal diffusion ratios . . . 90
3.10 Boundary Conditions . . . 92
3.11 Surface Chemistry . . . 93
3.12 Numerical Method . . . 94
3.13 Results and Discussion . . . 95
3.14 Conclusion . . . 99
Bibliography . . . 100

4 Simulation of a Silane-Hydrogen Radio-Frequency Plasma Discharge 103
4.1 Introduction . . . 103
4.2 Radio-Frequency Reactor . . . 104
4.3 General Equations for a Multicomponent Plasma . . . 105
4.3.1 Conservation equations . . . 105
4.3.2 Thermodynamics . . . 106
4.3.3 Transport fluxes . . . 108
4.4 Simplified Model . . . 108
4.4.1 Equations . . . 109
4.4.2 Self similar formulation . . . 109
4.4.3 Transport fluxes . . . 110
4.5 Transport coefficients . . . 111
4.6 Silane-Hydrogen Plasma Chemistry . . . 111
4.7 Energy exchange term . . . 116
4.8 Boundary Conditions . . . 117
4.9 External Circuit . . . 120
4.10 Numerical Implementation . . . 122
4.10.1 Discretization . . . 122

4.10.2 Resolution . . . 124
4.11 Results and Discussion . . . 124
4.11.1 Symmetric Discharge . . . 127
4.11.2 Asymmetric Excitation . . . 129
4.12 Conclusion . . . 132
Bibliography . . . 133

5 Nanoparticle Formation in a Silane-Hydrogen Plasma Discharge 139
5.1 Introduction . . . 139
5.2 Sectional Model . . . 141
5.3 Nucleation . . . 142
5.4 Coagulation . . . 143
5.5 Nanoparticle Surface Growth . . . 146
5.5.1 Sectional growth rate . . . 146
5.5.2 Average surface flux . . . 147
5.6 Charge fluctuations rate . . . 148
5.7 Nanoparticle Transport . . . 148
5.8 Plasma-Nanoparticle Model . . . 150
5.9 Results and Discussion . . . 150
5.9.1 Parameters . . . 151
5.9.2 Investigation of nanoparticle surface growth rate . . . 153
5.9.3 Study of a silane-hydrogen discharge during the early stages of nanoparticle formation . . . 154
5.10 Conclusion . . . 158
Bibliography . . . 159

6 Conclusion and Perspectives 163

Chapter 1

Introduction

Plasma processing covers a wide variety of processes used in industrial applications, including semiconductor processing, production of flat panel displays, but also plasma treatments used in aerospace, automotive, biomedical, or waste management industries. Many examples of plasma processing applications can be found in [LL05] [CC02]. Plasma is generally described as a fourth state of matter, in which molecules and atoms are ionized into freely moving charged particles, namely electrons and ions. Plasma discharges used for industrial applications are generally obtained via electric or magnetic excitation of a feedstock gas. In most industrial applications, plasmas are low-temperature, in the sense that the heavy species temperature remains close to the room temperature, while electron temperature is of the order of a few eVs. Such plasmas are in general weakly ionized.

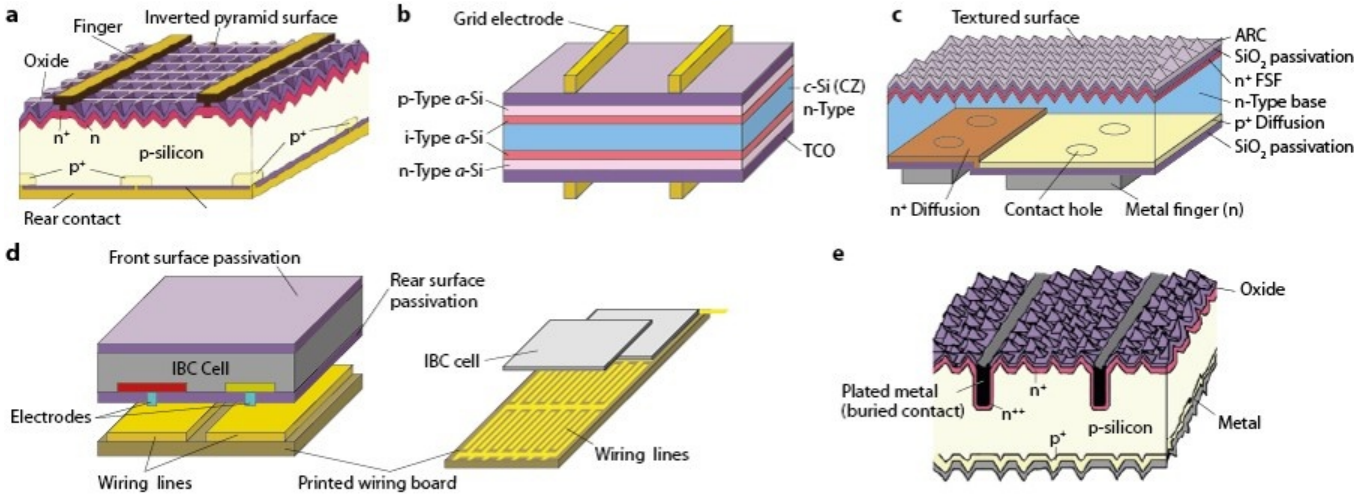

Figure 1.1 – Schematics of various crystalline solar cell structures, as presented in [Sag10]. (a) PERL. (b) HIT. (c) BC-BJ. (d) Interdigitated back-contact (IBC) cell. (e) Buried-contact cell structure.

Plasma enhanced chemical vapor deposition (PECVD) is commonly used in the production of photovoltaic solar cells. This technique has indeed a lot of advantages for the deposition of thin-film semiconductor materials. Compared to thermal chemical vapor deposition, PECVD is a low-temperature process, which can be required when depositing over a temperature-sensitive structure, or over a multilayer structure with different thermal expansion coefficients. Besides, plasma discharge processes in general allow to enhance gas-phase and heterogeneous reactions, possibly resulting in an increase in the deposition rate and a better use of feedstock gas. In particular, PECVD is commonly used in crystalline silicon (c-Si) solar cells manufacturing for anti-reflective coating and passivation by SiN_x deposition.

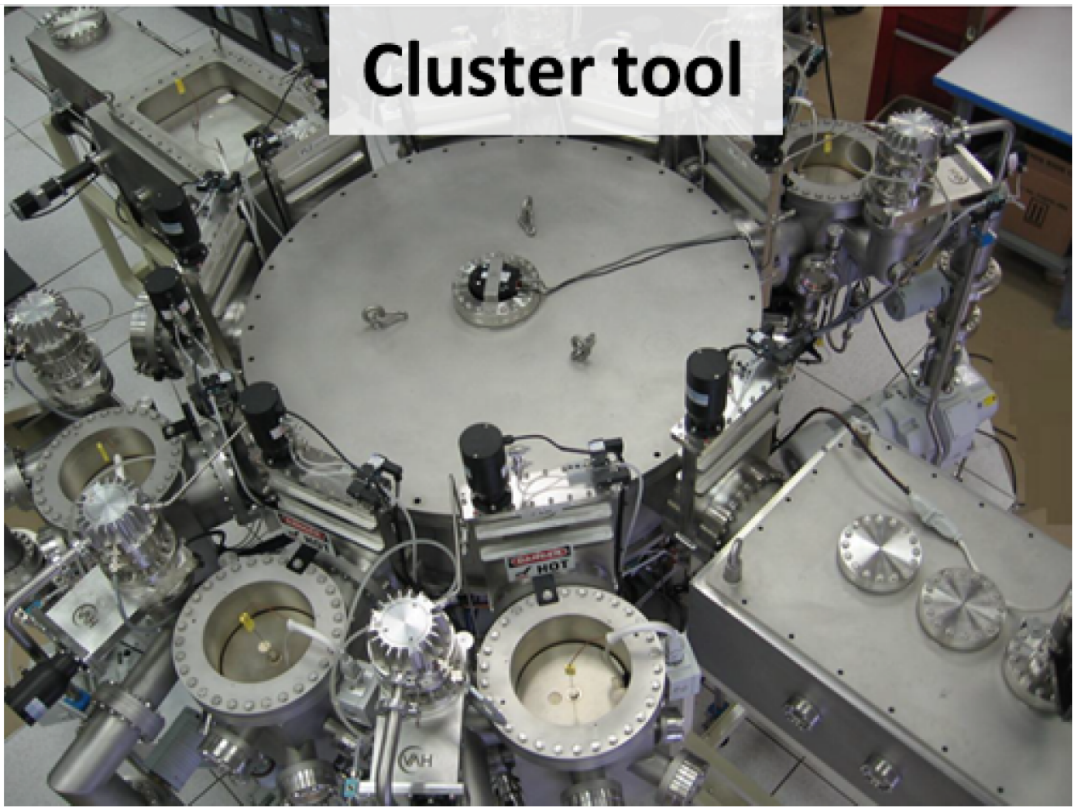

Figure 1.2 – PECVD cluster with six plasma chambers, a sputtering and a vacuum characterization chamber, used in LPICM facility [Car14]. The equipment was bought by Total and is shared with LPICM.

As illustrated in Figure 1.1, the structure of crystalline silicon solar cells has evolved considerably over the last decades, allowing for a dramatic improvement of cell efficiency. The fabrication process now involves a complex step-by-step procedure similar to semiconductor devices, and in many cases plasma processing is seen as an interesting alternative to other available deposition or texturing techniques. Figure 1.2 shows a picture of a cluster tool used in Laboratoire de Physique des Interfaces et des Couches Minces (LPICM), allowing for automated multi-step processing of solar cells without breaking the vacuum. Many kinds of plasma processing techniques may be used depending on the technology. Aside from PECVD, plasma may be used in texturing, sputtering, etching or cleaning processes.

The apparition of nanoparticles and microparticles in silane plasma discharges has been observed very early and is now well referenced [BB93] [PBEL94] [BBH96] [Bou99]. In semiconductor manufacturing, the need for size reduction made such "dust" particles highly undesirable. Semi-conductor industry is now heading towards devices of 10 nm or smaller [ITR15], a scale at which even "small" nanometer-sized particles are a potential threat to material quality. Although solar cell fabrication does not require so far such a high-resolution material processing as semiconductors, electronic defaults are an important source of efficiency reduction and lifetime degradation, and micrometer or nanometer-sized particles may also have undesirable effects during solar cell fabrication processes.

It is well known that the particle formation process generally occurs in three distinct phases [BB93] [RiCNTD$^+$07]. In the first phase, nanoparticles are rapidly nucleated with radius up to 10 nm and concentrations up to 10^9-10^{10} cm^{-3}. In a second phase, particles tend to agglomerate and form clusters with up to 50−60 nm diameter, and the nanoparticle density decreases drastically. In the last phase, large particles continue to grow by surface deposition of SiH_x molecular species. As illustrated in Figure 1.3, dust formation also strongly depends on pressure. For low values of pressure, no dust

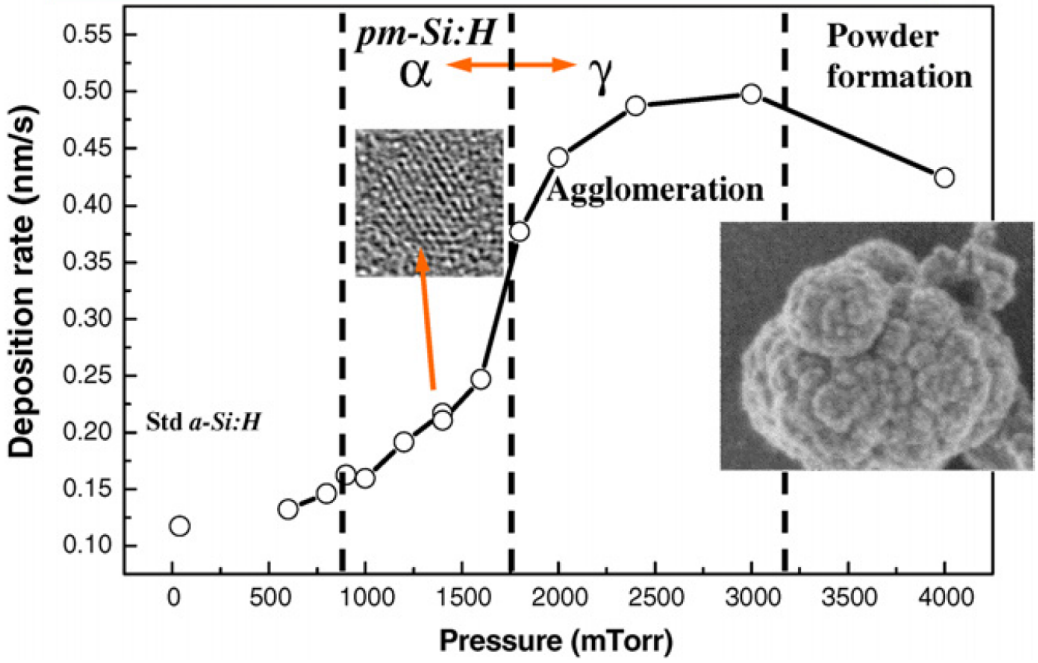

Figure 1.3 – Deposition rate of silicon thin films as a function of pressure for a 3 % silane in hydrogen mixture at 250 °C under an RF power of 22 W. The deposition rate of a standard a-Si:H film is also given for comparison. [RiCNTD$^+$07].

formation occurs, while increasing the pressure lowers the time for onset of nanoparticle coagulation. In this thesis we are interested in the transition between pristine conditions, corresponding to the deposition of amorphous silicon, and conditions of dust formation, where deposition is strongly perturbed by the presence of dusts in the reactor. This transition is associated with an optimum in the deposition rate, as can be seen in Figure 1.3, and material quality [RiCNTD$^+$07].

Several studies have proved that the presence of nanoparticles, initially seen as a device killer, can actually enhance the deposition rate or improve the material property. In particular, for the conditions of Figure 1.3, when the pressure is around 2 Torr, it is possible to maintain a high nanoparticle nucleation rate while still avoiding powder formation [RiCNTD$^+$07]. Under such conditions, silicon thin films with improved material properties can be obtained, also called "polymorphous silicon", or "pm-Si" [RiCHS$^+$98] [RiCFiMP02]. Polymorphous films consist in an amorphous matrix in which nanometer-scaled crystalline structures are embedded. They exhibit optical properties similar to those of standard amorphous silicon (a-Si:H), but improved transport properties and stability [RiCHS$^+$98] [LKRiC$^+$98], generally attributed to the embedded microstructures. On the other hand, microcrystalline silicon is made of an amorphous matrix with embedded crystalline domains of up to several nanometers, and exhibits poor optical properties compared to amorphous silicon, but improved electrical properties and stability. Polymorphous silicon thus combines the advantages of both amorphous silicon and microcrystalline silicon [RiCHS$^+$98], with intermediate properties between a-Si:H and μc-Si:H [SHSRiC98].

Similarly, when a (100) crystalline substrate is used under conditions close to powder formation, low-temperature plasma enhanced epitaxy can be achieved with a deposition rate above 1 Å.s^{-1}, a sharp porous interface, and film thickness up to $2-4$ μm [CLRiC11] [RCL12]. Figure 1.4 shows images obtained via high resolution transmission electron microscopy (HRTEM) of an epitaxial silicon layer (epi-Si) on a crystalline silicon (c-Si) wafer [Car14], assessing the quality of the epitaxial layer. Such an epitaxial growth of ultrathin crystalline silicon is now seen as an interesting technique to reduce further material cost in the production of crystalline silicon solar cells. Indeed, reducing the thickness of the active material up to a few μm requires to develop new techniques, since

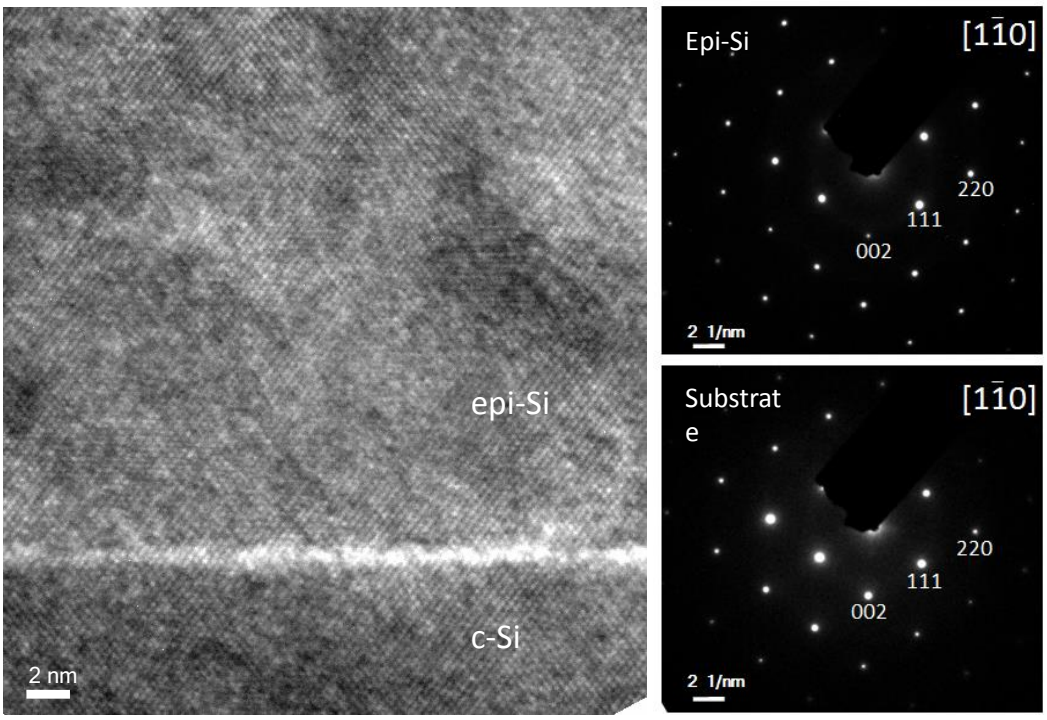

Figure 1.4 – HRTEM cross section image of the epi-Si/c-Si interface (Left), and diffraction patterns obtained in the bulk of the epitaxial layer (Upper right), respectively in the substrate (Lower right) [Car14].

traditional wafer slicing techniques are reaching their limit of capability and induce a significant material waste. Besides, low cost ultra thin silicon layers are required to develop flexible solar cells or large area electronics. Encouragingly, a transfer process of PECVD-grown ultrathin crystalline silicon layer onto a glass substrate has been developed, thus allowing for potential reuse of the single-crystal parent substrate for several epitaxial growth [CCCB$^+$16]. The ability to control the thickness and doping profile of the epitaxial layer is also an interesting possibility for photovoltaic applications. Finally, epitaxy of silicon on GaAs has also been achieved, opening the path for an improved integration of III-V semiconductors with silicon in photovoltaic tandem devices [CCM$^+$16].

Due to the extreme complexity of PECVD process and the relatively scarce experimental characterizations available, numerical modeling is highly desirable for studying chemically reactive non-thermal plasma discharges. Two main approaches are generally followed, depending on the Knudsen number, which is the ratio of the characteristic mean free path l^0 to the reference macroscopic length L^0

$$\mathrm{K}_n = \frac{l^0}{L^0}.$$

The kinetic approach is required for high values of the Knudsen number, although it might reveal computationally expensive, and fluid models are usually preferable for low values of K_n. In this thesis, the pressure considered range from 600 mTorr to 2 or 3 Torr. For such relatively high pressures, the Knudsen number is sufficiently high to justify the use of a fluid model. An upper bound for the mean free path in a weakly ionized mixture can be estimated from the carrier gas characteristic density n^0 and the characteristic elastic scattering collision cross-section σ^0, as

$$l^0 = \frac{1}{n^0 \sigma^0}.$$

An estimation of the Knudsen number for a 2 cm-gap hydrogen plasma discharge reactor, at a gas temperature of 500 K is presented for different values of pressure in Table 1.1. The results

confirm that the fluid approximation is justified in this work. Additionally, fluid models are less computationally intensive than kinetic models.

Table 1.1 – Estimation of the Knudsen number for different pressures in a 2 cm-gap hydrogen plasma discharge reactor, at a gas temperature of 500 K. The molecular radius of hydrogen is taken equal to 1.372 Å [CC70].

p (Torr)	n ($\mathrm{cm^{-3}}$)	K_n
0.5	9.5×10^{15}	8.9×10^{-2}
0.75	1.4×10^{16}	5.9×10^{-2}
1.0	1.9×10^{16}	4.4×10^{-2}
2.0	3.8×10^{16}	2.2×10^{-2}
2.5	4.8×10^{16}	1.8×10^{-2}

An important challenge is then the full derivation of macroscopic fluid equations from the Boltzmann equation for non-thermal plasmas. The first derivation of fluid equations for multicomponent partially ionized two-temperature plasmas from the kinetic theory was achieved by Magin and coworkers [MD04] [GMM09]. They work used a scaling proposed by Petit and Darrozes [DP75] accounting for the strong disparity of masses between electrons and heavy species, thus filling the gap between the Lorentz gas model and traditional Chapman-Enskog theory of multicomponent gas mixtures. The effect of magnetic field and chemical reactions were also taken into account [GG03] [GMM09] [GGMM10]. The description of internal energy levels is also an important feature of a multicomponent reacting gas mixture [WT62] [MYM63] [Gio99]. Therefore, an extension of two-temperature kinetic theory of partially ionized reactive plasmas to the case of polyatomic mixtures is highly desirable.

In both pure silane and silane-hydrogen plasma discharges the complexity is increased due to the combined presence of silicon containing molecules of various sizes and charges, and light molecules such as atomic and molecular hydrogen, and hydrogen ions. The chemical kinetics of hydrogen plasma has been extensively studied and a number of numerical studies have been carried out on H_2 plasma discharges. We mention in particular the tremendous work carried out by Capitelli and coworkers from Università degli Studi di Bari [GCC$^+$92] [DCL05] [LD09], and also by Hassouni and coworkers from Université de Villetaneuse [HGCL99] [HGG99] [HLG$^+$05], on hydrogen plasma chemical kinetics and hydrogen discharge modeling. On the other hand, silane plasma discharges have also been investigated numerically [Kus88] [SGA02] [LAM06]. However, due to the very large number of chemical species involved, the chemical kinetics of silane plasma discharges is not known with such a high precision as for pure H_2 discharges, and comparison with experimental data are scarcer than for H_2. Investigation of regimes in which nanoparticle nucleate and grow have also been carried out for different conditions. The main contributions to the description of particle formation and particle dynamics are due to Girshick and coworkers [BKG03] [WG07] [AG12] from University of Minnesota, and to Bogaerts and coworkers [dBGG04] [dBG06] from Universiteit Antwerpen.

In this thesis, a model for a radio-frequency silane-plasma discharge reactor has been developed, implemented, and applied successfully to the study of silicon thin films deposition by PECVD. A new fluid model for multicomponent non-thermal polyatomic reactive plasmas has been derived from the kinetic theory. This derivation extends the pioneering work of Magin and coworkers [MD04] [GMM09] to the case of polyatomic molecules and ions. In the limiting case of neutral multicomponent gas mixtures one retrieves classical multicomponent Navier-Stokes-Fourier equations and

self-consistent expressions for transport coefficients [Gio99] [GMM09]. The latter "neutral" model has been implemented numerically, and applied to the modeling of chemical vapor deposition of silicon for validation against a benchmark model from the literature. The CVD numerical model has then been extended to the modeling of radio-frequency silane plasma discharges in the Torr regime. The software has been used to study the deposition of amorphous silicon by PECVD under discharge conditions intermediate between a-Si:H and μc-Si:H, that is conditions where nucleation of nanoparticles is enhanced but coagulation remains controlled. Results are in line with available numerical and experimental data. The influence of silane dilution ratio and RF power has also been investigated. The study of the DC bias potential under asymmetric excitation was also carried out for the first time in silane-hydrogen. Finally, the model was enriched with a sectional model for nanoparticles with sections of size and charge, following the work of Girshick and coworkers [WG07] [AG12]. The nanoparticle surface growth rate was tested against experimental data, and simulations have been performed under conditions close to powder formation in the early stages of nanoparticle growth. The outline of this work is detailed below.

In Chapter 2, a self-consistent fluid two-temperature plasma model for a multicomponent reactive polyatomic mixture is derived from the kinetic theory of gases. A generalized Chapman-Enskog method is used on the basis of an asymptotic analysis of the Boltzmann equation taking into account the strong mass disparity of masses between electrons and heavy plasma species. The zeroth-order "Euler-type" and the first-order "Navier-Stokes-type" fluid equations, are given along with self-consistent expressions for transport fluxes in terms of macroscopic variable gradients and transport coefficients. The transport coefficients are expressed as bracket products of the perturbed species distribution functions. This complete model derived from kinetic theory is a generalization of standard non-thermal plasma fluid models, and opens the path for an improvement of low temperature plasma fluid modeling.

In Chapter 3, a numerical implementation of a chemical vapor deposition (CVD) model is carried out. A software has been written in FORTRAN, and has been validated against a numerical benchmark for thermal chemical vapor deposition of silane. The results show an excellent agreement with the benchmark model.

In Chapter 4, the software is enriched and applied to the modeling of a radiofrequency discharge in silane-hydrogen. The equations derived in Chapter 2 are simplified and standard fluid plasma equations are retrieved. Conditions close to powder formation are investigated. The results are in good qualitative agreement with previous studies of nanoparticle nucleation in silane-hydrogen discharge. A self-consistent calculation of the DC bias voltage is further implemented, to evaluate the effect of the discharge chemistry on the DC bias under asymmetric electrical excitation.

In Chapter 5, the model is enriched with a sectional model for nanoparticles. The effects of nucleation, coagulation, surface growth, transport and charging of nanoparticles are taken into account. The software is fully coupled and fully non-stationary, thus allowing for an investigation of the early phase of nanoparticle formation. The influence of the nanoparticle surface growth rate on nanoparticles is studied, and compared to experimental data. The temporal evolution of the main plasma and nanoparticle species density profiles are also investigated.

Finally, in Chapter 6, this work is summarized and perspectives are drawn for future work.

Bibliography

[AG12] P. Agarwal and S. L. Girshick. Sectional modeling of nanoparticle size and charge distributions in dusty plasmas. *Plasma Sources Sci. Technol.*, 21:055023, 2012. 5, 6, 140, 141, 145, 158

[BB93] A. Bouchoule and L. Boufendi. Particulate formation and dusty plasma behaviour in argon-silane RF discharge. *Plasma Sources Sci. Technol.*, 2:204–213, 1993. 2, 156

[BBH96] L. Boufendi, A. Bouchoule, and T. Hbid. Electrical characterization and modeling of a dust forming plasma in a radio frequency discharge. *Journal of Vacuum Science and Technology A*, 14(2):572–576, 1996. 2, 129, 156

[BKG03] U. Bhandarkar, U. Kortshagen, and S. L. Girshick. Numerical study of the effect of gas temperature on the time for onset of particle nucleation in argon-silane low-pressure plasmas. *J. Phys. D: Appl. Phys.*, 36:1399–1408, 2003. 5, 139

[Bou99] A. Bouchoule, editor. *Dusty Plasmas: Physics, Chemistry and Technological Impacts in Plasma Processing.* Wiley, 1999. 2, 139

[Car14] R. Cariou. *Epitaxial growth of Si(Ge) materials on Si and GaAs by low temperature PECVD: towards tandem devices.* PhD thesis, Ecole Polytechnique, 2014. 2, 3, 4

[CC70] S. Chapman and T. G. Cowling. *The Mathematical Theory of Non-Uniform Gases.* Cambridge University Press, Cambridge, 1970. 5, 11, 12, 14, 18, 20, 21, 32, 33, 47, 82, 88, 111, 118, 145, 153

[CC02] F. F. Chen and J. P. Chang. *Lecture Notes on Principles of Plasma Processing.* Plenum/Kluwer, 2002. 1

[CCCB+16] R. Cariou, W. Chen, I. Cosme-Bolanos, J.-L. Maurice, M. Foldyna, V. Depauw, G. Patriarche, A. Gaucher, A. Cattoni, I. Massiot, S. Collin, E. Cadel, P. Pareige, and P. Roca i Cabarrocas. Ultrathin PECVD epitaxial Si solar cells on glass via low-temperature transfer process. *Progress in Photovoltaics: Research and Applications*, 24(8):1075–1084, 2016. 4

[CCM+16] R. Cariou, W. Chen, J.-L. Maurice, L. Yu, G. Partiarche, O. Mauguin, L. Largeau, J. Decobert, and P. Roca i Cabarrocas. Low temperature plasma enhanced cvd epitaxial growth of silicon on GaAs: a new paradigm for III-V/Si integration. *Nature Scientific Reports*, 6:25674, 2016. 4

[CLRiC11] R. Cariou, M. Labrune, and P. Roca i Cabarrocas. Thin crystalline silicon solar cells based on epitaxial films grown at 165 °C by RF-PECVD. *Solar Energy Materials & Solar Cells*, 95:2260–2263, 2011. 3

[dBG06] K. de Bleecker, A. Bogaerts, and W. Goedheer. Modelling of nanoparticle coagulation and transport dynamics in dusty silane discharges. *New Journal of Physics*, 8:178, 2006. 5, 140, 143, 158

[dBGG04] K. de Bleecker, A. Bogaerts, R. Gijbels, and W. Goedheer. Numerical investigation of particle formation mechanisms in silane discharges. *Physical Review E*, 69:056409, 2004. 5, 104, 117, 139

[DCL05] P. Diomede, M. Capitelli, and S. Longo. Effect of discharge voltage on capacitively coupled, parallel plate rf hydrogen plasmas. *Plasma Sources Science and Technology*, 14:459–466, 2005. 5, 116, 128

[DP75] J.-S. Darrozes and J.-P. Petit. Une nouvelle formulation des équations du mouvement d'un gaz ionisé dans un régime dominé par les collisions. *J. Méc*, 14(745), 1975. 5, 12, 20, 21

[GCC+92] C. Gorse, R. Celiberto, M. Cacciatore, A. Laganà, and M. Capitelli. From dynamics to modeling of plasma complex systems: negative ion (h^-) sources. *Chemical Physics*, 161:211–227, 1992. 5, 104

[GG03] V. Giovangigli and B. Graille. Kinetic theory of partially ionized reactive gas mixtures. *Physica A*, 327:313–348, 2003. 5, 12, 40

[GGMM10] V. Giovangigli, B. Graille, T. E. Magin, and M. Massot. Multicomponent transport in weakly ionized mixtures. *Plasma Sources Sci. Technol.*, 19(3):034003, 2010. 5, 59, 69, 73

[Gio99] V. Giovangigli. *Multicomponent Flow Modeling*. MESST Series. Birkhauser, Boston, 1999. 5, 6, 13, 14, 15, 17, 18, 20, 32, 33, 47, 59, 73, 75, 76, 77, 79, 80, 82, 84, 85, 88, 89, 90, 92, 110, 111

[GMM09] B. Graille, T. E. Magin, and M. Massot. Kinetic theory of plasmas: Translational energy. *M3AS*, 19(4):527–599, 2009. 5, 6, 12, 14, 15, 19, 20, 21, 22, 24, 28, 32, 33, 35, 40, 47, 52, 56, 59, 61, 62, 68, 69

[HGCL99] K. Hassouni, A. Gicquel, M. Capitelli, and J. Loureiro. Chemical kinetics and energy transfer in moderate pressure h_2 plasmas used in diamond mpacvd processes. *Plasma Sources Sci. Technol.*, 8:494–512, 1999. 5

[HGG99] K. Hassouni, T. A. Grotjohn, and A. Gicquel. Self-consistent microwave field and plasma discharge simulations for a moderate pressure hydrogen discharge reactor. *Journal of Applied Physics*, 86(1):134–151, 1999. 5, 104

[HLG+05] K. Hassouni, G. Lombardi, A. Gicquel, V. A. Shakhatov, and O. De Pascale. Nonequilibrium vibrational excitation of h2 in radiofrequency discharges: A theoretical approach based on coherent anti-stokes raman spectroscopy measurements. *Physics of Plasmas*, 12:073301, 2005. 5

[ITR15] International technology roadmap for semiconductors 2.0, 2015. 2

[Kus88] M. Kushner. A model for the discharge kinetics and plasma chemistry during plasma enhanced chemical vapor deposition of amorphous silicon. *Journal of Applied Physics*, 63:2532–2551, 1988. 5

[LAM06] B. Lyka, E. Amanatides, and D. Mataras. Simulation of the electrical properties of sih_4/h_2 discharges. *Japanese Journal of Applied Physics*, 45(10B):8172–8176, 2006. 5, 104

[LD09] S. Longo and P. Diomede. Modeling of capacitively coupled rf plasmas in h_2. *Plasma Process. Polym.*, 6:370âĂŞ379, 2009. 5

[LKRiC+98] C. Longeaud, J.-P. Kleider, P. Roca i Cabarrocas, S. Hamma, R. Meaudre, and M. Meaudre. Properties of a new a-Si:H-like material: hydrogenated polymorphous silicon. *Journal of Non-Crystalline Solids*, 227–230:96–99, 1998. 3

[LL05] M. A. Lieberman and A. J. Lichtenberg. *Principles of Plasma Discharges and Materials Processing*. Wiley, 2005. 1

[MD04] T. E. Magin and G. Degrez. Transport properties of partially ionized and unmagnetized plasmas. *Physical Review E*, 70(046412), 2004. 5, 12

[MYM63] L. Monchick, K. S. Yun, and E. A. Mason. Formal kinetic theory of transport phenomena in polyatomic gas mixtures. *Journal of Chemical Physics*, 39(3):654–669, 1963. 5, 11, 75, 90

[PBEL94] J. Perrin, C. Böhm, R. Etemadi, and A. Lloret. Possible routes for cluster growth and particle formation in RF silane discharges. *Plasma Sources Sci. Technol.*, 3:252–261, 1994. 2, 116, 139, 156

[RCL12] Pere Roca i Cabarrocas, Romain Cariou, and Martin Labrune. Low temperature plasma deposition of silicon thin films. *J. Non Cryst. Solids*, 358:2000–2003, 2012. 3, 104, 124, 139, 140, 151

[RiCFiMP02] P. Roca i Cabarrocas, A. Fontcuberta i Morral, and Y. Poissant. Growth and optoelectronic properties of polymorphous silicon thin films. *Thin Solid Films*, 403–404:39–46, 2002. 3

[RiCHS+98] P. Roca i Cabarrocas, S. Hamma, S. N. Sharma, G. Viera, and E. Bertran. Nanoparticle formation in low-pressure silane plasmas: bridging the gap between a-Si:H and μc-Si films. *Journal of Non-Crystalline Solids*, 227–230:871–875, 1998. 3, 139, 140

[RiCNTD+07] P. Roca i Cabarrocas, Th. Nguyen-Tran, Y. Djeridane, A. Abramov, E. Johnson, and G. Patriarche. Synthesis of silicon nanocrystals in silane plasmas for nanoelectronics and large area electronic devices. *J. Phys. D.: Appl. Phys.*, 40:2258–2266, 2007. 2, 3, 103, 141

[Sag10] T. Saga. Advances in crystalline silicon solar cell technology for industrial mass production. *NPG Asia Mater.*, 2(3):96–102, 2010. 1

[SGA02] A. Salabas, G. Gousset, and L. L. Alves. Two-dimensional fluid modelling of charged particle transport in radio-frequency capacitively coupled discharges. *Plasma Sources Sci. Technol.*, 11:448–465, 2002. 5, 127, 128

[SHSRiC98] P. St'ahel, S. Hamma, P. Sladek, and P. Roca i Cabarrocas. Metastability studies in silicon thin films: from short range ordered to medium and long range ordered materials. *Journal of Non-Crystalline Solids*, 227-230:276–280, 1998. 3

[WG07] S. Warthesen and S. Girshick. Numerical simulation of the spatiotemporal evolution of a nanoparticle-plasma system. *Plasma Chemistry and Plasma Processing*, 27(3):292–310, 2007. 5, 6, 117, 140, 141, 142, 145

[WT62] L. Waldmann and E. Trübenbacher. Formale kinetische Theorie von Gasgemischen aus anregbaren Molekülen. *Zeitschr. Naturforschg.*, 17a:363–376, 1962. 5, 11, 13, 17, 18, 75, 82

Chapter 2

Kinetic Theory of Non-Thermal Reactive Polyatomic Plasmas

2.1 Introduction

One of the main challenges in the field of plasma fluid modeling is the comprehensive derivation of macroscopic fluid equations. At the kinetic scale, the plasma is well described by the fundamental Boltzmann equations. Thus, the full derivation from the kinetic theory is the only way to develop a self-consistent fluid model for a given plasma regime on a sound basis. Moreover, only the kinetic theory yields the transport coefficients for fluid models, and the knowledge of the mathematical structure of the conservation equations is desirable for the design of appropriate numerical methods.

Two main methods may be used for the derivation of fluid equations from kinetic models [Str05]: the moment-based method [Gra58] [Zhd02], and the Chapman-Enskog procedure [CC70] [FK72] [HCB64], which have notably proven successful in the analysis of multicomponent neutral gas mixtures. Both methods rely on approximating the Boltzmann equations by using a finite number of moments of the species distribution functions. They differ in the choice of moments and the closure.

The Chapman-Enskog method was first developed by Chapman [Cha16] and Enskog [Ens17] separately, for a simple gas or a binary gas mixture of monoatomic molecules. The method was then extended to multicomponent monoatomic gas mixtures by Hellund [Hel40], Hirschfelder and Curtiss [CH49], and Waldmann [Wal58], to simple polyatomic gases by Wang Chang and Uhlenbeck [WCU51], and finally to multicomponent mixtures of polyatomic molecules by Waldmann and Trübenbacher [Wal58] [WT62] and by Monchick, Yun and Mason [MYM63]. A fully quantum mechanical treatment was given by McCourt and Snider [MS64] [MS65] using the quantum mechanical Boltzmann equation derived by Waldmann [Wal57] and Snider [Sni60]. Later on, chemically reactive collisions have been taken into account in the case of monoatomic [PX49] or polyatomic gas mixtures [LH60] [ACG94] [GG95] [EG94].

On the other hand, the moment method was first developed by Grad [Gra58], and had been put aside for a long time, because the associated entropy production rate was not positive. Recent developments in the field of rarefied gases have led to the derivation of a 13 moments regularized system, also called "R13" [Str05], which has the desirable entropy structure [ST07] [Tor12], and yields smooth shock structures at all Mach numbers [TS04]. Such moment equations are a good candidate for bridging the gap between the microscopic or molecular Boltzmann equation and the macroscopic Euler or Navier-Stokes-Fourier equations, unlike the Burnett and Super-Burnett equations corresponding to the second-order and third-order of the Chapman-Enskog expansion, respectively, which are known to yield an unproper entropy structure and are unstable [Bob82] [Tor16]. In this work we will consider fluid models corresponding to the first-order Chapman-Enskog expansion, because Navier-Stokes type equations are sufficient for the modelling of silicon deposition processes.

The first kinetic model for a binary gas mixture composed of light and heavy species was derived

by Lorentz [Lor05] [CC70]. This model, also referred to as the "Lorentzian gas", assumed that the heavy molecules were not altered by their collisions with light particles, and that mutual encounters between light particles were of negligible influence compared to encounters with heavy molecules. However, when considering a multiscale analysis of the Boltzmann equations for ionized gases in the fluid regime, both the Knudsen number K_n *and* the ratio of the electron mass over the heavy-species characteristic mass

$$\varepsilon = \sqrt{\frac{\mathfrak{m}_e^0}{\mathfrak{m}_h^0}} \tag{2.1.1}$$

tend to zero. As shown by Petit and Darrozes [DP75], the Boltzmann equations exhibit a singularity in the limit $\varepsilon \to 0, \mathrm{K}_n \to 0$, which might be solved upon assuming that the Knudsen number is proportional to the small parameter ε

$$\mathrm{K}_n \propto \varepsilon. \tag{2.1.2}$$

Such a scaling accounting for the disparity of masses allows for thermal non-equilibrium between light and heavy species, and is the scaling considered in the present work. This scaling was first applied by Degond and Lucquin [DLD96] [Deg07] to the derivation of a two-temperature macroscopic fluid model for a binary mixture made of electrons and positive ions.

Another important feature of multicomponent plasmas is the influence of the magnetic field, which induces anisotropic transport fluxes [CC70] [FK72]. Giovangigli and Graille [GG03] [GG09] derived macroscopic equations together with expressions for transport fluxes and transport coefficients for magnetized plasmas. Their work included the effects of internal degrees of freedom and chemically reactive collisions, along with new symmetric formulation of the nonisotropic transport coefficients, but they did not take into account the strong disparity of masses nor the possibly associated thermal non-equilibrium between electrons and heavy species.

In the meantime, Magin and Degrez [MD04] developed a model for multicomponent non-thermal plasmas, where they introduced the scaling of Petit and Darrozes [DP75] in order to account for thermal non-equilibrium. Their model was improved by Graille, Magin and Massot [GMM09], who further investigated the strongly magnetized case. They also accounted for electron impact and ion or neutral impact ionization reactions [GMM08] [MGM09]. However, none of these models considered the case of polyatomic molecules and ions.

In this chapter, we derive from kinetic theory a unified multicomponent fluid model for partially ionized plasmas taking into account the following features

- Thermal non-equilibrium between electrons and heavy species, namely neutrals, negative or positive ions.
- Presence of polyatomic molecules with excitation or de-excitation of the heavy species' internal degrees of freedom.
- Influence of the external electro-magnetic field $\mathbf{E}$ and $\mathbf{B}$ on the plasma, under the assumption that the magnetic field is weak.
- Occurrence of chemically reactive collisions.

We will follow the framework adopted in [GG03] [GMM09], generalizing the Chapman-Enskog procedure in the wake of a dimensional analysis of the Boltzmann equation.

In section 2.2, we introduce the kinetic framework. In section 2.3, we set the scaling hypotheses and derive an asymptotic expansion of the Boltzmann equations. In section 2.4, the Chapman-Enskog procedure is applied on the basis of the proposed scaling. The transport fluxes are expressed in terms of macroscopic variable gradients and transport coefficients in section 2.5. Finally, section 2.6 synthesizes the macroscopic equations obtained.

2.2 Kinetic Framework

We consider a plasma composed of electrons and a mixture of heavy species, namely atoms, molecules, or ions. We adopt a semi-classical framework, in which the translational motion of the particles is treated classically, whereas the internal degrees of freedom are treated quantum mechanically [Wal58] [WT62] [Gio99]. Moreover, the system is considered to be sufficiently dilute so that one can consider only binary collisions.

2.2.1 Species distribution functions

The plasma is described as a multicomponent gas mixture of electrons, neutrals, and ions. To each species is associated a corresponding distribution function. The electron has only one internal degree of freedom, namely its ground state, and its distribution function reads $f_e\left(t, \boldsymbol{x}, \boldsymbol{c}_e\right)$, where t is the time, $\boldsymbol{x}$ is the three-dimensional spatial coordinate, and $\boldsymbol{c}_e$ the velocity of the electron. The quantity $f_e\left(t, \boldsymbol{x}, \boldsymbol{c}_e\right) \mathrm{d}\boldsymbol{x}\mathrm{d}\boldsymbol{c}_e$ represents the expected number of electrons in the volume element $\mathrm{d}\boldsymbol{x}$ located at $\boldsymbol{x}$, whose velocity lies in $\mathrm{d}\boldsymbol{c}_e$ about velocity $\boldsymbol{c}_e$ at time t.

On the other hand, we denote by $\mathfrak{H}$ the indexing set of heavy species, which can be ionized or not. For each $i \in \mathfrak{H}$, we introduce the set of internal degrees of freedom associated with the i^{th} heavy species $\mathfrak{Q}_i$. The distribution function for the i^{th} heavy species then reads $f_i\left(t, \boldsymbol{x}, \boldsymbol{c}_i, \mathrm{I}\right)$, where $\boldsymbol{c}_i$ denotes the velocity of the molecule, and $\mathrm{I} \in \mathfrak{Q}_i$ its quantum state. The quantity $f_i\left(t, \boldsymbol{x}, \boldsymbol{c}_i, \mathrm{I}\right) \mathrm{d}\boldsymbol{x}\mathrm{d}\boldsymbol{c}_i$ represents the expected number of molecules of the i^{th} heavy species, having internal state I, in the volume element $\mathrm{d}\boldsymbol{x}$ located at $\boldsymbol{x}$, and whose velocity lies in $\mathrm{d}\boldsymbol{c}_i$ about velocity $\boldsymbol{c}_i$, at time t. Finally, we denote by $\mathfrak{S} = \mathfrak{H} \cup \{e\}$ the indexing set of the plasma species.

In the kinetic framework, the macroscopic properties of the mixture can be recovered as moments of the species distribution functions. Indeed, for each $k \in \mathfrak{S}$, the number density of the k^{th} species, i.e., the number of particles per unit volume, is given by

$$n_k = \sum_{\mathrm{K} \in \mathfrak{Q}_k} \int f_k \, \mathrm{d}\boldsymbol{c}_k, \tag{2.2.1}$$

so that the mass density of the k^{th} species is

$$\rho_k = \mathfrak{m}_k n_k = \sum_{\mathrm{K} \in \mathfrak{Q}_k} \int \mathfrak{m}_k f_k \, \mathrm{d}\boldsymbol{c}_k, \tag{2.2.2}$$

where we have denoted by $\mathfrak{m}_k$ the mass of the k^{th} species. We also introduce the molar mass of the k^{th} species

$$m_k = \mathcal{N}_{\mathrm{A}} \mathfrak{m}_k. \tag{2.2.3}$$

The hydrodynamic velocity of the mixture $\boldsymbol{v}$ is given by

$$\rho \boldsymbol{v} = \sum_{k \in \mathfrak{S}} \sum_{\mathrm{K} \in \mathfrak{Q}_k} \int \mathfrak{m}_k \boldsymbol{c}_k f_k \, \mathrm{d}\boldsymbol{c}_k, \tag{2.2.4}$$

where $\rho = \sum_{k \in \mathfrak{S}} \rho_k$ is the total density. Finally, the internal energy per unit volume of the mixture $\mathcal{E}$ is given by

$$\tfrac{1}{2}\rho \, \boldsymbol{v} \cdot \boldsymbol{v} + \mathcal{E} = \sum_{k \in \mathfrak{S}} \sum_{\mathrm{K} \in \mathfrak{Q}_k} \int \left(\tfrac{1}{2} \mathfrak{m}_k \boldsymbol{c}_k \cdot \boldsymbol{c}_k + E_{k\mathrm{K}} \right) f_k \, \mathrm{d}\boldsymbol{c}_k, \tag{2.2.5}$$

where $E_{k\mathrm{K}}$ is the internal energy of the k^{th} species in the K^{th} quantum state.

The species distribution functions are then governed by generalized Boltzmann equations that take into account the reactive aspect of the mixture.

2.2.2 Boltzmann equations

We denote by $f_h = (f_i)_{i\in\mathfrak{H}}$ the family of heavy-species distribution functions, and by $f = (f_k)_{k\in\mathfrak{S}} = (f_e, f_h)$ the complete family of species distribution functions. The subscript "h" refers to the set of heavy species. The Boltzmann equations governing the species distribution functions read in an inertial reference frame [CC70] [FK72] [Gio99] [GMM09]

$$\partial_t f_e + \boldsymbol{c}_e \cdot \boldsymbol{\partial}_{\boldsymbol{x}} f_e + \frac{q_e}{\mathfrak{m}_e}\left[\mathbf{E} + \boldsymbol{c}_e \wedge \mathbf{B}\right] \cdot \boldsymbol{\partial}_{\boldsymbol{c}_e} f_e = \mathcal{S}_e\left(f\right) + \mathcal{C}_e\left(f\right), \tag{2.2.6}$$

$$\partial_t f_i + \boldsymbol{c}_i \cdot \boldsymbol{\partial}_{\boldsymbol{x}} f_i + \frac{q_i}{\mathfrak{m}_i}\left[\mathbf{E} + \boldsymbol{c}_i \wedge \mathbf{B}\right] \cdot \boldsymbol{\partial}_{\boldsymbol{c}_i} f_i = \mathcal{S}_i\left(f\right) + \mathcal{C}_i\left(f\right), \quad i \in \mathfrak{H}. \tag{2.2.7}$$

For $k \in \mathfrak{S}$, the term $\mathcal{S}_k\left(f\right)$, denotes the scattering or nonreactive source term for the k^{th} species, $\mathcal{C}_k\left(f\right)$ the chemically reactive source term, and q_k the charge carried by the k^{th} species, while $\mathbf{E}$ and $\mathbf{B}$ refer to the electric and magnetic fields, respectively. We will often formulate the Boltzmann equations (2.2.6), (2.2.7) in the more condensed version

$$\mathcal{D}_k(f_k) = \mathcal{S}_k(f) + \mathcal{C}_k(f), \quad k \in \mathfrak{S}, \tag{2.2.8}$$

where $\mathcal{D}_k$ denotes the usual streaming differential operator

$$\mathcal{D}_k(f_k) = \partial_t f_k + \boldsymbol{c}_k \cdot \boldsymbol{\partial}_{\boldsymbol{x}} f_k + \frac{q_k}{\mathfrak{m}_k}\left[\mathbf{E} + \boldsymbol{c}_k \wedge \mathbf{B}\right] \cdot \boldsymbol{\partial}_{\boldsymbol{c}_k} f_k. \tag{2.2.9}$$

Scattering source term The general scattering source term $\mathcal{S}_k$ for the k^{th} species, where $k \in \mathfrak{S}$, accounts for the change in the k^{th} species distribution function due to nonreactive collisions with any other species $l \in \mathfrak{S}$. Since we have assumed that the system is dilute, we can consider only binary collisions, and $\mathcal{S}_k$ is in the form

$$\mathcal{S}_k\left(f\right) = \sum_{l\in\mathfrak{S}} \mathcal{S}_{kl}\left(f_k, f_l\right), \tag{2.2.10}$$

where $\mathcal{S}_{kl}$ denotes the scattering source term for the k^{th} species due to nonreactive collisions with molecules of the l^{th} species

$$\mathcal{S}_{kl}\left(f\right) = \sum_{\substack{\mathrm{K}'\in\mathfrak{Q}_k \\ \mathrm{L},\mathrm{L}'\in\mathfrak{Q}_l}} \int \left(f'_k f'_l \frac{a_{k\mathrm{K}} a_{l\mathrm{L}}}{a_{k\mathrm{K}'} a_{l\mathrm{L}'}} - f_k f_l\right) |\boldsymbol{c}_k - \boldsymbol{c}_l| \sigma_{kl}^{\mathrm{KLK'L'}} \, \mathrm{d}\boldsymbol{\omega}'_{kl} \mathrm{d}\boldsymbol{c}_l. \tag{2.2.11}$$

The variables $\boldsymbol{c}_k, \boldsymbol{c}'_k$ represent the velocities of the k^{th} species respectively before and after collision, K, K' refer to the internal energy states of the k^{th} species respectively before and after collision, $\boldsymbol{c}_l, \boldsymbol{c}'_l$ represent the velocities of the l^{th} collision partner, and L, L' refer to the internal energy states of the l^{th} species, respectively before and after the collision

$$(\boldsymbol{c}_k, \mathrm{K}) + (\boldsymbol{c}_l, \mathrm{L}) \to (\boldsymbol{c}'_k, \mathrm{K}') + (\boldsymbol{c}'_l, \mathrm{L}'). \tag{2.2.12}$$

For $k \in \mathfrak{S}$, $\mathrm{K} \in \mathfrak{Q}_k$, $a_{k\mathrm{K}}$ is the degeneracy of the K^{th} quantum energy shell of the k^{th} species, and $f_k = f_k(t, \boldsymbol{x}, \boldsymbol{c}_k, \mathrm{K})$, $f'_k = f_k(t, \boldsymbol{x}, \boldsymbol{c}'_k, \mathrm{K}')$ denote the distribution functions of the k^{th} species, respectively before and after collision. We have also introduced the directions of the relative velocities respectively before and after collision

$$\boldsymbol{\omega}_{kl} = \frac{\boldsymbol{c}_k - \boldsymbol{c}_l}{|\boldsymbol{c}_k - \boldsymbol{c}_l|}, \qquad \boldsymbol{\omega}'_{kl} = \frac{\boldsymbol{c}'_k - \boldsymbol{c}'_l}{|\boldsymbol{c}'_k - \boldsymbol{c}'_l|}, \tag{2.2.13}$$

and we have denoted by $\sigma_{kl}^{\mathrm{KLK'L'}}$ the collision cross-section, also called the "differential cross-section", associated with a binary collision between the k^{th} and l^{th} species. One could also work with transition probabilities $\mathcal{W}_{kl}^{\mathrm{KLK'L'}}$ rather than with classical collision cross-sections $\sigma_{kl}^{\mathrm{KLK'L'}}$. Transition probabilities are notably interesting with reactive collisions, since the term $\mathcal{C}_k(f)$ is then much easier to write. For binary collisions, we also have the identity [LH60] [ACG94] [GG95]

$$|\boldsymbol{c}_k - \boldsymbol{c}_l| \sigma_{kl}^{\mathrm{KLK'L'}} \, \mathrm{d}\boldsymbol{\omega}'_{kl} = \mathcal{W}_{kl}^{\mathrm{KLK'L'}} \, d\boldsymbol{c}'_k d\boldsymbol{c}'_l. \tag{2.2.14}$$

Reactive source term For the reactive, or chemistry, source term $\mathcal{C}_k(f)$, we consider a chemical reaction mechanism composed of an arbitrary number of elementary reactions. Unlike for the scattering process, we take into account multiple reactive collisions, including triple reactive collisions since recombination reactions cannot often proceed otherwise [Kuš91] [ACG94] [GG95]. If we denote by $\mathscr{R}$ the set of reactions, each chemical reaction $r \in \mathscr{R}$ can be written in the form

$$\sum_{k\in\mathfrak{F}^r} \mathfrak{M}_k \rightleftharpoons \sum_{k\in\mathfrak{B}^r} \mathfrak{M}_k, \quad r \in \mathscr{R}, \tag{2.2.15}$$

where $\mathfrak{M}_k$ denotes the chemical symbol of the k^{th} species, and where $\mathfrak{F}^r$ and $\mathfrak{B}^r$ are, respectively, the indices for the reactant and product species in the r^{th} elementary reaction, counted with their order of multiplicity. The letters $\mathfrak{F}^r$ and $\mathfrak{B}^r$ are mnemonic for the forward and backward directions, respectively. We denote by ν^{f}_{kr} and ν^{b}_{kr} the stoichiometric coefficients of the k^{th} species among reactants and products, respectively, and we also denote by F^r and B^r the indices of internal energy states for reactants and products, respectively. In other words, the forward and backward coefficients ν^{f}_{kr} and ν^{b}_{kr} are the order of multiplicity of the k^{th} species in $\mathfrak{F}^r$ and $\mathfrak{B}^r$, respectively. For a given $k \in \mathfrak{S}$, $\mathfrak{F}^r_k$ denotes the set of reactant indices where the index for the k^{th} species has been removed only once and we introduce a similar notation for $\mathfrak{B}^r_k$, F^r_{K} and B^r_{K}.

The reactive source term, $\mathcal{C}_k(f)$, then reads

$$\mathcal{C}_k(f) = \sum_{r\in\mathscr{R}} \mathcal{C}^r_k(f), \tag{2.2.16}$$

where $\mathcal{C}^r_k(f)$ is the source term for the k^{th} species due to the r^{th} elementary reaction

$$\begin{aligned}\mathcal{C}^r_k(f) = \nu^{r\text{f}}_k \sum_{\text{F}^r_{\text{K}},\text{B}^r} \int \Big(\prod_{j\in\mathfrak{B}^r} f_j \, \frac{\prod_{j\in\mathfrak{B}^r} \beta_{j\text{J}}}{\prod_{i\in\mathfrak{F}^r} \beta_{i\text{I}}} - \prod_{i\in\mathfrak{F}^r} f_i \Big) \mathcal{W}^{\text{F}^r\text{B}^r}_{\mathfrak{F}^r\mathfrak{B}^r} \prod_{i\in\mathfrak{F}^r_k} \mathrm{d}\boldsymbol{c}_i \prod_{j\in\mathfrak{B}^r} \mathrm{d}\boldsymbol{c}_j \\ + \nu^{r\text{b}}_k \sum_{\text{F}^r,\text{B}^r_{\text{K}}} \int \Big(\prod_{i\in\mathfrak{F}^r} f_i - \frac{\prod_{j\in\mathfrak{B}^r} \beta_{j\text{J}}}{\prod_{i\in\mathfrak{F}^r} \beta_{i\text{I}}} \prod_{j\in\mathfrak{B}^r} f_j \Big) \mathcal{W}^{\text{F}^r\text{B}^r}_{\mathfrak{F}^r\mathfrak{B}^r} \prod_{i\in\mathfrak{F}^r} \mathrm{d}\boldsymbol{c}_i \prod_{j\in\mathfrak{B}^r_k} \mathrm{d}\boldsymbol{c}_j.\end{aligned} \tag{2.2.17}$$

In these expressions, the statistical weight $\beta_{k\text{K}}$ is given by

$$\beta_{k\text{K}} = \frac{h^3_{\text{P}}}{a_{k\text{K}}\mathfrak{m}^3_k}, \tag{2.2.18}$$

where h_{P} is the Planck constant, $\mathfrak{m}_k$ is the mass of the k^{th} species, and $a_{k\text{K}}$ the degeneracy of the K^{th} energy shell of the k^{th} species. Finally, $\mathcal{W}^{\text{F}^r\text{B}^r}_{\mathfrak{F}^r\mathfrak{B}^r}$ is the transition probability for a reactive collision in which the reactants $\mathfrak{F}^r$ with internal energy states F^r are transformed into products $\mathfrak{B}^r$ with internal energy states B^r. The sums over F^r, respectively F^r_{K}, represent the sums over $\text{I} \in \mathfrak{Q}_i$ for all $i \in \mathfrak{F}^r$, respectively $i \in \mathfrak{F}^r_k$. Similarly, the sums over B^r, respectively B^r_{K}, represent the sums over $\text{J} \in \mathfrak{Q}_j$ for all $j \in \mathfrak{B}^r$, respectively $j \in \mathfrak{B}^r_k$. Several examples for different types of reactions are given in [Gio99].

2.2.3 Heavy-species reference frame

Given the strong disparity of masses between electrons and heavy species, it is natural to choose a reference frame associated with the motion of the heavy species [GMM09]. We thus introduce the

mean electron velocity and mean heavy-species velocity

$$\rho_e \boldsymbol{v}_e = \int \mathfrak{m}_e \boldsymbol{c}_e f_e \, \mathrm{d}\boldsymbol{c}_e, \tag{2.2.19}$$

$$\rho_h \boldsymbol{v}_h = \sum_{j\in\mathfrak{H}} \sum_{\mathrm{J}\in\mathfrak{Q}_j} \int \mathfrak{m}_j \boldsymbol{c}_j f_j \, \mathrm{d}\boldsymbol{c}_j, \tag{2.2.20}$$

where the subscript "h" refers to the set of heavy species. The heavy-species mass density reads $\rho_h = \sum_{j\in\mathfrak{H}} \rho_j$, so that

$$\rho = \rho_e + \rho_h. \tag{2.2.21}$$

The hydrodynamic velocity of the fluid defined in (2.2.4) is then such that

$$\rho \boldsymbol{v} = \rho_e \boldsymbol{v}_e + \rho_h \boldsymbol{v}_h. \tag{2.2.22}$$

We also introduce the peculiar velocity of the k^{th} species with respect to the heavy-species reference frame

$$\boldsymbol{C}_k = \boldsymbol{c}_k - \boldsymbol{v}_h, \quad k \in \mathfrak{S}, \tag{2.2.23}$$

and denote by $f_k(t, \boldsymbol{x}, \boldsymbol{C}_k, \mathrm{K})$ the distribution function of the k^{th} species in the new reference frame. In this frame, the streaming operator $\mathcal{D}_k$ reads

$$\begin{aligned}\mathcal{D}_k(f_k) = \partial_t f_k + (\boldsymbol{C}_k + \boldsymbol{v}_h) \cdot \boldsymbol{\partial}_{\boldsymbol{x}} f_k + \frac{q_k}{\mathfrak{m}_k} \left[\mathbf{E} + (\boldsymbol{C}_k + \boldsymbol{v}_h) \wedge \mathbf{B}\right] \cdot \boldsymbol{\partial}_{\boldsymbol{C}_k} f_k \\ - \frac{D\boldsymbol{v}_h}{Dt} \cdot \boldsymbol{\partial}_{\boldsymbol{C}_k} f_k - (\boldsymbol{\partial}_{\boldsymbol{C}_k} f_k \otimes \boldsymbol{C}_k) : \boldsymbol{\partial}_{\boldsymbol{x}} \boldsymbol{v}_h,\end{aligned} \tag{2.2.24}$$

where $\frac{D}{Dt}$ is the time derivative following the heavy-species velocity reference frame

$$\frac{D}{Dt} = \partial_t + \boldsymbol{v}_h \cdot \boldsymbol{\partial}_{\boldsymbol{x}}. \tag{2.2.25}$$

The scattering source term (2.2.11) may be rewritten using the new velocities $\boldsymbol{C}_k$, $k \in \mathfrak{S}$, in the form

$$\mathcal{S}_{kl}\left(f_k, f_l\right) = \sum_{l\in\mathfrak{S}} \sum_{\substack{\mathrm{K}'\in\mathfrak{Q}_k \\ \mathrm{L},\mathrm{L}'\in\mathfrak{Q}_l}} \int \left(f'_k f'_l \frac{a_{k\mathrm{K}} a_{l\mathrm{L}}}{a_{k\mathrm{K}'} a_{l\mathrm{L}'}} - f_k f_l\right) |\boldsymbol{C}_k - \boldsymbol{C}_l| \sigma_{kl}^{\mathrm{KLK'L'}} \, \mathrm{d}\boldsymbol{\omega}'_{kl} \mathrm{d}\boldsymbol{C}_l, \tag{2.2.26}$$

where $\sigma_{kl}^{\mathrm{KLK'L'}}$ is the collision cross-section in the new reference frame, and the unit vectors read

$$\boldsymbol{\omega}_{kl} = \frac{\boldsymbol{C}_k - \boldsymbol{C}_l}{|\boldsymbol{C}_k - \boldsymbol{C}_l|}, \qquad \boldsymbol{\omega}'_{kl} = \frac{\boldsymbol{C}'_k - \boldsymbol{C}'_l}{|\boldsymbol{C}'_k - \boldsymbol{C}'_l|}. \tag{2.2.27}$$

Finally, the reactive source term (2.2.17) now reads in the new reference frame

$$\begin{aligned}\mathcal{C}_k^r(f) = \nu_k^{\mathrm{rf}} \sum_{\mathrm{F}^r_{\mathrm{K}}, \mathrm{B}^r} \int \Big(\prod_{j\in\mathfrak{B}^r} f_j \, \frac{\prod_{j\in\mathfrak{B}^r} \beta_{j\mathrm{J}}}{\prod_{i\in\mathfrak{F}^r} \beta_{i\mathrm{I}}} - \prod_{i\in\mathfrak{F}^r} f_i \Big) \mathcal{W}^{\mathrm{F}^r\mathrm{B}^r}_{\mathfrak{F}^r\mathfrak{B}^r} \prod_{i\in\mathfrak{F}_k^r} \mathrm{d}\boldsymbol{C}_i \prod_{j\in\mathfrak{B}^r} \mathrm{d}\boldsymbol{C}_j \\ + \nu_k^{\mathrm{rb}} \sum_{\mathrm{F}^r, \mathrm{B}^r_{\mathrm{K}}} \int \Big(\prod_{i\in\mathfrak{F}^r} f_i - \frac{\prod_{j\in\mathfrak{B}^r} \beta_{j\mathrm{J}}}{\prod_{i\in\mathfrak{F}^r} \beta_{i\mathrm{I}}} \prod_{j\in\mathfrak{B}^r} f_j \Big) \mathcal{W}^{\mathrm{F}^r\mathrm{B}^r}_{\mathfrak{F}^r\mathfrak{B}^r} \prod_{i\in\mathfrak{F}^r} \mathrm{d}\boldsymbol{C}_i \prod_{j\in\mathfrak{B}_k^r} \mathrm{d}\boldsymbol{C}_j.\end{aligned} \tag{2.2.28}$$

From now on, we will remain in the heavy-species reference frame. The full electron scattering source term $\mathcal{S}_e$ then reads

$$\begin{aligned}\mathcal{S}_e\left(f\right) &= \mathcal{S}_{ee} + \sum_{j\in\mathfrak{H}} \mathcal{S}_{ej},\\ &= \int \sigma_{e\tilde{e}}\ |\boldsymbol{C}_e - \widetilde{\boldsymbol{C}}_e| \left(f'_e \tilde{f}'_e - f_e \tilde{f}_e\right) \mathrm{d}\boldsymbol{\omega}'_{e\tilde{e}} \mathrm{d}\widetilde{\boldsymbol{C}}_e \\ &+ \sum_{j\in\mathfrak{H}} \sum_{\mathrm{J},\mathrm{J}'\in\mathfrak{Q}_j} \int \sigma_{ej}^{\mathrm{J}\mathrm{J}'}\ |\boldsymbol{C}_e - \boldsymbol{C}_j| \big(f'_e f'_j \frac{a_{j\mathrm{J}}}{a_{j\mathrm{J}'}} - f_e f_j\big)\, \mathrm{d}\boldsymbol{\omega}'_{ej} \mathrm{d}\boldsymbol{C}_j,\end{aligned} \tag{2.2.29}$$

where $\widetilde{\boldsymbol{C}}_e$ denotes the velocity of the electron collision partner over which the integration is carried out, $\tilde{f}_e = f_e(t, \boldsymbol{x}, \widetilde{\boldsymbol{C}}_e)$ denotes the distribution function of the electron collision partner, $\boldsymbol{\omega}_{e\tilde{e}} = \frac{\boldsymbol{C}_e - \widetilde{\boldsymbol{C}}_e}{|\boldsymbol{C}_e - \widetilde{\boldsymbol{C}}_e|}$, and so forth. As well, the full scattering source term $\mathcal{S}_i$ for the i^{th} heavy species in the I^{th} internal energy state reads

$$\begin{aligned}\mathcal{S}_i\left(f\right) &= \mathcal{S}_{ie} + \sum_{j\in\mathfrak{H}} \mathcal{S}_{ij},\\ &= \sum_{\mathrm{I}'\in\mathfrak{Q}_i} \int \sigma_{ie}^{\mathrm{I}\mathrm{I}'}\ |\boldsymbol{C}_i - \boldsymbol{C}_e| \big(f'_i f'_e \frac{a_{i\mathrm{I}}}{a_{i\mathrm{I}'}} - f_i f_e\big)\, \mathrm{d}\boldsymbol{\omega}'_{ie} \mathrm{d}\boldsymbol{C}_e, \\ &+ \sum_{j\in\mathfrak{H}} \sum_{\substack{\mathrm{I}'\in\mathfrak{Q}_i \\ \mathrm{J},\mathrm{J}'\in\mathfrak{Q}_j}} \int \sigma_{ij}^{\mathrm{I}\mathrm{J}\mathrm{I}'\mathrm{J}'}\ |\boldsymbol{C}_i - \boldsymbol{C}_j| \big(f'_i f'_j \frac{a_{i\mathrm{I}} a_{j\mathrm{J}}}{a_{i\mathrm{I}'} a_{j\mathrm{J}'}} - f_i f_j\big)\, \mathrm{d}\boldsymbol{\omega}'_{ij} \mathrm{d}\boldsymbol{C}_j.\end{aligned} \tag{2.2.30}$$

2.2.4 Conservation laws and reciprocity relations

In the above formulations of the scattering operator $\mathcal{S}_{kl}$, variables before and after collision are implicitly linked by the following conservation relations

$$\mathfrak{M}_k = \mathfrak{M}'_k, \qquad \mathfrak{M}_l = \mathfrak{M}'_l, \tag{2.2.31}$$

$$\mathfrak{m}_k \boldsymbol{C}_k + \mathfrak{m}_l \boldsymbol{C}_l = \mathfrak{m}_k \boldsymbol{C}'_k + \mathfrak{m}_l \boldsymbol{C}'_l, \tag{2.2.32}$$

$$\frac{1}{2}\mu_{kl} g_{kl}^2 + E_{k\mathrm{K}} + E_{l\mathrm{L}} = \frac{1}{2}\mu_{kl} g_{kl}'^2 + E_{k\mathrm{K}'} + E_{l\mathrm{L}'}, \tag{2.2.33}$$

where $\mathfrak{M}_k$ is the symbol for molecules of the k^{th} species, and $g_{kl} = |\boldsymbol{C}_k - \boldsymbol{C}_l|$ and $g'_{kl} = |\boldsymbol{C}'_k - \boldsymbol{C}'_l|$ are the relative velocities of colliding species respectively before and after collision. The first relation (2.2.31) states the conservation of the chemical species during a binary scattering collision. The second relation (2.2.32) states the conservation of total momentum during the collision process, written in the heavy-species reference frame. The third relation (2.2.33) states the conservation of energy during the collision, written in the center-of-mass frame. Such conservation relations are taken into account by means of dirac delta functions in the collision cross-sections [LH60] [ACG94] [GG95] [Gio99].

As is classical, the forward and reverse collision cross-sections exhibit reciprocity relations in the form [Wal58] [WT62] [EG94]

$$a_{k\mathrm{K}} a_{l\mathrm{L}}\ g_{kl}^2\ \sigma_{kl}^{\mathrm{K}\mathrm{L}\mathrm{K}'\mathrm{L}'} = a_{k\mathrm{K}'} a_{l\mathrm{L}'}\ g_{kl}'^2\ \sigma_{kl}^{\mathrm{K}'\mathrm{L}'\mathrm{K}\mathrm{L}}. \tag{2.2.34}$$

Since from (2.2.32) (2.2.33)

$$\begin{aligned} g'_{kl}\,\mathrm{d}\boldsymbol{C}_k\mathrm{d}\boldsymbol{C}_l\mathrm{d}\boldsymbol{\omega}'_{kl} &= g'_{kl}\,\mathrm{d}(\boldsymbol{C}_k-\boldsymbol{C}_l)\mathrm{d}\boldsymbol{C}_l\mathrm{d}\boldsymbol{\omega}'_{kl}\\ &= g'_{kl}g_{kl}^2\,\mathrm{d}g_{kl}\mathrm{d}\boldsymbol{\omega}_{kl}\mathrm{d}\boldsymbol{C}_l\mathrm{d}\boldsymbol{\omega}'_{kl}\\ &= g_{kl}g_{kl}'^2\,\mathrm{d}g'_{kl}\mathrm{d}\boldsymbol{\omega}_{kl}\mathrm{d}\boldsymbol{C}_l\mathrm{d}\boldsymbol{\omega}'_{kl}\\ &= g_{kl}g_{kl}'^2\,\mathrm{d}g'_{kl}\mathrm{d}\boldsymbol{\omega}'_{kl}\mathrm{d}\boldsymbol{C}'_l\mathrm{d}\boldsymbol{\omega}_{kl}\\ &= g_{kl}\,\mathrm{d}(\boldsymbol{C}'_k-\boldsymbol{C}'_l)\mathrm{d}\boldsymbol{C}'_l\mathrm{d}\boldsymbol{\omega}_{kl}\\ &= g_{kl}\,\mathrm{d}\boldsymbol{C}'_k\mathrm{d}\boldsymbol{C}'_l\mathrm{d}\boldsymbol{\omega}_{kl}, \end{aligned}$$

we have consequently [Wal58] [WT62] [CC70] [FK72]

$$a_{k\mathrm{K}}a_{l\mathrm{L}}\;g_{kl}\;\sigma_{kl}^{\mathrm{KLK'L'}}\,\mathrm{d}\boldsymbol{C}_k\mathrm{d}\boldsymbol{C}_l\mathrm{d}\boldsymbol{\omega}'_{kl} = a_{k\mathrm{K}'}a_{l\mathrm{L}'}\;g'_{kl}\;\sigma_{kl}^{\mathrm{K'L'KL}}\,\mathrm{d}\boldsymbol{C}'_k\mathrm{d}\boldsymbol{C}'_l\mathrm{d}\boldsymbol{\omega}_{kl}. \tag{2.2.35}$$

Similarly, the reactive transition probabilities $\mathcal{W}_{\mathfrak{F}^r\mathfrak{B}^r}^{\mathfrak{F}^r\mathfrak{B}^r}$ exhibit symmetry properties [LH60] [GG95] [ACG94] [Gio99]. Indeed, for a given reaction $r\in\mathscr{R}$

$$\mathcal{W}_{\mathfrak{F}^r\mathfrak{B}^r}^{\mathrm{F}^r\mathrm{B}^r}\prod_{j\in\mathfrak{B}^r}\beta_{j\mathrm{J}} = \mathcal{W}_{\mathfrak{B}^r\mathfrak{F}^r}^{\mathrm{B}^r\mathrm{F}^r}\prod_{i\in\mathfrak{F}^r}\beta_{i\mathrm{I}}. \tag{2.2.36}$$

Unlike for the nonreactive source term, the species are not conserved during reactive collisions, and only elements are conserved [Gio99]

$$\sum_{k\in\mathfrak{S}}\nu_k^{\mathrm{rf}}\mathfrak{a}_{kl} = \sum_{k\in\mathfrak{S}}\nu_k^{\mathrm{rb}}\mathfrak{a}_{kl},\quad r\in\mathscr{R},\ l\in\mathfrak{A}, \tag{2.2.37}$$

where $\mathfrak{a}_{kl}$ is the number of l^{th} atom in the k^{th} species, and $\mathfrak{A}$ denotes the indexing set for the atoms present in the mixture. The conservation of total mass during reactive collisions follows from equation (2.2.37)

$$\sum_{k\in\mathfrak{S}}\nu_k^{\mathrm{rf}}\mathfrak{m}_k = \sum_{k\in\mathfrak{S}}\nu_k^{\mathrm{rb}}\mathfrak{m}_k. \tag{2.2.38}$$

2.2.5 Collisional invariants of the scattering operator

Collisional invariants are associated with macroscopic conservation equations and are therefore of fundamental importance. Collisional invariants of the scattering operator $\mathcal{S}$ appearing in the Boltzmann equation (2.2.6)-(2.2.7) are functionals $\psi=(\psi_l)_{l\in\mathfrak{S}}$, where $\psi_l=\psi_l(t,\boldsymbol{x},\boldsymbol{C}_l,\mathrm{L})$ is a scalar or tensor function of t, $\boldsymbol{x}$, $\boldsymbol{C}_l$, and L, whose values summed over the particles involved in a nonreactive collision do not change during the collision:

$$\psi_k+\psi_l = \psi'_k+\psi'_l, \qquad\qquad k,l\in\mathfrak{S}, \tag{2.2.39}$$

where $\psi'_k=\psi_k(t,\boldsymbol{x},\boldsymbol{C}'_k,\mathrm{K}')$ and $\psi'_l=\psi_l(t,\boldsymbol{x},\boldsymbol{C}'_l,\mathrm{L}')$.

There are n^s+4 linearly independent scalar collisional invariants, which can be taken in the form [WT62]

$$\begin{cases} \psi^k = (\delta_{kl})_{l\in\mathfrak{S}}\,, & k\in\mathfrak{S},\\ \psi^{n^s+\nu} = (\mathfrak{m}_l C_{l\nu})_{l\in\mathfrak{S}}\,, & \nu\in\{1,2,3\}\,,\\ \psi^{n^s+4} = \Big(\dfrac{1}{2}\mathfrak{m}_l\boldsymbol{C}_l\cdot\boldsymbol{C}_l+E_{l\mathrm{L}}\Big)_{l\in\mathfrak{S}}. \end{cases} \tag{2.2.40}$$

where n^s is the number of species in $\mathfrak{S}$, and $C_{l\nu}$ is the component of $\boldsymbol{C}_l$ in the ν^{th} spatial coordinate. The three kinds of collisional invariants thus defined correspond respectively to the conservation of

chemical species, the conservation of momentum, and the conservation of energy during nonreactive collisions. For micropolar fluids there is an additional linearly independent summational invariant, accounting for the conservation of angular momentum [Gra04] [KA61], but we only consider in this study isotropic mixtures, so that there is no micropolar effects. We name $\mathcal{I}$ the space of collisional invariants with respect to the scattering operator $\mathcal{S}$, i.e., the space spanned by the family $(\psi^p)_{1\leq p\leq n^s+4}$.

We further introduce a tensorial product defined for scalar functions $\xi = (\xi_l)_{l\in\mathfrak{S}}$ and $\zeta = (\zeta_l)_{l\in\mathfrak{S}}$ as

$$\langle\!\langle \xi, \zeta \rangle\!\rangle = \sum_{k\in\mathfrak{S}} \sum_{\mathrm{K}\in\mathfrak{Q}_k} \int \xi_k \zeta_k \, \mathrm{d}\boldsymbol{C}_k, \tag{2.2.41}$$

and more generally for tensors $\boldsymbol{\xi} = (\boldsymbol{\xi}_l)_{l\in\mathfrak{S}}$ and $\boldsymbol{\zeta} = (\boldsymbol{\zeta}_l)_{l\in\mathfrak{S}}$ as

$$\langle\!\langle \boldsymbol{\xi}, \boldsymbol{\zeta} \rangle\!\rangle = \sum_{k\in\mathfrak{S}} \sum_{\mathrm{K}\in\mathfrak{Q}_k} \int \boldsymbol{\xi}_k \odot \boldsymbol{\zeta}_k \, \mathrm{d}\boldsymbol{C}_k, \tag{2.2.42}$$

where $\odot$ stands for the fully contracted product in space [EG94] [Gra04].

The scattering operator $\mathcal{S}$ and the corresponding collisional invariants then satisfy the relations

$$\langle\!\langle \psi^p, \mathcal{S}(f) \rangle\!\rangle = 0, \qquad p \in \{1, \dots, n^s + 4\}. \tag{2.2.43}$$

Indeed, using the reciprocity relation (2.2.35) and symmetrizing between k and l, one can establish that for any $\psi = (\psi_l)_{l\in\mathfrak{S}}$

$$\begin{aligned} 4\langle\!\langle \psi, \mathcal{S}(f) \rangle\!\rangle \;=\; & \sum_{k,l\in\mathfrak{S}} \sum_{\mathrm{K},\mathrm{K}'\in\mathfrak{Q}_k} \sum_{\mathrm{L},\mathrm{L}'\in\mathfrak{Q}_l} \int \left(\psi_k + \psi_l - \psi'_k - \psi'_l\right) \\ & \times \left(f'_k f'_l \frac{a_{k\mathrm{K}} a_{l\mathrm{L}}}{a_{k\mathrm{K}'} a_{l\mathrm{L}'}} - f_k f_l\right) g_{kl} \, \sigma_{kl}^{\mathrm{KLK'L'}} \, \mathrm{d}\boldsymbol{\omega}'_{kl} \, \mathrm{d}\boldsymbol{C}_k \mathrm{d}\boldsymbol{C}_l, \end{aligned} \tag{2.2.44}$$

which is zero as soon as ψ is a collisional invariant.

For our case of interest, it turns out that we have additional orthogonality relations, by considering pairwise interaction terms separately. Indeed, we can decompose the scalar product $\langle\!\langle \cdot \rangle\!\rangle$ as

$$\langle\!\langle \xi, \zeta \rangle\!\rangle = \langle\!\langle \xi_e, \zeta_e \rangle\!\rangle_e + \langle\!\langle \xi_h, \zeta_h \rangle\!\rangle_h, \tag{2.2.45}$$

where

$$\langle\!\langle \xi_e, \zeta_e \rangle\!\rangle_e = \int \xi_e \odot \zeta_e \, \mathrm{d}\boldsymbol{C}_e, \tag{2.2.46}$$

$$\langle\!\langle \xi_h, \zeta_h \rangle\!\rangle_h = \sum_{j\in\mathfrak{H}} \sum_{\mathrm{J}\in\mathfrak{Q}_j} \int \xi_j \odot \zeta_j \, \mathrm{d}\boldsymbol{C}_j, \tag{2.2.47}$$

and obtain, as in [GMM09], the following orthogonality property for pairwise interactions:

$$\langle\!\langle \psi^p_e, \mathcal{S}_{ee} \rangle\!\rangle_e = 0, \tag{2.2.48}$$

$$\langle\!\langle \psi^p_h, \mathcal{S}_{he} \rangle\!\rangle_h + \sum_{j\in\mathfrak{H}} \langle\!\langle \psi^p_e, \mathcal{S}_{ej} \rangle\!\rangle_e = 0, \tag{2.2.49}$$

$$\sum_{j\in\mathfrak{H}} \langle\!\langle \psi^p_h, \mathcal{S}_{hj} \rangle\!\rangle_h = 0, \tag{2.2.50}$$

for any $p \in \{1, \dots, n^s + 4\}$.

2.2.6 Scattering cross-sections

The differential cross-section is taken the following form [Wal58] [CC70] [FK72] [GMM09]:

$$\sigma_{kl}^{\mathrm{KLK'L'}} = \sigma_{kl}^{\mathrm{KLK'L'}} \left(\frac{\mu_{kl} g_{kl}^2}{k_{\mathrm{B}} T^0}, \boldsymbol{\omega}_{kl} \cdot \boldsymbol{\omega}'_{kl} \right), \tag{2.2.51}$$

where $\mu_{kl} = \frac{\mathfrak{m}_k \mathfrak{m}_l}{\mathfrak{m}_k + \mathfrak{m}_l}$ is the reduced mass of the pair of particles, $g_{kl} = |\boldsymbol{C}_k - \boldsymbol{C}_l| = |\boldsymbol{c}_k - \boldsymbol{c}_l|$ is their relative velocity, T^0 is a reference temperature, which is common to all species, and k_{B} is the Boltzmann constant.

2.3 Asymptotic Expansion of the Boltzmann Equations

Dimensional analysis is a necessary preliminary to the Chapman-Enskog procedure. In this regard, we follow the scaling first introduced by Petit and Darrozes [DP75]. We take as small parameter ε the square root of the ratio between the characteristic masses. As shown by Petit and Darrozes, when both the Knudsen number $\mathrm{K}n$ and the mass ratio ε tend to zero, $\mathrm{K}n$ must be chosen proportional to ε. The scaling introduced here will serve as a basis for the derivation of a scaled Boltzmann equation, in which the different terms will depend on the small parameter ε [CC70] [FK72] [Gio99] [GMM09].

2.3.1 Choice of scaling

The reference quantities used in the scaling are denoted by the superscript "0". Most of the reference quantities are common to all species, though it is necessary to distinguish between electron and heavy-species respective characteristic masses, velocities, and kinetic timescales. Also, the characteristic cross-section for inelastic scattering of electrons against heavy species is denoted by $\sigma_{eh}^{\mathrm{in},0} = \sigma_{he}^{\mathrm{in},0}$, while the characteristic cross-section for other scattering processes is denoted by σ^0.

Mass ratio The ratio of the electron mass $\mathfrak{m}_e^0 = \mathfrak{m}_e$ to the characteristic heavy-species mass $\mathfrak{m}_h^0$ is such that

$$\sqrt{\frac{\mathfrak{m}_e^0}{\mathfrak{m}_h^0}} = \varepsilon \ll 1. \tag{2.3.1}$$

The non-dimensional number ε will be the key parameter driving the asymptotic analysis of the plasma.

Temperatures The reference temperature is the same for electrons and heavy species [GMM09]:

$$T_e^0 = T_h^0 = T^0. \tag{2.3.2}$$

This means that the electron temperature T_e and the heavy-species temperature T_h will remain of the same order of magnitude in the model.

Velocities As a consequence of assumptions (2.3.1)-(2.3.2), electrons exhibit a larger thermal speed than heavy species

$$C_h^0 = \sqrt{\frac{k_{\mathrm{B}} T^0}{\mathfrak{m}_h^0}}, \tag{2.3.3}$$

$$C_e^0 = \sqrt{\frac{k_{\mathrm{B}} T^0}{\mathfrak{m}_e^0}} = \frac{1}{\varepsilon} C_h^0. \tag{2.3.4}$$

Table 2.1 – Reference quantities [GMM09].

Physical entity	**Common to all species**	
Temperature	T^0	
Number density	n^0	
Charge	q^0	
Scattering cross-section	σ^0	
Mean free path	$l^0 = \frac{1}{n^0\sigma^0}$	
Macroscopic time scale	t^0	
Hydrodynamic velocity	v^0	
Macroscopic length	$L^0 = v^0 t^0$	
Electric field	E^0	
Magnetic field	B^0	
Reactive source term	$\mathcal{C}_k^0$, $k \in \mathfrak{S}$	
	Electrons	**Heavy species**
Mass	$\mathfrak{m}_e^0 = \mathfrak{m}_e$	$\mathfrak{m}_h^0$
Thermal speed	C_e^0	C_h^0
Kinetic timescale	$t_e^0 = \frac{l^0}{C_e^0}$	$t_h^0 = \frac{l^0}{C_h^0}$
	Hybrid	
Inelastic scattering cross-sections	$\sigma_{he}^{\mathrm{in},0}$	

Besides, the pseudo-Mach number, defined as the reference hydrodynamic velocity v^0 divided by the heavy-species thermal speed C_h^0, is of order one [GMM09]:

$$M_h = \frac{v^0}{C_h^0} \propto 1. \tag{2.3.5}$$

In other words, there is only one reference velocity for the heavy species.

Densities As stated in [DP75], the "weakly ionized" limit is not singular with respect to the limits $\mathrm{K}_n \to 0$ and $\sqrt{\mathfrak{m}_e^0/\mathfrak{m}_h^0} \to 0$. Therefore, we adopt the same scaling for both electron and heavy-species densities:

$$n_e^0 = n_h^0 = n^0. \tag{2.3.6}$$

The results for a weakly ionized plasma will then follow by taking the limit $n_e^0/n_h^0 \to 0$.

Mean free path The characteristic mean free path [GMM09]

$$l^0 = \frac{1}{n^0\sigma^0}. \tag{2.3.7}$$

is imposed by the carrier gas density n^0 and the reference elastic scattering cross-section σ^0 [CC70] [FK72], and is thus common to all species [GMM09]. The reference elastic scattering cross-section

is taken common to all species, since the species molecular diameters are of the same order of magnitude, and Coulomb collisions are negligible in the plasma regime we consider [Hag16a].

Time scales From (2.3.3) and (2.3.4), the kinetic timescales, or the relaxation times of the distribution functions towards their respective quasi-equilibrium states, are given by

$$t_e^0 = \frac{l^0}{C_e^0}, \tag{2.3.8}$$

$$t_h^0 = \frac{l^0}{C_h^0}, \tag{2.3.9}$$

and therefore [GMM09] $t_e^0 = \varepsilon t_h^0$. The macroscopic timescale t^0 is one order of magnitude higher than the heavy-species kinetic timescale t_h^0, so that there are three distinct relevant time scales [GMM09]

$$t_e^0 = \varepsilon t_h^0 = \varepsilon^2 t^0. \tag{2.3.10}$$

Inelastic scattering cross-sections As can be seen from (2.3.10), the thermalization of the electrons is the fastest process corresponding to the kinetic scale t_e^0. This thermalization is ensured by scattering collisions between electrons, and elastic collisions between electrons and heavy species, which given the strong mass disparity do not involve any energy exchange at the lowest order, but allow for isotropization of the electron distribution function in the heavy-species reference frame [GMM09]. Since the heavy species' internal degrees of freedom thermalize at T_h, further allowing for energy exchange between these internal degrees of freedom and electrons at the lowest order would actually require $T_e = T_h$. Thus the reference differential cross-section associated with inelastic scattering between heavy species and electrons $\sigma_{he}^{\mathrm{in},0}$ must be negligible compared to the reference cross-section σ^0 for other scattering collisions.

The second fastest kinetic process is the thermalization of heavy species [GMM09], corresponding to the time scale $t_h^0 = \varepsilon^{-1} t_e^0$ as described in (2.3.10). This thermalization arises from elastic and inelastic collisions between heavy species, while elastic collisions with electrons are of negligible influence at this order due to the strong mass disparity. Again, since the heavy species' internal degrees of freedom thermalize at T_h, inelastic collisions between electrons and heavy species must be neglibible at the lowest order of the Chapman-Enskog expansion for heavy species, otherwise one would have $T_h = T_e$. In other words, $\sigma_{he}^{\mathrm{in},0}$ must be negligible before $\varepsilon\sigma^0$.

Therefore, the inelastic scattering collisions between electrons and heavy species are assumed to be two orders of magnitude slower than the corresponding elastic collisions

$$\sigma_{he}^{\mathrm{in},0} = \varepsilon^2 \sigma^0. \tag{2.3.11}$$

The latter requirement will be discussed in more details in subsection 2.4.5, and other regimes are addressed in the conclusion.

Knudsen number The macroscopic length scale is based on a reference convective length

$$L^0 = v^0 t^0. \tag{2.3.12}$$

As a consequence of the proposed scaling, the Knudsen number

$$\mathrm{K}_n = \frac{l^0}{L^0} = \frac{\varepsilon}{M_h} \tag{2.3.13}$$

is small compared to 1, justifying the choice of a continuum description of the gas.

Electric field The reference electrical and thermal energies are of the same order of magnitude, namely

$$q^0 E^0 L^0 = k_{\text{B}} T^0. \tag{2.3.14}$$

Magnetic field The intensity of the magnetic field is related to the Hall numbers of electron and heavy species, defined as the Larmor frequencies, respectively $\frac{q^0 B^0}{\mathfrak{m}_e}$ and $\frac{q^0 B^0}{\mathfrak{m}_h^0}$, multiplied by the corresponding kinetic timescales. The magnetic field is assumed to be proportional to a power of ε by means of an integer $0 \leq b \leq 1$:

$$\beta_e = \frac{q^0 B^0}{\mathfrak{m}_e^0} t_e^0 = \varepsilon^{1-b}, \tag{2.3.15}$$

$$\beta_h = \frac{q^0 B^0}{\mathfrak{m}_h^0} t_h^0 = \varepsilon \beta_e. \tag{2.3.16}$$

The case $b = 1$ corresponds to strongly magnetized plasmas, the case $b = 0$ to weakly magnetized plasmas.

Table 2.2 – Relative scales for the main plasma physical properties.

Reference quantity	**Scaling relationships**
Characteristic masses	$\mathfrak{m}_e^0 = \varepsilon^2 \, \mathfrak{m}_h^0$
Time scales	$t_e^0 = \varepsilon \, t_h^0 = \varepsilon^2 \, t^0$
Length scales	$l^0 = \frac{\varepsilon}{M_h} \, L^0$
Velocities	$v^0 = M_h \, C_h^0 = \varepsilon M_h \, C_e^0$
Energies	$\mathfrak{m}_e^0 \big(C_e^0\big)^2 = \mathfrak{m}_h^0 \big(C_h^0\big)^2 = q^0 E^0 L^0 = k_{\text{B}} T^0$
Larmor frequencies	$\frac{q^0 B^0}{\mathfrak{m}_h^0} t_h^0 = \varepsilon \, \frac{q^0 B^0}{\mathfrak{m}_e^0} t_e^0 = \varepsilon^{2-b}$
Differential cross-sections	$\sigma_{he}^{\text{in},0} = \sigma_{eh}^{\text{in},0} = \varepsilon^2 \sigma^0$
Reactive source term	$\mathcal{C}_k^0 = \varepsilon \frac{n^0}{t^0 (C_k^0)^3}$, $k \in \mathfrak{S}$

Chemistry The chemical reactions are slow compared to other plasma phenomena, and the reactive source term for the k^{th} species $\mathcal{C}_k(f)$ is of order 1 in ε

$$\mathcal{C}_k^0 = \varepsilon \frac{n^0}{t^0 (C_k^0)^3}, \quad k \in \mathfrak{S}, \tag{2.3.17}$$

where C_k^0 is the order of magnitude of the k^{th} species peculiar velocity, irrespective of the detailed scaling properties of each chemical reaction r. The reference quantities and the scaling adopted are summarized in Table 2.1 and Table 2.2, respectively.

Remark The range of applicability of the fluid model developed here is subject to the assumption of Maxwellian equilibrium distributions that will be obtained in the following section. Apart from the thermal non-equilibrium between electrons and heavy species, two kind of deviation from the

local thermal equilibrium might occur. First, when the ratio of the electric field over the pressure $\frac{E}{p}$ is "too high", namely when the assumption $q^0 E^0 l^0 = \varepsilon k_{\text{B}} T_e^0 = \varepsilon k_{\text{B}} T^0$ is not valid, or when $E/p \gtrsim (\sigma^0/q)(T_e^0/T^0)$ [Rax05], the electron distribution function can depart strongly from a Maxwellian distribution. Second, in the case of high frequency oscillations, namely when the collision frequencies $1/t_e^0$ and $1/t_h^0 = \varepsilon 1/t_e^0$ are comparable with the electric field frequency ν_{RF}, the species distribution function may also depart strongly from the Maxwellian equilibrium [Rax05]. In both cases, one would need a kinetic model rather than a fluid model.

2.3.2 Scaled Boltzmann equations

The dimensional analysis above is applied to Boltzmann equations (2.2.8), written in the heavy-species reference frame. For each variable ϕ, we denote by

$$\hat{\phi} = \frac{\phi}{\phi^0} \tag{2.3.18}$$

the corresponding adimensionalized quantity. The adimensionalized Boltzmann equations then read

$$\begin{aligned}
&\partial_{\hat{t}} \hat{f}_e + \frac{1}{\varepsilon} \left(\widehat{\boldsymbol{C}}_e + \varepsilon\, \widehat{\boldsymbol{v}}_h\right) \cdot \boldsymbol{\partial}_{\widehat{\boldsymbol{x}}} \hat{f}_e + \varepsilon^{-(1+b)}\, \frac{\hat{q}_e}{\widehat{\mathfrak{m}}_e} \left[\left(\widehat{\boldsymbol{C}}_e + \varepsilon\, \widehat{\boldsymbol{v}}_h\right) \wedge \widehat{\mathbf{B}}\right] \cdot \boldsymbol{\partial}_{\widehat{\boldsymbol{C}}_e} \hat{f}_e \\
&\quad + \Big(\frac{1}{\varepsilon}\, \frac{\hat{q}_e}{\widehat{\mathfrak{m}}_e} \widehat{\mathbf{E}} - \varepsilon\, \frac{D\widehat{\boldsymbol{v}}_h}{D\hat{t}}\Big) \cdot \boldsymbol{\partial}_{\widehat{\boldsymbol{C}}_e} \hat{f}_e - \left(\boldsymbol{\partial}_{\widehat{\boldsymbol{C}}_e} \hat{f}_e \otimes \widehat{\boldsymbol{C}}_e\right) : \boldsymbol{\partial}_{\widehat{\boldsymbol{x}}} \widehat{\boldsymbol{v}}_h \\
&\quad = \frac{1}{\varepsilon^2}\, \widehat{\mathcal{S}}_{ee}(\hat{f}_e, \hat{f}_e) + \frac{1}{\varepsilon^2} \sum_{j \in \mathfrak{H}} \widehat{\mathcal{S}}_{ej}(\hat{f}_e, \hat{f}_j) + \varepsilon\, \widehat{\mathcal{C}}_e(\hat{f}),
\end{aligned} \tag{2.3.19}$$

$$\begin{aligned}
&\partial_{\hat{t}} \hat{f}_i + \left(\widehat{\boldsymbol{C}}_i + \widehat{\boldsymbol{v}}_h\right) \cdot \boldsymbol{\partial}_{\widehat{\boldsymbol{x}}} \hat{f}_i + \varepsilon^{1-b}\, \frac{\hat{q}_i}{\widehat{\mathfrak{m}}_i} \left[\left(\widehat{\boldsymbol{C}}_i + \widehat{\boldsymbol{v}}_h\right) \wedge \widehat{\mathbf{B}}\right] \cdot \boldsymbol{\partial}_{\widehat{\boldsymbol{C}}_i} \hat{f}_i \\
&\quad + \Big(\frac{\hat{q}_i}{\widehat{\mathfrak{m}}_i} \widehat{\mathbf{E}} - \frac{D\widehat{\boldsymbol{v}}_h}{D\hat{t}}\Big) \cdot \boldsymbol{\partial}_{\widehat{\boldsymbol{C}}_i} \hat{f}_i - \left(\boldsymbol{\partial}_{\widehat{\boldsymbol{C}}_i} \hat{f}_i \otimes \widehat{\boldsymbol{C}}_i\right) : \boldsymbol{\partial}_{\widehat{\boldsymbol{x}}} \widehat{\boldsymbol{v}}_h \\
&\quad = \frac{1}{\varepsilon^2}\, \widehat{\mathcal{S}}_{ie}(\hat{f}_i, \hat{f}_e) + \frac{1}{\varepsilon} \sum_{j \in \mathfrak{H}} \widehat{\mathcal{S}}_{ij}(\hat{f}_i, \hat{f}_j) + \varepsilon\, \widehat{\mathcal{C}}_i(\hat{f}), \qquad i \in \mathfrak{H}.
\end{aligned} \tag{2.3.20}$$

The Chapman-Enskog method is applied to the adimensionalized Boltzmann equations (2.3.19)-(2.3.20) [GMM09]. For the sake of simplicity the Mach number, which is of order 1 from (2.3.5), can be taken equal to 1, and the "hat" symbol can be dropped, without affecting the fluid equations and transport fluxes derived. Alternatively, equations (2.3.19)-(2.3.20) can be redimensionalized before applying the Chapman-Enskog method, keeping the parameter ε as a formal parameter driving the asymptotic expansion. In this case, ε is equal to 1, eventually. For both methods, the scaled Boltzmann equations are thus written as

$$\begin{aligned}
&\partial_t f_e + \frac{1}{\varepsilon}\, \left(\boldsymbol{C}_e + \varepsilon\, \boldsymbol{v}_h\right) \cdot \boldsymbol{\partial}_{\boldsymbol{x}} f_e + \varepsilon^{-(1+b)}\, \frac{q_e}{\mathfrak{m}_e} \left[\left(\boldsymbol{C}_e + \varepsilon\, \boldsymbol{v}_h\right) \wedge \mathbf{B}\right] \cdot \boldsymbol{\partial}_{\boldsymbol{C}_e} f_e \\
&\quad + \Big(\frac{1}{\varepsilon}\, \frac{q_e}{\mathfrak{m}_e} \mathbf{E} - \varepsilon\, \frac{D\boldsymbol{v}_h}{Dt}\Big) \cdot \boldsymbol{\partial}_{\boldsymbol{C}_e} f_e - \left(\boldsymbol{\partial}_{\boldsymbol{C}_e} f_e \otimes \boldsymbol{C}_e\right) : \boldsymbol{\partial}_{\boldsymbol{x}} \boldsymbol{v}_h \\
&\quad = \frac{1}{\varepsilon^2}\, \mathcal{S}_{ee}\left(f_e, f_e\right) + \frac{1}{\varepsilon^2} \sum_{j \in \mathfrak{H}} \mathcal{S}_{ej}\left(f_e, f_j\right) + \varepsilon\, \mathcal{C}_e\left(f\right),
\end{aligned} \tag{2.3.21}$$

$$\begin{aligned}
&\partial_t f_i + \left(\boldsymbol{C}_i + \boldsymbol{v}_h\right) \cdot \boldsymbol{\partial}_{\boldsymbol{x}} f_i + \varepsilon^{1-b}\, \frac{q_i}{\mathfrak{m}_i} \left[\left(\boldsymbol{C}_i + \boldsymbol{v}_h\right) \wedge \mathbf{B}\right] \cdot \boldsymbol{\partial}_{\boldsymbol{C}_i} f_i \\
&\quad + \Big(\frac{q_i}{\mathfrak{m}_i} \mathbf{E} - \frac{D\boldsymbol{v}_h}{Dt}\Big) \cdot \boldsymbol{\partial}_{\boldsymbol{C}_i} f_i - \left(\boldsymbol{\partial}_{\boldsymbol{C}_i} f_i \otimes \boldsymbol{C}_i\right) : \boldsymbol{\partial}_{\boldsymbol{x}} \boldsymbol{v}_h \\
&\quad = \frac{1}{\varepsilon^2}\, \mathcal{S}_{ie}\left(f_i, f_e\right) + \frac{1}{\varepsilon} \sum_{j \in \mathfrak{H}} \mathcal{S}_{ij}\left(f_i, f_j\right) + \varepsilon\, \mathcal{C}_i\left(f\right), \qquad i \in \mathfrak{H},
\end{aligned} \tag{2.3.22}$$

where the partial scattering operators $\mathcal{S}_{kl}$, $k,l \in \mathfrak{S}$, depend on ε, and are analyzed as follows.

For electron electron collisions the scaled scattering source term reads

$$\mathcal{S}_{ee}(f_e, \tilde{f}_e)\,(\boldsymbol{C}_e) = \int \sigma_{e\tilde{e}} g_{e\tilde{e}} \big(f'_e \tilde{f}'_e - f_e \tilde{f}_e\big)\, \mathrm{d}\boldsymbol{\omega}'_{e\tilde{e}} \mathrm{d}\widetilde{\boldsymbol{C}}_e, \tag{2.3.23}$$

where $f_e = f_e(t, \boldsymbol{x}, \boldsymbol{C}_e)$, $f'_e = f_e(t, \boldsymbol{x}, \boldsymbol{C}'_e)$, $\tilde{f}_e = f_e(t, \boldsymbol{x}, \widetilde{\boldsymbol{C}}_e)$, $\tilde{f}'_e = f_e(t, \boldsymbol{x}, \widetilde{\boldsymbol{C}}'_e)$, where

$$\boldsymbol{\omega}_{e\tilde{e}} = \frac{\boldsymbol{C}_e - \widetilde{\boldsymbol{C}}_e}{|\boldsymbol{C}_e - \widetilde{\boldsymbol{C}}_e|}, \qquad \boldsymbol{\omega}'_{e\tilde{e}} = \frac{\boldsymbol{C}'_e - \widetilde{\boldsymbol{C}}'_e}{|\boldsymbol{C}'_e - \widetilde{\boldsymbol{C}}'_e|}, \tag{2.3.24}$$

$g_{e\tilde{e}} = |\boldsymbol{C}_e - \widetilde{\boldsymbol{C}}_e|$, $g'_{e\tilde{e}} = |\boldsymbol{C}'_e - \widetilde{\boldsymbol{C}}'_e|$, and where

$$\sigma_{e\tilde{e}} = \sigma_{ee}\left(\frac{1}{2}\mathfrak{m}_e g^2_{e\tilde{e}}, \boldsymbol{\omega}_{e\tilde{e}} \cdot \boldsymbol{\omega}'_{e\tilde{e}}\right).$$

The formula for electron heavy-species scattering source term is similar, although we have to distinguish between elastic and inelastic collisions:

$$\begin{aligned}\mathcal{S}_{ei}\,(f_e, f_i)\,(\boldsymbol{C}_e) = &\sum_{\mathrm{I}\in\mathfrak{Q}_i} \int \sigma^{\mathrm{II}}_{ei} g_{ei} \big(f'_e f'_i - f_e f_i\big)\, \mathrm{d}\boldsymbol{\omega}'_{ei} \mathrm{d}\boldsymbol{C}_i \\ &+ \varepsilon^2 \sum_{\substack{\mathrm{I},\mathrm{I}'\in\mathfrak{Q}_i \\ \mathrm{I}'\neq\mathrm{I}}} \int \sigma^{\mathrm{II}'}_{ei} g_{ei} \big(f'_e f'_i \frac{a_{i\mathrm{I}}}{a_{i\mathrm{I}'}} - f_e f_i\big)\, \mathrm{d}\boldsymbol{\omega}'_{ei} \mathrm{d}\boldsymbol{C}_i,\end{aligned} \tag{2.3.25}$$

where $f_e = f_e(t, \boldsymbol{x}, \boldsymbol{C}_e)$, $f'_e = f_e(t, \boldsymbol{x}, \boldsymbol{C}'_e)$, $f_i = f_i(t, \boldsymbol{x}, \boldsymbol{C}_i, \mathrm{I})$, $f'_i = f_i(t, \boldsymbol{x}, \boldsymbol{C}'_i, \mathrm{I}')$, where

$$\boldsymbol{\omega}_{ei} = \frac{\boldsymbol{C}_e - \varepsilon \boldsymbol{C}_i}{|\boldsymbol{C}_e - \varepsilon \boldsymbol{C}_i|}, \qquad \boldsymbol{\omega}'_{ei} = \frac{\boldsymbol{C}'_e - \varepsilon \boldsymbol{C}'_i}{|\boldsymbol{C}'_e - \varepsilon \boldsymbol{C}'_i|}, \tag{2.3.26}$$

$g_{ei} = |\boldsymbol{C}_e - \varepsilon \boldsymbol{C}_i|$, $g'_{ei} = |\boldsymbol{C}'_e - \varepsilon \boldsymbol{C}'_i|$, and where

$$\sigma^{\mathrm{II}'}_{ei} = \sigma^{\mathrm{II}'}_{ei}\left(\mu_{ei} g^2_{ei}, \boldsymbol{\omega}_{ei} \cdot \boldsymbol{\omega}'_{ei}\right),$$

with $\mu_{ie} = \mathfrak{m}_e \mathfrak{m}_i / (\mathfrak{m}_i + \varepsilon^2 \mathfrak{m}_e)$.

We obtain as well the source term corresponding to collisions of heavy species against electrons

$$\begin{aligned}\mathcal{S}_{ie}\,(f_i, f_e)\,(\boldsymbol{C}_i, \mathrm{I}) = &\int \sigma^{\mathrm{II}}_{ie} g_{ie} \big(f'_i f'_e - f_i f_e\big)\, \mathrm{d}\boldsymbol{\omega}'_{ie} \mathrm{d}\boldsymbol{C}_e \\ &+ \varepsilon^2 \sum_{\substack{\mathrm{I}'\in\mathfrak{Q}_i \\ \mathrm{I}'\neq\mathrm{I}}} \int \sigma^{\mathrm{II}'}_{ie} g_{ie} \big(f'_i f'_e \frac{a_{i\mathrm{I}}}{a_{i\mathrm{I}'}} - f_i f_e\big)\, \mathrm{d}\boldsymbol{\omega}'_{ie} \mathrm{d}\boldsymbol{C}_e,\end{aligned} \tag{2.3.27}$$

where $g_{ie} = |\varepsilon \boldsymbol{C}_i - \boldsymbol{C}_e|$, $g'_{ie} = |\varepsilon \boldsymbol{C}'_i - \boldsymbol{C}'_e|$, where

$$\boldsymbol{\omega}_{ie} = \frac{\varepsilon \boldsymbol{C}_i - \boldsymbol{C}_e}{|\varepsilon \boldsymbol{C}_i - \boldsymbol{C}_e|}, \qquad \boldsymbol{\omega}'_{ie} = \frac{\varepsilon \boldsymbol{C}'_i - \boldsymbol{C}'_e}{|\varepsilon \boldsymbol{C}'_i - \boldsymbol{C}'_e|}, \tag{2.3.28}$$

and where

$$\sigma^{\mathrm{II}'}_{ie} = \sigma^{\mathrm{II}'}_{ie}\left(\mu_{ie} g^2_{ie}, \boldsymbol{\omega}_{ie} \cdot \boldsymbol{\omega}'_{ie}\right),$$

with $\mu_{ie} = \mu_{ei} = \mathfrak{m}_e \mathfrak{m}_i / (\mathfrak{m}_i + \varepsilon^2 \mathfrak{m}_e)$.

Finally, we obtain for collisions between two heavy species

$$\mathcal{S}_{ij}\left(f_i,f_j\right)\left(\boldsymbol{C}_i,\mathrm{I}\right)=\sum_{\mathrm{I}'\in\mathfrak{Q}_i}\sum_{\mathrm{J},\mathrm{J}'\in\mathfrak{Q}_j}\int\sigma_{ij}^{\mathrm{IJI}'\mathrm{J}'}g_{ij}\big(f_i'f_j'\frac{a_{i\mathrm{I}}a_{j\mathrm{J}}}{a_{i\mathrm{I}'}a_{j\mathrm{J}'}}-f_if_j\big)\,\mathrm{d}\boldsymbol{\omega}_{ij}'\mathrm{d}\boldsymbol{C}_j, \tag{2.3.29}$$

where

$$\sigma_{ij}^{\mathrm{IJI}'\mathrm{J}'}=\sigma_{ij}^{\mathrm{IJI}'\mathrm{J}'}\left(\mu_{ij}g_{ij}^2,\boldsymbol{\omega}_{ij}\cdot\boldsymbol{\omega}_{ij}'\right),$$

Unlike for the nonreactive source terms just stated, we do not consider the different orders of magnitude in ε associated with the motion of heavy species and electrons when computing the chemistry source terms. We only consider as a first approximation that chemical reactions occur "slowly", namely at order ε, and thus retain expression (2.2.28) for $\mathcal{C}_e(f)$, $\mathcal{C}_i(f)$, $i\in\mathfrak{H}$.

2.3.3 Scaled collisional invariants

We also apply the scaling above to the space $\mathcal{I}$ of collisional invariants of the scattering operator. The space of collisional invariants after scaling, denoted by $\mathcal{I}^\varepsilon$, is spanned by the family $\psi^l=(\psi_e^l,\psi_h^l)$, $l\in\{1,\dots,n^s+4\}$, defined as

$$\begin{cases}\psi_e^k=\delta_{ke}, & \psi_h^k=\left(\delta_{kj}\right)_{j\in\mathfrak{H}}, & k\in\mathfrak{S},\\ \psi_e^{n^s+\nu}=\varepsilon\ \mathfrak{m}_eC_{e\nu}, & \psi_h^{n^s+\nu}=\left(\mathfrak{m}_jC_{j\nu}\right)_{j\in\mathfrak{H}}, & \nu\in\{1,2,3\},\\ \psi_e^{n^s+4}=\dfrac{1}{2}\mathfrak{m}_e\boldsymbol{C}_e\cdot\boldsymbol{C}_e, & \psi_h^{n^s+4}=\Big(\dfrac{1}{2}\mathfrak{m}_j\boldsymbol{C}_j\cdot\boldsymbol{C}_j+E_{j\mathrm{J}}\Big)_{j\in\mathfrak{H}}.\end{cases} \tag{2.3.30}$$

From now on, ψ^l, $l\in\{1,\dots,n^s+4\}$ will refer only to the collisional invariants after scaling. We have seen in the previous section that the nonreactive collision operator can be written as

$$\mathcal{S}=\left(\frac{1}{\varepsilon^2}\mathcal{S}_e,\frac{1}{\varepsilon}\mathcal{S}_h\right), \tag{2.3.31}$$

where $\mathcal{S}_e=\mathcal{S}_{ee}+\sum_{j\in\mathfrak{H}}\mathcal{S}_{ej}$ and $\mathcal{S}_i=\frac{1}{\varepsilon}\mathcal{S}_{ie}+\sum_{j\in\mathfrak{H}}\mathcal{S}_{ij}$, $i\in\mathfrak{H}$, are the full scattering source terms for electron and heavy-particle species, respectively. We also recall the expression of the scalar product defined above (2.2.45):

$$\begin{aligned}\langle\!\langle\xi,\zeta\rangle\!\rangle &= \langle\!\langle\xi_e,\zeta_e\rangle\!\rangle_e+\langle\!\langle\xi_h,\zeta_h\rangle\!\rangle_h\\ &= \int\xi_e\odot\zeta_e\,\mathrm{d}\boldsymbol{C}_e+\sum_{j\in\mathfrak{H}}\sum_{\mathrm{J}\in\mathfrak{Q}_j}\int\xi_j\odot\zeta_j\,\mathrm{d}\boldsymbol{C}_j.\end{aligned}$$

The orthogonality relations (2.2.48), (2.2.49), (2.2.50) remain valid after scaling, and the cross-collision identities (2.2.49) now read

$$\sum_{j\in\mathfrak{H}}\langle\!\langle\psi_e^e,\mathcal{S}_{ej}\rangle\!\rangle_e=0,\qquad\qquad\langle\!\langle\psi_h^i,\mathcal{S}_{he}\rangle\!\rangle_h=0,\quad i\in\mathfrak{H}, \tag{2.3.32}$$

$$\langle\!\langle\mathfrak{m}_hC_{h\nu},\mathcal{S}_{he}\rangle\!\rangle_h+\varepsilon\sum_{j\in\mathfrak{H}}\langle\!\langle\mathfrak{m}_eC_{e\nu},\mathcal{S}_{ej}\rangle\!\rangle_e=0,\quad\nu\in\{1,2,3\}, \tag{2.3.33}$$

$$\langle\!\langle\psi_h^{n^s+4},\mathcal{S}_{he}\rangle\!\rangle_h+\sum_{j\in\mathfrak{H}}\langle\!\langle\psi_e^{n^s+4},\mathcal{S}_{ej}\rangle\!\rangle_e=0. \tag{2.3.34}$$

We also introduce two vector spaces obtained by projection of the space of collisional invariants $\mathcal{I}$. For all ε, $\mathcal{I}_e^\varepsilon$ is the space spanned by

$$\begin{cases}\psi_e^e=1,\\ \psi_e^{n^s+\nu}=\varepsilon\ \mathfrak{m}_eC_{e\nu}, & \nu\in\{1,2,3\},\\ \psi_e^{n^s+4}=\dfrac{1}{2}\mathfrak{m}_e\boldsymbol{C}_e\cdot\boldsymbol{C}_e,\end{cases} \tag{2.3.35}$$

and $\mathcal{I}_h$ is the space spanned by

$$\begin{cases} \psi_h^i = (\delta_{ij})_{j\in\mathfrak{H}}\,, \\ \psi_h^{n^s+\nu} = (\mathfrak{m}_j C_{j\nu})_{j\in\mathfrak{H}}\,, & \nu\in\{1,2,3\}\,, \\ \psi_h^{n^s+4} = \Big(\dfrac{1}{2}\mathfrak{m}_j \boldsymbol{C}_j\cdot\boldsymbol{C}_j + E_{j\text{I}}\Big)_{j\in\mathfrak{H}}. \end{cases} \tag{2.3.36}$$

The macrosopic properties of the fluid mixture can then be expressed as partial scalar products of the partial distribution functions f_e and f_h with the electron and heavy-species collisional invariants, respectively. When taking into account the scaling, one obtains

$$\begin{cases} \langle\!\langle f_e, \psi_e^e\rangle\!\rangle_e = n_e \\ \dfrac{1}{\varepsilon}\,\langle\!\langle f_e, \mathfrak{m}_e C_{e\nu}\rangle\!\rangle_e = \rho_e\,(v_{e\nu}-v_{h\nu})\,, \quad \nu\in\{1,2,3\} \\ \langle\!\langle f_e, \psi_e^{n^s+4}\rangle\!\rangle_e = \mathcal{E}_e + \varepsilon^2\,\dfrac{1}{2}\rho_e\,(\boldsymbol{v}_e-\boldsymbol{v}_h)\cdot(\boldsymbol{v}_e-\boldsymbol{v}_h) \end{cases} \tag{2.3.37}$$

for electrons, and

$$\begin{cases} \langle\!\langle f_h, \psi_h^j\rangle\!\rangle_h = n_j, & j\in\mathfrak{H} \\ \langle\!\langle f_h, \psi_h^{n^s+\nu}\rangle\!\rangle_h = 0, & \nu\in\{1,2,3\} \\ \langle\!\langle f_h, \psi_h^{n^s+4}\rangle\!\rangle_h = \mathcal{E}_h \end{cases} \tag{2.3.38}$$

for the heavy species, where $\mathcal{E}_e$ and $\mathcal{E}_h$ denote the respective internal energies per unit volume.

Note in particular that, in the limit $\varepsilon\to 0$, the space of electron collisional invariants $\mathcal{I}_e^\varepsilon$, is reduced to the space of isotropic invariants, denoted by $\mathcal{I}_e^0$, which is spanned by

$$\begin{cases} \psi_e^e = 1, \\ \psi_e^{n^s+4} = \dfrac{1}{2}\mathfrak{m}_e \boldsymbol{C}_e\cdot\boldsymbol{C}_e. \end{cases} \tag{2.3.39}$$

In other words, the electron momentum collisional invariant vanishes in the limit $\varepsilon\to 0$. This is because electron momentum is negligible before heavy-species momentum, and is related to the isotropization of the zeroth-order electron distribution function, as shall be seen later. The relevant sets of collisional invariants for our purpose are thus $\mathcal{I}_e^0$ and $\mathcal{I}_h$.

2.3.4 Asymptotic expansion of collision operators

We now derive asymptotic expansions in powers of ε for the scattering operators $\mathcal{S}_{ei}$ and $\mathcal{S}_{ie}$, $i\in\mathfrak{H}$. Conservation of momentum and energy during a binary collision between an electron and a molecule of the i^{th} heavy species read, when taking into account the scaling with respect to ε

$$\begin{cases} \mathfrak{m}_i\boldsymbol{C}_i + \varepsilon\ \mathfrak{m}_e\boldsymbol{C}_e = \mathfrak{m}_i\boldsymbol{C}_i' + \varepsilon\ \mathfrak{m}_e\boldsymbol{C}_e', \\ \dfrac{1}{2}\mathfrak{m}_e\dfrac{1}{\big(1+\varepsilon^2\frac{\mathfrak{m}_e}{\mathfrak{m}_i}\big)}g^2 + E_{i\text{I}} = \dfrac{1}{2}\mathfrak{m}_e\dfrac{1}{\big(1+\varepsilon^2\frac{\mathfrak{m}_e}{\mathfrak{m}_i}\big)}g'^2 + E_{i\text{I}'}, \end{cases} \tag{2.3.40}$$

where we have denoted by $g=g_{ie}=g_{ei}=|\varepsilon\boldsymbol{C}_i-\boldsymbol{C}_e|$ and by $g'=g'_{ie}=g'_{ei}=|\varepsilon\boldsymbol{C}'_i-\boldsymbol{C}'_e|$ the relative velocities of colliding species respectively before and after collision. Setting $\Delta E_{\text{I}'}=E_{i\text{I}'}-E_{i\text{I}}$, we rewrite the latter expression in the form

$$\begin{cases} \mathfrak{m}_i\boldsymbol{C}_i + \varepsilon\ \mathfrak{m}_e\boldsymbol{C}_e = \mathfrak{m}_i\boldsymbol{C}_i' + \varepsilon\ \mathfrak{m}_e\boldsymbol{C}_e', \\ \Delta E_{\text{I}'} + \dfrac{1}{2}\mathfrak{m}_e\dfrac{1}{\big(1+\varepsilon^2\frac{\mathfrak{m}_e}{\mathfrak{m}_i}\big)}\big(g'^2-g^2\big) = 0. \end{cases} \tag{2.3.41}$$

Scattering of the heavy species against electrons

The scattering operator for i^{th}-heavy-species electron collisions $\mathcal{S}_{ie}$ was stated above in equation (2.3.27). The change of variable $\boldsymbol{C}_e^{(0)} = \frac{\boldsymbol{C}_e - \varepsilon \boldsymbol{C}_i}{\left(1+\varepsilon^2 \frac{\mathfrak{m}_e}{\mathfrak{m}_i}\right)^{\frac{1}{2}}}$, with

$$\mathrm{d}\boldsymbol{C}_e = \left(1 + \varepsilon^2 \frac{\mathfrak{m}_e}{\mathfrak{m}_i}\right)^{\frac{3}{2}} \mathrm{d}\boldsymbol{C}_e^{(0)},$$

allows us to eliminate the dependance in ε of the differential cross-section [GMM09], yielding

$$\begin{aligned} \mathcal{S}_{ie}\left(f_i, f_e\right)(C_i, \mathrm{I}) = & \int \sigma_{ie}^{\mathrm{II}} |\boldsymbol{C}_e^{(0)}| \left(1 + \varepsilon^2 \frac{\mathfrak{m}_e}{\mathfrak{m}_i}\right)^2 \left(f_i' f_e' - f_i f_e\right) \mathrm{d}\boldsymbol{\omega}_{ie}' \mathrm{d}\boldsymbol{C}_e^{(0)} \\ & + \varepsilon^2 \sum_{\substack{\mathrm{I}' \in \mathfrak{Q}_i \\ \mathrm{I}' \neq \mathrm{I}}} \int \sigma_{ie}^{\mathrm{II}'} |\boldsymbol{C}_e^{(0)}| \left(1 + \varepsilon^2 \frac{\mathfrak{m}_e}{\mathfrak{m}_i}\right)^2 \left(f_i' f_e' \frac{a_{i\mathrm{I}}}{a_{i\mathrm{I}'}} - f_i f_e\right) \mathrm{d}\boldsymbol{\omega}_{ie}' \mathrm{d}\boldsymbol{C}_e^{(0)}, \end{aligned} \tag{2.3.42}$$

where

$$\sigma_{ie}^{\mathrm{II}'} = \sigma_{ie}^{\mathrm{II}'} \left(\mathfrak{m}_e |\boldsymbol{C}_e^{(0)}|^2, \frac{\boldsymbol{C}_e^{(0)}}{|\boldsymbol{C}_e^{(0)}|} \cdot \boldsymbol{\omega}_{ie}' \right). \tag{2.3.43}$$

The variable $\boldsymbol{C}_e^{(0)}$ is the zeroth-order electron velocity before collision.

Expansion of the species velocities Conservation equations (2.3.41) associated with collisions between molecules of the i^{th} heavy species and electrons read, after change of variable

$$\begin{cases} \boldsymbol{C}_i' = \boldsymbol{C}_i + \varepsilon \dfrac{\mathfrak{m}_e}{\mathfrak{m}_i} \dfrac{1}{\left(1 + \varepsilon^2 \frac{\mathfrak{m}_e}{\mathfrak{m}_i}\right)^{\frac{1}{2}}} \left(\boldsymbol{C}_e^{(0)} + |\boldsymbol{C}_e^{(0)}| \left(1 - \dfrac{\Delta E_{\mathrm{II}'}}{\frac{1}{2}\mathfrak{m}_e |\boldsymbol{C}_e^{(0)}|^2}\right)^{\frac{1}{2}} \boldsymbol{\omega}_{ie}' \right), \\ \boldsymbol{C}_e' = \varepsilon \boldsymbol{C}_i - \dfrac{1}{\left(1 + \varepsilon^2 \frac{\mathfrak{m}_e}{\mathfrak{m}_i}\right)^{\frac{1}{2}}} \left(|\boldsymbol{C}_e^{(0)}| \left(1 - \dfrac{\Delta E_{\mathrm{II}'}}{\frac{1}{2}\mathfrak{m}_e |\boldsymbol{C}_e^{(0)}|^2}\right)^{\frac{1}{2}} \boldsymbol{\omega}_{ie}' - \varepsilon^2 \dfrac{\mathfrak{m}_e}{\mathfrak{m}_i} \boldsymbol{C}_e^{(0)} \right), \end{cases} \tag{2.3.44}$$

yielding the following asymptotic expansion:

$$\begin{cases} \boldsymbol{C}_i' = \boldsymbol{C}_i - \varepsilon \dfrac{\mathfrak{m}_e}{\mathfrak{m}_i} (\boldsymbol{C}_e'^{(0)} - \boldsymbol{C}_e^{(0)}) + O(\varepsilon^3), \\ \boldsymbol{C}_e' = \boldsymbol{C}_e'^{(0)} + \varepsilon\, \boldsymbol{C}_i - \dfrac{\varepsilon^2}{2} \dfrac{\mathfrak{m}_e}{\mathfrak{m}_i} (\boldsymbol{C}_e'^{(0)} - 2\boldsymbol{C}_e^{(0)}) + O(\varepsilon^4), \\ \boldsymbol{C}_e = \boldsymbol{C}_e^{(0)} + \varepsilon\, \boldsymbol{C}_i + \dfrac{\varepsilon^2}{2} \dfrac{\mathfrak{m}_e}{\mathfrak{m}_i} \boldsymbol{C}_e^{(0)} + O(\varepsilon^4), \end{cases} \tag{2.3.45}$$

where $\boldsymbol{C}_e'^{(0)}$ is the zeroth-order electron velocity after collision

$$\boldsymbol{C}_e'^{(0)} = -|\boldsymbol{C}_e'^{(0)}|\, \boldsymbol{\omega}_{ie}' = -|\boldsymbol{C}_e^{(0)}| \left(1 - \frac{\Delta E_{\mathrm{II}'}}{\frac{1}{2}\mathfrak{m}_e |\boldsymbol{C}_e^{(0)}|^2}\right)^{\frac{1}{2}} \boldsymbol{\omega}_{ie}'. \tag{2.3.46}$$

We thus obtain an expansion of the distribution functions

$$f_i\left(\boldsymbol{C}_i', \mathrm{I}'\right) = f_i\left(\boldsymbol{C}_i, \mathrm{I}'\right) - \varepsilon\, \frac{\mathfrak{m}_e}{\mathfrak{m}_i}\, \boldsymbol{\partial}_{\boldsymbol{C}_i} f_i\left(\boldsymbol{C}_i, \mathrm{I}'\right) \cdot \left(\boldsymbol{C}_e'^{(0)} - \boldsymbol{C}_e^{(0)}\right) \tag{2.3.47}$$
$$+ \frac{\varepsilon^2}{2}\, \frac{\mathfrak{m}_e^2}{\mathfrak{m}_i^2}\, \boldsymbol{\partial}_{\boldsymbol{C}_i \boldsymbol{C}_i} f_i\left(\boldsymbol{C}_i, \mathrm{I}'\right) : \left(\boldsymbol{C}_e'^{(0)} - \boldsymbol{C}_e^{(0)}\right) \otimes \left(\boldsymbol{C}_e'^{(0)} - \boldsymbol{C}_e^{(0)}\right) + O(\varepsilon^3),$$

$$f_e\left(\boldsymbol{C}_e'\right) = f_e(\boldsymbol{C}_e'^{(0)}) + \varepsilon\, \boldsymbol{\partial}_{\boldsymbol{C}_e} f_e(\boldsymbol{C}_e'^{(0)}) \cdot \boldsymbol{C}_i + \frac{\varepsilon^2}{2}\, \boldsymbol{\partial}_{\boldsymbol{C}_e \boldsymbol{C}_e} f_e(\boldsymbol{C}_e'^{(0)}) : \boldsymbol{C}_i \otimes \boldsymbol{C}_i \tag{2.3.48}$$
$$- \frac{\varepsilon^2}{2}\, \frac{\mathfrak{m}_e}{\mathfrak{m}_i}\, \boldsymbol{\partial}_{\boldsymbol{C}_e} f_e(\boldsymbol{C}_e'^{(0)}) \cdot \left(\boldsymbol{C}_e'^{(0)} - 2\boldsymbol{C}_e^{(0)}\right) + O(\varepsilon^3),$$

$$f_e\left(\boldsymbol{C}_e\right) = f_e(\boldsymbol{C}_e^{(0)}) + \varepsilon\, \boldsymbol{\partial}_{\boldsymbol{C}_e} f_e(\boldsymbol{C}_e^{(0)}) \cdot \boldsymbol{C}_i + \frac{\varepsilon^2}{2}\, \boldsymbol{\partial}_{\boldsymbol{C}_e \boldsymbol{C}_e} f_e(\boldsymbol{C}_e^{(0)}) : \boldsymbol{C}_i \otimes \boldsymbol{C}_i \tag{2.3.49}$$
$$+ \frac{\varepsilon^2}{2}\, \frac{\mathfrak{m}_e}{\mathfrak{m}_i}\, \boldsymbol{\partial}_{\boldsymbol{C}_e} f_e(\boldsymbol{C}_e^{(0)}) \cdot \boldsymbol{C}_e^{(0)} + O(\varepsilon^3).$$

Expansion of $\mathcal{S}_{ie}$ Upon introducing the asymptotic development (2.3.47)-(2.3.49) in expression (2.3.42), the collision operator $\mathcal{S}_{ie}$, $i \in \mathfrak{H}$, can be expanded in the form

$$\mathcal{S}_{ie} = \varepsilon\, \mathcal{S}_{ie}^1 + \ \varepsilon^2\, \mathcal{S}_{ie}^2 + \ O(\varepsilon^3). \tag{2.3.50}$$

The zeroth-order collision operator $\mathcal{S}_{ie}^0$ cancels. Indeed, from (2.3.42)

$$\begin{aligned}\mathcal{S}_{ie}^0\left(f_i, f_e\right)\left(C_i, \mathrm{I}\right) &= \int \sigma_{ie}^{\mathrm{II}} |\boldsymbol{C}_e^{(0)}| \left(f_i(\boldsymbol{C}_i, \mathrm{I}) f_e(\boldsymbol{C}_e'^{(0)}) - f_i(\boldsymbol{C}_i, \mathrm{I}) f_e(\boldsymbol{C}_e^{(0)})\right) \mathrm{d}\boldsymbol{\omega}_{ie}' \mathrm{d}\boldsymbol{C}_e^{(0)} \\ &= f_i(\boldsymbol{C}_i, \mathrm{I}) \int \sigma_{ie}^{\mathrm{II}} |\boldsymbol{C}_e^{(0)}| \left(f_e(-|\boldsymbol{C}_e^{(0)}| \boldsymbol{\omega}_{ie}') - f_e(\boldsymbol{C}_e^{(0)})\right) \mathrm{d}\boldsymbol{\omega}_{ie}' \mathrm{d}\boldsymbol{C}_e^{(0)},\end{aligned}$$

where $\sigma_{ie}^{\mathrm{II}}$ was given in (2.3.43). The successive changes of variable $\boldsymbol{C}_e^{(0)} = -|\boldsymbol{C}_e^{(0)}| \boldsymbol{\omega}_{ie}$, with $\mathrm{d}\boldsymbol{C}_e^{(0)} = |\boldsymbol{C}_e^{(0)}|^2\, \mathrm{d}|\boldsymbol{C}_e^{(0)}| \mathrm{d}\boldsymbol{\omega}_{ie}$, and $(\boldsymbol{\omega_{ie}}', \boldsymbol{\omega_{ie}}) \leftrightarrow (\boldsymbol{\omega_{ie}}, \boldsymbol{\omega_{ie}}')$, then yield

$$\begin{aligned}&\mathcal{S}_{ie}^0\left(f_i, f_e\right)\left(C_i, \mathrm{I}\right) \\ &= f_i(\boldsymbol{C}_i, \mathrm{I}) \int \sigma_{ie}^{\mathrm{II}} |\boldsymbol{C}_e^{(0)}|^3 \left(f_e(-|\boldsymbol{C}_e^{(0)}| \boldsymbol{\omega}_{ie}') - f_e(-|\boldsymbol{C}_e^{(0)}| \boldsymbol{\omega}_{ie})\right) \mathrm{d}|\boldsymbol{C}_e^{(0)}| \mathrm{d}\boldsymbol{\omega}_{ie} \mathrm{d}\boldsymbol{\omega}_{ie}' \\ &= f_i(\boldsymbol{C}_i, \mathrm{I}) \int \sigma_{ie}^{\mathrm{II}} |\boldsymbol{C}_e^{(0)}|^3 \left(f_e(-|\boldsymbol{C}_e^{(0)}| \boldsymbol{\omega}_{ie}) - f_e(-|\boldsymbol{C}_e^{(0)}| \boldsymbol{\omega}_{ie}')\right) \mathrm{d}|\boldsymbol{C}_e^{(0)}| \mathrm{d}\boldsymbol{\omega}_{ie} \mathrm{d}\boldsymbol{\omega}_{ie}' \\ &= -\mathcal{S}_{ie}^0\left(f_i, f_e\right)\left(C_i, \mathrm{I}\right),\end{aligned}$$

where $\sigma_{ie}^{\mathrm{II}} = \sigma_{ie}^{\mathrm{II}}(\mathfrak{m}_e |\boldsymbol{C}_e^{(0)}|^2, \boldsymbol{\omega}_{ie} \cdot \boldsymbol{\omega}_{ie}')$, so that finally

$$\mathcal{S}_{ie}^0\left(f_i, f_e\right)\left(\boldsymbol{C}_i, \mathrm{I}\right) = 0, \qquad i \in \mathfrak{H}, \mathrm{I} \in \mathfrak{Q}_i. \tag{2.3.51}$$

From similar calculations, the first-order term $\mathcal{S}_{ie}^1\left(f_i, f_e\right)\left(\boldsymbol{C}_i, \mathrm{I}\right)$ reads, for $i \in \mathfrak{H}$, $\mathrm{I} \in \mathfrak{Q}_i$

$$\mathcal{S}_{ie}^1\left(f_i, f_e\right)\left(\boldsymbol{C}_i, \mathrm{I}\right) = -\frac{\mathfrak{m}_e}{\mathfrak{m}_i}\, \boldsymbol{\partial}_{\boldsymbol{C}_i} f_i(\boldsymbol{C}_i, \mathrm{I}) \cdot \int \Sigma_{\mathrm{II}}^{(1)}(|\boldsymbol{C}_e|^2)\, |\boldsymbol{C}_e|\, f_e(\boldsymbol{C}_e)\, \boldsymbol{C}_e\, \mathrm{d}\boldsymbol{C}_e, \tag{2.3.52}$$

where we have dropped the upperscript (0) on the integration variable $\boldsymbol{C}_e$ for the sake of simplicity. The generalized momentum cross-section in thermal non-equilibrium context $\Sigma_{\mathrm{II}'}^{(l)}$ is defined, for given $i \in \mathfrak{H}$, $\mathrm{I} \in \mathfrak{Q}_i$ and $\mathrm{I}' \in \mathfrak{Q}_i$, by

$$\Sigma_{\mathrm{II}'}^{(l)}(|\boldsymbol{C}_e|^2) = 2\pi \left(\frac{\mathfrak{m}_e}{\mathfrak{m}_i}\right)^l \int_0^\pi \sigma_{ie}^{\mathrm{II}'}\left(\mathfrak{m}_e |\boldsymbol{C}_e|^2, \cos\theta\right) \left(1 - \cos^l\theta\right) \sin\theta\, \mathrm{d}\theta, \quad l \in \mathbb{N}^*, \tag{2.3.53}$$

where the symbol θ represents the angle between the vectors $\boldsymbol{\omega}'_{ie} = \varepsilon \boldsymbol{C}'_i - \boldsymbol{C}'_e$ and $\boldsymbol{\omega}_{ie} = \varepsilon \boldsymbol{C}_i - \boldsymbol{C}_e$. For $l = 1$, this cross-section represents the average momentum transferred in encounters between electrons and molecules of the i^{th} heavy species with initial quantum state I and final quantum state I′, for a given initial value of the electron kinetic energy $\mathfrak{m}_e |\boldsymbol{C}_e|^2$. We also define

$$\Sigma^{(0)}_{\text{II}'}(|\boldsymbol{C}_e|^2) = 2\pi \int_0^\pi \sigma^{\text{II}'}_{ie}\big(\mathfrak{m}_e|\boldsymbol{C}_e|^2, \cos\theta\big) \sin\theta \, \mathrm{d}\theta, \qquad i \in \mathfrak{H}, \quad \text{I}, \text{I}' \in \mathfrak{Q}_i. \tag{2.3.54}$$

Finally, the second-order term can be decomposed into an elastic and an inelastic contributions:

$$\mathcal{S}^2_{ie} = \mathcal{S}^{2,\text{el}}_{ie} + \mathcal{S}^{2,\text{in}}_{ie}. \tag{2.3.55}$$

The elastic contribution $\mathcal{S}^{2,\text{el}}_{ie}\left(f_i, f_e\right)(\boldsymbol{C}_i, \text{I})$ reads, for $i \in \mathfrak{H}$, $\text{I} \in \mathfrak{Q}_i$

$$\begin{aligned}
&\mathcal{S}^{2,\text{el}}_{ie}\left(f_i, f_e\right)(\boldsymbol{C}_i, \text{I}) = \qquad (2.3.56)\\
&-\frac{\mathfrak{m}_e}{\mathfrak{m}_i}\, \boldsymbol{\partial}_{\boldsymbol{C}_i}\left(f_i(\boldsymbol{C}_i, \text{I})\boldsymbol{C}_i\right) : \int \Sigma^{(1)}_{\text{II}}(|\boldsymbol{C}_e|^2)\, |\boldsymbol{C}_e| \left(\boldsymbol{C}_e \otimes \boldsymbol{\partial}_{\boldsymbol{C}_e} f_e(\boldsymbol{C}_e)\right) \mathrm{d}\boldsymbol{C}_e\\
&+\frac{1}{4}\frac{\mathfrak{m}_e^2}{\mathfrak{m}_i^2}\, \boldsymbol{\partial}_{\boldsymbol{C}_i\boldsymbol{C}_i} f_i(\boldsymbol{C}_i, \text{I}) : \int \Sigma^{(2)}_{\text{II}}(|\boldsymbol{C}_e|^2)\, |\boldsymbol{C}_e|\, f_e(\boldsymbol{C}_e) \left(|\boldsymbol{C}_e|^2 \mathbb{I} - 3\boldsymbol{C}_e \otimes \boldsymbol{C}_e\right) \mathrm{d}\boldsymbol{C}_e\\
&+\frac{\mathfrak{m}_e^2}{\mathfrak{m}_i^2}\, \boldsymbol{\partial}_{\boldsymbol{C}_i\boldsymbol{C}_i} f_i(\boldsymbol{C}_i, \text{I}) : \int \Sigma^{(1)}_{\text{II}}(|\boldsymbol{C}_e|^2)\, |\boldsymbol{C}_e|\, f_e(\boldsymbol{C}_e) \left(\boldsymbol{C}_e \otimes \boldsymbol{C}_e\right) \mathrm{d}\boldsymbol{C}_e,
\end{aligned}$$

while the inelastic term can be written as

$$\begin{aligned}
&\mathcal{S}^{2,\text{in}}_{ie}\left(f_i, f_e\right)(\boldsymbol{C}_i, \text{I}) \qquad (2.3.57)\\
&= \sum_{\substack{\text{I}' \in \mathfrak{Q}_i \\ \text{I}' \neq \text{I}}} \int \sigma^{\text{II}'}_{ie} |\boldsymbol{C}_e| \Big(f_i(\boldsymbol{C}_i, \text{I}') f_e(\boldsymbol{C}'^{(0)}_e) \frac{a_{i\text{I}}}{a_{i\text{I}'}} - f_i\left(\boldsymbol{C}_i, \text{I}\right) f_e(\boldsymbol{C}_e) \Big) \, \mathrm{d}\boldsymbol{\omega}'_{ie} \mathrm{d}\boldsymbol{C}_e\\
&= \sum_{\substack{\text{I}' \in \mathfrak{Q}_i \\ \text{I}' \neq \text{I}}} \int \left(\Sigma^{(0)}_{\text{I}'\text{I}}(|\boldsymbol{C}_e|^2) f_i(\boldsymbol{C}_i, \text{I}') - \Sigma^{(0)}_{\text{II}'}(|\boldsymbol{C}_e|^2) f_i(\boldsymbol{C}_i, \text{I}) \right) |\boldsymbol{C}_e| f_e(\boldsymbol{C}_e) \, \mathrm{d}\boldsymbol{C}_e.
\end{aligned}$$

Scattering of electrons against the heavy species

The electron heavy-species scattering term $\mathcal{S}_{ei}$ was stated above in (2.3.25). Unlike for the heavy-species electron case, there is no change of variable allowing to eliminate the dependance in ε of the scattering cross-section $\sigma^{\text{II}'}_{ei}$, and we retain the set of variables $(\boldsymbol{C}_e, \boldsymbol{C}_i, \boldsymbol{\omega}'_{ei})$.

Expansion of the species velocities Conservation equations (2.3.41) for collisions between electrons and molecules of the i^{th} heavy species yield the following asymptotic expansion:

$$g'_{ei} = g'^{(0)}_{ei} + \varepsilon\, g'^{(1)}_{ei} + \varepsilon^2\, g'^{(2)}_{ei} + O(\varepsilon^3), \tag{2.3.58}$$

$$\boldsymbol{C}'_e = \boldsymbol{C}'^{(0)}_e + \varepsilon\, \boldsymbol{C}'^{(1)}_e + \varepsilon^2\, \boldsymbol{C}'^{(2)}_e + O(\varepsilon^3), \tag{2.3.59}$$

$$\boldsymbol{C}'_i = \boldsymbol{C}'^{(0)}_i + \varepsilon\, \boldsymbol{C}'^{(1)}_i + \varepsilon^2\, \boldsymbol{C}'^{(2)}_i + O(\varepsilon^3), \tag{2.3.60}$$

where the coefficients for the amplitude of the relative velocity after collision g'_{ei} read in terms of the variables $(\boldsymbol{C}_e, \boldsymbol{C}_i, \boldsymbol{\omega}'_{ei})$

$$\left\{\begin{array}{l} g'^{(0)}_{ei} = |\boldsymbol{C}_e|\Big(1 - \dfrac{\Delta E_{\mathrm{II}'}}{\frac{1}{2}\mathfrak{m}_e|\boldsymbol{C}_e|^2}\Big)^{\frac{1}{2}}, \\ g'^{(1)}_{ei} = -\dfrac{\boldsymbol{C}_e \cdot \boldsymbol{C}_i}{g'^{(0)}_{ei}}, \\ g'^{(2)}_{ei} = \dfrac{1}{2}\dfrac{|\boldsymbol{C}_i|^2}{g'^{(0)}_{ei}}\Big(1 - \dfrac{\Delta E_{\mathrm{II}'}}{\frac{1}{2}\mathfrak{m}_i|\boldsymbol{C}_i|^2}\Big) - \dfrac{1}{2}\dfrac{(\boldsymbol{C}_e \cdot \boldsymbol{C}_i)^2}{\big(g'^{(0)}_{ei}\big)^3}, \end{array}\right. \tag{2.3.61}$$

and the coefficients for the velocities after collisions $\boldsymbol{C}'_e$, $\boldsymbol{C}'_i$ are given by

$$\left\{\begin{array}{lll} \boldsymbol{C}'^{(0)}_e = g'^{(0)}_{ei}\boldsymbol{\omega}'_{ei}, & \boldsymbol{C}'^{(1)}_e = \boldsymbol{C}_i + g'^{(1)}_{ei}\boldsymbol{\omega}'_{ei}, & \boldsymbol{C}'^{(2)}_e = \boldsymbol{C}'^{(1)}_i + g'^{(2)}_{ei}\boldsymbol{\omega}'_{ei}, \\ \boldsymbol{C}'^{(0)}_i = \boldsymbol{C}_i, & \boldsymbol{C}'^{(1)}_i = \dfrac{\mathfrak{m}_e}{\mathfrak{m}_i}\big(\boldsymbol{C}_e - \boldsymbol{C}'^{(0)}_e\big), & \boldsymbol{C}'^{(2)}_i = -\dfrac{\mathfrak{m}_e}{\mathfrak{m}_i}\boldsymbol{C}'^{(1)}_e. \end{array}\right. \tag{2.3.62}$$

Expansion of $\mathcal{S}_{ei}$ Relations (2.3.58)-(2.3.60) allow one to determine, after a few calculations, the asymptotic expansion of the electron heavy-species scattering operator

$$\mathcal{S}_{ei} = \mathcal{S}^0_{ei} + \varepsilon\ \mathcal{S}^1_{ei} + \ \varepsilon^2\ \mathcal{S}^2_{ei} + \ O(\varepsilon^3).$$

The zeroth-order collision operator reads

$$\begin{aligned} &\mathcal{S}^0_{ei}\left(f_e, f_i\right)(\boldsymbol{C}_e) = \\ &\quad \sum_{\mathrm{I}\in\mathfrak{Q}_i}\left(\int f_i(\boldsymbol{C}_i, \mathrm{I})\,\mathrm{d}\boldsymbol{C}_i\right)\int \sigma^{\mathrm{II}}_{ei}\ |\boldsymbol{C}_e|\big(f_e(|\boldsymbol{C}_e|\boldsymbol{\omega}'_{ei}) - f_e(\boldsymbol{C}_e)\big)\,\mathrm{d}\boldsymbol{\omega}'_{ei}, \end{aligned} \tag{2.3.63}$$

where

$$\sigma^{\mathrm{II}}_{ei} = \sigma^{\mathrm{II}}_{ei}\left(\mathfrak{m}_e|\boldsymbol{C}_e|^2, \frac{\boldsymbol{C}_e}{|\boldsymbol{C}_e|}\cdot\boldsymbol{\omega}'_{ei}\right).$$

The first-order term $\mathcal{S}^1_{ei}\left(f_e, f_i\right)(\boldsymbol{C}_e)$ reads

$$\begin{aligned} &\mathcal{S}^1_{ei}\left(f_e, f_i\right)(\boldsymbol{C}_e) = \\ &+ \sum_{\mathrm{I}\in\mathfrak{Q}_i}\int f_i(\boldsymbol{C}_i, \mathrm{I})\boldsymbol{C}_i\,\mathrm{d}\boldsymbol{C}_i \cdot \int \sigma^{\mathrm{II}}_{ei}\ |\boldsymbol{C}_e|\big(\boldsymbol{\partial}_{\boldsymbol{C}_e} f_e(|\boldsymbol{C}_e|\boldsymbol{\omega}'_{ei}) - \boldsymbol{\partial}_{\boldsymbol{C}_e} f_e(\boldsymbol{C}_e)\big)\,\mathrm{d}\boldsymbol{\omega}'_{ei} \\ &- \sum_{\mathrm{I}\in\mathfrak{Q}_i}\int f_i(\boldsymbol{C}_i, \mathrm{I})\boldsymbol{C}_i\,\mathrm{d}\boldsymbol{C}_i \cdot \boldsymbol{\partial}_{\boldsymbol{C}_e}\left[\int \sigma^{\mathrm{II}}_{ei}\ |\boldsymbol{C}_e|\big(f_e(|\boldsymbol{C}_e|\boldsymbol{\omega}'_{ei}) - f_e(\boldsymbol{C}_e)\big)\,\mathrm{d}\boldsymbol{\omega}'_{ei}\right]. \end{aligned} \tag{2.3.64}$$

Finally, the second-order term can be decomposed into an elastic and an inelastic contributions

$$\mathcal{S}^2_{ei} = \mathcal{S}^{2,\mathrm{el}}_{ei} + \mathcal{S}^{2,\mathrm{in}}_{ei}. \tag{2.3.65}$$

The elastic term reads

$$\begin{aligned} \mathcal{S}^{2,\mathrm{el}}_{ei}\left(f_e, f_i\right)(\boldsymbol{C}_e) \ &= \ \frac{\mathfrak{m}_e}{\mathfrak{m}_i}\sum_{\mathrm{I}\in\mathfrak{Q}_i}\left(\int f_i(\boldsymbol{C}_i, \mathrm{I})\,\mathrm{d}\boldsymbol{C}_i\right)\ K^{\mathrm{I},1}_{ei}(\boldsymbol{C}_e) \\ &+ \ \frac{1}{2}\sum_{\mathrm{I}\in\mathfrak{Q}_i}\int f_i(\boldsymbol{C}_i, \mathrm{I})\,\boldsymbol{C}_i\otimes\boldsymbol{C}_i\,\mathrm{d}\boldsymbol{C}_i\ :\ K^{\mathrm{I},2}_{ei}(\boldsymbol{C}_e), \end{aligned} \tag{2.3.66}$$

where

$$
\begin{aligned}
K_{ei}^{\mathrm{I},1}(\boldsymbol{C}_e) &= \boldsymbol{\partial}_{\boldsymbol{C}_e} \cdot \left[\int \sigma_{ei}^{\mathrm{II}} \, |\boldsymbol{C}_e| \, (\boldsymbol{C}_e - |\boldsymbol{C}_e| \boldsymbol{\omega}'_{ei}) \, f_e(|\boldsymbol{C}_e| \boldsymbol{\omega}'_{ei}) \, \mathrm{d}\boldsymbol{\omega}'_{ei} \right] \\
&- \frac{1}{2} |\boldsymbol{C}_e| \boldsymbol{C}_e \cdot \int \boldsymbol{\partial}_{\boldsymbol{C}_e} \sigma_{ei}^{\mathrm{II}} \, \left(f_e(|\boldsymbol{C}_e| \boldsymbol{\omega}'_{ei}) - f_e(\boldsymbol{C}_e) \right) \mathrm{d}\boldsymbol{\omega}'_{ei},
\end{aligned}
\tag{2.3.67}
$$

and

$$
\begin{aligned}
K_{ei}^{\mathrm{I},2}(\boldsymbol{C}_e) &= \boldsymbol{\partial}_{\boldsymbol{C}_e \boldsymbol{C}_e} \left[\int \sigma_{ei}^{\mathrm{II}} \, |\boldsymbol{C}_e| \, \left(f_e(|\boldsymbol{C}_e| \boldsymbol{\omega}'_{ei}) - f_e(\boldsymbol{C}_e) \right) \mathrm{d}\boldsymbol{\omega}'_{ei} \right] \\
&+ 2 \int \boldsymbol{\partial}_{\boldsymbol{C}_e} \left[|\boldsymbol{C}_e| \sigma_{ei}^{\mathrm{II}} \right] \otimes \left(\boldsymbol{\partial}_{\boldsymbol{C}_e} f_e(\boldsymbol{C}_e) - \boldsymbol{\partial}_{\boldsymbol{C}_e} f_e(|\boldsymbol{C}_e| \boldsymbol{\omega}'_{ei}) \right) \mathrm{d}\boldsymbol{\omega}'_{ei} \\
&+ |\boldsymbol{C}_e| \int \sigma_{ei}^{\mathrm{II}} \left(\boldsymbol{\partial}_{\boldsymbol{C}_e \boldsymbol{C}_e} f_e(\boldsymbol{C}_e) + \boldsymbol{\partial}_{\boldsymbol{C}_e \boldsymbol{C}_e} f_e(|\boldsymbol{C}_e| \boldsymbol{\omega}'_{ei}) \right) \mathrm{d}\boldsymbol{\omega}'_{ei} \\
&- 2 |\boldsymbol{C}_e| \int \sigma_{ei}^{\mathrm{II}} \, \boldsymbol{\partial}_{\boldsymbol{C}_e \boldsymbol{C}_e} f_e(|\boldsymbol{C}_e| \boldsymbol{\omega}'_{ei}) \cdot \boldsymbol{\omega}'_{ei} \otimes \frac{\boldsymbol{C}_e}{|\boldsymbol{C}_e|} \, \mathrm{d}\boldsymbol{\omega}'_{ei}.
\end{aligned}
\tag{2.3.68}
$$

The inelastic term reads

$$
\begin{aligned}
&\mathcal{S}_{ei}^{2,\mathrm{in}} \left(f_e, f_i \right) (\boldsymbol{C}_e) = \\
&\qquad \sum_{\substack{\mathrm{I},\mathrm{I}' \in \mathfrak{Q}_i \\ \mathrm{I}' \neq \mathrm{I}}} \int \sigma_{ei}^{\mathrm{II}'} |\boldsymbol{C}_e| \Big(f_e(\boldsymbol{C}_e'^{(0)}) f_i(\boldsymbol{C}_i, \mathrm{I}') \frac{a_{i\mathrm{I}}}{a_{i\mathrm{I}'}} - f_e(\boldsymbol{C}_e) f_i(\boldsymbol{C}_i, \mathrm{I}) \Big) \, \mathrm{d}\boldsymbol{\omega}'_{ei} \mathrm{d}\boldsymbol{C}_i,
\end{aligned}
\tag{2.3.69}
$$

where

$$
\begin{aligned}
\sigma_{ei}^{\mathrm{II}'} &= \sigma_{ei}^{\mathrm{II}'} \left(\mathfrak{m}_e |\boldsymbol{C}_e|^2, \frac{\boldsymbol{C}_e}{|\boldsymbol{C}_e|} \cdot \boldsymbol{\omega}'_{ei} \right), \\
\boldsymbol{C}_e'^{(0)} &= |\boldsymbol{C}_e| \left(1 - \frac{\Delta E_{\mathrm{II}'}}{\frac{1}{2} \mathfrak{m}_e |\boldsymbol{C}_e|^2} \right)^{\frac{1}{2}} \boldsymbol{\omega}'_{ei}.
\end{aligned}
$$

2.4 Chapman-Enskog Expansion of the Species Distribution Functions

In this section, we apply the classical procedure proposed by Enskog [CC70] [FK72] [Gio99], adapted to non-thermal plasmas [DLD96] [GMM09]. The species distribution functions are expanded in powers of the Knudsen number ε and injected in the Boltzmann equations (2.3.21)-(2.3.22). Projection of the electron Boltzmann equation at order ε^{-2} yields electron thermalization and isotropization in the heavy-species reference frame. As well, projection of the heavy-species Boltzmann equations at order ε^{-1} yields the thermalization of heavy species. Euler type equations arise from the expansion of macroscopic equations at order ε^0, while expansion at order ε^1 yields Navier-Stokes type equations. As is classical, the closure of the equations is ensured by assuming that the perturbation of the distribution function from its Maxwellian equilibrium is orthogonal to the collisional invariants of the scattering operator [CC70] [FK72] [Gio99].

2.4.1 Chapman-Enskog method

We derive an approximate solution to the Boltzmann equations by expanding the species distribution functions as

$$f_e = f_e^0 \left(1 + \varepsilon\phi_e + \varepsilon^2\phi_e^2\right) + O(\varepsilon^3), \tag{2.4.1}$$
$$f_i = f_i^0 \left(1 + \varepsilon\phi_i\right) + O(\varepsilon^2),\ i \in \mathfrak{H}. \tag{2.4.2}$$

Traditionally, in the Chapman-Enskog's method [CC70] [FK72] [Gio99], the zeroth-order distribution function f_e^0 is assumed to yield the same local macroscopic properties as f_e in the limit $\varepsilon \to 0$ [GMM09], namely

$$\begin{cases} \langle\!\langle f_e^0, \psi_e^e \rangle\!\rangle_e = n_e \\ \langle\!\langle f_e^0, \psi_e^{n^s+4} \rangle\!\rangle_e = \mathcal{E}_e \end{cases} \tag{2.4.3}$$

for electrons, and as well

$$\begin{cases} \langle\!\langle f_h^0, \psi_h^j \rangle\!\rangle_h = n_j, & j \in \mathfrak{H} \\ \langle\!\langle f_h^0, \psi_h^{n^s+\nu} \rangle\!\rangle_h = 0, & \nu \in \{1,2,3\} \\ \langle\!\langle f_h^0, \psi_h^{n^s+4} \rangle\!\rangle_h = \mathcal{E}_h \end{cases} \tag{2.4.4}$$

for heavy species, where $\mathcal{E}_e$ and $\mathcal{E}_h$ denote the respective internal energies per unit volume.

The Boltzmann equations (2.3.21),(2.3.22) can be written in the compact form

$$\mathcal{D}_e(f_e) = \frac{1}{\varepsilon^2}\,\mathcal{S}_{ee}\left(f_e, f_e\right) + \frac{1}{\varepsilon^2}\,\sum_{j\in\mathfrak{H}} \mathcal{S}_{ej}\left(f_e, f_j\right) + \varepsilon\,\mathcal{C}_e\left(f\right), \tag{2.4.5}$$

$$\mathcal{D}_i(f_i) = \frac{1}{\varepsilon^2}\,\mathcal{S}_{ie}\left(f_i, f_e\right) + \frac{1}{\varepsilon}\sum_{j\in\mathfrak{H}} \mathcal{S}_{ij}\left(f_i, f_j\right) + \varepsilon\,\mathcal{C}_i\left(f\right), \qquad i \in \mathfrak{H}. \tag{2.4.6}$$

We have derived in the previous paragraph asymptotic expansions for the scattering operators $\mathcal{S}_{ee}, \mathcal{S}_{ej}, \mathcal{S}_{je}, \mathcal{S}_{ij}$, $i, j \in \mathfrak{H}$. We also expand the streaming operators $\mathcal{D}$ as

$$\mathcal{D}_e = \frac{1}{\varepsilon^2}\,\mathcal{D}_e^{-2} + \frac{1}{\varepsilon}\,\mathcal{D}_e^{-1} + \mathcal{D}_e^0 + \varepsilon\,\mathcal{D}_e^1 + O(\varepsilon^2), \tag{2.4.7}$$

$$\mathcal{D}_i = \mathcal{D}_i^0 + \varepsilon\,\mathcal{D}_i^1 + O(\varepsilon^2), \qquad i \in \mathfrak{H}, \tag{2.4.8}$$

where

$$\mathcal{D}_e^{-2}(f_e) = \delta_{b1}\frac{q_e}{\mathfrak{m}_e}\left[\boldsymbol{C}_e \wedge \mathbf{B}\right] \cdot \boldsymbol{\partial}_{\boldsymbol{C}_e} f_e, \tag{2.4.9}$$

$$\begin{aligned} \mathcal{D}_e^{-1}(f_e) = {} & \boldsymbol{C}_e \cdot \boldsymbol{\partial}_{\boldsymbol{x}} f_e + \delta_{b0}\frac{q_e}{\mathfrak{m}_e}\left[\boldsymbol{C}_e \wedge \mathbf{B}\right] \cdot \boldsymbol{\partial}_{\boldsymbol{C}_e} f_e + \delta_{b1}\frac{q_e}{\mathfrak{m}_e}\left[\boldsymbol{v}_h \wedge \mathbf{B}\right] \cdot \boldsymbol{\partial}_{\boldsymbol{C}_e} f_e \\ & + \frac{q_e}{\mathfrak{m}_e}\mathbf{E} \cdot \boldsymbol{\partial}_{\boldsymbol{C}_e} f_e, \end{aligned} \tag{2.4.10}$$

$$\begin{aligned} \mathcal{D}_e^0(f_e) = {} & \partial_t f_e + \boldsymbol{v}_h \cdot \boldsymbol{\partial}_{\boldsymbol{x}} f_e + \delta_{b(-1)}\frac{q_e}{\mathfrak{m}_e}\left[\boldsymbol{C}_e \wedge \mathbf{B}\right] \cdot \boldsymbol{\partial}_{\boldsymbol{C}_e} f_e + \delta_{b0}\frac{q_e}{\mathfrak{m}_e}\left[\boldsymbol{v}_h \wedge \mathbf{B}\right] \cdot \boldsymbol{\partial}_{\boldsymbol{C}_e} f_e \\ & - \left(\boldsymbol{\partial}_{\boldsymbol{C}_e} f_e \otimes \boldsymbol{C}_e\right) : \boldsymbol{\partial}_{\boldsymbol{x}} \boldsymbol{v}_h, \end{aligned} \tag{2.4.11}$$

$$\mathcal{D}_e^1(f_e) = \delta_{b(-2)}\frac{q_e}{\mathfrak{m}_e}\left[\boldsymbol{C}_e \wedge \mathbf{B}\right] \cdot \boldsymbol{\partial}_{\boldsymbol{C}_e} f_e + \delta_{b(-1)}\frac{q_e}{\mathfrak{m}_e}\left[\boldsymbol{v}_h \wedge \mathbf{B}\right] \cdot \boldsymbol{\partial}_{\boldsymbol{C}_e} f_e - \frac{D\boldsymbol{v}_h}{Dt} \cdot \boldsymbol{\partial}_{\boldsymbol{C}_e} f_e, \tag{2.4.12}$$

and

$$\begin{aligned} \mathcal{D}_i^0(f_i) = {} & \partial_t f_i + \left(\boldsymbol{C}_i + \boldsymbol{v}_h\right) \cdot \boldsymbol{\partial}_{\boldsymbol{x}} f_i + \delta_{b1}\frac{q_i}{\mathfrak{m}_i}\left[\left(\boldsymbol{C}_i + \boldsymbol{v}_h\right) \wedge \mathbf{B}\right] \cdot \boldsymbol{\partial}_{\boldsymbol{C}_i} f_i \\ & + \left(\frac{q_i}{\mathfrak{m}_i}\mathbf{E} - \frac{D\boldsymbol{v}_h}{Dt}\right) \cdot \boldsymbol{\partial}_{\boldsymbol{C}_i} f_i - \left(\boldsymbol{\partial}_{\boldsymbol{C}_i} f_i \otimes \boldsymbol{C}_i\right) : \boldsymbol{\partial}_{\boldsymbol{x}} \boldsymbol{v}_h, \end{aligned} \tag{2.4.13}$$

$$\mathcal{D}_i^1(f_i) = \delta_{b0}\frac{q_i}{\mathfrak{m}_i}\left[\left(\boldsymbol{C}_i + \boldsymbol{v}_h\right) \wedge \mathbf{B}\right] \cdot \boldsymbol{\partial}_{\boldsymbol{C}_i} f_i. \tag{2.4.14}$$

Equations (2.4.5), (2.4.6) are then projected against collisional invariants in $\mathcal{I}_e^\varepsilon$, $\mathcal{I}_h$. Making use of orthogonality properties (2.2.48), (2.2.50), one obtains

$$\langle\!\langle \psi_e^e, \mathcal{D}_e(f_e)\rangle\!\rangle_e = \varepsilon \langle\!\langle \psi_e^e, \mathcal{C}_e(f)\rangle\!\rangle_e, \tag{2.4.15}$$

$$\langle\!\langle \varepsilon \mathfrak{m}_e C_{e\nu}, \mathcal{D}_e(f_e)\rangle\!\rangle_e = \frac{1}{\varepsilon^2}\sum_{j\in\mathfrak{H}} \langle\!\langle \varepsilon \mathfrak{m}_e C_{e\nu}, \mathcal{S}_{ej}\rangle\!\rangle_e + \varepsilon \langle\!\langle \varepsilon \mathfrak{m}_e C_{e\nu}, \mathcal{C}_e(f)\rangle\!\rangle_e, \quad \nu \in \{1,2,3\}, \tag{2.4.16}$$

$$\langle\!\langle \psi_e^{n^s+4}, \mathcal{D}_e(f_e)\rangle\!\rangle_e = \frac{1}{\varepsilon^2}\sum_{j\in\mathfrak{H}} \langle\!\langle \psi_e^{n^s+4}, \mathcal{S}_{ej}\rangle\!\rangle_e + \varepsilon \langle\!\langle \psi_e^{n^s+4}, \mathcal{C}_e(f)\rangle\!\rangle_e, \tag{2.4.17}$$

for electrons, and

$$\langle\!\langle \psi_h^i, \mathcal{D}_h(f_h)\rangle\!\rangle_h = \varepsilon \langle\!\langle \psi_h^i, \mathcal{C}_h(f)\rangle\!\rangle_h, \qquad i \in \mathfrak{H}, \tag{2.4.18}$$

$$\langle\!\langle \psi_h^{n^s+\nu}, \mathcal{D}_h(f_h)\rangle\!\rangle_h = \frac{1}{\varepsilon^2}\langle\!\langle \psi_h^{n^s+\nu}, \mathcal{S}_{he}\rangle\!\rangle_h + \varepsilon \langle\!\langle \psi_h^{n^s+\nu}, \mathcal{C}_h(f)\rangle\!\rangle_h, \qquad \nu \in \{1,2,3\}, \tag{2.4.19}$$

$$\langle\!\langle \psi_h^{n^s+4}, \mathcal{D}_h(f_h)\rangle\!\rangle_h = \frac{1}{\varepsilon^2}\langle\!\langle \psi_h^{n^s+4}, \mathcal{S}_{he}\rangle\!\rangle_h + \varepsilon \langle\!\langle \psi_h^{n^s+4}, \mathcal{C}_h(f)\rangle\!\rangle_h, \tag{2.4.20}$$

for heavy species. Equations (2.4.15) and (2.4.18) account for conservation of matter, equations (2.4.16) and (2.4.19) for conservation of momentum, and equations (2.4.17) and (2.4.20) for conservation of energy. These equations are completed with the cross-collision orthogonality relations (2.3.32), (2.3.33), (2.3.34), together with the macroscopic constraints (2.4.3), (2.4.4).

2.4.2 Electron thermalization

We solve the electron Boltzmann equation (2.4.5) at order ε^{-2}, corresponding to the kinetic timescale t_e^0. We obtain the following equation for f_e^0:

$$\delta_{b1}\,\frac{q_e}{\mathfrak{m}_e}(\boldsymbol{C}_e \wedge \mathbf{B})\cdot\boldsymbol{\partial}_{\boldsymbol{C}_e} f_e^0 = \mathcal{S}_{ee}\left(f_e^0, f_e^0\right) + \sum_{j\in\mathfrak{H}} \mathcal{S}_{ej}^0\left(f_e^0, f_j^0\right). \tag{2.4.21}$$

Multiplying this equation by $\ln f_e^0$ and integrating over $\boldsymbol{C}_e$, we get

$$\Gamma_{ee}^0 \;+\; \sum_{j\in\mathfrak{H}} \Gamma_{ej}^0 \;+\; \delta_{b1}\; k_{\text{B}}\,\frac{q_e}{\mathfrak{m}_e}\int (\boldsymbol{C}_e \wedge \mathbf{B})\cdot\boldsymbol{\partial}_{\boldsymbol{C}_e} f_e^0 \;\ln f_e^0 \,\mathrm{d}\boldsymbol{C}_e = 0,$$

where Γ_{ee}^0 and Γ_{ej}^0 are the zeroth-order entropy production rates for electron electron and electron j^{th}-heavy-species collisions, respectively

$$\Gamma_{ee}^0 = -k_{\text{B}}\int \mathcal{S}_{ee}\left(f_e^0, f_e^0\right)(\boldsymbol{C}_e)\;\ln\left(f_e^0(\boldsymbol{C}_e)\right)\,\mathrm{d}\boldsymbol{C}_e, \tag{2.4.22}$$

$$\Gamma_{ej}^0 = -k_{\text{B}}\int \mathcal{S}_{ej}^0\left(f_e^0, f_j^0\right)(\boldsymbol{C}_e)\;\ln\left(f_e^0(\boldsymbol{C}_e)\right)\,\mathrm{d}\boldsymbol{C}_e, \qquad j \in \mathfrak{H}. \tag{2.4.23}$$

Noting that

$$\boldsymbol{\partial}_{\boldsymbol{C}_e} f_e^0 \;\ln f_e^0 = \boldsymbol{\partial}_{\boldsymbol{C}_e}\left[f_e^0 \;\ln f_e^0 - f_e^0\right],$$

and integrating by parts we obtain

$$\begin{aligned}\int (\boldsymbol{C}_e \wedge \mathbf{B})\cdot\boldsymbol{\partial}_{\boldsymbol{C}_e} f_e^0 \;\ln f_e^0 \,\mathrm{d}\boldsymbol{C}_e &= \int (\boldsymbol{C}_e \wedge \mathbf{B})\cdot\boldsymbol{\partial}_{\boldsymbol{C}_e}\left[f_e^0 \;\ln f_e^0 - f_e^0\right]\mathrm{d}\boldsymbol{C}_e \\ &= \int \boldsymbol{\partial}_{\boldsymbol{C}_e}\cdot\left[(f_e^0 \;\ln f_e^0 - f_e^0)(\boldsymbol{C}_e \wedge \mathbf{B})\right]\mathrm{d}\boldsymbol{C}_e,\end{aligned}$$

since $\boldsymbol{\partial}_{\boldsymbol{C}_e} \cdot [\boldsymbol{C}_e \wedge \mathbf{B}] = 0$. Now, for a given $R > 0$, if $\mathscr{B}(\mathbf{0}, R)$ is the ball of center $\mathbf{0}$ and radius R in the electron velocity space ($\boldsymbol{C}_e \in \mathbb{R}^3$), and $\mathscr{S}(0, R)$ is the corresponding sphere, then

$$\begin{aligned}\int_{\mathscr{B}(\mathbf{0},R)} \boldsymbol{\partial}_{\boldsymbol{C}_e} \cdot \left[(f_e^0 \ \ln f_e^0 - f_e^0)(\boldsymbol{C}_e \wedge \mathbf{B})\right] \mathrm{d}\boldsymbol{C}_e &= \int_{\mathscr{S}(\mathbf{0},R)} (f_e^0 \ \ln f_e^0 - f_e^0)(\boldsymbol{C}_e \wedge \mathbf{B}) \cdot \frac{\boldsymbol{C}_e}{|\boldsymbol{C}_e|} \mathrm{d}\boldsymbol{C}_e \\ &= 0,\end{aligned}$$

and this holds for all $R > 0$, so that

$$\int \boldsymbol{\partial}_{\boldsymbol{C}_e} \cdot \left[(f_e^0 \ \ln f_e^0 - f_e^0)(\boldsymbol{C}_e \wedge \mathbf{B})\right] \mathrm{d}\boldsymbol{C}_e = 0.$$

More generally, the latter statement can also be proven for any kind of force instead of the Lorentz force $q_e \boldsymbol{C}_e \wedge \mathbf{B}$, upon assuming that the electron distribution function f_e decreases sufficiently rapidly when $|\boldsymbol{C}_e| \to +\infty$ [Gra04]. Thus, one gets finally

$$\Gamma_{ee}^0 + \sum_{j \in \mathfrak{H}} \Gamma_{ej}^0 = 0. \tag{2.4.24}$$

Using the reciprocity relation (2.2.35) and symmetrizing, a classical derivation [GMM09] yields

$$\Gamma_{ee}^0 = \frac{k_{\mathrm{B}}}{4} \int \sigma_{e\tilde{e}} g_{e\tilde{e}} \Omega(f_e \tilde{f}_e, f'_e \tilde{f}'_e) \, \mathrm{d}\boldsymbol{\omega}'_{e\tilde{e}} \mathrm{d}\boldsymbol{C}_e \mathrm{d}\widetilde{\boldsymbol{C}}_e, \tag{2.4.25}$$

where $\tilde{f}_e = f_e(t, \boldsymbol{x}, \widetilde{\boldsymbol{C}}_e)$ and $\tilde{f}'_e = f_e(t, \boldsymbol{x}, \widetilde{\boldsymbol{C}}'_e)$, and where

$$\Omega(x, y) = \ln\left(\frac{x}{y}\right)(x - y) \tag{2.4.26}$$

is a nonnegative function. Similarly, the electron j^{th}-heavy-species entropy production term is expressed by means of (2.3.63) as

$$\begin{aligned}\Gamma_{ej}^0 &= -k_{\mathrm{B}} \int \mathcal{S}_{ej}^0 \left(f_e^0, f_j^0\right)(\boldsymbol{C}_e) \ \ln\left(f_e^0(\boldsymbol{C}_e)\right) \mathrm{d}\boldsymbol{C}_e \\ &= -k_{\mathrm{B}} \sum_{\mathrm{J} \in \mathfrak{Q}_j} \left(\int f_j^0(\boldsymbol{C}_j, \mathrm{J}) \, \mathrm{d}\boldsymbol{C}_j \right) \\ &\qquad \times \int \sigma_{ej}^{\mathrm{JJ}} \ |\boldsymbol{C}_e| \left(f_e^0(|\boldsymbol{C}_e|\boldsymbol{\omega}'_{ej}) - f_e^0(\boldsymbol{C}_e)\right) \ \ln\left(f_e^0(\boldsymbol{C}_e)\right) \mathrm{d}\boldsymbol{\omega}'_{ej} \mathrm{d}\boldsymbol{C}_e,\end{aligned}$$

which again by reciprocity relations and symmetrization is equal to

$$\Gamma_{ej}^0 = \frac{k_{\mathrm{B}}}{2} \sum_{\mathrm{J} \in \mathfrak{Q}_j} \left(\int f_j^0(\boldsymbol{C}_j, \mathrm{J}) \, \mathrm{d}\boldsymbol{C}_j \right) \int \sigma_{ej}^{\mathrm{JJ}} |\boldsymbol{C}_e| \ \Omega\left(f_e^0(|\boldsymbol{C}_e|\boldsymbol{\omega}'_{ej}), f_e^0(\boldsymbol{C}_e)\right) \mathrm{d}\boldsymbol{\omega}'_{ej} \mathrm{d}\boldsymbol{C}_e \geq 0. \tag{2.4.27}$$

A sum of positive terms is equal to zero if and only if each term of the sum is zero itself, thus the entropy production rates vanish: $\Gamma_{ee}^0 = 0$, and $\Gamma_{ej}^0 = 0$ for all $j \in \mathfrak{H}$.

Since $\Gamma_{ee}^0 = 0$, one can see from expression (2.4.25) and the definition of Ω that $\ln(f_e^0)$ must be a collisional invariant associated with the electron electron scattering operator, i.e., must lie in the space $\mathcal{I}_e^\varepsilon$, spanned by $\psi_e^e = 1$, $\psi_e^{n^s+\nu} = \varepsilon \mathfrak{m}_e C_{e\nu}$, $\nu \in \{1, 2, 3\}$, and $\psi_e^{n^s+4} = \frac{1}{2}\mathfrak{m}_e \boldsymbol{C}_e \cdot \boldsymbol{C}_e$. Similarly, one can see from expression (2.4.27) that f_e^0 has to be an isotropic function of $\boldsymbol{C}_e$, so that finally

$$\ln(f_e^0) \in \mathcal{I}_e^0 = \mathrm{Span}\left(1, \frac{1}{2}\mathfrak{m}_{\mathrm{e}} \boldsymbol{C}_{\mathrm{e}} \cdot \boldsymbol{C}_{\mathrm{e}}\right).$$

Using the macroscopic constraints (2.4.3) for conservation of matter and energy, we obtain finally the expression for the zeroth-order electron distribution function

$$f_e^0(\boldsymbol{C}_e) = n_e \left(\frac{\mathfrak{m}_e}{2\pi k_{\mathrm{B}} T_e}\right)^{\frac{3}{2}} \exp\left(-\frac{\mathfrak{m}_e}{2k_{\mathrm{B}} T_e}\, \boldsymbol{C}_e \cdot \boldsymbol{C}_e\right). \tag{2.4.28}$$

The electron population thus thermalizes to a quasi-equilibrium state described by a Maxwell-Boltzmann distribution at some temperature T_e, defined as

$$\mathcal{E}_e = \frac{3}{2} n_e k_{\mathrm{B}} T_e. \tag{2.4.29}$$

The Maxwellian distribution (2.4.28) is such that $\mathcal{S}_{ee}(f_e^0, f_e^0) = 0$ and $\mathcal{S}_{ej}^0(f_e^0, f_j^0) = 0$, for $j \in \mathfrak{H}$.

Finally, if one defines the electron partial pressure p_e as

$$p_e \mathbb{I} = \int \mathfrak{m}_e \boldsymbol{C}_e \otimes \boldsymbol{C}_e f_e^0 \,\mathrm{d}\boldsymbol{C}_e = \left(\frac{1}{3}\int \mathfrak{m}_e \boldsymbol{C}_e \cdot \boldsymbol{C}_e f_e^0 \,\mathrm{d}\boldsymbol{C}_e\right)\mathbb{I}, \tag{2.4.30}$$

where the latter equality comes from the isotropy of f_e^0, one retrieves the perfect gas law for the electrons

$$\rho_e = \frac{p_e m_e}{R T_e}, \tag{2.4.31}$$

where $m_e = \mathcal{N}_{\mathrm{A}} \mathfrak{m}_e$ is the molar mass of the electron, and R is the universal gas constant.

2.4.3 Heavy-species thermalization

Now we solve the i^{th}-heavy-species equation (2.4.6) at order ε^{-1}. Since $\mathcal{S}_{ie}^0 = 0$ from (2.3.51), this yields, for all $i \in \mathfrak{H}$

$$\mathcal{S}_{ie}^1(f_i^0, f_e^0) + \sum_{j\in\mathfrak{H}} \mathcal{S}_{ij}\left(f_i^0, f_j^0\right) = 0.$$

Since f_e^0 is isotropic, the term $\mathcal{S}_{ie}^1(f_i^0, f_e^0)$ given in (2.3.52) vanishes, in order that

$$\sum_{j\in\mathfrak{H}} \mathcal{S}_{ij}\left(f_i^0, f_j^0\right) = 0. \tag{2.4.32}$$

Multiplying this equation by $\ln(\beta_{i\mathrm{I}} f_i^0)$, integrating over $\boldsymbol{C}_i$, summing over $\mathrm{I} \in \mathfrak{Q}_i$ and then over $i \in \mathfrak{H}$, we get

$$\Gamma_{hh}^0 = 0, \tag{2.4.33}$$

where Γ_{hh}^0 is the zeroth-order entropy production rate associated with heavy-species collisions

$$\Gamma_{hh}^0 = -k_{\mathrm{B}} \sum_{i,j\in\mathfrak{H}} \sum_{\mathrm{I}\in\mathfrak{Q}_i} \int \mathcal{S}_{ij}\left(f_i^0, f_j^0\right)(\boldsymbol{C}_i)\ \ln\left(\beta_{i\mathrm{I}} f_i^0(\boldsymbol{C}_i)\right)\,\mathrm{d}\boldsymbol{C}_i. \tag{2.4.34}$$

From expression (2.3.29) for $\mathcal{S}_{ij}$, and using the reciprocity relation (2.2.35) and symmetrization, the latter term can be written in the form

$$\Gamma_{hh}^0 = \frac{k_{\mathrm{B}}}{4} \sum_{i,j\in\mathfrak{H}} \sum_{\mathrm{I},\mathrm{I}'\in\mathfrak{Q}_i} \sum_{\mathrm{J},\mathrm{J}'\in\mathfrak{Q}_j} \int \sigma_{ij}^{\mathrm{I}\mathrm{J}\mathrm{I}'\mathrm{J}'} g_{ij}\, \Omega\Big(\frac{a_{i\mathrm{I}} a_{j\mathrm{J}}}{a_{i\mathrm{I}'} a_{j\mathrm{J}'}} f_i^{0'} f_j^{0'}, f_i^0 f_j^0\Big)\,\mathrm{d}\boldsymbol{\omega}_{ij}' \mathrm{d}\boldsymbol{C}_i \mathrm{d}\boldsymbol{C}_j. \tag{2.4.35}$$

Since Ω is nonnegative, each term in the sum has to be zero, i.e.,

$$a_{i\mathrm{I}} a_{j\mathrm{J}} f_i^{0'} f_j^{0'} = a_{i\mathrm{I}'} a_{j\mathrm{J}'} f_i^0 f_j^0, \qquad i,j \in \mathfrak{H}, \mathrm{I}, \mathrm{I}', \in \mathfrak{Q}_i, \mathrm{J}, \mathrm{J}' \in \mathfrak{Q}_j.$$

In other words, $\big(\ln(\beta_{i\mathrm{I}} f_i^0)\big)_{i\in\mathfrak{H}}$ is a collisional invariant of the heavy-species scattering operator:

$$\big(\ln(\beta_{i\mathrm{I}} f_i^0)\big)_{i\in\mathfrak{H}} \in \mathcal{I}_h,$$

i.e., there exists constants α_i, $i\in\mathfrak{H}$, $\boldsymbol{w}$, and γ such that

$$\ln(\beta_{i\mathrm{I}} f_i^0) = \alpha_i - \boldsymbol{w}\cdot\mathfrak{m}_i\boldsymbol{C}_i - \gamma\big(\frac{1}{2}\mathfrak{m}_i\boldsymbol{C}_i\cdot\boldsymbol{C}_i + E_{i\mathrm{I}}\big), \qquad i\in\mathfrak{H},\ \mathrm{I}\in\mathfrak{Q}_i.$$

The constants α_i, $i\in\mathfrak{H}$, $\boldsymbol{w}$, and γ are obtained from the macroscopic constraints (2.4.4) for conservation of matter, momentum and energy, yielding the following expression for the zeroth-order heavy-species distribution function

$$f_i^0(\boldsymbol{C}_i,\mathrm{I}) = n_i\left(\frac{\mathfrak{m}_i}{2\pi k_{\mathrm{B}}T_h}\right)^{\frac{3}{2}}\frac{a_{i\mathrm{I}}}{Q_i^{\mathrm{int}}}\ \exp\left(-\frac{\mathfrak{m}_i}{2k_{\mathrm{B}}T_h}\ \boldsymbol{C}_i\cdot\boldsymbol{C}_i - \frac{E_{i\mathrm{I}}}{k_{\mathrm{B}}T_h}\right),\ i\in\mathfrak{H},\ \mathrm{I}\in\mathfrak{Q}_i, \tag{2.4.36}$$

where T_h is the heavy-species temperature, given by

$$\frac{3}{2}n_h k_{\mathrm{B}}T_h = \sum_{i\in\mathfrak{H}}\sum_{\mathrm{I}\in\mathfrak{Q}_i}\int\frac{1}{2}\mathfrak{m}_i\boldsymbol{C}_i\cdot\boldsymbol{C}_i\, f_i^0\,\mathrm{d}\boldsymbol{C}_i, \tag{2.4.37}$$

and where we have introduced the partition function for internal energy of the i^{th} species

$$Q_i^{\mathrm{int}} = \sum_{\mathrm{I}\in\mathfrak{Q}_i} a_{i\mathrm{I}}\exp\left(-\frac{E_{i\mathrm{I}}}{k_{\mathrm{B}}T_h}\right). \tag{2.4.38}$$

Alternatively, one can write

$$f_i^0(\boldsymbol{C}_i,\mathrm{I}) = n_i\frac{1}{\beta_{i\mathrm{I}}Q_i}\ \exp\left(-\frac{\mathfrak{m}_i}{2k_{\mathrm{B}}T_h}\ \boldsymbol{C}_i\cdot\boldsymbol{C}_i - \frac{E_{i\mathrm{I}}}{k_{\mathrm{B}}T_h}\right), \qquad i\in\mathfrak{H},\ \mathrm{I}\in\mathfrak{Q}_i, \tag{2.4.39}$$

where the statistical weights $\beta_{i\mathrm{I}}$ are given by

$$\beta_{i\mathrm{I}} = \frac{h_{\mathrm{P}}^3}{a_{i\mathrm{I}}\mathfrak{m}_i^3}, \qquad i\in\mathfrak{H},\ \mathrm{I}\in\mathfrak{Q}_i, \tag{2.4.40}$$

and where the translational and full partition functions per unit volume read

$$Q_i^{\mathrm{tr}} = \left(\frac{2\pi\mathfrak{m}_i k_{\mathrm{B}}T_h}{h_{\mathrm{P}}^2}\right)^{\frac{3}{2}}, \qquad Q_i = Q_i^{\mathrm{tr}}Q_i^{\mathrm{int}}, \qquad i\in\mathfrak{H}. \tag{2.4.41}$$

The Maxwellian distribution (2.4.36) is such that $\mathcal{S}_{ij}(f_i^0, f_j^0) = 0$, for $i,j\in\mathfrak{H}$.

As a consequence of expression (2.4.36), the heavy-species internal energy per unit volume reads

$$\mathcal{E}_h = \sum_{i\in\mathfrak{H}} n_i(\frac{3}{2}k_{\mathrm{B}}T_h + \overline{E}_i), \tag{2.4.42}$$

where

$$\overline{E}_i = \sum_{\mathrm{I}\in\mathfrak{Q}_i}\frac{a_{i\mathrm{I}}E_{i\mathrm{I}}}{Q_i^{\mathrm{int}}}\exp\left(-\frac{E_{i\mathrm{I}}}{k_{\mathrm{B}}T_h}\right) \tag{2.4.43}$$

is the mean excitation energy of the i^{th} species.

Finally, defining the heavy-species partial pressure as

$$p_h\,\mathbb{I} = \sum_{i\in\mathfrak{H}}\sum_{\mathrm{I}\in\mathfrak{Q}}\int\mathfrak{m}_i\,\boldsymbol{C}_i\otimes\boldsymbol{C}_i\,f_i^0\,\mathrm{d}\boldsymbol{C}_i = \left(\frac{1}{3}\sum_{i\in\mathfrak{H}}\sum_{\mathrm{I}\in\mathfrak{Q}}\int\mathfrak{m}_i\,\boldsymbol{C}_i\cdot\boldsymbol{C}_i\,f_i^0\,\mathrm{d}\boldsymbol{C}_i\right)\mathbb{I}, \tag{2.4.44}$$

we retrieve the perfect gas law for heavy species

$$\rho_h = \frac{p_h \overline{m}_h}{R T_h}, \tag{2.4.45}$$

where $\overline{m}_h$ is the mean heavy-species molar mass, given by

$$\frac{\rho_h}{\overline{m}_h} = \sum_{i \in \mathfrak{H}} \frac{\rho_i}{m_i}, \tag{2.4.46}$$

$m_i = \mathcal{N}_{\mathrm{A}} \mathfrak{m}_i$ being the molar mass of the i^{th} heavy species.

2.4.4 First-order perturbation function for electrons

We introduce the electron linearized collision operator $\mathcal{F}_e$, defined as

$$\mathcal{F}_e(\phi_e) = -\frac{1}{f_e^0}\left[\mathcal{S}_{ee}(\phi_e f_e^0, f_e^0) + \mathcal{S}_{ee}(f_e^0, \phi_e f_e^0) + \sum_{j \in \mathfrak{H}} \mathcal{S}_{ej}^0(\phi_e f_e^0, f_j^0)\right]. \tag{2.4.47}$$

The sum of the first two terms on the right hand side can be computed from (2.3.23) as follows:

$$-\frac{1}{f_e^0}\left[\mathcal{S}_{ee}(\phi_e f_e^0, f_e^0) + \mathcal{S}_{ee}(f_e^0, \phi_e f_e^0)\right] = \\ -\frac{1}{f_e^0}\int g_{e\tilde{e}}\sigma_{e\tilde{e}}\left(\phi_e' f_e^{0\prime}\tilde{f}_e^{0\prime} - \phi_e f_e^0 \tilde{f}_e^0 + f_e^{0\prime}\tilde{\phi}_e' \tilde{f}_e^{0\prime} - f_e^0 \tilde{\phi}_e \tilde{f}_e^0\right) \mathrm{d}\boldsymbol{\omega}'_{e\tilde{e}} \mathrm{d}\widetilde{\boldsymbol{C}}_e,$$

where $\tilde{\psi}_e = \psi_e(t, \boldsymbol{x}, \widetilde{\boldsymbol{C}}_e)$ and $\tilde{\psi}_e' = \psi_e(t, \boldsymbol{x}, \widetilde{\boldsymbol{C}}_e')$ for any function ψ_e of t, $\boldsymbol{x}$ and $\boldsymbol{C}_e$. The conservation of energy for electron-electron collisions reads

$$\frac{1}{2}\mathfrak{m}_e|\boldsymbol{C}_e|^2 + \frac{1}{2}\mathfrak{m}_e|\widetilde{\boldsymbol{C}}_e|^2 = \frac{1}{2}\mathfrak{m}_e|\boldsymbol{C}_e'|^2 + \frac{1}{2}\mathfrak{m}_e|\widetilde{\boldsymbol{C}}_e'|^2,$$

so that from (2.4.28)

$$f_e^{0\prime}\tilde{f}_e^{0\prime} = f_e^0 \tilde{f}_e^0, \tag{2.4.48}$$

and thus

$$-\frac{1}{f_e^0}\left[\mathcal{S}_{ee}(\phi_e f_e^0, f_e^0) + \mathcal{S}_{ee}(f_e^0, \phi_e f_e^0)\right] = -\frac{1}{f_e^0}\int g_{e\tilde{e}}\sigma_{e\tilde{e}} f_e^0 \tilde{f}_e^0 \left(\phi_e' - \phi_e + \tilde{\phi}_e' - \tilde{\phi}_e\right) \mathrm{d}\boldsymbol{\omega}'_{e\tilde{e}} \mathrm{d}\widetilde{\boldsymbol{C}}_e.$$

Similarly, from expression (2.3.63) of $\mathcal{S}_{ej}^0$, the last term on the right hand side reads

$$-\frac{1}{f_e^0}\sum_{j \in \mathfrak{H}} \mathcal{S}_{ej}^0(\phi_e f_e^0, f_j^0) \\ = -\frac{1}{f_e^0}\sum_{j \in \mathfrak{H}}\sum_{\mathrm{J} \in \mathfrak{Q}_j}\left(\int f_j^0(\boldsymbol{C}_j, \mathrm{J})\,\mathrm{d}\boldsymbol{C}_j\right)\int \sigma_{ej}^{\mathrm{JJ}}\,|\boldsymbol{C}_e|\left(\phi_e f_e^0(|\boldsymbol{C}_e|\boldsymbol{\omega}'_{ej}) - \phi_e f_e^0(\boldsymbol{C}_e)\right)\mathrm{d}\boldsymbol{\omega}'_{ej} \\ = -\frac{1}{f_e^0}\sum_{j \in \mathfrak{H}}\sum_{\mathrm{J} \in \mathfrak{Q}_j} n_j \frac{a_{j\mathrm{J}} e^{-\epsilon_{j\mathrm{J}}}}{Q_j^{\mathrm{int}}}\int \sigma_{ej}^{\mathrm{JJ}}\,|\boldsymbol{C}_e|\left(\phi_e f_e^0(|\boldsymbol{C}_e|\boldsymbol{\omega}'_{ej}) - \phi_e f_e^0(\boldsymbol{C}_e)\right)\mathrm{d}\boldsymbol{\omega}'_{ej},$$

where expression (2.4.36) for the zeroth-order j^{th}-heavy-species distribution function f_j^0 has been integrated over $\boldsymbol{C}_j$, and where we have introduced the reduced internal energy

$$\epsilon_{j\mathrm{J}} = \frac{E_{j\mathrm{J}}}{k_{\mathrm{B}} T_h}, \qquad j \in \mathfrak{H}, \mathrm{J} \in \mathfrak{Q}_j. \tag{2.4.49}$$

Since f_e^0 is isotropic, $f_e^0(|\boldsymbol{C}_e|\boldsymbol{\omega}'_{ej}) = f_e^0(\boldsymbol{C}_e)$, and the electron linearized collision operator finally reads

$$\begin{aligned}\mathcal{F}_e(\phi_e) = &- \int g_{e\tilde{e}}\sigma_{e\tilde{e}}\tilde{f}_e^0 \left(\phi'_e + \tilde{\phi}'_e - \phi_e - \tilde{\phi}_e\right) \mathrm{d}\boldsymbol{\omega}'_{e\tilde{e}}\mathrm{d}\widetilde{\boldsymbol{C}}_e \\ &- \sum_{j\in\mathfrak{H}}\sum_{\mathrm{J}\in\mathfrak{Q}_j} n_j \frac{a_{j\mathrm{J}}e^{-\epsilon_{j\mathrm{J}}}}{Q_j^{\mathrm{int}}} \int \sigma_{ej}^{\mathrm{JJ}}\, |\boldsymbol{C}_e| \left(\phi_e(|\boldsymbol{C}_e|\boldsymbol{\omega}'_{ej}) - \phi_e(\boldsymbol{C}_e)\right) \mathrm{d}\boldsymbol{\omega}'_{ej}.\end{aligned} \tag{2.4.50}$$

The kernel of $\mathcal{F}_e$ coincides with the set of electron collisional invariants $\mathcal{I}_e^0$. Indeed, if $\mathcal{F}_e(\phi_e) = 0$, then multiplying expression (2.4.50) above by $\phi_e f_e^0$, integrating over $\boldsymbol{C}_e$, and using the reciprocity relation (2.2.35) and symmetrization one obtains

$$\begin{aligned}\phi_e(|\boldsymbol{C}_e|\boldsymbol{\omega}'_{ej}) &= \phi_e(\boldsymbol{C}_e) \\ \phi_e(\boldsymbol{C}'_e) + \phi_e(\widetilde{\boldsymbol{C}}'_e) &= \phi_e(\boldsymbol{C}_e) + \phi_e(\widetilde{\boldsymbol{C}}_e),\end{aligned}$$

for all $\boldsymbol{C}_e$, $\widetilde{\boldsymbol{C}}_e$, $\boldsymbol{\omega}'_{e\tilde{e}}$, $\boldsymbol{\omega}'_{ej}$, i.e., $\phi_e \in \mathcal{I}_e^0$.

Furthermore, $\mathcal{F}_e$ is isotropic, i.e., it transforms a tensor constructed from $\boldsymbol{C}_e$ into another tensor of the same type [Wal58] [Gra04] [GG09]. This will be of great importance for the calculation of transport coefficients. We also introduce the associated integral bracket operator:

$$[\![\xi_e, \zeta_e]\!]_e = \langle\!\langle f_e^0 \xi_e, \mathcal{F}_e(\zeta_e)\rangle\!\rangle_e, \tag{2.4.51}$$

which can be expressed in the form

$$\begin{aligned}[\![\xi_e, \zeta_e]\!]_e = &\frac{1}{4}\int g_{e\tilde{e}}\sigma_{e\tilde{e}} f_e^0 \tilde{f}_e^0 \left(\xi'_e + \tilde{\xi}'_e - \xi_e - \tilde{\xi}_e\right)\left(\zeta'_e + \tilde{\zeta}'_e - \zeta_e - \tilde{\zeta}_e\right) \mathrm{d}\boldsymbol{\omega}'_{e\tilde{e}}\mathrm{d}\boldsymbol{C}_e\mathrm{d}\widetilde{\boldsymbol{C}}_e \\ &+ \frac{1}{2}\sum_{j\in\mathfrak{H}}\sum_{\mathrm{J}\in\mathfrak{Q}_j} n_j \frac{a_{j\mathrm{J}}e^{-\epsilon_{j\mathrm{J}}}}{Q_j^{\mathrm{int}}} \\ &\times \int \sigma_{ej}^{\mathrm{JJ}}\, |\boldsymbol{C}_e| f_e^0(\boldsymbol{C}_e) \left(\xi_e(|\boldsymbol{C}_e|\boldsymbol{\omega}'_{ej}) - \xi_e(\boldsymbol{C}_e)\right)\left(\zeta_e(|\boldsymbol{C}_e|\boldsymbol{\omega}'_{ej}) - \zeta_e(\boldsymbol{C}_e)\right) \mathrm{d}\boldsymbol{\omega}'_{ej}\mathrm{d}\boldsymbol{C}_e.\end{aligned} \tag{2.4.52}$$

From expression (2.4.52), the bracket operator $[\![\,\cdot\,]\!]_e$ is readily seen to be symmetric, i.e.,

$$[\![\xi_e, \zeta_e]\!]_e = [\![\zeta_e, \xi_e]\!]_e, \tag{2.4.53}$$

positive semi-definite:

$$[\![\xi_e, \xi_e]\!]_e \geq 0, \tag{2.4.54}$$

and its kernel is seen to coincide with the kernel of $\mathcal{F}_e$:

$$[\![\xi_e, \xi_e]\!]_e = 0 \Leftrightarrow \mathcal{F}_e(\xi_e) = 0 \Leftrightarrow \xi_e \in \mathcal{I}_e^0. \tag{2.4.55}$$

The electron Boltzmann equation (2.4.5) is now projected at order ε^{-1}. As long as f_e^0 is an isotropic function of $\boldsymbol{C}_e$, respectively f_j^0 is an isotropic function of $\boldsymbol{C}_j$, from (2.3.63) the term $\mathcal{S}_{ej}^0(f_e^0, \phi_j f_j^0)$ is shown to vanish:

$$\mathcal{S}_{ej}^0(f_e^0, \phi_j f_j^0) = 0, \tag{2.4.56}$$

respectively from (2.3.64)

$$\mathcal{S}_{ej}^1(f_e^0, f_j^0) = 0. \tag{2.4.57}$$

Thus, the first-order electron perturbation function ϕ_e is solution to the following linear equation:

$$\mathcal{F}_e(\phi_e) + \delta_{b1}\frac{q_e}{\mathfrak{m}_e}(\boldsymbol{C}_e \wedge \mathbf{B}) \cdot \boldsymbol{\partial}_{\boldsymbol{C}_e}\phi_e = \Psi_e, \tag{2.4.58}$$

where

$$\Psi_e = -\mathcal{D}_e^{-1}(\ln f_e^0). \tag{2.4.59}$$

Equation (2.4.58) must be completed with constraints (2.4.3) in order to be well posed

$$\langle\!\langle \phi_e f_e^0, \psi_e^l \rangle\!\rangle_e = 0, \quad l \in \{e, n^s + 4\}\,. \tag{2.4.60}$$

Indeed, the streaming operator $\Psi_e = -\mathcal{D}_e^{-1}(\ln f_e^0)$ on the right hand side of (2.4.58) is orthogonal to the electron collisional invariants [GMM09], and the second term on the left hand side of (2.4.58) is orthogonal to the electron isotropic collisional invariants [GG03] [Gra04] [GMM09], since if f_e^0 decreases sufficiently rapidly as $|\boldsymbol{C}_e| \to +\infty$, then

$$\begin{aligned}
\int f_e^0\, \psi_e^l\, (\boldsymbol{C}_e \wedge \mathbf{B}) \cdot \boldsymbol{\partial}_{\boldsymbol{C}_e} \phi_e \, \mathrm{d}\boldsymbol{C}_e &= -\int f_e^0 \phi_e \, \boldsymbol{\partial}_{\boldsymbol{C}_e} \cdot (\psi_e^l \boldsymbol{C}_e \wedge \mathbf{B}) \, \mathrm{d}\boldsymbol{C}_e, \\
&= -\int f_e^0 \phi_e \, (\boldsymbol{C}_e \wedge \mathbf{B}) \cdot \boldsymbol{\partial}_{\boldsymbol{C}_e} \psi_e^l \, \mathrm{d}\boldsymbol{C}_e, \\
&= 0,
\end{aligned}$$

for $l \in \{e, n^s + 4\}$. Besides, the relation

$$\begin{aligned}
\langle\!\langle f_e^0 \phi_e, (\boldsymbol{C}_e \wedge \mathbf{B}) \cdot \boldsymbol{\partial}_{\boldsymbol{C}_e} \phi_e \rangle\!\rangle_e &= \int f_e^0 \phi_e \, (\boldsymbol{C}_e \wedge \mathbf{B}) \cdot \boldsymbol{\partial}_{\boldsymbol{C}_e} \phi_e \, \mathrm{d}\boldsymbol{C}_e, \\
&= \int f_e^0 \, (\boldsymbol{C}_e \wedge \mathbf{B}) \cdot \boldsymbol{\partial}_{\boldsymbol{C}_e} \Big(\frac{1}{2} \phi_e^2 \Big) \, \mathrm{d}\boldsymbol{C}_e, \\
&= 0,
\end{aligned}$$

ensures that the set of solutions of the homogeneous linear equation associated with the linear equation (2.4.58) coincides with the kernel of $\mathcal{F}_e$, $\mathcal{I}_e^0$.

2.4.5 Scaling for inelastic collision cross-sections

We can now discuss in more details the choice of scaling adopted for $\sigma_{je}^{\mathrm{JJ}'}$, $j \in \mathfrak{H}$, $\mathrm{J}, \mathrm{J}' \in \mathfrak{Q}_j$, $\mathrm{J} \neq \mathrm{J}'$. We consider the two possible alternative scaling $\sigma_{he}^{\mathrm{in},0} = \sigma^0$ and $\sigma_{he}^{\mathrm{in},0} = \varepsilon\sigma^0$, instead of $\sigma_{he}^{\mathrm{in},0} = \varepsilon^2\sigma^0$. Other things being equal, in the former case the electron thermalization requires that the electron temperature is equal to the heavy-species temperature $T_e = T_h$, while in the latter case the thermalization of the heavy species induces $T_h = T_e$.

Electron thermalization

First, if the inelastic reference collision scaled as

$$\sigma_{he}^{\mathrm{in},0} = \sigma^0, \tag{2.4.61}$$

that is to say if there was only one relevant characteristic cross-section, then the right hand side of the electron Boltzmann equation at order ε^{-2} (2.4.21) would contain the additional term $\sum_{j\in\mathfrak{H}} \mathcal{S}_{ej}^{2,\mathrm{in}}\left(f_e^0, f_j^0\right)$. Thus, equation (2.4.24) for electron thermalization would be replaced by

$$\Gamma_{ee}^0 + \sum_{j\in\mathfrak{H}} \Gamma_{ej}^0 + \sum_{j\in\mathfrak{H}} \Gamma_{ej}^{2,\mathrm{in}} = 0, \tag{2.4.62}$$

where the entropy production rate due to inelastic scattering of electron against the j^{th} heavy species reads

$$\Gamma_{ej}^{2,\text{in}} = -k_{\text{B}} \int \mathcal{S}_{ej}^{2,\text{in}} \left(f_e^0(\boldsymbol{C}_e), f_j^0(\boldsymbol{C}_j)\right) \ln\left(f_e^0(\boldsymbol{C}_e)\right) \mathrm{d}\boldsymbol{C}_e, \tag{2.4.63}$$

$$\Gamma_{ej}^{2,\text{in}} = -k_{\text{B}} \sum_{\substack{\text{J},\text{J}'\in\mathfrak{Q}_j \\ \text{J}'\neq\text{J}}} \int \sigma_{ej}^{\text{J}\text{J}'} |\boldsymbol{C}_e| \Big(f_e^0(\boldsymbol{C}_e'^{(0)}) f_j^0(\boldsymbol{C}_j, \text{J}') \frac{\beta_{j\text{J}'}}{\beta_{j\text{J}}} - f_e^0(\boldsymbol{C}_e) f_j^0(\boldsymbol{C}_j, \text{J}) \Big) \tag{2.4.64}$$

$$\times \ln\left(f_e^0(\boldsymbol{C}_e)\right) \mathrm{d}\boldsymbol{\omega}'_{ej} \mathrm{d}\boldsymbol{C}_e \mathrm{d}\boldsymbol{C}_j,$$

where $\boldsymbol{C}_e'^{(0)} = |\boldsymbol{C}_e|\big(1 - \Delta E_{\text{J}\text{J}'}/\frac{1}{2}\mathfrak{m}_e|\boldsymbol{C}_e|^2\big)^{1/2}\boldsymbol{\omega}'_{ej}$ is the zeroth-order electron velocity after collision. Using again the reciprocity relation (2.2.35) in the form

$$\beta_{j\text{J}'} |\boldsymbol{C}_e| \sigma_{ej}^{\text{J}\text{J}'} \, \mathrm{d}\boldsymbol{\omega}'_{ej} \mathrm{d}\boldsymbol{C}_e \mathrm{d}\boldsymbol{C}_j = \beta_{j\text{J}} |\boldsymbol{C}_e'^{(0)}| \sigma_{ej}^{\text{J}'\text{J}} \, \mathrm{d}\boldsymbol{\omega}_{ej} \mathrm{d}\boldsymbol{C}_e'^{(0)} \mathrm{d}\boldsymbol{C}_j, \tag{2.4.65}$$

and symmetrizing, $\Gamma_{ej}^{2,\text{in}}$ may be expressed as

$$\Gamma_{ej}^{2,\text{in}} = k_{\text{B}} \sum_{\substack{\text{J},\text{J}'\in\mathfrak{Q}_j \\ \text{J}'\neq\text{J}}} \int \sigma_{ej}^{\text{J}\text{J}'} |\boldsymbol{C}_e| \big[\ln\left(f_e^0(\boldsymbol{C}_e)\right) - \ln\left(f_e^0(\boldsymbol{C}_e'^{(0)})\right) \big] f_e^0(\boldsymbol{C}_e) f_j^0(\boldsymbol{C}_j, \text{J}) \, \mathrm{d}\boldsymbol{\omega}'_{ej} \mathrm{d}\boldsymbol{C}_e \mathrm{d}\boldsymbol{C}_j. \tag{2.4.66}$$

Now, for the alternative scaling $\sigma_{he}^{\text{in},0} = \sigma^0$, the projection of the heavy species Boltzmann equation (2.3.22) at order ε^{-2} would be non trivial, and would yield

$$0 = \mathcal{S}_{je}^{2,\text{in}}(f_j^0, f_e^0) = \sum_{\substack{\text{J}'\in\mathfrak{Q}_j \\ \text{J}'\neq\text{J}}} \int \sigma_{je}^{\text{J}\text{J}'} |\boldsymbol{C}_e| \Big(f_e^0(\boldsymbol{C}_e'^{(0)}) f_j^0(\boldsymbol{C}_j, \text{J}') \frac{\beta_{j\text{J}'}}{\beta_{j\text{J}}} - f_e^0(\boldsymbol{C}_e) f_j^0(\boldsymbol{C}_j, \text{J}) \Big) \tag{2.4.67}$$

$$\times \, \mathrm{d}\boldsymbol{\omega}'_{je} \mathrm{d}\boldsymbol{C}_e \mathrm{d}\boldsymbol{C}_j.$$

Multiplying the latter equation by $\ln\left(\beta_{j\text{J}} f_j^0(\boldsymbol{C}_j, \text{J})\right)$, integrating over $\boldsymbol{C}_j$ and summing over $\text{J} \in \mathfrak{Q}_j$, and noting that $\boldsymbol{\omega}_{je} = -\boldsymbol{\omega}_{ej}$, $\boldsymbol{\omega}'_{je} = -\boldsymbol{\omega}'_{ej}$, and $\sigma_{je}^{\text{J}\text{J}'} = \sigma_{ej}^{\text{J}\text{J}'}$, one would obtain

$$0 = \sum_{\substack{\text{J},\text{J}'\in\mathfrak{Q}_j \\ \text{J}'\neq\text{J}}} \frac{1}{\beta_{j\text{J}}} \int \sigma_{ej}^{\text{J}\text{J}'} |\boldsymbol{C}_e| \ln\left(\beta_{j\text{J}} f_j^0(\boldsymbol{C}_j, \text{J})\right) \tag{2.4.68}$$

$$\times \left(\beta_{j\text{J}'} f_e^0(\boldsymbol{C}_e'^{(0)}) f_j^0(\boldsymbol{C}_j, \text{J}') - \beta_{j\text{J}} f_e^0(\boldsymbol{C}_e) f_j^0(\boldsymbol{C}_j, \text{J})\right) \mathrm{d}\boldsymbol{\omega}'_{ej} \mathrm{d}\boldsymbol{C}_e \mathrm{d}\boldsymbol{C}_j,$$

which by reciprocity and symmetry would yield

$$0 = \sum_{\substack{\text{J},\text{J}'\in\mathfrak{Q}_j \\ \text{J}'\neq\text{J}}} \frac{1}{\beta_{j\text{J}}} \int \sigma_{ej}^{\text{J}\text{J}'} |\boldsymbol{C}_e| \big[\ln\left(\beta_{j\text{J}'} f_j^0(\boldsymbol{C}_j, \text{J}')\right) - \ln\left(\beta_{j\text{J}} f_j^0(\boldsymbol{C}_j, \text{J})\right) \big] \tag{2.4.69}$$

$$\times \left(\beta_{j\text{J}'} f_e^0(\boldsymbol{C}_e'^{(0)}) f_j^0(\boldsymbol{C}_j, \text{J}') - \beta_{j\text{J}} f_e^0(\boldsymbol{C}_e) f_j^0(\boldsymbol{C}_j, \text{J})\right) \mathrm{d}\boldsymbol{\omega}'_{ej} \mathrm{d}\boldsymbol{C}_e \mathrm{d}\boldsymbol{C}_j,$$

so that the entropy production rate due to inelastic scattering of electron against the j^{th} heavy species would read

$$\Gamma_{ej}^{2,\text{in}} = \frac{k_{\text{B}}}{2} \sum_{\substack{\text{J},\text{J}'\in\mathfrak{Q}_j \\ \text{J}'\neq\text{J}}} \frac{1}{\beta_{j\text{J}}} \int \sigma_{ej}^{\text{J}\text{J}'} |\boldsymbol{C}_e| \Omega\big(\beta_{j\text{J}'} f_e^0(\boldsymbol{C}_e'^{(0)}) f_j^0(\boldsymbol{C}_j, \text{J}'), \beta_{j\text{J}} f_e^0(\boldsymbol{C}_e) f_j^0(\boldsymbol{C}_j, \text{J})\big) \tag{2.4.70}$$

$$\mathrm{d}\boldsymbol{\omega}'_{ej} \mathrm{d}\boldsymbol{C}_e \mathrm{d}\boldsymbol{C}_j,$$

where Ω is the function defined in (2.4.26). Since Ω is nonnegative, the ε^{-2} electron Boltzmann equation (2.4.62) would yield the thermalization of electrons (2.4.28) as in subsection 2.4.2. Besides, the electron j^{th}-heavy-species inelastic entropy production rate would vanish

$$\Gamma_{ej}^{2,\text{in}} = 0, \quad j \in \mathfrak{H}, \tag{2.4.71}$$

which would require

$$a_{j\text{J}} f_e^0(\boldsymbol{C}_e'^{(0)}) f_j^0(\boldsymbol{C}_j, \text{J}') = a_{j\text{J}'} f_e^0(\boldsymbol{C}_e) f_j^0(\boldsymbol{C}_j, \text{J}), \quad j \in \mathfrak{H}, \text{J}, \text{J}' \in \mathfrak{Q}_j, \text{J}' \neq \text{J}, \tag{2.4.72}$$

for Ω is nonnegative. From expression (2.4.28) for the electron Maxwellian distribution function, the latter equation is rewritten

$$a_{j\text{J}} f_j^0(\boldsymbol{C}_j, \text{J}') = \exp\Big(- \frac{\Delta E_{\text{JJ}'}}{k_\text{B} T_e} \Big) a_{j\text{J}'} f_j^0(\boldsymbol{C}_j, \text{J}), \quad j \in \mathfrak{H}, \text{J}, \text{J}' \in \mathfrak{Q}_j, \text{J}' \neq \text{J}. \tag{2.4.73}$$

Assuming that the zeroth-order heavy-species distribution functions f_j^0, $j \in \mathfrak{H}$, would still be Maxwellian of the form (2.4.36), equation (2.4.73) would be equivalent to

$$\frac{\Delta E_{\text{JJ}'}}{k_\text{B} T_h} = \frac{\Delta E_{\text{JJ}'}}{k_\text{B} T_e}, \quad j \in \mathfrak{H}, \text{J}, \text{J}' \in \mathfrak{Q}_j, \text{J}' \neq \text{J},$$

which would imply $T_e = T_h$.

Heavy-species thermalization

In the preceding paragraph it was shown that, other things being equal, the inelastic collisions between electrons and heavy species must be at least one order of magnitude slower than the corresponding elastic collisions. We now consider the alternative scaling

$$\sigma_{he}^{\text{in},0} = \varepsilon \sigma^0. \tag{2.4.74}$$

For such a scaling electron thermalization would proceed as in 2.4.2, since equation (2.4.24) would remain unchanged, and hence the zeroth-order electron distribution function f_e^0 would be a Maxwellian of the form (2.4.28).

The heavy-species Boltzmann equation at order ε^{-1} (2.4.32) would contain the additional term $\mathcal{S}_{ie}^{2,\text{in}}(f_i^0, f_e^0)$, so that equation (2.4.33) for heavy-species thermalization would be replaced by

$$\Gamma_{hh}^0 + \Gamma_{he}^{2,\text{in}} = 0, \tag{2.4.75}$$

where we have introduced the entropy production rate due to inelastic scattering of heavy species against electrons

$$\Gamma_{he}^{2,\text{in}} = -k_\text{B} \sum_{i \in \mathfrak{H}} \sum_{\text{I} \in \mathfrak{Q}_i} \int \ln\big(\beta_{i\text{I}} f_i^0(\boldsymbol{C}_i, \text{I})\big) \mathcal{S}_{ie}^{2,\text{in}}\big(f_i^0, f_e^0\big) \, \mathrm{d}\boldsymbol{C}_i. \tag{2.4.76}$$

From expression (2.3.57) for $\mathcal{S}_{ie}^{2,\text{in}}$, this inelastic entropy production rate is expanded as

$$\begin{aligned}
\Gamma_{he}^{2,\text{in}} = -k_\text{B} \sum_{i \in \mathfrak{H}} \sum_{\text{I} \in \mathfrak{Q}_i} \int & \sigma_{ie}^{\text{II}'} |\boldsymbol{C}_e| \ln\big(\beta_{i\text{I}} f_i^0(\boldsymbol{C}_i, \text{I})\big) \\
& \times \Big(f_i^0(\boldsymbol{C}_i, \text{I}') f_e^0(\boldsymbol{C}_e'^{(0)}) \frac{\beta_{i\text{I}'}}{\beta_{i\text{I}}} - f_i^0(\boldsymbol{C}_i, \text{I}) f_e^0(\boldsymbol{C}_e) \Big) \, \mathrm{d}\boldsymbol{\omega}_{ie}' \mathrm{d}\boldsymbol{C}_i \mathrm{d}\boldsymbol{C}_e, \\
\Gamma_{he}^{2,\text{in}} = \frac{k_\text{B}}{2} \sum_{i \in \mathfrak{H}} \sum_{\text{I} \in \mathfrak{Q}_i} \int & \sigma_{ie}^{\text{II}'} |\boldsymbol{C}_e| \big[\ln\big(\beta_{i\text{I}'} f_i^0(\boldsymbol{C}_i, \text{I}')\big) - \ln\big(\beta_{i\text{I}} f_i^0(\boldsymbol{C}_i, \text{I})\big) \big] \\
& \times \Big(f_i^0(\boldsymbol{C}_i, \text{I}') f_e^0(\boldsymbol{C}_e'^{(0)}) \frac{\beta_{i\text{I}'}}{\beta_{i\text{I}}} - f_i^0(\boldsymbol{C}_i, \text{I}) f_e^0(\boldsymbol{C}_e) \Big) \, \mathrm{d}\boldsymbol{\omega}_{ie}' \mathrm{d}\boldsymbol{C}_i \mathrm{d}\boldsymbol{C}_e,
\end{aligned} \tag{2.4.77}$$

where we have used the reciprocity relation (2.4.65) and symmetrization.

Now, for the scaling $\sigma_{he}^{\mathrm{in},0} = \varepsilon\sigma^0$ proposed, equation (2.4.58) obtained from the projection of the Boltzmann equation at order ε^{-1} would remain valid, but the source term Ψ_e would read

$$f_e^0\Psi_e = -\mathcal{D}_e^{-1}(f_e^0) + \sum_{j\in\mathfrak{H}} \mathcal{S}_{ej}^1(f_e^0, f_j^0) + \sum_{j\in\mathfrak{H}} \mathcal{S}_{ej}^{2,\mathrm{in}}(f_e^0, f_j^0), \tag{2.4.78}$$

where f_j^0 would remain unknown at this point. Since the streaming operator, the electron linearized collision operator $\mathcal{F}_e$, and the term $(\boldsymbol{C}_e\wedge\mathbf{B})\cdot\boldsymbol{\partial}_{\boldsymbol{C}_e}\phi_e$ are orthogonal to the electron isotropic collisional invariants $\mathcal{I}_e^0$

$$\langle\!\langle \mathcal{D}_e^{-1}(f_e), \psi_e^l\rangle\!\rangle_e = 0, \quad l \in \{e, n^s + 4\}\,, \tag{2.4.79}$$

$$\langle\!\langle f_e^0\mathcal{F}_e(\phi_e), \psi_e^l\rangle\!\rangle_e = 0, \quad l \in \{e, n^s + 4\}\,, \tag{2.4.80}$$

$$\langle\!\langle f_e^0(\boldsymbol{C}_e \wedge \mathbf{B})\cdot\boldsymbol{\partial}_{\boldsymbol{C}_e}\phi_e, \psi_e^l\rangle\!\rangle_e = 0, \quad l \in \{e, n^s + 4\}\,, \tag{2.4.81}$$

and since $\ln f_e^0$ belongs to $\mathcal{I}_e^0$, multiplying (2.4.78) by $\ln f_e^0$ and integrating over $\boldsymbol{C}_e$ one would obtain

$$\sum_{j\in\mathfrak{H}} \langle\!\langle \mathcal{S}_{ej}^1(f_e^0, f_j^0), \ln f_e^0\rangle\!\rangle_e + \sum_{j\in\mathfrak{H}} \langle\!\langle \mathcal{S}_{ej}^{2,\mathrm{in}}(f_e^0, f_j^0), \ln f_e^0\rangle\!\rangle_e = 0. \tag{2.4.82}$$

The first term on the left hand side would be shown to vanish since from expression (2.3.64) $\mathcal{S}_{ej}^1(f_e^0, f_j^0) = 0$ as long as f_e^0 is given by a Maxwellian of the form (2.4.28). Thus, the second term on the left hand side would be zero:

$$\begin{aligned}
0 &= \sum_{j\in\mathfrak{H}} \langle\!\langle \mathcal{S}_{ej}^{2,\mathrm{in}}(f_e^0, f_j^0), \ln f_e^0\rangle\!\rangle_e \\
&= \sum_{j\in\mathfrak{H}} \sum_{\mathrm{J}\in\mathfrak{Q}_j} \int \sigma_{je}^{\mathrm{JJ}'}|\boldsymbol{C}_e| \ln\left(f_e^0(\boldsymbol{C}_e)\right) \\
&\qquad\qquad \times \left(f_j^0(\boldsymbol{C}_j, \mathrm{J}')f_e^0(\boldsymbol{C}_e'^{(0)})\frac{\beta_{j\mathrm{J}'}}{\beta_{j\mathrm{J}}} - f_j^0(\boldsymbol{C}_j, \mathrm{J})f_e^0(\boldsymbol{C}_e)\right) \mathrm{d}\boldsymbol{\omega}_{ej}'\mathrm{d}\boldsymbol{C}_j\mathrm{d}\boldsymbol{C}_e, \\
&= -\frac{1}{2}\sum_{j\in\mathfrak{H}} \sum_{\mathrm{J}\in\mathfrak{Q}_j} \int \sigma_{je}^{\mathrm{JJ}'}|\boldsymbol{C}_e|\left[\ln\left(f_e^0(\boldsymbol{C}_e'^{(0)})\right) - \ln\left(f_e^0(\boldsymbol{C}_e)\right)\right] \\
&\qquad\qquad \times \left(f_j^0(\boldsymbol{C}_j, \mathrm{J}')f_e^0(\boldsymbol{C}_e'^{(0)})\frac{\beta_{j\mathrm{J}'}}{\beta_{j\mathrm{J}}} - f_j^0(\boldsymbol{C}_j, \mathrm{J})f_e^0(\boldsymbol{C}_e)\right) \mathrm{d}\boldsymbol{\omega}_{je}'\mathrm{d}\boldsymbol{C}_j\mathrm{d}\boldsymbol{C}_e.
\end{aligned}$$

Combining the latter equation with equation (2.4.77), the heavy-species electron inelastic entropy production rate would finally read

$$\Gamma_{he}^{2,\mathrm{in}} = \frac{k_{\mathrm{B}}}{2}\sum_{i\in\mathfrak{H}} \sum_{\mathrm{I}\in\mathfrak{Q}_i} \int \sigma_{ie}^{\mathrm{II}'}\,|\boldsymbol{C}_e|\,\Omega\Big(\frac{\beta_{i\mathrm{I}'}}{\beta_{i\mathrm{I}}} f_i^0(\boldsymbol{C}_i, \mathrm{I}')f_e^0(\boldsymbol{C}_e'^{(0)}), f_i^0(\boldsymbol{C}_i, \mathrm{I})f_e^0(\boldsymbol{C}_e)\Big) \mathrm{d}\boldsymbol{\omega}_{ie}'\mathrm{d}\boldsymbol{C}_i\mathrm{d}\boldsymbol{C}_e, \tag{2.4.83}$$

Since Ω is nonnegative, equation (2.4.75) would induce the thermalization of the heavy species as in subsection 2.4.3, and additionnally we would retrieve (2.4.73), and thus $T_h = T_e$ as in the preceding paragraph.

A possible extension where some of the heavy species internal modes thermalize at T_e is discussed in the conclusion.

2.4.6 Zeroth-order macroscopic equations for electrons

Equations (2.4.15), (2.4.16), (2.4.17) are now expanded at order ε^0. Conservation of matter and energy yield a system of Navier-Stokes type drift-diffusion equations for electrons, from which the equation for conservation of momentum uncouples.

Equation (2.4.15) for conservation of matter yields at order ε^0 the following mass conservation equation for electrons:

$$\partial_t \rho_e + \boldsymbol{\partial}_{\boldsymbol{x}} \cdot \left(\rho_e \boldsymbol{v}_h + \rho_e \boldsymbol{\mathcal{V}}_e^0 \right) = 0, \tag{2.4.84}$$

where we have introduced the electron zeroth-order diffusion velocity

$$n_e \boldsymbol{\mathcal{V}}_e^0 = \int \boldsymbol{C}_e \phi_e f_e^0 \, \mathrm{d}\boldsymbol{C}_e. \tag{2.4.85}$$

On the other hand, the energy conservation equation (2.4.17) yields at order ε^0

$$\partial_t \mathcal{E}_e + \boldsymbol{\partial}_{\boldsymbol{x}} \cdot (\mathcal{E}_e \boldsymbol{v}_h) = -p_e \boldsymbol{\partial}_{\boldsymbol{x}} \cdot \boldsymbol{v}_h - \boldsymbol{\partial}_{\boldsymbol{x}} \cdot \boldsymbol{\mathcal{Q}}_e^0 + \boldsymbol{J}_e^0 \cdot \mathbf{E}' + \Delta E_{eh}^0, \tag{2.4.86}$$

where $p_e = n_e k_{\mathrm{B}} T_e$ is the electron partial pressure, $\boldsymbol{J}_e^0 = n_e q_e \boldsymbol{\mathcal{V}}_e^0$ is the zeroth-order electron conduction current density in the heavy-species reference frame, and $\mathbf{E}'$ is the electric field expressed in the heavy-species reference frame

$$\mathbf{E}' = \mathbf{E} + \delta_{b1} \boldsymbol{v}_h \wedge \mathbf{B}. \tag{2.4.87}$$

We have denoted by $\boldsymbol{\mathcal{Q}}_e^0$ the zeroth-order electron heat flux

$$\boldsymbol{\mathcal{Q}}_e^0 = \int \phi_e f_e^0 \, \left(\frac{1}{2} \mathfrak{m}_e \boldsymbol{C}_e \cdot \boldsymbol{C}_e \right) \boldsymbol{C}_e \, \mathrm{d}\boldsymbol{C}_e, \tag{2.4.88}$$

while ΔE_{eh}^0 is an energy exchange term due to scattering collisions between electrons and heavy species

$$\Delta E_{eh}^0 = \sum_{j \in \mathfrak{H}} \langle\!\langle \psi_e^{n^s+4}, \mathcal{S}_{ej}^2(f_e^0, f_j^0) \rangle\!\rangle_e, \tag{2.4.89}$$

where $\mathcal{S}_{ej}^2$ is the second-order electron j^{th}-heavy-species scattering source term (2.3.65). The zeroth-order electron mean velocity in the inertial reference frame is defined as

$$\boldsymbol{v}_e^0 = \boldsymbol{v}_h + \boldsymbol{\mathcal{V}}_e^0. \tag{2.4.90}$$

Finally, momentum conservation equation (2.4.16) yields the following momentum relation:

$$\boldsymbol{\partial}_{\boldsymbol{x}} p_e = n_e q_e \mathbf{E} + \delta_{b1} \boldsymbol{j}_e^0 \wedge \mathbf{B} + \boldsymbol{F}_{eh}^0, \tag{2.4.91}$$

where $\boldsymbol{j}_e^0 = n_e q_e \boldsymbol{v}_e^0$ is the zeroth-order electron current density in the inertial reference frame, and

$$\boldsymbol{F}_{eh}^0 = \sum_{j \in \mathfrak{H}} \langle\!\langle \mathcal{S}_{ej}^0(\phi_e f_e^0, f_j^0), \mathfrak{m}_e \boldsymbol{C}_e \rangle\!\rangle_e \tag{2.4.92}$$

is the average force exerted by the heavy species on electrons due to scattering collisions, which can be expressed as

$$\boldsymbol{F}_{eh}^0 = \sum_{j \in \mathfrak{H}} n_j \boldsymbol{F}_{ej}^0, \tag{2.4.93}$$

where $\boldsymbol{F}_{ej}^0$ is the average force exerted by the j^{th} heavy species on electrons. We can further decompose

$$\boldsymbol{F}_{ej}^0 = \sum_{\mathrm{J} \in \mathfrak{Q}_j} \frac{a_{j\mathrm{J}} e^{-\epsilon_{j\mathrm{J}}}}{Q_j^{\text{int}}} \boldsymbol{F}_{ej}^{\mathrm{J},0}, \tag{2.4.94}$$

where $\boldsymbol{F}_{ej}^{\mathrm{J},0}$ is the average force exerted on electrons by molecules of the j^{th} heavy species in the J^{th} internal state:

$$\boldsymbol{F}_{ej}^{\mathrm{J},0} = -\mathfrak{m}_e \int \Sigma_{\mathrm{JJ}}^{(1)}(|\boldsymbol{C}_e|^2) |\boldsymbol{C}_e| \phi_e(\boldsymbol{C}_e) f_e^0(\boldsymbol{C}_e) \boldsymbol{C}_e \, \mathrm{d}\boldsymbol{C}_e. \tag{2.4.95}$$

Equation (2.4.91) thus provides an expression for the average force $\boldsymbol{F}_{eh}^0$ in terms of the macroscopic variable gradients and external fields, which will be useful in the derivation of the heavy-species momentum equation.

2.4.7 Zeroth-order macroscopic equations for the heavy species

We now expand equations (2.4.18), (2.4.19), (2.4.20) at order ε^0. First, equation (2.4.18) yields the following mass conservation equation:

$$\partial_t \rho_i + \boldsymbol{\partial_x} \cdot (\rho_i \boldsymbol{v}_h) = 0, \qquad i \in \mathfrak{H}. \tag{2.4.96}$$

Then, expansion of equation (2.4.19) at order ε^0 reads

$$\partial_t (\rho_h \boldsymbol{v}_h) + \boldsymbol{\partial_x} \cdot (\rho_h \boldsymbol{v}_h \otimes \boldsymbol{v}_h + p_h \mathbb{I}) = n_h q_h \mathbf{E} + \delta_{b1}\, \boldsymbol{j}_h^0 \wedge \mathbf{B} + \boldsymbol{F}_{he}^0, \tag{2.4.97}$$

where $p_h = n_h k_{\text{B}} T_h$ is the heavy-species partial pressure, $n_h = \sum_{j\in\mathfrak{H}} n_j$ the heavy-species density, $n_h q_h = \sum_{j\in\mathfrak{H}} n_j q_j$ the heavy-species charge density, $\boldsymbol{j}_h^0 = n_h q_h \boldsymbol{v}_h$ the zeroth-order heavy-species current density in the inertial reference frame, and

$$\boldsymbol{F}_{he}^0 = \langle\!\langle \mathcal{S}_{he}^1(f_h^0, \phi_e f_e^0) + \mathcal{S}_{he}^2(f_h^0, f_e^0), \mathfrak{m}_h \boldsymbol{C}_h \rangle\!\rangle_h \tag{2.4.98}$$

is the average force exerted by electrons on the heavy species due to scattering collisions. Indeed, we recall that from (2.3.51) $\mathcal{S}_{ie}^0 = 0$, and from (2.3.52) it is readily seen that

$$\mathcal{S}_{ie}^1(\phi_i f_i^0, f_e^0) = 0, \tag{2.4.99}$$

as long as f_e^0 is isotropic. Due to orthogonality relation (2.3.33), the following reciprocity relation holds:

$$\boldsymbol{F}_{he}^0 = -\boldsymbol{F}_{eh}^0. \tag{2.4.100}$$

As a consequence, making use of the electron momentum relation (2.4.91), the momentum conservation equation (2.4.97) for the heavy species can be rewritten

$$\partial_t (\rho_h \boldsymbol{v}_h) + \boldsymbol{\partial_x} \cdot (\rho_h \boldsymbol{v}_h \otimes \boldsymbol{v}_h + p\, \mathbb{I}) = nq\mathbf{E} + \delta_{b1}\, \boldsymbol{j}^0 \wedge \mathbf{B}, \tag{2.4.101}$$

where $p = p_h + p_e$ is the total pressure, $n = n_h + n_e$ the total density, $nq = n_h q_h + n_e q_e$ the total charge density, and $\boldsymbol{j}^0 = \boldsymbol{j}_h^0 + \boldsymbol{j}_e^0$ is the zeroth-order current density in the inertial reference frame.

Finally, equation (2.4.20) yields the following energy conservation equation at order zero:

$$\partial_t \mathcal{E}_h + \boldsymbol{\partial_x} \cdot (\mathcal{E}_h \boldsymbol{v}_h) = -p_h\, \boldsymbol{\partial_x} \cdot \boldsymbol{v}_h + \Delta E_{he}^0, \tag{2.4.102}$$

where $\Delta E_{he}^0 = \langle\!\langle \mathcal{S}_{he}^2(f_h^0, f_e^0), \psi_h^{n^s+4} \rangle\!\rangle_h$ is an energy exchange term due to scattering collisions between heavy species and electrons. Given orthogonality property (2.3.34), energy exchange terms are shown to be symmetric as momentum exchange terms in (2.4.100):

$$\Delta E_{he}^0 = -\Delta E_{eh}^0. \tag{2.4.103}$$

The energy exchange term splits into an elastic and an inelastic contributions:

$$\Delta E_{he}^0 = \Delta E_{he}^{0,\text{el}} + \Delta E_{he}^{0,\text{in}}. \tag{2.4.104}$$

The elastic term $\Delta E_{he}^{0,\text{el}} = \langle\!\langle \mathcal{S}_{he}^{2,\text{el}}(f_h^0, f_e^0), \psi_h^{n^s+4} \rangle\!\rangle_h$ is computed from expression (2.3.56) for the second-order i^{th}-heavy-species electron elastic scattering source term $\mathcal{S}_{ie}^{2,\text{el}}$, and reads

$$\Delta E_{he}^{0,\text{el}} = \frac{3}{2} n_h k_{\text{B}} (T_e - T_h) \frac{1}{\tau^{\text{el}}}, \tag{2.4.105}$$

where τ^{el} is the average collision time at which elastic energy transfer occurs:

$$\frac{1}{\tau^{\mathrm{el}}} = \frac{2}{3}\sum_{i\in\mathfrak{H}} \frac{n_i}{n_h}\frac{\mathfrak{m}_e}{\mathfrak{m}_i}\nu_{ie}^{\mathrm{el}}, \tag{2.4.106}$$

$$\nu_{ie}^{\mathrm{el}} = \sum_{\mathrm{I}\in\mathfrak{Q}_i} \frac{a_{i\mathrm{I}}e^{-E_{i\mathrm{I}}/k_{\mathrm{B}}T_h}}{Q_i^{\mathrm{int}}}\nu_{ie}^{\mathrm{II}}, \tag{2.4.107}$$

$$\nu_{ie}^{\mathrm{II}} = \frac{\mathfrak{m}_e}{k_{\mathrm{B}}T_e}\int \Sigma_{\mathrm{II}}^{(1)}(|\boldsymbol{C}_e|^2)\,|\boldsymbol{C}_e|^3\, f_e^0(\boldsymbol{C}_e)\,\mathrm{d}\boldsymbol{C}_e. \tag{2.4.108}$$

The inelastic contribution can be expressed using (2.3.57) as

$$\Delta E_{he}^{0,\mathrm{in}} = \frac{1}{2}\sum_{i\in\mathfrak{H}}\sum_{\substack{\mathrm{I},\mathrm{I}'\in\mathfrak{Q}_i\\ \mathrm{I}'\neq\mathrm{I}}} \Delta E_{\mathrm{II}'}\frac{n_i a_{i\mathrm{I}}}{Q_i^{\mathrm{int}}}\nu_{ie}^{\mathrm{II}'}\left(e^{-E_{i\mathrm{I}}/k_{\mathrm{B}}T_h} - \exp\left(\frac{\Delta E_{\mathrm{II}'}}{k_{\mathrm{B}}T_e}\right)e^{-E_{i\mathrm{I}'}/k_{\mathrm{B}}T_h}\right), \tag{2.4.109}$$

where $\nu_{ie}^{\mathrm{II}'}$ is the collision frequency between a molecule of the i^{th} heavy species with initial quantum state I and final quantum state I' and an electron:

$$\nu_{ie}^{\mathrm{II}'} = \int \Sigma_{\mathrm{II}'}^{(0)}(|\boldsymbol{C}_e|^2)\,|\boldsymbol{C}_e|\, f_e^0(\boldsymbol{C}_e)\,\mathrm{d}\boldsymbol{C}_e, \qquad \mathrm{I}'\neq\mathrm{I}. \tag{2.4.110}$$

Expression (2.4.109) can be rewritten in terms of the temperature difference $T_e - T_h$

$$\Delta E_{he}^{0,\mathrm{in}} = \frac{3}{2}n_h k_{\mathrm{B}}(T_e - T_h)\frac{1}{\tau^{\mathrm{in}}}, \tag{2.4.111}$$

where τ^{in} is the average collision time at which inelastic energy transfer occurs:

$$\frac{1}{\tau^{\mathrm{in}}} = \frac{2}{3}\frac{T_h}{T_e}\sum_{i\in\mathfrak{H}}\frac{n_i}{n_h}\nu_{ie}^{\mathrm{in}}, \tag{2.4.112}$$

$$\nu_{ie}^{\mathrm{in}} = \sum_{\substack{\mathrm{I},\mathrm{I}'\in\mathfrak{Q}_i\\ \mathrm{I}'\neq\mathrm{I}}} \frac{\left(\Delta\epsilon_{\mathrm{II}'}\right)^2}{2}\frac{a_{i\mathrm{I}}e^{-\epsilon_{i\mathrm{I}}}}{Q_i^{\mathrm{int}}}g\Big(\Delta\epsilon_{\mathrm{II}'}\big(1-\frac{T_h}{T_e}\big)\Big)\nu_{ie}^{\mathrm{II}'}, \tag{2.4.113}$$

where $\Delta\epsilon_{\mathrm{II}'} = \epsilon_{i\mathrm{I}'} - \epsilon_{i\mathrm{I}} = \frac{\Delta E_{\mathrm{II}'}}{k_{\mathrm{B}}T_h}$, and where we have introduced the function g defined by

$$\begin{cases} g(u) = \dfrac{1-e^{-u}}{u}, & u\neq 0,\\ g(0) = 1. \end{cases} \tag{2.4.114}$$

We can also formulate ΔE_{he}^0 as

$$\Delta E_{he}^0 = \frac{3}{2}n_h k_{\mathrm{B}}(T_e - T_h)\frac{1}{\tau}, \tag{2.4.115}$$

where

$$\frac{1}{\tau} = \frac{1}{\tau^{\mathrm{el}}} + \frac{1}{\tau^{\mathrm{in}}}. \tag{2.4.116}$$

2.4.8 First-order perturbation for the heavy species

As for electrons, we introduce the heavy-species linearized collision operator $\mathcal{F}_h = (\mathcal{F}_i)_{i\in\mathfrak{H}}$, defined as

$$\mathcal{F}_i(\phi_h) = -\frac{1}{f_i^0}\sum_{j\in\mathfrak{H}}\left[\mathcal{S}_{ij}(\phi_i f_i^0, f_j^0) + \mathcal{S}_{ij}(f_i^0, \phi_j f_j^0)\right], \qquad i\in\mathfrak{H}. \tag{2.4.117}$$

Again, using the reciprocity relation (2.2.35) and symmetrization [CC70] [FK72] [GMM09], the linearized collision operator is expressed as

$$f_i^0 \mathcal{F}_i(\phi_h) = \sum_{j\in\mathfrak{H}} \sum_{\mathrm{I}'\in\mathfrak{Q}_i} \sum_{\mathrm{J},\mathrm{J}'\in\mathfrak{Q}_j} \int g_{ij} \sigma_{ij}^{\mathrm{I}\mathrm{J}\mathrm{I}'\mathrm{J}'} f_i^0 f_j^0 \left(\phi_i + \phi_j - \phi_i' - \phi_j'\right) \mathrm{d}\boldsymbol{\omega}_{ij}' \mathrm{d}\boldsymbol{C}_j. \tag{2.4.118}$$

The kernel of $\mathcal{F}_h$ coincides with the set of heavy-species collisional invariants $\mathcal{I}_h$. We also introduce the associated integral bracket operator

$$[\![\xi_h, \zeta_h]\!]_h = \langle\!\langle f_h^0 \xi_h, \mathcal{F}_h(\zeta_h) \rangle\!\rangle_h = \sum_{i\in\mathfrak{H}} \sum_{\mathrm{I}\in\mathfrak{Q}_i} \int f_i^0 \xi_i \mathcal{F}_i(\zeta_h) \, \mathrm{d}\boldsymbol{C}_i, \tag{2.4.119}$$

which can be expressed in the form

$$\begin{aligned}[\![\xi_h, \zeta_h]\!]_h = \frac{1}{4} \sum_{i,j\in\mathfrak{H}} \sum_{\mathrm{I},\mathrm{I}'\in\mathfrak{Q}_i} \sum_{\mathrm{J},\mathrm{J}'\in\mathfrak{Q}_j} \\ \times \int g_{ij} \sigma_{ij}^{\mathrm{I}\mathrm{J}\mathrm{I}'\mathrm{J}'} f_i^0 f_j^0 \left(\xi_i' + \xi_j' - \xi_i - \xi_j\right) \left(\zeta_i' + \zeta_j' - \zeta_i - \zeta_j\right) \mathrm{d}\boldsymbol{\omega}_{ij}' \mathrm{d}\boldsymbol{C}_j \mathrm{d}\boldsymbol{C}_i.\end{aligned} \tag{2.4.120}$$

From expression (2.4.120), the bracket operator $[\![\,\cdot\,]\!]_h$ is shown to be symmetric, i.e.,

$$[\![\xi_h, \zeta_h]\!]_h = [\![\zeta_h, \xi_h]\!]_h, \tag{2.4.121}$$

positive semi-definite:

$$[\![\xi_h, \xi_h]\!]_h \geq 0, \tag{2.4.122}$$

and its kernel is seen to coincide with the kernel of $\mathcal{F}_h$:

$$[\![\xi_h, \xi_h]\!]_h = 0 \Leftrightarrow \mathcal{F}_h(\xi_h) = 0 \Leftrightarrow \xi_h \in \mathcal{I}_h. \tag{2.4.123}$$

Projecting the heavy-species Boltzmann equations (2.4.6) at order ε^0, the first-order heavy-species perturbation function ϕ_h is shown to be solution to the following linear equation:

$$\mathcal{F}_i(\phi_h) = \Psi_i, \qquad i \in \mathfrak{H}, \tag{2.4.124}$$

where

$$\Psi_i = -\mathcal{D}_i^0(\ln f_i^0) + \frac{1}{f_i^0} \mathcal{S}_{ie}^1(f_i^0, \phi_e f_e^0) + \frac{1}{f_i^0} \mathcal{S}_{ie}^2(f_i^0, f_e^0). \tag{2.4.125}$$

Indeed, $\mathcal{S}_{ie}^0 = 0$, and $\mathcal{S}_{ie}^1(\phi_i f_i^0, f_e^0) = 0$ since f_e^0 is isotropic. Equation (2.4.124) must be completed with the constraints (2.4.4) in order to be well posed [CC70] [FK72] [Gio99]

$$\langle\!\langle \phi_h f_h^0, \psi_h^l \rangle\!\rangle_h = 0, \quad l \in \mathfrak{H} \cup \{n^s + 1, \ldots, n^s + 4\}. \tag{2.4.126}$$

2.4.9 Second-order perturbation for electrons

We project the electron Boltzmann equation (2.4.5) at order ε^0 and after a few calculations, the second-order electron perturbation function ϕ_e^2 is found to be solution to the following linear integral equation [GMM09]:

$$f_e^0 \mathcal{F}_e(\phi_e^2) + \delta_{b1} \frac{q_e}{\mathfrak{m}_e} (\boldsymbol{C}_e \wedge \mathbf{B}) \cdot \boldsymbol{\partial}_{\boldsymbol{C}_e} (\phi_e^2 f_e^0) = \Psi_e^2, \tag{2.4.127}$$

where

$$\begin{aligned}\Psi_e^2 = &- \mathcal{D}_e^0(f_e^0) - \mathcal{D}_e^{-1}(\phi_e f_e^0) + \mathcal{S}_{ee}(\phi_e f_e^0, \phi_e f_e^0) \\ &+ \sum_{j\in\mathfrak{H}} \left[\mathcal{S}_{ej}^0(\phi_e f_e^0, \phi_j f_j^0) + \mathcal{S}_{ej}^1(f_e^0, \phi_j f_j^0) + \mathcal{S}_{ej}^2(f_e^0, f_j^0)\right].\end{aligned} \tag{2.4.128}$$

Indeed, by (2.3.63) $\mathcal{S}_{ej}^0(f_e^0, \phi_j^2 f_j^0) = 0$ since f_e^0 is isotropic, and by (2.3.64) $\mathcal{S}_{ej}^1(\phi_e f_e^0, f_j^0) = 0$ since f_j^0 is isotropic. Equation (2.4.127) is completed with the constraints (2.4.3) in order to be well posed

$$\langle\!\langle \phi_e^2 f_e^0, \psi_e^l \rangle\!\rangle_e = 0, \quad l \in \{e, n^s + 4\}. \tag{2.4.129}$$

2.4.10 First-order macroscopic equations for electrons

Equations (2.4.15), (2.4.16), (2.4.17) are now expanded at order ε^1. The following first-order drift-diffusion equations for electrons follow

$$\partial_t \rho_e + \boldsymbol{\partial_x} \cdot \left(\rho_e \boldsymbol{v}_h + \rho_e \boldsymbol{\mathcal{V}}_e^0 + \varepsilon\, \rho_e \boldsymbol{\mathcal{V}}_e^1\right) = \varepsilon\, \mathfrak{m}_e \mathfrak{w}_e, \tag{2.4.130}$$

$$\begin{aligned}\partial_t \mathcal{E}_e + \boldsymbol{\partial_x} \cdot (\mathcal{E}_e \boldsymbol{v}_h) = -p_e \boldsymbol{\partial_x} \cdot \boldsymbol{v}_h - \varepsilon\, \boldsymbol{\partial_x} \boldsymbol{v}_h : \boldsymbol{\Pi}_e - \boldsymbol{\partial_x} \cdot \boldsymbol{\mathcal{Q}}_e^0 - \varepsilon\, \boldsymbol{\partial_x} \cdot \boldsymbol{\mathcal{Q}}_e^1 \\ + \boldsymbol{J}_e^0 \cdot \mathbf{E}' + \varepsilon\, \boldsymbol{J}_e^1 \cdot \mathbf{E}' + \varepsilon\, \delta_{b0}\, \boldsymbol{J}_e^0 \cdot (\boldsymbol{v}_h \wedge \mathbf{B}) + \Delta E_{eh}^0 + \varepsilon\, \Delta E_{eh}^1,\end{aligned} \tag{2.4.131}$$

where we have introduced the electron first-order diffusion velocity, heat flux, viscous tensor, and the electron first-order conduction current density in the heavy-species reference frame, respectively

$$n_e \boldsymbol{\mathcal{V}}_e^1 = \int \phi_e^2 f_e^0\, \boldsymbol{C}_e\, \mathrm{d}\boldsymbol{C}_e, \tag{2.4.132}$$

$$\boldsymbol{\mathcal{Q}}_e^1 = \int \phi_e^2 f_e^0 \left(\frac{1}{2} \mathfrak{m}_e \boldsymbol{C}_e \cdot \boldsymbol{C}_e\right) \boldsymbol{C}_e\, \mathrm{d}\boldsymbol{C}_e, \tag{2.4.133}$$

$$\boldsymbol{\Pi}_e = \int \phi_e f_e^0\, \mathfrak{m}_e\, \boldsymbol{C}_e \otimes \boldsymbol{C}_e\, \mathrm{d}\boldsymbol{C}_e, \tag{2.4.134}$$

$$\boldsymbol{J}_e^1 = n_e q_e \boldsymbol{\mathcal{V}}_e^1. \tag{2.4.135}$$

We have denoted by $\mathfrak{w}_e$ the zeroth-order molecular production rate of electrons due to chemically reactive collisions:

$$\mathfrak{w}_e = \langle\!\langle \psi_e^e, \mathcal{C}_e(f^0) \rangle\!\rangle_e = \int \mathcal{C}_e(f^0)\, \mathrm{d}\boldsymbol{C}_e, \tag{2.4.136}$$

and ΔE_{eh}^1 is the first-order energy exchange term arising from chemically reactive collisions on the one hand, and scattering collisions on the other hand:

$$\Delta E_{eh}^1 = \Delta E_{eh}^{1,\mathrm{chem}} + \Delta E_{eh}^{1,\mathrm{scatt}}. \tag{2.4.137}$$

The reactive term reads

$$\Delta E_{eh}^{1,\mathrm{chem}} = \int \left(\frac{1}{2} \mathfrak{m}_e \boldsymbol{C}_e \cdot \boldsymbol{C}_e\right) \mathcal{C}_e(f^0)\, \mathrm{d}\boldsymbol{C}_e, \tag{2.4.138}$$

and the scattering term is in turn decomposed into an elastic and an inelastic contribution

$$\Delta E_{eh}^{1,\mathrm{scatt}} = \Delta E_{eh}^{1,\mathrm{el}} + \Delta E_{eh}^{1,\mathrm{in}}, \tag{2.4.139}$$

where

$$\Delta E_{eh}^{1,\mathrm{el}} = -\langle\!\langle \psi_h^{n^s+4}, \mathcal{S}_{he}^1(\phi_h f_h^0, \phi_e f_e^0) + \mathcal{S}_{he}^{2,\mathrm{el}}(\phi_h f_h^0, f_e^0) + \mathcal{S}_{he}^{2,\mathrm{el}}(f_h^0, \phi_e f_e^0) \rangle\!\rangle_h, \tag{2.4.140}$$

$$\Delta E_{eh}^{1,\mathrm{in}} = -\langle\!\langle \psi_h^{n^s+4}, \mathcal{S}_{he}^{2,\mathrm{in}}(\phi_h f_h^0, f_e^0) + \mathcal{S}_{he}^{2,\mathrm{in}}(f_h^0, \phi_e f_e^0) \rangle\!\rangle_h. \tag{2.4.141}$$

Finally, the momentum electron conservation equation (2.4.16) yields the following first-order momentum relation for electrons:

$$\boldsymbol{\partial_x} p_e + \varepsilon\, \boldsymbol{\partial_x} \cdot \boldsymbol{\Pi}_e = n_e q_e \mathbf{E} + \varepsilon\, \delta_{b0}\, \boldsymbol{j}_e^0 \wedge \mathbf{B} + \delta_{b1}\, (\boldsymbol{j}_e^0 + \varepsilon\, \boldsymbol{J}_e^1) \wedge \mathbf{B} + \boldsymbol{F}_{eh}^0 + \varepsilon\, \boldsymbol{F}_{eh}^1, \tag{2.4.142}$$

where $\boldsymbol{F}_{eh}^1$ is the first-order average force exerted by the heavy species on electrons:

$$\boldsymbol{F}_{eh}^1 = \sum_{j \in \mathfrak{H}} \langle\!\langle \mathfrak{m}_e \boldsymbol{C}_e, \mathcal{S}_{ej}^0(\phi_e^2 f_e^0, f_j^0) + \mathcal{S}_{ej}^0(\phi_e f_e^0, \phi_j f_j^0) + \mathcal{S}_{ej}^1(f_e^0, \phi_j f_j^0) + \mathcal{S}_{ej}^2(f_e^0, f_j^0) \rangle\!\rangle_e. \tag{2.4.143}$$

2.4.11 First-order macroscopic equations for the heavy species

Proceeding as for the zeroth-order macroscopic equations, we obtain the following set of Navier-Stokes type equations for the heavy species:

$$\partial_t \rho_i + \boldsymbol{\partial_x} \cdot (\rho_i \boldsymbol{v}_h + \varepsilon\, \rho_i \boldsymbol{\mathcal{V}}_i) = \varepsilon\, \mathfrak{m}_i \mathfrak{w}_i, \qquad i \in \mathfrak{H}, \tag{2.4.144}$$

$$\begin{aligned} \partial_t (\rho_h \boldsymbol{v}_h) + \boldsymbol{\partial_x} \cdot (\rho_h \boldsymbol{v}_h \otimes \boldsymbol{v}_h + p\, \mathbb{I}) &= -\varepsilon\, \boldsymbol{\partial_x} \cdot (\boldsymbol{\Pi}_e + \boldsymbol{\Pi}_h) + nq\mathbf{E} \\ &+\varepsilon\, \delta_{b0}\, \boldsymbol{j}^0 \wedge \mathbf{B} + \delta_{b1}\, \boldsymbol{j}^1 \wedge \mathbf{B}, \end{aligned} \tag{2.4.145}$$

$$\begin{aligned} \partial_t \mathcal{E}_h + \boldsymbol{\partial_x} \cdot (\mathcal{E}_h \boldsymbol{v}_h) &= -p_h\, \boldsymbol{\partial_x} \cdot \boldsymbol{v}_h - \varepsilon\, \boldsymbol{\partial_x} \boldsymbol{v}_h : \boldsymbol{\Pi}_h - \varepsilon\, \boldsymbol{\partial_x} \cdot \boldsymbol{\mathcal{Q}}_h \\ &+\varepsilon\, \boldsymbol{J}_h \cdot \mathbf{E}' + \Delta E^0_{he} + \varepsilon\, \Delta E^1_{he}, \end{aligned} \tag{2.4.146}$$

where we have introduced the diffusion velocity of the i^{th} heavy species $\boldsymbol{\mathcal{V}}_i$, the heavy-species viscous tensor $\boldsymbol{\Pi}_h$, and the heavy-species heat flux $\boldsymbol{\mathcal{Q}}_h$:

$$n_i \boldsymbol{\mathcal{V}}_i = \sum_{\mathrm{I} \in \mathfrak{Q}_i} \int \phi_i f_i^0 \boldsymbol{C}_i \, \mathrm{d}\boldsymbol{C}_i, \quad i \in \mathfrak{H}, \tag{2.4.147}$$

$$\boldsymbol{\Pi}_h = \sum_{j \in \mathfrak{H}} \sum_{\mathrm{J} \in \mathfrak{Q}_j} \int \phi_j f_j^0\, \mathfrak{m}_j\, \boldsymbol{C}_j \otimes \boldsymbol{C}_j \, \mathrm{d}\boldsymbol{C}_j, \tag{2.4.148}$$

$$\boldsymbol{\mathcal{Q}}_h = \sum_{j \in \mathfrak{H}} \sum_{\mathrm{J} \in \mathfrak{Q}_j} \int \phi_j f_j^0 \Big(\frac{1}{2} \mathfrak{m}_j \boldsymbol{C}_j \cdot \boldsymbol{C}_j + E_{j\mathrm{J}}\Big) \boldsymbol{C}_j \, \mathrm{d}\boldsymbol{C}_j. \tag{2.4.149}$$

We denote by $\boldsymbol{J}_h$ the heavy-species conduction current density in the heavy-species reference frame, $\boldsymbol{j}^1_h$ the first-order heavy-species current density in the inertial reference frame, and $\boldsymbol{j}^1_e$ the first-order electron current density in the inertial reference frame:

$$\boldsymbol{J}_h = \sum_{j \in \mathfrak{H}} n_j q_j \boldsymbol{\mathcal{V}}_j, \tag{2.4.150}$$

$$\boldsymbol{j}^1_h = \sum_{j \in \mathfrak{H}} n_j q_j (\boldsymbol{v}_h + \varepsilon \boldsymbol{\mathcal{V}}_j) = n_h q_h \boldsymbol{v}_h + \varepsilon \boldsymbol{J}_h, \tag{2.4.151}$$

$$\boldsymbol{j}^1_e = n_e q_e (\boldsymbol{v}_h + \boldsymbol{\mathcal{V}}^0_e + \varepsilon \boldsymbol{\mathcal{V}}^1_e) = n_e q_e \boldsymbol{v}_e + \varepsilon \boldsymbol{J}^1_e, \tag{2.4.152}$$

where $\boldsymbol{J}^1_e = n_e q_e \boldsymbol{\mathcal{V}}^1_e$ is the first-order electron conduction current density in the heavy-species reference frame. The zeroth-order and first-order current density in the inertial reference frame, $\boldsymbol{j}^0$ and $\boldsymbol{j}^1$, respectively, are given by

$$\boldsymbol{j}^0 = \boldsymbol{j}^0_h + \boldsymbol{j}^0_e, \tag{2.4.153}$$

$$\boldsymbol{j}^1 = \boldsymbol{j}^1_h + \boldsymbol{j}^1_e. \tag{2.4.154}$$

Finally, $\mathfrak{w}_i, i \in \mathfrak{H}$ is the zeroth-order molecular production rate of the i^{th} species due to chemically reactive collisions:

$$\mathfrak{w}_i = \langle\!\langle \psi^i_h, \mathcal{C}_h(f^0) \rangle\!\rangle_h = \sum_{\mathrm{I} \in \mathfrak{Q}_i} \int \mathcal{C}_i(f^0) \, \mathrm{d}\boldsymbol{C}_i, \tag{2.4.155}$$

and ΔE^1_{he} is the first-order energy exchange term, involving both scattering and reactive energy transfer. Again, due to relation (2.3.34), energy exchange terms are symmetric:

$$\Delta E^1_{he} = -\Delta E^1_{eh}. \tag{2.4.156}$$

2.4.12 Chemistry source terms

For $k \in \mathfrak{S}$, the chemically reactive source term reads

$$\mathfrak{w}_k = \sum_{\mathrm{K} \in \mathfrak{Q}_k} \int \mathcal{C}_k(f^0)\, \mathrm{d}\boldsymbol{C}_k. \tag{2.4.157}$$

This term can be expressed as follows. We first recall the decomposition (2.2.16)

$$\mathcal{C}_k(f) = \sum_{r \in \mathscr{R}} \mathcal{C}_k^r(f), \tag{2.4.158}$$

where $\mathcal{C}_k^r(f)$ was expressed in (2.2.28). This yields the following decomposition:

$$\mathfrak{w}_k = \sum_{r \in \mathscr{R}} \left(\nu_k^{r\mathrm{b}} - \nu_k^{r\mathrm{f}}\right) \tau_r, \tag{2.4.159}$$

where τ_r is the reaction rate of progress of the r^{th} reaction, which can be written

$$\tau_r = \mathcal{K}_r^{\mathrm{f}} \prod_{l \in \mathfrak{S}} n_l^{\nu_l^{r\mathrm{f}}} - \mathcal{K}_r^{\mathrm{b}} \prod_{k \in \mathfrak{S}} n_k^{\nu_k^{r\mathrm{b}}}, \tag{2.4.160}$$

where the forward and backward constant rates associated with reaction r read

$$\begin{aligned} \mathcal{K}_r^{\mathrm{f}} = \frac{1}{\prod_{l \in \mathfrak{S}} Q_l^{\nu_l^{r\mathrm{f}}}} \sum_{\mathrm{F}^r, \mathrm{B}^r} \int \frac{1}{\prod\limits_{l \in \mathfrak{F}^r} \beta_{l_{\mathrm{L}}}} \exp\left(- \sum_{l \in \mathfrak{F}^r} \frac{\frac{1}{2}\mathfrak{m}_l \boldsymbol{C}_l \cdot \boldsymbol{C}_l + E_{l_{\mathrm{L}}}}{k_{\mathrm{B}} T_l} \right) \\ \times \mathcal{W}_{\mathfrak{F}^r \mathfrak{B}^r}^{\mathrm{F}^r \mathrm{B}^r} \prod_{l \in \mathfrak{F}^r} \mathrm{d}\boldsymbol{C}_l \prod_{k \in \mathfrak{B}^r} \mathrm{d}\boldsymbol{C}_k, \end{aligned} \tag{2.4.161}$$

$$\begin{aligned} \mathcal{K}_r^{\mathrm{b}} = \frac{1}{\prod_{k \in \mathfrak{S}} Q_k^{\nu_k^{r\mathrm{b}}}} \sum_{\mathrm{F}^r, \mathrm{B}^r} \int \frac{1}{\prod\limits_{l \in \mathfrak{F}^r} \beta_{l_{\mathrm{L}}}} \exp\left(- \sum_{k \in \mathfrak{B}^r} \frac{\frac{1}{2}\mathfrak{m}_k \boldsymbol{C}_k \cdot \boldsymbol{C}_k + E_{k_{\mathrm{K}}}}{k_{\mathrm{B}} T_k} \right) \\ \times \mathcal{W}_{\mathfrak{F}^r \mathfrak{B}^r}^{\mathrm{F}^r \mathrm{B}^r} \prod_{l \in \mathfrak{F}^r} \mathrm{d}\boldsymbol{C}_l \prod_{k \in \mathfrak{B}^r} \mathrm{d}\boldsymbol{C}_k. \end{aligned} \tag{2.4.162}$$

From equation (2.2.38), the production rates $\mathfrak{w}_k$, $k \in \mathfrak{S}$ satisfy the mass conservation constraint

$$\sum_{k \in \mathfrak{S}} \mathfrak{m}_k \mathfrak{w}_k = 0. \tag{2.4.163}$$

We now distinguish between two cases. First, if the reaction does not involve any electron, one retrieves the law of mass action. Indeed, in that case, all the species temperatures equal T_h, and the following relation for conservation of energy holds:

$$\sum_{l \in \mathfrak{F}^r} \left(\frac{1}{2}\mathfrak{m}_l \boldsymbol{C}_l \cdot \boldsymbol{C}_l + E_{l_{\mathrm{L}}}\right) = \sum_{k \in \mathfrak{B}^r} \left(\frac{1}{2}\mathfrak{m}_k \boldsymbol{C}_k \cdot \boldsymbol{C}_k + E_{k_{\mathrm{K}}}\right), \tag{2.4.164}$$

so that $\mathcal{K}_r^{\mathrm{f}}$ and $\mathcal{K}_r^{\mathrm{b}}$ read

$$\mathcal{K}_r^{\mathrm{f}} = \frac{\mathcal{K}_r}{\prod_{j \in \mathfrak{H}} Q_j^{\nu_j^{r\mathrm{f}}}} \tag{2.4.165}$$

$$\mathcal{K}_r^{\mathrm{b}} = \frac{\mathcal{K}_r}{\prod_{j \in \mathfrak{H}} Q_j^{\nu_j^{r\mathrm{b}}}}, \tag{2.4.166}$$

where

$$\mathcal{K}_r = \frac{1}{\prod\limits_{l\in\mathfrak{F}^r}\beta_{l_{\mathrm{L}}}} \sum_{\mathrm{F}^r,\mathrm{B}^r} \int \exp\left(-\sum_{l\in\mathfrak{F}^r} \frac{\frac{1}{2}\mathfrak{m}_l \boldsymbol{C}_l\cdot\boldsymbol{C}_l + E_{l_{\mathrm{L}}}}{k_{\mathrm{B}}T_h}\right) \times \mathcal{W}^{\mathrm{F}^r\mathrm{B}^r}_{\mathfrak{F}^r\mathfrak{B}^r} \prod_{l\in\mathfrak{F}^r} \mathrm{d}\boldsymbol{C}_l \prod_{k\in\mathfrak{B}^r} \mathrm{d}\boldsymbol{C}_k, \tag{2.4.167}$$

$$= \frac{1}{\prod\limits_{l\in\mathfrak{F}^r}\beta_{l_{\mathrm{L}}}} \sum_{\mathrm{F}^r,\mathrm{B}^r} \int \exp\left(-\sum_{k\in\mathfrak{B}^r} \frac{\frac{1}{2}\mathfrak{m}_k \boldsymbol{C}_k\cdot\boldsymbol{C}_k + E_{k_{\mathrm{K}}}}{k_{\mathrm{B}}T_h}\right) \times \mathcal{W}^{\mathrm{F}^r\mathrm{B}^r}_{\mathfrak{F}^r\mathfrak{B}^r} \prod_{l\in\mathfrak{F}^r} \mathrm{d}\boldsymbol{C}_l \prod_{k\in\mathfrak{B}^r} \mathrm{d}\boldsymbol{C}_k.$$

If we introduce the equilibrium constant of the r^{th} reaction

$$\mathcal{K}^{\mathrm{e}}_r = \prod_{j\in\mathfrak{H}} Q_j^{\nu_j^{r\mathrm{b}} - \nu_j^{r\mathrm{f}}}, \tag{2.4.168}$$

we have finally

$$\mathcal{K}^{\mathrm{e}}_r = \frac{\mathcal{K}^{\mathrm{f}}_r}{\mathcal{K}^{\mathrm{b}}_r}. \tag{2.4.169}$$

On the other side, when the reaction r involves one or more electrons, the equilibrium constant $\mathcal{K}^{\mathrm{e}}_r$ is undefined, since in general $T_e \neq T_h$. However, in specific cases, depending on the form of the reaction considered, e.g., electron impact ionization or ion impact ionization, a generalized law of mass action can be derived where the equilibrium constant might depend on either of the temperatures T_e or T_h. For example, for an electron impact ionization in the form

$$\mathfrak{M}_e + \mathfrak{M}_n \rightleftharpoons \mathfrak{M}_i + \mathfrak{M}_e + \mathfrak{M}_e, \tag{2.4.170}$$

where the subscripts e, n, and i refer to the electron, the neutral species and the corresponding positive ion, respectively, the law of mass action obtained for the monoatomic case in [GMM08] is a generalization of the well-known "Saha" equation, and reads

$$\mathcal{K}^{\mathrm{e}}_r = \frac{\mathcal{K}^{\mathrm{f}}_r}{\mathcal{K}^{\mathrm{b}}_r} = \left(\frac{\mathfrak{m}_i}{\mathfrak{m}_n}\right)^{\frac{3}{2}} \left(\frac{2\pi\mathfrak{m}_e k_{\mathrm{B}} T_e}{h_{\mathrm{P}}^2}\right)^{\frac{3}{2}} \exp\left(-\frac{\Delta\mathcal{E}_{\mathrm{ioniz}}}{k_{\mathrm{B}}T_e}\right), \tag{2.4.171}$$

where $\Delta\mathcal{E}_{\mathrm{ioniz}}$ is the ionization energy associated with reaction (2.4.170). The first two factors of equation (2.4.171) correspond to the translational partition functions of the respective species at their respective temperatures, and the term in the exponential factor corresponds to the ionization energy divided by the electron temperature. Indeed, the colliding electron is providing the energy required for the ionization to occur [GMM08]. Equation (2.4.171) can also be derived from non-equilibrium thermodynamics [vdSSP+89] [GC02].

Finally, the energy exchange term $\Delta E^{1,\mathrm{chem}}_{eh} = -\Delta E^{1,\mathrm{chem}}_{he}$ associated with chemically reactive collisions can be decomposed in the form

$$\Delta E^{1,\mathrm{chem}}_{eh} = \sum_{r\in\mathscr{R}} \Delta E_r = \sum_{r\in\mathscr{R}_e} \Delta E_r, \tag{2.4.172}$$

where the sum has been reduced to the set of reactions involving one or more electrons $\mathscr{R}_e$. Upon introducing the net average energy $\Delta\mathcal{E}_{er}$ gained by electrons during reaction r, defined as

$$\Delta\mathcal{E}_{er} = \frac{1}{\tau_r} \sum_{\mathrm{F}^r,\mathrm{B}^r} \int \left(\nu_e^{r\mathrm{b}} \frac{1}{2}\mathfrak{m}_e \boldsymbol{C}_e^{\mathrm{b}}\cdot\boldsymbol{C}_e^{\mathrm{b}} - \nu_e^{r\mathrm{f}} \frac{1}{2}\mathfrak{m}_e \boldsymbol{C}_e^{\mathrm{f}}\cdot\boldsymbol{C}_e^{\mathrm{f}}\right) \tag{2.4.173}$$

$$\times \Big(\prod_{j\in\mathfrak{F}^r} f_j \;-\; \prod_{k\in\mathfrak{B}^r} f_k \frac{\prod\limits_{k\in\mathfrak{B}^r}\beta_{k_{\mathrm{K}}}}{\prod\limits_{j\in\mathfrak{F}^r}\beta_{j_{\mathrm{J}}}}\Big) \mathcal{W}^{\mathrm{F}^r\mathrm{B}^r}_{\mathfrak{F}^r\mathfrak{B}^r} \prod_{j\in\mathfrak{F}^r} \mathrm{d}\boldsymbol{C}_j \prod_{k\in\mathfrak{B}^r} \mathrm{d}\boldsymbol{C}_k,$$

where τ_r is the rate of progress of the r^{th} reaction, and where $\boldsymbol{C}_e^{\text{f}}$, $\boldsymbol{C}_e^{\text{b}}$ denote the electron velocity where electron is taken as a reactant or product, respectively, one can express the chemistry energy exchange term as

$$\Delta E_{eh}^{1,\text{chem}} = \sum_{r \in \mathscr{R}_e} \Delta \mathcal{E}_{er} \tau_r. \tag{2.4.174}$$

As a first approximation, due to the strong mass disparity between electrons and heavy species, the net energy $\nu_e^{r\text{f}} \frac{1}{2} \mathfrak{m}_e \boldsymbol{C}_e^{\text{f}} \cdot \boldsymbol{C}_e^{\text{f}} - \nu_e^{r\text{b}} \frac{1}{2} \mathfrak{m}_e \boldsymbol{C}_e^{\text{b}} \cdot \boldsymbol{C}_e^{\text{b}}$ lost by electrons during the r^{th} electron collision reaction can be taken constant, independent of the velocities $\boldsymbol{C}_e^{\text{f}}$, $\boldsymbol{C}_e^{\text{b}}$, and equal to the threshold energy of the collision process considered [GMM08], so that the net average energy lost $-\Delta \mathcal{E}_{er}$ can be identified with the threshold energy of the r^{th} reaction. This assumption is customary in practical applications [Nie98] [KNF+04] [Hag16b].

2.5 Transport Fluxes

In this section, we derive an expression for the transport fluxes, namely the diffusion velocities $\boldsymbol{\mathcal{V}}_i$, $i \in \mathfrak{H}$, $\boldsymbol{\mathcal{V}}_e^0$, $\boldsymbol{\mathcal{V}}_e^1$, the viscous tensors $\boldsymbol{\Pi}_h$, $\boldsymbol{\Pi}_e$, and the heat fluxes $\boldsymbol{\mathcal{Q}}_h$, $\boldsymbol{\mathcal{Q}}_e^0$, $\boldsymbol{\mathcal{Q}}_e^1$, in terms of macroscopic variable gradients. These expressions involve transport coefficients, which are also stated in terms of bracket products of the perturbed distribution functions. For the sake of simplicity, we assume that the plasma is weakly magnetized, i.e., $b = 0$.

2.5.1 Electron transport coefficients

In the case when $b = 0$, equation (2.4.58) for the first-order electron perturbation ϕ_e becomes

$$\mathcal{F}_e(\phi_e) = \Psi_e, \tag{2.5.1}$$

where

$$\Psi_e = -\mathcal{D}_e^{-1}(\ln f_e^0), \tag{2.5.2}$$

under the constraints

$$\langle\!\langle \phi_e f_e^0, \psi_e^l \rangle\!\rangle_e = 0, \quad l \in \{e, n^s + 4\}. \tag{2.5.3}$$

Given expression (2.4.28) for f_e^0, Ψ_e can be decomposed into

$$\Psi_e = -\boldsymbol{\Psi}_e^{D_e} \cdot (\boldsymbol{\partial}_{\boldsymbol{x}} p_e - n_e q_e \mathbf{E}) - \boldsymbol{\Psi}_e^{\hat{\lambda}_e} \cdot \boldsymbol{\partial}_{\boldsymbol{x}} \left(\frac{1}{k_{\text{B}} T_e} \right), \tag{2.5.4}$$

where

$$\begin{cases} \boldsymbol{\Psi}_e^{D_e} = \dfrac{1}{p_e} \boldsymbol{C}_e \\ \boldsymbol{\Psi}_e^{\hat{\lambda}_e} = \left(\dfrac{5}{2} k_{\text{B}} T_e - \dfrac{1}{2} \mathfrak{m}_e \boldsymbol{C}_e \cdot \boldsymbol{C}_e \right) \boldsymbol{C}_e. \end{cases} \tag{2.5.5}$$

Making use of the linearity of the electron linearized collision operator $\mathcal{F}_e$ [GG09] [GMM09], we can expand the first-order perturbation function ϕ_e as follows:

$$\phi_e = -\boldsymbol{\Phi}_e^{D_e} \cdot (\boldsymbol{\partial}_{\boldsymbol{x}} p_e - n_e q_e \mathbf{E}) - \boldsymbol{\Phi}_e^{\hat{\lambda}_e} \cdot \boldsymbol{\partial}_{\boldsymbol{x}} \left(\frac{1}{k_{\text{B}} T_e} \right). \tag{2.5.6}$$

For each $\mu = D_e, \hat{\lambda}_e$, the function $\boldsymbol{\Phi}_e^{\mu}$ is solution to the following system of equations:

$$\mathcal{F}_e(\boldsymbol{\Phi}_e^{\mu}) = \boldsymbol{\Psi}_e^{\mu} \tag{2.5.7}$$

$$\langle\!\langle f_e^0 \boldsymbol{\Phi}_e^{\mu}, \psi_e^l \rangle\!\rangle_e = 0, \qquad l \in \{e, n^s + 4\}, \tag{2.5.8}$$

which is well posed since for both values of μ

$$\langle\!\langle f_e^0 \boldsymbol{\Psi}_e^\mu, \psi_e^l \rangle\!\rangle_e = 0, \qquad l \in \{e, n^s + 4\}\,. \tag{2.5.9}$$

Additionally, because of the linearity and the space isotropy of $\mathcal{F}_e$, $\boldsymbol{\Phi}_e^{D_e}$ and $\boldsymbol{\Phi}_e^{\hat{\lambda}_e}$ can be taken in the form

$$\boldsymbol{\Phi}_e^{D_e} = \phi_e^{D_e}\, \boldsymbol{C}_e \tag{2.5.10}$$

$$\boldsymbol{\Phi}_e^{\hat{\lambda}_e} = \phi_e^{\hat{\lambda}_e}\, \boldsymbol{C}_e, \tag{2.5.11}$$

where $\phi_e^{D_e}$, $\phi_e^{\hat{\lambda}_e}$ are scalar isotropic functions of $\boldsymbol{C}_e \cdot \boldsymbol{C}_e$.

Thanks to this decomposition of ϕ_e, the electron viscous tensor $\boldsymbol{\Pi}_e$ can be shown to vanish:

$$\boldsymbol{\Pi}_e = 0. \tag{2.5.12}$$

Defining the zeroth-order electron self-diffusion coefficient D_{ee}^0 and the zeroth-order electron electron-temperature thermal diffusion coefficient θ_{ee}^0 by

$$D_{ee}^0 = \frac{p k_\mathrm{B} T_e}{3} [\![\boldsymbol{\Phi}_e^{D_e}, \boldsymbol{\Phi}_e^{D_e}]\!]_e, \tag{2.5.13}$$

$$\theta_{ee}^0 = -\frac{1}{3} [\![\boldsymbol{\Phi}_e^{\hat{\lambda}_e}, \boldsymbol{\Phi}_e^{D_e}]\!]_e, \tag{2.5.14}$$

respectively, the zeroth-order electron diffusion velocity is expressed in the form

$$\boldsymbol{\mathcal{V}}_e^0 = -D_{ee}^0 \hat{\boldsymbol{d}}_e - \theta_{ee}^0 \boldsymbol{\partial}_{\boldsymbol{x}} \ln T_e, \tag{2.5.15}$$

where we have introduced the unconstrained electron diffusion driving force

$$\hat{\boldsymbol{d}}_e = \frac{1}{p} \left(\boldsymbol{\partial}_{\boldsymbol{x}} p_e - n_e q_e \mathbf{E} \right). \tag{2.5.16}$$

Finally, upon defining the zeroth-order electron self-partial-thermal-conductivity

$$\hat{\lambda}_{ee}^0 = \frac{1}{3 k_\mathrm{B} T_e^2} [\![\boldsymbol{\Phi}_e^{\hat{\lambda}_e}, \boldsymbol{\Phi}_e^{\hat{\lambda}_e}]\!]_e, \tag{2.5.17}$$

the zeroth-order electron heat flux $\boldsymbol{\mathcal{Q}}_e^0$ is found in the form

$$\boldsymbol{\mathcal{Q}}_e^0 = -p \theta_{ee}^0 \hat{\boldsymbol{d}}_e - \hat{\lambda}_{ee}^0 \boldsymbol{\partial}_{\boldsymbol{x}} T_e + \Big(\frac{5}{2} k_\mathrm{B} T_e \Big) n_e \boldsymbol{\mathcal{V}}_e^0. \tag{2.5.18}$$

2.5.2 Heavy-species transport coefficients

We recall that from (2.4.124) and (2.4.126) the first-order heavy-species perturbation function ϕ_h is solution to the following constrained linear system of integral equations:

$$\mathcal{F}_i(\phi_h) = \Psi_i, \qquad i \in \mathfrak{H} \tag{2.5.19}$$

$$\langle\!\langle f_h^0 \phi_h, \psi_h^j \rangle\!\rangle_h = 0, \qquad j \in \mathfrak{H} \cup \{n^s + 1, \ldots, n^s + 4\}\,, \tag{2.5.20}$$

where Ψ_i, $i \in \mathfrak{H}$, is given by (2.4.125). After a lengthy calculation, Ψ_i can be decomposed into

$$\begin{aligned} \Psi_i = &- \boldsymbol{\Psi}_i^{\eta_h} : \boldsymbol{\partial}_{\boldsymbol{x}} \boldsymbol{v}_h - \frac{1}{3} \Psi_i^{\kappa_h} \left(\boldsymbol{\partial}_{\boldsymbol{x}} \cdot \boldsymbol{v}_h \right) - \sum_{j \in \mathfrak{H}} \boldsymbol{\Psi}_i^{D_j} \cdot \left(\boldsymbol{\partial}_{\boldsymbol{x}} p_j - n_j q_j \mathbf{E} \right) - \boldsymbol{\Psi}_i^{D_e} \cdot \left(\boldsymbol{\partial}_{\boldsymbol{x}} p_e - n_e q_e \mathbf{E} \right) \\ &- \boldsymbol{\Psi}_i^{\hat{\lambda}_h} \cdot \boldsymbol{\partial}_{\boldsymbol{x}} \left(\frac{1}{k_\mathrm{B} T_h} \right) - \boldsymbol{\Psi}_i^{\hat{\lambda}_e} \cdot \boldsymbol{\partial}_{\boldsymbol{x}} \left(\frac{1}{k_\mathrm{B} T_e} \right) - \Psi_i^\Theta \left(T_e - T_h \right), \quad i \in \mathfrak{H}. \end{aligned} \tag{2.5.21}$$

The expansion coefficients are given by

$$\boldsymbol{\Psi}_i^{\eta_h} = \frac{\mathfrak{m}_i}{k_{\mathrm{B}} T_h}\left[\boldsymbol{C}_i \otimes \boldsymbol{C}_i - \frac{1}{3}\boldsymbol{C}_i \cdot \boldsymbol{C}_i \,\mathbb{I}\right] \tag{2.5.22}$$

$$\Psi_i^{\kappa_h} = \frac{2c^{\mathrm{int}}}{c_v k_{\mathrm{B}} T_h}\left[\frac{1}{2}\mathfrak{m}_i \boldsymbol{C}_i \cdot \boldsymbol{C}_i - \frac{3}{2}k_{\mathrm{B}} T_h\right] + \frac{2c_v^{\mathrm{tr}}}{c_v k_{\mathrm{B}} T_h}(\overline{E}_i - E_{i\mathrm{I}}) \tag{2.5.23}$$

$$\boldsymbol{\Psi}_i^{D_j} = \frac{1}{p_i}\left[\delta_{ij} - Y_i^h\right]\boldsymbol{C}_i \tag{2.5.24}$$

$$\boldsymbol{\Psi}_i^{D_e} = \frac{\mathfrak{m}_e}{3}\sum_{j\in\mathfrak{H}}\sum_{\mathrm{J}\in\mathfrak{Q}_j} n_j \frac{1}{p_i}\left(\delta_{ij}\delta_{\mathrm{IJ}} - Y_i^h \frac{a_{j\mathrm{J}} e^{-\epsilon_{j\mathrm{J}}}}{Q_j^{\mathrm{int}}}\right)\boldsymbol{C}_i \tag{2.5.25}$$
$$\times \int \Sigma_{\mathrm{JJ}}^{(1)}(|\boldsymbol{C}_e|^2)|\boldsymbol{C}_e| f_e^0(\boldsymbol{C}_e)\; \boldsymbol{C}_e \cdot \boldsymbol{\Phi}_e^{D_e}\,\mathrm{d}\boldsymbol{C}_e$$

$$\boldsymbol{\Psi}_i^{\hat{\lambda}_e} = \frac{\mathfrak{m}_e}{3}\sum_{j\in\mathfrak{H}}\sum_{\mathrm{J}\in\mathfrak{Q}_j} n_j \frac{1}{p_i}\left(\delta_{ij}\delta_{\mathrm{IJ}} - Y_i^h \frac{a_{j\mathrm{J}} e^{-\epsilon_{j\mathrm{J}}}}{Q_j^{\mathrm{int}}}\right)\boldsymbol{C}_i \tag{2.5.26}$$
$$\times \int \Sigma_{\mathrm{JJ}}^{(1)}(|\boldsymbol{C}_e|^2)|\boldsymbol{C}_e| f_e^0(\boldsymbol{C}_e)\; \boldsymbol{C}_e \cdot \boldsymbol{\Phi}_e^{\hat{\lambda}_e}\,\mathrm{d}\boldsymbol{C}_e$$

$$\boldsymbol{\Psi}_i^{\hat{\lambda}_h} = \left(\frac{5}{2}k_{\mathrm{B}} T_h - \frac{1}{2}\mathfrak{m}_i \boldsymbol{C}_i \cdot \boldsymbol{C}_i + \overline{E}_i - E_{i\mathrm{I}}\right)\boldsymbol{C}_i \tag{2.5.27}$$

$$\Psi_i^{\Theta} = \frac{3}{2}\frac{1}{\tau}\frac{1}{c_v T_h^2}\left(\frac{1}{2}\mathfrak{m}_i \boldsymbol{C}_i \cdot \boldsymbol{C}_i + E_{i\mathrm{I}} - \overline{E}_i - \frac{3}{2}k_{\mathrm{B}} T_h\right) \tag{2.5.28}$$
$$+ \frac{2}{3}\frac{\mathfrak{m}_e}{\mathfrak{m}_i}\frac{1}{k_{\mathrm{B}} T_h^2}\left(\frac{3}{2}k_{\mathrm{B}} T_h - \frac{1}{2}\mathfrak{m}_i \boldsymbol{C}_i \cdot \boldsymbol{C}_i\right)\nu_{ie}^{\mathrm{II}} + \frac{1}{k_{\mathrm{B}} T_e T_h}\sum_{\substack{\mathrm{I}'\in\mathfrak{Q}_i \\ \mathrm{I}'\neq\mathrm{I}}} \Delta E_{\mathrm{II}'}\; g_{\mathrm{II}'}\nu_{ie}^{\mathrm{II}'},$$

where Y_i^h is the mass fraction of the i^{th} species with respect to the heavy species, which is proportional to the mass fraction $Y_i = \frac{\rho_i}{\rho}$ of the i^{th} species with respect to the whole mixture:

$$Y_i^h = \frac{\rho_i}{\rho_h} = \frac{\rho}{\rho_h}Y_i, \qquad i \in \mathfrak{H}, \tag{2.5.29}$$

and where

$$g_{\mathrm{II}'} = g\Big(\Delta\epsilon_{\mathrm{II}'}\big(1 - \frac{T_h}{T_e}\big)\Big). \tag{2.5.30}$$

We also denote by X_i^h the mole fraction of the i^{th} species with respect to the heavy species. If m_i is the molar mass of the i^{th} heavy species, and $\overline{m}_h$ is the mean molar mass of the heavy species, given by (2.4.46), then

$$X_i^h = \frac{n_i}{n_h} = \frac{\overline{m}_h}{m_i}Y_i^h, \qquad i \in \mathfrak{H}. \tag{2.5.31}$$

In (2.5.22)-(2.5.28), the symbol c_v^{tr} denotes the translational constant-volume specific heat per molecule, c^{int} the heavy-species internal specific heat per molecule, c_v the heavy-species constant-volume specific heat per molecule

$$\begin{cases} c_v^{\mathrm{tr}} = \dfrac{3}{2}k_{\mathrm{B}} \\ c^{\mathrm{int}} = \displaystyle\sum_{i\in\mathfrak{H}} X_i^h c_i^{\mathrm{int}} \\ c_v = c_v^{\mathrm{tr}} + c^{\mathrm{int}}, \end{cases} \tag{2.5.32}$$

and c_i^{int} denotes the internal heat capacity of the i^{th} species

$$c_i^{\text{int}} = \frac{d\overline{E}_i}{dT}, \qquad i \in \mathfrak{H}. \tag{2.5.33}$$

As for the first-order electron perturbation, making use of the linearity of the linearized collision operator, the perturbation functions $\phi_i, i \in \mathfrak{H}$ can be decomposed in the form

$$\begin{aligned}\phi_i = &- \boldsymbol{\Phi}_i^{\eta_h} : \boldsymbol{\partial}_{\boldsymbol{x}} \boldsymbol{v}_h - \frac{1}{3}\phi_i^{\kappa_h} \left(\boldsymbol{\partial}_{\boldsymbol{x}} \cdot \boldsymbol{v}_h\right) - \sum_{j \in \mathfrak{H}} \boldsymbol{\Phi}_i^{D_j} \cdot \left(\boldsymbol{\partial}_{\boldsymbol{x}} p_j - n_j q_j \mathbf{E}\right) - \boldsymbol{\Phi}_i^{D_e} \cdot \left(\boldsymbol{\partial}_{\boldsymbol{x}} p_e - n_e q_e \mathbf{E}\right) \\ &- \boldsymbol{\Phi}_i^{\hat{\lambda}_h} \cdot \boldsymbol{\partial}_{\boldsymbol{x}} \left(\frac{1}{k_{\text{B}} T_h}\right) - \boldsymbol{\Phi}_i^{\hat{\lambda}_e} \cdot \boldsymbol{\partial}_{\boldsymbol{x}} \left(\frac{1}{k_{\text{B}} T_e}\right) - \phi_i^{\Theta} \left(T_e - T_h\right), \qquad i \in \mathfrak{H}. \end{aligned} \tag{2.5.34}$$

Note that one can also expand the coefficient Ψ_i^{Θ} as

$$\Psi_i^{\Theta} = -\frac{1}{2T_h}\frac{1}{\tau}\Psi_i^{\kappa_h} + \Psi_i^{\Theta^{\text{el}}} + \Psi_i^{\Theta^{\text{in}}}, \tag{2.5.35}$$

where the elastic and inelastic contributions are given by

$$\Psi_i^{\Theta^{\text{el}}} = \frac{1}{k_{\text{B}} T_h^2}\left(\frac{1}{\tau^{\text{el}}} - \frac{2}{3}\frac{\mathfrak{m}_e}{\mathfrak{m}_i}\nu_{ie}^{\text{II}}\right)\left(\frac{1}{2}\mathfrak{m}_i \boldsymbol{C}_i \cdot \boldsymbol{C}_i - \frac{3}{2}k_{\text{B}} T_h\right) \tag{2.5.36}$$

$$\Psi_i^{\Theta^{\text{in}}} = \frac{1}{k_{\text{B}} T_h^2}\frac{1}{\tau^{\text{in}}}\left(\frac{1}{2}\mathfrak{m}_i \boldsymbol{C}_i \cdot \boldsymbol{C}_i - \frac{3}{2}k_{\text{B}} T_h\right) + \frac{1}{k_{\text{B}} T_e T_h}\sum_{\text{I}' \in \mathfrak{Q}_i} \Delta E_{\text{II}'} g_{\text{II}'} \nu_{ie}^{\text{II}'}, \tag{2.5.37}$$

and the corresponding decomposition for ϕ_i^{Θ} reads

$$\phi_i^{\Theta} = -\frac{1}{2T_h}\frac{1}{\tau}\phi_i^{\kappa_h} + \phi_i^{\Theta^{\text{el}}} + \phi_i^{\Theta^{\text{in}}}, \qquad i \in \mathfrak{H}. \tag{2.5.38}$$

For each value of $\mu = \eta_h, \kappa_h, D_j, j \in \mathfrak{H}, D_e, \hat{\lambda}_h, \hat{\lambda}_e, \Theta, \Theta^{\text{el}}, \Theta^{\text{in}}$, the functional ϕ_h^{μ} is solution of the following constrained linear system of integral equations:

$$\mathcal{F}_i(\phi_h^{\mu}) = \Psi_i^{\mu}, \qquad i \in \mathfrak{H} \tag{2.5.39}$$

$$\langle\!\langle f_h^0 \phi_h^{\mu}, \psi_h^j \rangle\!\rangle_h = 0, \qquad j \in \mathfrak{H} \cup \{n^s + 1, \ldots, n^s + 4\}, \tag{2.5.40}$$

which is well posed since

$$\langle\!\langle f_h^0 \Psi_h^{\mu}, \psi_h^j \rangle\!\rangle_h = 0, \qquad j \in \mathfrak{H} \cup \{n^s + 1, \ldots, n^s + 4\}. \tag{2.5.41}$$

Furthermore, because of the isotropy of the linearized collision operator $\mathcal{F}_h$, each ϕ_h^{μ} is of the same tensorial type as Ψ_h^{μ} [Gra04].

Upon defining the heavy-species diffusion coefficients, the heavy-species electron diffusion coefficients, the heavy-species heavy-temperature thermal diffusion coefficients, and the heavy-species electron-temperature thermal diffusion coefficients by

$$D_{ij} = \frac{p k_{\text{B}} T_h}{3} [\![\boldsymbol{\Phi}_h^{D_i}, \boldsymbol{\Phi}_h^{D_j}]\!]_h, \qquad i \in \mathfrak{H}, j \in \mathfrak{H}, \tag{2.5.42}$$

$$D_{ie} = D_{ei} = \frac{p k_{\text{B}} T_h}{3} [\![\boldsymbol{\Phi}_h^{D_i}, \boldsymbol{\Phi}_h^{D_e}]\!]_h, \qquad i \in \mathfrak{H}, \tag{2.5.43}$$

$$\theta_{ih} = \theta_{hi} = -\frac{1}{3} [\![\boldsymbol{\Phi}_h^{D_i}, \boldsymbol{\Phi}_h^{\hat{\lambda}_h}]\!]_h, \qquad i \in \mathfrak{H}, \tag{2.5.44}$$

$$\theta_{ie} = \theta_{ei} = -\frac{1}{3}\frac{T_h}{T_e} [\![\boldsymbol{\Phi}_h^{D_i}, \boldsymbol{\Phi}_h^{\hat{\lambda}_e}]\!]_h, \qquad i \in \mathfrak{H}, \tag{2.5.45}$$

the heavy-species diffusion velocities are expressed in the form

$$\boldsymbol{\mathcal{V}}_i = -\sum_{j\in\mathfrak{H}} D_{ij}\hat{\boldsymbol{d}}_j - D_{ie}\hat{\boldsymbol{d}}_e - \theta_{ih}\boldsymbol{\partial}_{\boldsymbol{x}}\ln T_h - \theta_{ie}\boldsymbol{\partial}_{\boldsymbol{x}}\ln T_e, \quad i\in\mathfrak{H}, \tag{2.5.46}$$

where we have introduced the heavy-species diffusion driving forces

$$\hat{\boldsymbol{d}}_i = \frac{1}{p}\left(\boldsymbol{\partial}_{\boldsymbol{x}}p_i - n_i q_i \mathbf{E}\right), \quad i\in\mathfrak{H}. \tag{2.5.47}$$

We also define the shear viscosity, the volume viscosity, and the thermal non-equilibrium viscosity, respectively:

$$\eta_h = \frac{k_{\mathrm{B}}T_h}{10}[\![\boldsymbol{\Phi}_h^{\eta_h}, \boldsymbol{\Phi}_h^{\eta_h}]\!]_h \tag{2.5.48}$$

$$\kappa_h = \frac{k_{\mathrm{B}}T_h}{9}[\![\phi_h^{\kappa_h}, \phi_h^{\kappa_h}]\!]_h \tag{2.5.49}$$

$$\zeta = \frac{k_{\mathrm{B}}T_h}{3}[\![\phi_h^{\Theta}, \phi_h^{\kappa_h}]\!]_h, \tag{2.5.50}$$

so that the viscous tensor reads

$$\boldsymbol{\Pi}_h = -\eta_h\left(\boldsymbol{\partial}_{\boldsymbol{x}}\boldsymbol{v}_h + (\boldsymbol{\partial}_{\boldsymbol{x}}\boldsymbol{v}_h)^{\mathrm{T}} - \frac{2}{3}(\boldsymbol{\partial}_{\boldsymbol{x}}\cdot\boldsymbol{v}_h)\,\mathbb{I}\right) - \kappa_h(\boldsymbol{\partial}_{\boldsymbol{x}}\cdot\boldsymbol{v}_h)\,\mathbb{I} - \zeta(T_e - T_h)\,\mathbb{I}. \tag{2.5.51}$$

Finally, if we introduce the heavy-species self-partial-thermal-conductivity, the heavy-species electron-temperature partial thermal conductivity, respectively

$$\hat{\lambda}_{hh} = \frac{1}{3k_{\mathrm{B}}T_h^2}[\![\boldsymbol{\Phi}_h^{\hat{\lambda}_h}, \boldsymbol{\Phi}_h^{\hat{\lambda}_h}]\!]_h, \tag{2.5.52}$$

$$\hat{\lambda}_{he} = \frac{1}{3k_{\mathrm{B}}T_e^2}[\![\boldsymbol{\Phi}_h^{\hat{\lambda}_h}, \boldsymbol{\Phi}_h^{\hat{\lambda}_e}]\!]_h, \tag{2.5.53}$$

and the electron heavy-temperature thermal diffusion coefficient

$$\theta_{he} = \theta_{eh} = -\frac{1}{3}[\![\boldsymbol{\Phi}_h^{\hat{\lambda}_h}, \boldsymbol{\Phi}_h^{D_e}]\!]_h, \tag{2.5.54}$$

the heavy-species heat flux can be expressed as

$$\boldsymbol{\mathcal{Q}}_h = -p\sum_{j\in\mathfrak{H}}\theta_{hj}\hat{\boldsymbol{d}}_j - p\theta_{he}\hat{\boldsymbol{d}}_e - \hat{\lambda}_{hh}\boldsymbol{\partial}_{\boldsymbol{x}}T_h - \hat{\lambda}_{he}\boldsymbol{\partial}_{\boldsymbol{x}}T_e + \sum_{j\in\mathfrak{H}}\left(\frac{5}{2}k_{\mathrm{B}}T_h + \overline{E}_j\right)n_j\boldsymbol{\mathcal{V}}_j. \tag{2.5.55}$$

The second and fourth terms of the respective expressions for the heavy-species diffusion velocities (2.5.46) and the heavy-species heat flux (2.5.55) are the "heavy-species Kolesnikov diffusion fluxes". They arise from the coupling between heavy species and electrons as first described by Kolesnikov [GMM09] [Kol74].

We also introduce the new bracket

$$[\![\boldsymbol{\xi}_h, \boldsymbol{\zeta}_e]\!]_{he} = \sum_{j\in\mathfrak{H}}\sum_{\mathrm{J}\in\mathfrak{Q}_j}\frac{1}{3}\frac{\mathfrak{m}_e}{k_{\mathrm{B}}T_e}\left(\int \boldsymbol{\xi}_j\cdot\boldsymbol{C}_j\; f_j^0\,\mathrm{d}\boldsymbol{C}_j\right)\int f_e^0|\boldsymbol{C}_e|\Sigma_{\mathrm{JJ}}^{(1)}(|\boldsymbol{C}_e|^2)\;\boldsymbol{\zeta}_e\cdot\boldsymbol{C}_e\,\mathrm{d}\boldsymbol{C}_e, \tag{2.5.56}$$

which is non trivial when $\boldsymbol{\xi}_h$, $\boldsymbol{\zeta}_e$ are vectors but would be trivial for scalars or traceless symmetric tensors of rank 2. The following relations hold:

$$D_{ie} = \frac{pk_{\mathrm{B}}T_h}{3}[\![\boldsymbol{\Phi}_h^{D_i}, \boldsymbol{\Phi}_h^{D_e}]\!]_h = \frac{pk_{\mathrm{B}}T_e}{3}[\![\boldsymbol{\Phi}_h^{D_i}, \boldsymbol{\Phi}_e^{D_e}]\!]_{he}, \qquad i\in\mathfrak{H}, \tag{2.5.57}$$

$$\theta_{ie} = -\frac{1}{3}\frac{T_h}{T_e}[\![\boldsymbol{\Phi}_h^{D_i}, \boldsymbol{\Phi}_h^{\hat{\lambda}_e}]\!]_h = -\frac{1}{3}[\![\boldsymbol{\Phi}_h^{D_i}, \boldsymbol{\Phi}_e^{\hat{\lambda}_e}]\!]_{he}, \qquad i\in\mathfrak{H}, \tag{2.5.58}$$

$$\hat{\lambda}_{he} = \frac{1}{3k_{\mathrm{B}}T_e^2}[\![\boldsymbol{\Phi}_h^{\hat{\lambda}_h}, \boldsymbol{\Phi}_h^{\hat{\lambda}_e}]\!]_h = \frac{1}{3k_{\mathrm{B}}T_eT_h}[\![\boldsymbol{\Phi}_h^{\hat{\lambda}_h}, \boldsymbol{\Phi}_e^{\hat{\lambda}_e}]\!]_{he}, \tag{2.5.59}$$

$$\theta_{he} = -\frac{1}{3}[\![\boldsymbol{\Phi}_h^{\hat{\lambda}_h}, \boldsymbol{\Phi}_h^{D_e}]\!]_h = -\frac{1}{3}\frac{T_e}{T_h}[\![\boldsymbol{\Phi}_h^{\hat{\lambda}_h}, \boldsymbol{\Phi}_e^{D_e}]\!]_{he}. \tag{2.5.60}$$

We only prove the first one of those relations. The other ones can be derived by similar arguments. By definition of $[\![\cdot]\!]_h$ and by (2.5.25), D_{ie} reads

$$\begin{aligned}
D_{ie} &= \frac{pk_{\mathrm{B}}T_h}{3}[\![\boldsymbol{\Phi}_h^{D_i}, \boldsymbol{\Phi}_h^{D_e}]\!]_h \\
&= \frac{pk_{\mathrm{B}}T_h}{3}\sum_{k\in\mathfrak{H}}\sum_{\mathrm{K}\in\mathfrak{Q}_k}\int f_k^0 \boldsymbol{\Phi}_k^{D_i}\cdot\boldsymbol{\Psi}_k^{D_e}\,\mathrm{d}\boldsymbol{C}_k \\
&= \frac{pk_{\mathrm{B}}T_h}{3}\frac{\mathfrak{m}_e}{3}\sum_{k\in\mathfrak{H}}\sum_{\mathrm{K}\in\mathfrak{Q}_k}\sum_{j\in\mathfrak{H}}\sum_{\mathrm{J}\in\mathfrak{Q}_j} n_j\left(\int f_k^0\boldsymbol{\Phi}_k^{D_i}\cdot\frac{1}{p_k}\left(\delta_{kj}\delta_{\mathrm{KJ}}-Y_k^h\frac{a_{j\mathrm{J}}e^{-\epsilon_{j\mathrm{J}}}}{Q_j^{\mathrm{int}}}\right)\boldsymbol{C}_k\,\mathrm{d}\boldsymbol{C}_k\right) \\
&\qquad\times\int\Sigma_{\mathrm{JJ}}^{(1)}(|\boldsymbol{C}_e|^2)|\boldsymbol{C}_e|f_e^0(\boldsymbol{C}_e)\;\boldsymbol{C}_e\cdot\boldsymbol{\Phi}_e^{D_e}\,\mathrm{d}\boldsymbol{C}_e \\
&= \frac{pk_{\mathrm{B}}T_h}{3}\frac{\mathfrak{m}_e}{3}\sum_{j\in\mathfrak{H}}\sum_{\mathrm{J}\in\mathfrak{Q}_j} n_j\left(\sum_{k\in\mathfrak{H}}\sum_{\mathrm{K}\in\mathfrak{Q}_k}\int f_k^0\boldsymbol{\Phi}_k^{D_i}\cdot\frac{1}{p_k}\left(\delta_{kj}\delta_{\mathrm{KJ}}-Y_k^h\frac{a_{j\mathrm{J}}e^{-\epsilon_{j\mathrm{J}}}}{Q_j^{\mathrm{int}}}\right)\boldsymbol{C}_k\,\mathrm{d}\boldsymbol{C}_k\right) \\
&\qquad\times\int\Sigma_{\mathrm{JJ}}^{(1)}(|\boldsymbol{C}_e|^2)|\boldsymbol{C}_e|f_e^0(\boldsymbol{C}_e)\;\boldsymbol{C}_e\cdot\boldsymbol{\Phi}_e^{D_e}\,\mathrm{d}\boldsymbol{C}_e.
\end{aligned}$$

Since

$$\begin{aligned}
\sum_{k\in\mathfrak{H}}\sum_{\mathrm{K}\in\mathfrak{Q}_k}\frac{Y_k}{p_k}\frac{a_{j\mathrm{J}}e^{-\epsilon_{j\mathrm{J}}}}{Q_j^{\mathrm{int}}}\int f_k^0\boldsymbol{\Phi}_k^{D_i}\cdot\boldsymbol{C}_k\,\mathrm{d}\boldsymbol{C}_k &= \frac{1}{\rho k_{\mathrm{B}}T_h}\frac{a_{j\mathrm{J}}e^{-\epsilon_{j\mathrm{J}}}}{Q_j^{\mathrm{int}}}\sum_{k\in\mathfrak{H}}\sum_{\mathrm{K}\in\mathfrak{Q}_k}\int f_k^0\boldsymbol{\Phi}_k^{D_i}\cdot\mathfrak{m}_k\boldsymbol{C}_k\,\mathrm{d}\boldsymbol{C}_k \\
&= \frac{1}{\rho k_{\mathrm{B}}T_h}\frac{a_{j\mathrm{J}}e^{-\epsilon_{j\mathrm{J}}}}{Q_j^{\mathrm{int}}}\langle\!\langle\boldsymbol{\Phi}_h^{D_i}f_h^0,\mathfrak{m}_h\boldsymbol{C}_h\rangle\!\rangle_h,
\end{aligned}$$

and since $\langle\!\langle\boldsymbol{\Phi}_h^{D_i}f_h^0,\mathfrak{m}_h\boldsymbol{C}_h\rangle\!\rangle_h = 0$ by (2.5.40), the i^{th}-heavy-species electron diffusion coefficient reads finally

$$D_{ie} = \frac{p}{3}\frac{\mathfrak{m}_e}{3}\sum_{j\in\mathfrak{H}}\sum_{\mathrm{J}\in\mathfrak{Q}_j}\int f_j^0\boldsymbol{\Phi}_j^{D_i}\cdot\boldsymbol{C}_j\,\mathrm{d}\boldsymbol{C}_j\int\Sigma_{\mathrm{JJ}}^{(1)}(|\boldsymbol{C}_e|^2)|\boldsymbol{C}_e|f_e^0(\boldsymbol{C}_e)\;\boldsymbol{C}_e\cdot\boldsymbol{\Phi}_e^{D_e}\,\mathrm{d}\boldsymbol{C}_e,$$

which completes the proof.

2.5.3 Properties of the heavy-species transport coefficients

The matrix $D_h = (D_{ij})_{i,j\in\mathfrak{H}}$ is symmetric, i.e.,

$$D_{ij} = D_{ji}, \qquad i\in\mathfrak{H}, j\in\mathfrak{H}. \tag{2.5.61}$$

Indeed, $D_{ij} = \frac{1}{3}pk_{\mathrm{B}}T_h[\![\boldsymbol{\Phi}_h^{D_i},\boldsymbol{\Phi}_h^{D_j}]\!]_h$ and the bracket $[\![\cdot]\!]_h$ is symmetric (2.4.121). D_h is also positive semi-definite, i.e., for any $U = (U_i)_{i\in\mathfrak{H}}$:

$$U^{\mathrm{T}}D_hU \geq 0, \tag{2.5.62}$$

and its kernel is the space spanned by the vector $Y_h = (Y_i)_{i\in\mathfrak{H}}$, i.e.,

$$N(D_h) = \mathbb{R}Y_h. \tag{2.5.63}$$

Indeed, since the bracket $[\![\cdot]\!]_h$ is bilinear by definition and positive semi-definite by (2.4.122):

$$\begin{aligned} U^{\mathrm{T}} D_h U &= \sum_{i\in\mathfrak{H}}\sum_{j\in\mathfrak{H}} D_{ij}U_iU_j \\ &= \frac{pk_{\mathrm{B}}T_h}{3}\sum_{i\in\mathfrak{H}}\sum_{j\in\mathfrak{H}}[\![\mathbf{\Phi}_h^{D_i},\mathbf{\Phi}_h^{D_j}]\!]_h U_iU_j \\ &= \frac{pk_{\mathrm{B}}T_h}{3}[\![\sum_{i\in\mathfrak{H}}\mathbf{\Phi}_h^{D_i}U_i,\sum_{j\in\mathfrak{H}}\mathbf{\Phi}_h^{D_j}U_j]\!]_h \\ &\geq 0. \end{aligned}$$

Since the kernel of $[\![\cdot]\!]_h$ is $\mathcal{I}_h$ from (2.4.123), the latter calculation also yields

$$U^{\mathrm{T}} D_h U = 0 \Leftrightarrow \sum_{i\in\mathfrak{H}}\mathbf{\Phi}_h^{D_i}U_i \in \mathcal{I}_h.$$

Since by definition the $\mathbf{\Phi}_h^{D_i}$, $i\in\mathfrak{H}$, are orthogonal to $\mathcal{I}_h$ with respect to the scalar product $\langle\!\langle \cdot \rangle\!\rangle_h$, $\sum_{i\in\mathfrak{H}}\mathbf{\Phi}_h^{D_i}U_i$ is orthogonal to $\mathcal{I}_h$ as well, and thus

$$U^{\mathrm{T}} D_h U = 0 \Leftrightarrow \sum_{i\in\mathfrak{H}}\mathbf{\Phi}_h^{D_i}U_i = 0. \tag{2.5.64}$$

More generally, the space spanned by the vectors $\mathbf{\Phi}_h^{D_i}$, $i\in\mathfrak{H}$, is orthogonal to $\mathcal{I}_h$, the kernel of $\mathcal{F}_h$, so $\mathcal{F}_h$ is invertible over this vector space, and

$$\sum_{i\in\mathfrak{H}}\mathbf{\Phi}_h^{D_i}U_i = 0 \Leftrightarrow \mathcal{F}_h\Big(\sum_{i\in\mathfrak{H}}\mathbf{\Phi}_h^{D_i}U_i\Big) = 0 \Leftrightarrow \sum_{i\in\mathfrak{H}}\mathbf{\Psi}_h^{D_i}U_i = 0. \tag{2.5.65}$$

From (2.5.24), the set of solutions to the latter equation is the one-dimensional space $\mathbb{R}Y_h$, which proves (2.5.63). Furthermore, since from (2.5.24) $\sum_{i\in\mathfrak{H}}Y_i\mathbf{\Psi}_h^{D_i} = 0$, we deduce from (2.5.65) that

$$\sum_{i\in\mathfrak{H}}Y_i\mathbf{\Phi}_h^{D_i} = 0, \tag{2.5.66}$$

so that from (2.5.42)-(2.5.45)

$$\sum_{i\in\mathfrak{H}}Y_iD_{ij} = 0, \qquad j\in\mathfrak{H}, \tag{2.5.67}$$

$$\sum_{i\in\mathfrak{H}}Y_iD_{ie} = 0, \tag{2.5.68}$$

and as well

$$\sum_{i\in\mathfrak{H}}Y_i\theta_{ih} = 0, \tag{2.5.69}$$

$$\sum_{i\in\mathfrak{H}}Y_i\theta_{ie} = 0. \tag{2.5.70}$$

Finally, from expressions (2.5.48), (2.5.49) and (2.5.52), respectively, the shear viscosity η_h, the volume viscosity κ_h, and the heavy-species self-partial-thermal-conductivity $\hat{\lambda}_{hh}$, have the same sign as $[\![\mathbf{\Phi}_h^{\eta_h},\mathbf{\Phi}_h^{\eta_h}]\!]_h$, $[\![\phi_h^{\kappa_h},\phi_h^{\kappa_h}]\!]_h$, and $[\![\mathbf{\Phi}_h^{\hat{\lambda}_h},\mathbf{\Phi}_h^{\hat{\lambda}_h}]\!]_h$, respectively. For $\mu=\eta_h$, κ_h and $\hat{\lambda}_h$, it is readily seen

that $[\![\phi_h^\mu, \phi_h^\mu]\!]_h \geq 0$ since the bracket product is positive semi-definite. Moreover, if $[\![\phi_h^\mu, \phi_h^\mu]\!]_h = 0$, then ϕ_h^μ must be in $\mathcal{I}_h$ by (2.4.123). Because of the constraints (2.5.40), ϕ_h^μ must also be orthogonal to $\mathcal{I}_h$, so that $\phi_h^\mu = 0$. Now, from expressions (2.5.22), (2.5.23) and (2.5.27), the expansion coefficients $\boldsymbol{\Psi}_h^{\eta_h}$ and $\boldsymbol{\Psi}_h^{\hat{\lambda}_h}$ cannot vanish, while the expansion coefficient $\Psi_h^{\kappa_h}$ can vanish if there is no internal energy levels. By linearity the same is true for the perturbation coefficients $\boldsymbol{\Phi}_h^{\eta_h}$, $\boldsymbol{\Phi}_h^{\hat{\lambda}_h}$, and $\phi_h^{\kappa_h}$, so that finally [Gio99]

$$\eta_h > 0, \tag{2.5.71}$$

$$\kappa_h \geq 0, \tag{2.5.72}$$

$$\hat{\lambda}_{hh} > 0. \tag{2.5.73}$$

2.5.4 Electron Kolesnikov transport coefficients

The resolution of the linearized Boltzmann equation for the second-order electron perturbation function ϕ_e^2 yields first-order electron transport fluxes and associated transport coefficients. These transport fluxes should not be confused with Burnett transport coefficients [GMM09] [FK72], since one retrieves the first-order Chapman-Enskog expansion for multicomponent mixtures in the limit $T_e = T_h$ [GGMM10].

In the case of a weakly magnetized plasma, i.e., when $b = 0$, equation (2.4.127) for the second-order electron perturbation function ϕ_e^2 becomes

$$\mathcal{F}_e(\phi_e^2) = \Psi_e^2, \tag{2.5.74}$$

where

$$\begin{aligned}\Psi_e^2 = &- \mathcal{D}_e^0(\ln f_e^0) - \frac{1}{f_e^0}\mathcal{D}_e^{-1}(\phi_e f_e^0) + \frac{1}{f_e^0}\mathcal{S}_{ee}(\phi_e f_e^0, \phi_e f_e^0) \\ &+ \sum_{j\in\mathfrak{H}} \frac{1}{f_e^0}\left[\mathcal{S}_{ej}^0(\phi_e f_e^0, \phi_j f_j^0) + \mathcal{S}_{ej}^1(f_e^0, \phi_j f_j^0) + \mathcal{S}_{ej}^2(f_e^0, f_j^0)\right],\end{aligned} \tag{2.5.75}$$

under the constraints

$$\langle\!\langle \phi_e^2 f_e^0, \psi_e^l \rangle\!\rangle_e = 0, \quad l \in \{e, n^s + 4\}. \tag{2.5.76}$$

After some lengthy calculations, the right-member Ψ_e^2 of equation (2.5.74) can be expanded in the form

$$\begin{aligned}\Psi_e^2 = &- \boldsymbol{\Psi}_e^{\eta_e} : \boldsymbol{\partial}_{\boldsymbol{x}} \boldsymbol{v}_h - \delta_{b0} \boldsymbol{\Psi}_e^{D_e} \cdot (-n_e q_e \boldsymbol{v}_h \wedge \mathbf{B}) \\ &- \delta_{b0} \frac{q_e}{\mathfrak{m}_e} \boldsymbol{\Phi}_e^{D_e} \cdot \left[(\boldsymbol{\partial}_{\boldsymbol{x}} p_e - n_e q_e \mathbf{E}) \wedge \mathbf{B}\right] - \delta_{b0} \frac{q_e}{\mathfrak{m}_e} \boldsymbol{\Phi}_e^{\hat{\lambda}_e} \cdot \left[\boldsymbol{\partial}_{\boldsymbol{x}} \left(\frac{1}{k_{\mathrm{B}} T_e}\right) \wedge \mathbf{B}\right] \\ &- \frac{1}{3} \boldsymbol{\Psi}_e^{\kappa_h D_e} \cdot (\boldsymbol{\partial}_{\boldsymbol{x}} \cdot \boldsymbol{v}_h) \, (\boldsymbol{\partial}_{\boldsymbol{x}} p_e - n_e q_e \mathbf{E}) - \frac{1}{3} \boldsymbol{\Psi}_e^{\kappa_h \hat{\lambda}_e} \cdot (\boldsymbol{\partial}_{\boldsymbol{x}} \cdot \boldsymbol{v}_h) \, \boldsymbol{\partial}_{\boldsymbol{x}} \left(\frac{1}{k_{\mathrm{B}} T_e}\right) \\ &- \boldsymbol{\Psi}_e^{\Theta D_e} \cdot (T_e - T_h) \, (\boldsymbol{\partial}_{\boldsymbol{x}} p_e - n_e q_e \mathbf{E}) - \boldsymbol{\Psi}_e^{\Theta \hat{\lambda}_e} \cdot (T_e - T_h) \, \boldsymbol{\partial}_{\boldsymbol{x}} \left(\frac{1}{k_{\mathrm{B}} T_e}\right) \\ &- \sum_{j\in\mathfrak{H}} \boldsymbol{\Psi}_e^{D_j} \cdot (\boldsymbol{\partial}_{\boldsymbol{x}} p_j - n_j q_j \mathbf{E}) - \boldsymbol{\Psi}_e^{D_e^2} \cdot (\boldsymbol{\partial}_{\boldsymbol{x}} p_e - n_e q_e \mathbf{E}) \\ &- \boldsymbol{\Psi}_e^{\hat{\lambda}_h} \cdot \boldsymbol{\partial}_{\boldsymbol{x}} \left(\frac{1}{k_{\mathrm{B}} T_h}\right) - \boldsymbol{\Psi}_e^{\hat{\lambda}_e^2} \cdot \boldsymbol{\partial}_{\boldsymbol{x}} \left(\frac{1}{k_{\mathrm{B}} T_e}\right) - \tilde{\Psi}_e^2,\end{aligned} \tag{2.5.77}$$

where $\tilde{\Psi}_e^2$ is a scalar function of $\boldsymbol{C}_e \cdot \boldsymbol{C}_e$. Other expansion coefficients are given by

$$\boldsymbol{\Psi}_e^{\eta_e} = \frac{\mathfrak{m}_e}{k_{\mathrm{B}} T_e} \left[\boldsymbol{C}_e \otimes \boldsymbol{C}_e - \frac{1}{3} \boldsymbol{C}_e \cdot \boldsymbol{C}_e \, \mathbb{I} \right] \tag{2.5.78}$$

$$\boldsymbol{\Psi}_e^{D_i} = \sum_{j \in \mathfrak{H}} \sum_{\mathrm{J} \in \mathfrak{Q}_j} \frac{1}{3} \frac{\mathfrak{m}_e}{k_{\mathrm{B}} T_e} |\boldsymbol{C}_e| \Sigma_{\mathrm{JJ}}^{(1)}(|\boldsymbol{C}_e|^2) \left(\int \boldsymbol{\Phi}_j^{D_i} \cdot \boldsymbol{C}_j \; f_j^0 \, \mathrm{d}\boldsymbol{C}_j \right) \boldsymbol{C}_e \tag{2.5.79}$$

$$\boldsymbol{\Psi}_e^{D_e^2} = \sum_{j \in \mathfrak{H}} \sum_{\mathrm{J} \in \mathfrak{Q}_j} \frac{1}{3} \frac{\mathfrak{m}_e}{k_{\mathrm{B}} T_e} |\boldsymbol{C}_e| \Sigma_{\mathrm{JJ}}^{(1)}(|\boldsymbol{C}_e|^2) \left(\int \boldsymbol{\Phi}_j^{D_e} \cdot \boldsymbol{C}_j \; f_j^0 \, \mathrm{d}\boldsymbol{C}_j \right) \boldsymbol{C}_e \tag{2.5.80}$$

$$\boldsymbol{\Psi}_e^{\hat{\lambda}_h} = \sum_{j \in \mathfrak{H}} \sum_{\mathrm{J} \in \mathfrak{Q}_j} \frac{1}{3} \frac{\mathfrak{m}_e}{k_{\mathrm{B}} T_e} |\boldsymbol{C}_e| \Sigma_{\mathrm{JJ}}^{(1)}(|\boldsymbol{C}_e|^2) \left(\int \boldsymbol{\Phi}_j^{\hat{\lambda}_h} \cdot \boldsymbol{C}_j \; f_j^0 \, \mathrm{d}\boldsymbol{C}_j \right) \boldsymbol{C}_e \tag{2.5.81}$$

$$\boldsymbol{\Psi}_e^{\hat{\lambda}_e^2} = \sum_{j \in \mathfrak{H}} \sum_{\mathrm{J} \in \mathfrak{Q}_j} \frac{1}{3} \frac{\mathfrak{m}_e}{k_{\mathrm{B}} T_e} |\boldsymbol{C}_e| \Sigma_{\mathrm{JJ}}^{(1)}(|\boldsymbol{C}_e|^2) \left(\int \boldsymbol{\Phi}_j^{\hat{\lambda}_e} \cdot \boldsymbol{C}_j \; f_j^0 \, \mathrm{d}\boldsymbol{C}_j \right) \boldsymbol{C}_e, \tag{2.5.82}$$

and

$$\boldsymbol{\Psi}_e^{\kappa_h D_e} = \sum_{j \in \mathfrak{H}} \sum_{\mathrm{J} \in \mathfrak{Q}_j} \left(\int \phi_j^{\kappa_h} f_j^0 \, \mathrm{d}\boldsymbol{C}_j \right) |\boldsymbol{C}_e| \Sigma_{\mathrm{JJ}}^{(1)}(|\boldsymbol{C}_e|^2) \boldsymbol{\Phi}_e^{D_e} \tag{2.5.83}$$

$$\boldsymbol{\Psi}_e^{\kappa_h \hat{\lambda}_e} = \sum_{j \in \mathfrak{H}} \sum_{\mathrm{J} \in \mathfrak{Q}_j} \left(\int \phi_j^{\kappa_h} f_j^0 \, \mathrm{d}\boldsymbol{C}_j \right) |\boldsymbol{C}_e| \Sigma_{\mathrm{JJ}}^{(1)}(|\boldsymbol{C}_e|^2) \boldsymbol{\Phi}_e^{\hat{\lambda}_e} \tag{2.5.84}$$

$$\boldsymbol{\Psi}_e^{\Theta D_e} = \sum_{j \in \mathfrak{H}} \sum_{\mathrm{J} \in \mathfrak{Q}_j} \left(\int \phi_j^{\Theta} f_j^0 \, \mathrm{d}\boldsymbol{C}_j \right) |\boldsymbol{C}_e| \Sigma_{\mathrm{JJ}}^{(1)}(|\boldsymbol{C}_e|^2) \boldsymbol{\Phi}_e^{D_e} \tag{2.5.85}$$

$$\boldsymbol{\Psi}_e^{\Theta \hat{\lambda}_e} = \sum_{j \in \mathfrak{H}} \sum_{\mathrm{J} \in \mathfrak{Q}_j} \left(\int \phi_j^{\Theta} f_j^0 \, \mathrm{d}\boldsymbol{C}_j \right) |\boldsymbol{C}_e| \Sigma_{\mathrm{JJ}}^{(1)}(|\boldsymbol{C}_e|^2) \boldsymbol{\Phi}_e^{\hat{\lambda}_e}. \tag{2.5.86}$$

Thanks to the linearity of the linearized collision operator $\mathcal{F}_e$, the following similar expansion holds for ϕ_e^2:

$$\begin{aligned}
\phi_e^2 = & - \boldsymbol{\Phi}_e^{\eta_e} : \boldsymbol{\partial}_{\boldsymbol{x}} \boldsymbol{v}_h - \delta_{b0} \boldsymbol{\Phi}_e^{D_e} \cdot (-n_e q_e \boldsymbol{v}_h \wedge \mathbf{B}) \\
& - \delta_{b0} \frac{q_e}{\mathfrak{m}_e} \boldsymbol{\Xi}_e^{D_e} \cdot \left[(\boldsymbol{\partial}_{\boldsymbol{x}} p_e - n_e q_e \mathbf{E}) \wedge \mathbf{B} \right] - \delta_{b0} \frac{q_e}{\mathfrak{m}_e} \boldsymbol{\Xi}_e^{\hat{\lambda}_e} \cdot \left[\boldsymbol{\partial}_{\boldsymbol{x}} \left(\frac{1}{k_{\mathrm{B}} T_e} \right) \wedge \mathbf{B} \right] \\
& - \frac{1}{3} \boldsymbol{\Phi}_e^{\kappa_h D_e} \cdot (\boldsymbol{\partial}_{\boldsymbol{x}} \cdot \boldsymbol{v}_h) \; (\boldsymbol{\partial}_{\boldsymbol{x}} p_e - n_e q_e \mathbf{E}) - \frac{1}{3} \boldsymbol{\Phi}_e^{\kappa_h \hat{\lambda}_e} \cdot (\boldsymbol{\partial}_{\boldsymbol{x}} \cdot \boldsymbol{v}_h) \; \boldsymbol{\partial}_{\boldsymbol{x}} \left(\frac{1}{k_{\mathrm{B}} T_e} \right) \\
& - \boldsymbol{\Phi}_e^{\Theta D_e} \cdot (T_e - T_h) \; (\boldsymbol{\partial}_{\boldsymbol{x}} p_e - n_e q_e \mathbf{E}) - \boldsymbol{\Phi}_e^{\Theta \hat{\lambda}_e} \cdot (T_e - T_h) \; \boldsymbol{\partial}_{\boldsymbol{x}} \left(\frac{1}{k_{\mathrm{B}} T_e} \right) \\
& - \sum_{j \in \mathfrak{H}} \boldsymbol{\Phi}_e^{D_j} \cdot (\boldsymbol{\partial}_{\boldsymbol{x}} p_j - n_j q_j \mathbf{E}) - \boldsymbol{\Phi}_e^{D_e^2} \cdot (\boldsymbol{\partial}_{\boldsymbol{x}} p_e - n_e q_e \mathbf{E}) \\
& - \boldsymbol{\Phi}_e^{\hat{\lambda}_h} \cdot \boldsymbol{\partial}_{\boldsymbol{x}} \left(\frac{1}{k_{\mathrm{B}} T_h} \right) - \boldsymbol{\Phi}_e^{\hat{\lambda}_e^2} \cdot \boldsymbol{\partial}_{\boldsymbol{x}} \left(\frac{1}{k_{\mathrm{B}} T_e} \right) - \tilde{\phi}_e^2.
\end{aligned} \tag{2.5.87}$$

where for each value of $\mu = \eta_e, D_e, \kappa_h D_e, \kappa_h \hat{\lambda}_e, \Theta D_e, \Theta \hat{\lambda}_e, D_j, j \in \mathfrak{H}, D_e^2, \hat{\lambda}_h, \hat{\lambda}_e^2$, the function ϕ_e^μ is solution to

$$\mathcal{F}_e(\phi_e^\mu) = \Psi_e^\mu \tag{2.5.88}$$

$$\langle\!\langle f_e^0 \phi_e^\mu, \psi_e^l \rangle\!\rangle_e = 0, \qquad l \in \{e, n^s + 4\}, \tag{2.5.89}$$

while for each value of $\mu = D_e, \hat{\lambda}_e$, the function $\boldsymbol{\Xi}_e^\mu$ is solution to

$$\mathcal{F}_e(\boldsymbol{\Xi}_e^\mu) = \boldsymbol{\Phi}_e^\mu \tag{2.5.90}$$

$$\langle\!\langle f_e^0 \boldsymbol{\Xi}_e^\mu, \psi_e^l \rangle\!\rangle_e = 0, \qquad l \in \{e, n^s + 4\}\,. \tag{2.5.91}$$

Furthermore, because of the isotropy of $\mathcal{F}_e$, $\tilde{\phi}_e^2$ is a scalar function of $\boldsymbol{C}_e \cdot \boldsymbol{C}_e$, and each ϕ_e^μ, respectively $\boldsymbol{\Xi}_e^\mu$, is of the same tensorial type [Gra04] as Ψ_e^μ, respectively $\boldsymbol{\Phi}_e^\mu$.

The first-order electron self-diffusion coefficient, the first-order electron electron-temperature thermal diffusion coefficient, and the first-order electron self-partial-thermal-conductivity are given by

$$D_{ee}^1 = \frac{p k_{\text{B}} T_e}{3} [\![\boldsymbol{\Phi}_h^{D_e}, \boldsymbol{\Phi}_e^{D_e}]\!]_{he}, \tag{2.5.92}$$

$$\theta_{ee}^1 = -\frac{1}{3} [\![\boldsymbol{\Phi}_h^{\hat{\lambda}_e}, \boldsymbol{\Phi}_e^{D_e}]\!]_{he} = -\frac{1}{3} [\![\boldsymbol{\Phi}_h^{D_e}, \boldsymbol{\Phi}_e^{\hat{\lambda}_e}]\!]_{he}, \tag{2.5.93}$$

$$\hat{\lambda}_{ee}^1 = \frac{1}{3 k_{\text{B}} T_e^2} [\![\boldsymbol{\Phi}_h^{\hat{\lambda}_e}, \boldsymbol{\Phi}_e^{\hat{\lambda}_e}]\!]_{he}. \tag{2.5.94}$$

The electron heavy-temperature partial thermal conductivity is given by

$$\hat{\lambda}_{eh} = \frac{T_e}{T_h} \hat{\lambda}_{he} = \frac{1}{3 k_{\text{B}} T_e T_h} [\![\boldsymbol{\Phi}_h^{\hat{\lambda}_h}, \boldsymbol{\Phi}_h^{\hat{\lambda}_e}]\!]_h, \tag{2.5.95}$$

where $\hat{\lambda}_{he}$ is the heavy-species electron-temperature partial thermal conductivity. We also introduce the additional transport coefficients

$$D_{ee}^{\kappa_h} = \frac{p k_{\text{B}} T_e}{9} \, [\![\phi_h^{\kappa_h}, \boldsymbol{\Phi}_e^{D_e}, \boldsymbol{\Phi}_e^{D_e}]\!]_{hee}, \tag{2.5.96}$$

$$\theta_{ee}^{\kappa_h} = -\frac{1}{9} \, [\![\phi_h^{\kappa_h}, \boldsymbol{\Phi}_e^{\hat{\lambda}_e}, \boldsymbol{\Phi}_e^{D_e}]\!]_{hee}, \tag{2.5.97}$$

$$\hat{\lambda}_{ee}^{\kappa_h} = \frac{1}{9 k_{\text{B}} T_e^2} [\![\phi_h^{\kappa_h}, \boldsymbol{\Phi}_e^{\hat{\lambda}_e}, \boldsymbol{\Phi}_e^{\hat{\lambda}_e}]\!]_{hee}, \tag{2.5.98}$$

$$D_{ee}^{\Theta} = \frac{p k_{\text{B}} T_e}{3} \, [\![\phi_h^{\Theta}, \boldsymbol{\Phi}_e^{D_e}, \boldsymbol{\Phi}_e^{D_e}]\!]_{hee}, \tag{2.5.99}$$

$$\theta_{ee}^{\Theta} = -\frac{1}{3} \, [\![\phi_h^{\Theta}, \boldsymbol{\Phi}_e^{\hat{\lambda}_e}, \boldsymbol{\Phi}_e^{D_e}]\!]_{hee}, \tag{2.5.100}$$

$$\hat{\lambda}_{ee}^{\Theta} = \frac{1}{3 k_{\text{B}} T_e^2} [\![\phi_h^{\Theta}, \boldsymbol{\Phi}_e^{\hat{\lambda}_e}, \boldsymbol{\Phi}_e^{\hat{\lambda}_e}]\!]_{hee}, \tag{2.5.101}$$

and the magnetic transport coefficients [GG09] [GMM09]

$$D_{ee}^{\odot} = -\frac{p k_{\text{B}} T_e}{3} ((\boldsymbol{\Phi}_e^{D_e}, \boldsymbol{\Phi}_e^{D_e}))_e, \tag{2.5.102}$$

$$\theta_{ee}^{\odot} = \frac{1}{3} ((\boldsymbol{\Phi}_e^{D_e}, \boldsymbol{\Phi}_e^{\hat{\lambda}_e}))_e, \tag{2.5.103}$$

$$\hat{\lambda}_e^{\odot} = -\frac{1}{3 k_{\text{B}} T_e^2} ((\boldsymbol{\Phi}_e^{\hat{\lambda}_e}, \boldsymbol{\Phi}_e^{\hat{\lambda}_e}))_e, \tag{2.5.104}$$

where we have introduced the brackets

$$((\boldsymbol{\xi}_e, \boldsymbol{\zeta}_e))_e = \frac{q_e |\mathbf{B}|}{\mathfrak{m}_e} \int f_e^0 \; \boldsymbol{\xi}_e \odot \boldsymbol{\zeta}_e \, \mathrm{d}\boldsymbol{C}_e, \tag{2.5.105}$$

$$[\![\xi_h, \boldsymbol{\zeta}_e, \boldsymbol{\delta}_e]\!]_{hee} = \sum_{j \in \mathfrak{H}} \sum_{\text{J} \in \mathfrak{Q}_j} \left(\int \xi_j f_j^0 \, \mathrm{d}\boldsymbol{C}_j \right) \int f_e^0 |\boldsymbol{C}_e| \Sigma_{\text{JJ}}^{(1)}(|\boldsymbol{C}_e|^2) \; \boldsymbol{\zeta}_e \odot \boldsymbol{\delta}_e \, \mathrm{d}\boldsymbol{C}_e. \tag{2.5.106}$$

The following expressions are then derived for the first-order electron diffusion velocity

$$\begin{aligned}\boldsymbol{\mathcal{V}}_e^1 =& - D_{ee}^1 \hat{\boldsymbol{d}}_e - \sum_{i\in\mathfrak{H}} D_{ei}\hat{\boldsymbol{d}}_i - \theta_{ee}^1 \boldsymbol{\partial}_{\boldsymbol{x}} \ln T_e - \theta_{eh}\boldsymbol{\partial}_{\boldsymbol{x}} \ln T_h \\ & - \left[D_{ee}^{\kappa_h}\ (\boldsymbol{\partial}_{\boldsymbol{x}}\cdot\boldsymbol{v}_h) + D_{ee}^{\Theta}\ (T_e - T_h)\right]\ \hat{\boldsymbol{d}}_e - \left[\theta_{ee}^{\kappa_h}\ (\boldsymbol{\partial}_{\boldsymbol{x}}\cdot\boldsymbol{v}_h) + \theta_{ee}^{\Theta}\ (T_e - T_h)\right]\ \boldsymbol{\partial}_{\boldsymbol{x}} \ln T_e \\ & - \delta_{b0}\frac{n_e q_e |\mathbf{B}|}{p} D_{ee}^0\ \boldsymbol{\mathscr{B}}\wedge\boldsymbol{v}_h - \delta_{b0} D_{ee}^{\odot}\ \boldsymbol{\mathscr{B}}\wedge\hat{\boldsymbol{d}}_e - \delta_{b0}\theta_{ee}^{\odot}\ \boldsymbol{\mathscr{B}}\wedge\boldsymbol{\partial}_{\boldsymbol{x}}\ln T_e,\end{aligned} \tag{2.5.107}$$

and heat flux

$$\begin{aligned}\boldsymbol{\mathcal{Q}}_e^1 =& - p\theta_{ee}^1 \hat{\boldsymbol{d}}_e - p\sum_{i\in\mathfrak{H}} \theta_{ei}\hat{\boldsymbol{d}}_i - \hat{\lambda}_{ee}^1 \boldsymbol{\partial}_{\boldsymbol{x}} T_e - \hat{\lambda}_{eh}\boldsymbol{\partial}_{\boldsymbol{x}} T_h + n_e\Big(\frac{5}{2}k_{\mathrm{B}}T_e\Big)\boldsymbol{\mathcal{V}}_e^1 \\ & - p\left[\theta_{ee}^{\kappa_h}\ (\boldsymbol{\partial}_{\boldsymbol{x}}\cdot\boldsymbol{v}_h) + \theta_{ee}^{\Theta}\ (T_e - T_h)\right]\ \hat{\boldsymbol{d}}_e - \left[\hat{\lambda}_{ee}^{\kappa_h}\ (\boldsymbol{\partial}_{\boldsymbol{x}}\cdot\boldsymbol{v}_h) + \hat{\lambda}_{ee}^{\Theta}\ (T_e - T_h)\right]\ \boldsymbol{\partial}_{\boldsymbol{x}} T_e \\ & - \delta_{b0} n_e q_e |\mathbf{B}| \theta_{ee}^0\ \boldsymbol{\mathscr{B}}\wedge\boldsymbol{v}_h - \delta_{b0} p\theta_{ee}^{\odot}\ \boldsymbol{\mathscr{B}}\wedge\hat{\boldsymbol{d}}_e - \delta_{b0}\hat{\lambda}_e^{\odot}\ \boldsymbol{\mathscr{B}}\wedge\boldsymbol{\partial}_{\boldsymbol{x}} T_e,\end{aligned} \tag{2.5.108}$$

where $\boldsymbol{\mathscr{B}}$ denotes the direction of the magnetic field vector

$$\boldsymbol{\mathscr{B}} = \frac{1}{|\mathbf{B}|}\mathbf{B}. \tag{2.5.109}$$

Except for the last three terms associated with the magnetic field effect on the electrons, all the terms in expressions (2.5.107) and (2.5.108) for $\boldsymbol{\mathcal{V}}_e^1$ and $\boldsymbol{\mathcal{Q}}_e^1$, respectively, are due to the coupling between electrons and heavy species. They may thus be referred to as the "electron Kolesnikov fluxes" [Kol74] [GMM09].

The terms in the first lines of both (2.5.107) and (2.5.108) were already present in the monoatomic case [GMM09], though the corresponding transport coefficients (2.5.43), (2.5.45), (2.5.54), and (2.5.92)-(2.5.95) are different. The terms proportional to $(\boldsymbol{\partial}_{\boldsymbol{x}}\cdot\boldsymbol{v}_h)$ are new and specific to the polyatomic case, since the volume viscosity κ_h vanishes in the monoatomic limit. The terms proportional to $(T_e - T_h)$ are also new, because the corresponding transport coefficients vanish in the monoatomic limit [GMM09]. This is because the term

$$\int \phi_j^{\Theta} f_j^0\, \mathrm{d}\boldsymbol{C}_j \tag{2.5.110}$$

appearing in expressions (2.5.99)-(2.5.101) for D_{ee}^{Θ}, θ_{ee}^{Θ} and $\hat{\lambda}_{ee}^{\Theta}$, respectively, becomes equal to $\langle\!\langle \phi_h^{\Theta} f_h^0, \psi_h^j \rangle\!\rangle_h$ in the monoatomic limit and thus vanishes, since the number of particles in the j^{th} species is a collisional invariant of the scattering operator. Conversely, in the polyatomic case, the term (2.5.110) does not necessarily vanish. Indeed, the number of molecules of the j^{th} species in the J^{th} internal energy state is not conserved in general in scattering collisions, since the elastic collision cross-section $\sigma_{je}^{\mathrm{JJ}}$ may depend on the energy level J. Physically speaking, the transport fluxes appearing in the second lines of (2.5.107) and (2.5.108) are associated with the nonuniform diffusion of electrons against the different internal energy states of each heavy species. The last lines of (2.5.107) and (2.5.108), respectively, embed the magnetic field induced electron transport fluxes, and have the same structure in the polyatomic and monoatomic cases, for the last two terms were overlooked in the case $b = 0$ in [GMM09].

Finally, we obtain the following expression for the first-order energy exchange term due to scat-

tering collisions:

$$\begin{aligned}\Delta E_{he}^{1,\mathrm{scatt}} = &\sum_{i\in\mathfrak{H}}\sum_{\mathrm{I}\in\mathfrak{Q}_i} n_i \boldsymbol{\mathcal{V}}_{i\mathrm{I}}\cdot\boldsymbol{F}_{ie}^{I,0} \\ &+\sum_{i\in\mathfrak{H}}\sum_{\mathrm{I}\in\mathfrak{Q}_i}\frac{2}{3}\frac{\mathfrak{m}_e}{\mathfrak{m}_i}\nu_{ie}^{\mathrm{II}}\int f_i^0\phi_i\Big(\frac{3}{2}k_{\mathrm{B}}T_e-\frac{1}{2}\mathfrak{m}_i\boldsymbol{C}_i\cdot\boldsymbol{C}_i\Big)\,\mathrm{d}\boldsymbol{C}_i \\ &+\sum_{i\in\mathfrak{H}}\sum_{\mathrm{I},\mathrm{I}'\in\mathfrak{Q}_i}\nu_{ie}^{\mathrm{II}'}\Delta E_{\mathrm{II}'}\int f_i^0\phi_i\,\mathrm{d}\boldsymbol{C}_i.\end{aligned} \tag{2.5.111}$$

One may prefer the alternative formulation

$$\begin{aligned}\Delta E_{he}^{1,\mathrm{scatt}} = &\, p\sum_{j\in\mathfrak{H}} D_{je}\hat{\boldsymbol{d}}_j\cdot\hat{\boldsymbol{d}}_e + p\sum_{j\in\mathfrak{H}}\theta_{je}\hat{\boldsymbol{d}}_j\cdot\boldsymbol{\partial}_{\boldsymbol{x}}\ln T_e \\ &+ pD_{ee}^1\hat{\boldsymbol{d}}_e\cdot\hat{\boldsymbol{d}}_e + p\theta_{ee}^1\hat{\boldsymbol{d}}_e\cdot\boldsymbol{\partial}_{\boldsymbol{x}}\ln T_e \\ &+ p\theta_{he}\boldsymbol{\partial}_{\boldsymbol{x}}\ln T_h\cdot\hat{\boldsymbol{d}}_e + T_e\hat{\lambda}_{he}\boldsymbol{\partial}_{\boldsymbol{x}}\ln T_h\cdot\boldsymbol{\partial}_{\boldsymbol{x}}\ln T_e \\ &+ p\theta_{ee}^1\boldsymbol{\partial}_{\boldsymbol{x}}\ln T_e\cdot\hat{\boldsymbol{d}}_e + T_e\hat{\lambda}_{ee}^1\boldsymbol{\partial}_{\boldsymbol{x}}\ln T_e\cdot\boldsymbol{\partial}_{\boldsymbol{x}}\ln T_e \\ &+ k_{\mathrm{B}}T_h^2\langle\!\langle f_h^0\phi_h,\Psi_h^{\Theta}\rangle\!\rangle_h \\ &+ k_{\mathrm{B}}(T_e-T_h)\sum_{i\in\mathfrak{H}}\sum_{\mathrm{I}\in\mathfrak{Q}_i}\frac{\mathfrak{m}_e}{\mathfrak{m}_i}\nu_{ie}^{\mathrm{II}}\int f_i^0\phi_i\,\mathrm{d}\boldsymbol{C}_i \\ &+\sum_{i\in\mathfrak{H}}\sum_{\mathrm{I},\mathrm{I}'\in\mathfrak{Q}_i}\Big(1-\frac{T_h}{T_e}g_{\mathrm{II}'}\Big)\nu_{ie}^{\mathrm{II}'}\Delta E_{\mathrm{II}'}\int f_i^0\phi_i\,\mathrm{d}\boldsymbol{C}_i,\end{aligned} \tag{2.5.112}$$

where $\int f_i^0\phi_i\,\mathrm{d}\boldsymbol{C}_i$ can be further expanded in the form

$$\begin{aligned}\int f_i^0\phi_i\,\mathrm{d}\boldsymbol{C}_i = &-(\boldsymbol{\partial}_{\boldsymbol{x}}\cdot\boldsymbol{v}_h)\int f_i^0\phi_i^{\kappa_h}\,\mathrm{d}\boldsymbol{C}_i \\ &-(T_e-T_h)\int f_i^0\phi_i^{\Theta}\,\mathrm{d}\boldsymbol{C}_i.\end{aligned} \tag{2.5.113}$$

2.6 Fluid Equations

In this section, we summarize the macroscopic equations obtained for multicomponent plasmas in the Navier-Stokes regime. The fluid equations (2.4.130), (2.4.131), (2.4.144), (2.4.145) and (2.4.146) and the transport fluxes derived from the Chapman-Enskog expansion are redimensionalized. This is equivalent to setting $\varepsilon = 1$ in the full-dimension equations where ε is taken as a formal parameter.

2.6.1 Conservation of mass, momentum, and energy

The fluid equations (2.4.130), (2.4.131), (2.4.144), (2.4.145) and (2.4.146) are rewritten in the form

$$\partial_t\rho_e + \boldsymbol{\partial}_{\boldsymbol{x}}\cdot(\rho_e\boldsymbol{v}_h + \rho_e\boldsymbol{\mathcal{V}}_e) = \mathfrak{m}_e\mathfrak{w}_e, \tag{2.6.1}$$

$$\partial_t\mathcal{E}_e + \boldsymbol{\partial}_{\boldsymbol{x}}\cdot(\mathcal{E}_e\boldsymbol{v}_h) = -p_e\,\boldsymbol{\partial}_{\boldsymbol{x}}\cdot\boldsymbol{v}_h - \boldsymbol{\partial}_{\boldsymbol{x}}\cdot\boldsymbol{\mathcal{Q}}_e + \Delta E_{eh} + \boldsymbol{J}_e\cdot\mathbf{E}' + \delta_{b0}\,\boldsymbol{J}_e^0\cdot(\boldsymbol{v}_h\wedge\mathbf{B}), \tag{2.6.2}$$

for electrons, and

$$\partial_t \rho_i + \boldsymbol{\partial}_{\boldsymbol{x}} \cdot (\rho_i \boldsymbol{v}_h + \rho_i \boldsymbol{\mathcal{V}}_i) = \mathfrak{m}_i \mathfrak{w}_i, \qquad i \in \mathfrak{H}, \tag{2.6.3}$$

$$\partial_t (\rho_h \boldsymbol{v}_h) + \boldsymbol{\partial}_{\boldsymbol{x}} \cdot (\rho_h \boldsymbol{v}_h \otimes \boldsymbol{v}_h + p\, \mathbb{I}) = -\boldsymbol{\partial}_{\boldsymbol{x}} \cdot \boldsymbol{\Pi}_h + nq\mathbf{E} + \boldsymbol{j} \wedge \mathbf{B}, \tag{2.6.4}$$

$$\partial_t \mathcal{E}_h + \boldsymbol{\partial}_{\boldsymbol{x}} \cdot (\mathcal{E}_h \boldsymbol{v}_h) = -p_h\, \boldsymbol{\partial}_{\boldsymbol{x}} \cdot \boldsymbol{v}_h - \boldsymbol{\partial}_{\boldsymbol{x}} \boldsymbol{v}_h : \boldsymbol{\Pi}_h - \boldsymbol{\partial}_{\boldsymbol{x}} \cdot \boldsymbol{\mathcal{Q}}_h + \Delta E_{he} + \boldsymbol{J}_h \cdot \mathbf{E}', \tag{2.6.5}$$

for the heavy species.

The electron diffusion velocity in the heavy-species reference frame is given by

$$\boldsymbol{\mathcal{V}}_e = \boldsymbol{\mathcal{V}}_e^0 + \boldsymbol{\mathcal{V}}_e^1, \tag{2.6.6}$$

the electron heat flux in the heavy-species reference frame by

$$\boldsymbol{\mathcal{Q}}_e = \boldsymbol{\mathcal{Q}}_e^0 + \boldsymbol{\mathcal{Q}}_e^1, \tag{2.6.7}$$

and the electron conduction current density in the heavy-species reference frame by

$$\boldsymbol{J}_e = \boldsymbol{J}_e^0 + \boldsymbol{J}_e^1 = n_e q_e \boldsymbol{\mathcal{V}}_e. \tag{2.6.8}$$

We also introduce the heat flux

$$\boldsymbol{\mathcal{Q}} = \boldsymbol{\mathcal{Q}}_e + \boldsymbol{\mathcal{Q}}_h, \tag{2.6.9}$$

and conduction current of the mixture

$$\boldsymbol{J} = \boldsymbol{J}_e + \boldsymbol{J}_h = n_e q_e \boldsymbol{\mathcal{V}}_e + \sum_{j \in \mathfrak{H}} n_j q_j \boldsymbol{\mathcal{V}}_j, \tag{2.6.10}$$

and the energy exchange terms

$$\Delta E_{eh} = \Delta E_{eh}^0 + \Delta E_{eh}^1, \tag{2.6.11}$$

$$\Delta E_{he} = \Delta E_{he}^0 + \Delta E_{he}^1, \tag{2.6.12}$$

which satisfy the reciprocity relation

$$\Delta E_{he} = -\Delta E_{eh}. \tag{2.6.13}$$

We also restate the expressions for the zeroth-order and first-order current densities of the mixture in the inertial reference frame

$$\boldsymbol{j}^0 = n_h q_h \boldsymbol{v}_h + n_e q_e (\boldsymbol{v}_h + \boldsymbol{\mathcal{V}}_e^0), \tag{2.6.14}$$

$$\boldsymbol{j}^1 = n_h q_h \boldsymbol{v}_h + \sum_{j \in \mathfrak{H}} n_j q_j \boldsymbol{\mathcal{V}}_j + n_e q_e (\boldsymbol{v}_h + \boldsymbol{\mathcal{V}}_e^0 + \boldsymbol{\mathcal{V}}_e^1), \tag{2.6.15}$$

and denote by

$$\boldsymbol{j} = \delta_{b0} \boldsymbol{j}^0 + \delta_{b1} \boldsymbol{j}^1 \tag{2.6.16}$$

the current density of the mixture in the inertial reference frame.

From equations (2.5.67)-(2.5.70), the heavy species diffusion velocities satisfy the mass conservation constraint

$$\sum_{i \in \mathfrak{H}} \rho_i \boldsymbol{\mathcal{V}}_i = 0, \tag{2.6.17}$$

so that summing equation (2.6.3) over $i \in \mathfrak{H}$, the equation for conservation of the heavy-species mass is obtained

$$\partial_t \rho_h + \boldsymbol{\partial}_{\boldsymbol{x}} \cdot (\rho_h \boldsymbol{v}_h) = \sum_{i \in \mathfrak{H}} \mathfrak{m}_i \mathfrak{w}_i. \tag{2.6.18}$$

Since the total mass is conserved in reactive collisions, the conservation constraint

$$\mathfrak{m}_e \mathfrak{w}_e + \sum_{i \in \mathfrak{H}} \mathfrak{m}_i \mathfrak{w}_i = 0 \tag{2.6.19}$$

is satisfied. Thus, the total mass conservation equation is obtained by summing (2.6.1) and (2.6.18), and reads

$$\partial_t \rho + \boldsymbol{\partial}_{\boldsymbol{x}} \cdot (\rho \boldsymbol{v}) = 0, \tag{2.6.20}$$

where

$$\rho = \rho_e + \rho_h \tag{2.6.21}$$

is the mass density of the mixture, and the mixture-averaged velocity $\boldsymbol{v}$ is given by

$$\rho \boldsymbol{v} = \rho_e \boldsymbol{v}_e + \rho_h \boldsymbol{v}_h = \rho \boldsymbol{v}_h + \rho_e \boldsymbol{\mathcal{V}}_e, \tag{2.6.22}$$

where the mean electron velocity in the inertial reference frame reads

$$\boldsymbol{v}_e = \boldsymbol{v}_h + \boldsymbol{\mathcal{V}}_e. \tag{2.6.23}$$

The electron momentum relation (2.4.142) is also rewritten in the form

$$\boldsymbol{\partial}_{\boldsymbol{x}} p_e = n_e q_e \mathbf{E} + \boldsymbol{j}_e^0 \wedge \mathbf{B} + \delta_{b1}\, \boldsymbol{J}_e^1 \wedge \mathbf{B} + \boldsymbol{F}_{eh}, \tag{2.6.24}$$

where $\boldsymbol{F}_{eh} = -\boldsymbol{F}_{he}$ is the average force exerted on electrons by the heavy species:

$$\boldsymbol{F}_{eh} = \boldsymbol{F}_{eh}^0 + \boldsymbol{F}_{eh}^1. \tag{2.6.25}$$

Finally, summing equations (2.6.2) and (2.6.5), we obtain the following equation for conservation of the total internal energy $\mathcal{E} = \mathcal{E}_e + \mathcal{E}_h$:

$$\partial_t \mathcal{E} + \boldsymbol{\partial}_{\boldsymbol{x}} \cdot (\mathcal{E} \boldsymbol{v}_h) = -\, p\, \boldsymbol{\partial}_{\boldsymbol{x}} \cdot \boldsymbol{v}_h - \boldsymbol{\partial}_{\boldsymbol{x}} \boldsymbol{v}_h : \boldsymbol{\Pi}_h - \boldsymbol{\partial}_{\boldsymbol{x}} \cdot \boldsymbol{\mathcal{Q}} + \boldsymbol{J} \cdot \mathbf{E}' + \delta_{b0}\, \boldsymbol{J}_e^0 \cdot (\boldsymbol{v}_h \wedge \mathbf{B}). \tag{2.6.26}$$

2.6.2 Transport fluxes

The electron diffusion velocity is obtained from (2.5.15) and (2.5.107) in the form

$$\begin{aligned} \boldsymbol{\mathcal{V}}_e = &- D_{ee} \hat{\boldsymbol{d}}_e - \sum_{i \in \mathfrak{H}} D_{ei} \hat{\boldsymbol{d}}_i - \theta_{ee} \boldsymbol{\partial}_{\boldsymbol{x}} \ln T_e - \theta_{eh} \boldsymbol{\partial}_{\boldsymbol{x}} \ln T_h \\ &- \left[D_{ee}^{\kappa_h}\, (\boldsymbol{\partial}_{\boldsymbol{x}} \cdot \boldsymbol{v}_h) + D_{ee}^{\Theta}\, (T_e - T_h) \right] \hat{\boldsymbol{d}}_e - \left[\theta_{ee}^{\kappa_h}\, (\boldsymbol{\partial}_{\boldsymbol{x}} \cdot \boldsymbol{v}_h) + \theta_{ee}^{\Theta}\, (T_e - T_h) \right] \boldsymbol{\partial}_{\boldsymbol{x}} \ln T_e \\ &- \delta_{b0} \frac{n_e q_e |\mathbf{B}|}{p} D_{ee}^0\, \boldsymbol{\mathscr{B}} \wedge \boldsymbol{v}_h - \delta_{b0} D_{ee}^{\odot}\, \boldsymbol{\mathscr{B}} \wedge \hat{\boldsymbol{d}}_e - \delta_{b0} \theta_{ee}^{\odot}\, \boldsymbol{\mathscr{B}} \wedge \boldsymbol{\partial}_{\boldsymbol{x}} \ln T_e, \end{aligned} \tag{2.6.27}$$

where the electron self-diffusion coefficient and the electron electron-temperature thermal diffusion coefficient read

$$D_{ee} = D_{ee}^0 + D_{ee}^1, \tag{2.6.28}$$

$$\theta_{ee} = \theta_{ee}^0 + \theta_{ee}^1, \tag{2.6.29}$$

and the unconstrained diffusion driving force read

$$\hat{\boldsymbol{d}}_e = \frac{1}{p} (\boldsymbol{\partial}_{\boldsymbol{x}} p_e - n_e q_e \mathbf{E}), \tag{2.6.30}$$

$$\hat{\boldsymbol{d}}_i = \frac{1}{p} (\boldsymbol{\partial}_{\boldsymbol{x}} p_i - n_i q_i \mathbf{E}), \quad i \in \mathfrak{H}. \tag{2.6.31}$$

Similarly, the electron self-partial-thermal-conductivity is given by

$$\hat{\lambda}_{ee} = \hat{\lambda}^0_{ee} + \hat{\lambda}^1_{ee}, \tag{2.6.32}$$

and from (2.5.18) and (2.5.108) the electron heat flux thus reads

$$\begin{aligned}\boldsymbol{\mathcal{Q}}_e =& - p\theta_{ee}\hat{\boldsymbol{d}}_e - p\sum_{i\in\mathfrak{H}}\theta_{ei}\hat{\boldsymbol{d}}_i - \hat{\lambda}_{ee}\boldsymbol{\partial}_{\boldsymbol{x}}T_e - \hat{\lambda}_{eh}\boldsymbol{\partial}_{\boldsymbol{x}}T_h + n_e\Big(\frac{5}{2}k_{\text{B}}T_e\Big)\boldsymbol{\mathcal{V}}_e \\ & - p\big[\theta^{\kappa_h}_{ee}\ (\boldsymbol{\partial}_{\boldsymbol{x}}\cdot\boldsymbol{v}_h) + \theta^{\Theta}_{ee}\ (T_e - T_h)\big]\ \hat{\boldsymbol{d}}_e - \big[\hat{\lambda}^{\kappa_h}_{ee}\ (\boldsymbol{\partial}_{\boldsymbol{x}}\cdot\boldsymbol{v}_h) + \hat{\lambda}^{\Theta}_{ee}\ (T_e - T_h)\big]\ \boldsymbol{\partial}_{\boldsymbol{x}}T_e \\ & - \delta_{b0}n_eq_e|\mathbf{B}|\theta^0_{ee}\ \boldsymbol{\mathscr{B}}\wedge\boldsymbol{v}_h - \delta_{b0}p\theta^{\odot}_{ee}\ \boldsymbol{\mathscr{B}}\wedge\hat{\boldsymbol{d}}_e - \delta_{b0}\hat{\lambda}^{\odot}_e\ \boldsymbol{\mathscr{B}}\wedge\boldsymbol{\partial}_{\boldsymbol{x}}T_e.\end{aligned} \tag{2.6.33}$$

The heavy-species diffusion velocities, viscous tensor and heat flux where stated in (2.5.46), (2.5.51) and (2.5.55), respectively. We recall here their expressions

$$\boldsymbol{\mathcal{V}}_i = -\sum_{j\in\mathfrak{H}} D_{ij}\hat{\boldsymbol{d}}_j - D_{ie}\hat{\boldsymbol{d}}_e - \theta_{ih}\boldsymbol{\partial}_{\boldsymbol{x}}\ln T_h - \theta_{ie}\boldsymbol{\partial}_{\boldsymbol{x}}\ln T_e, \quad i\in\mathfrak{H}, \tag{2.6.34}$$

$$\boldsymbol{\Pi}_h = -\eta_h\Big(\boldsymbol{\partial}_{\boldsymbol{x}}\boldsymbol{v}_h + (\boldsymbol{\partial}_{\boldsymbol{x}}\boldsymbol{v}_h)^{\text{T}} - \frac{2}{3}(\boldsymbol{\partial}_{\boldsymbol{x}}\cdot\boldsymbol{v}_h)\,\mathbb{I}\Big) - \kappa_h(\boldsymbol{\partial}_{\boldsymbol{x}}\cdot\boldsymbol{v}_h)\,\mathbb{I} - \zeta(T_e - T_h)\,\mathbb{I}, \tag{2.6.35}$$

$$\boldsymbol{\mathcal{Q}}_h = -p\sum_{j\in\mathfrak{H}}\theta_{hj}\hat{\boldsymbol{d}}_j - p\theta_{he}\hat{\boldsymbol{d}}_e - \hat{\lambda}_{hh}\boldsymbol{\partial}_{\boldsymbol{x}}T_h - \hat{\lambda}_{he}\boldsymbol{\partial}_{\boldsymbol{x}}T_e + \sum_{j\in\mathfrak{H}}\big(\frac{5}{2}k_{\text{B}}T_h + \overline{E}_j\big)n_j\boldsymbol{\mathcal{V}}_j. \tag{2.6.36}$$

2.7 Center-of-Mass Reference Frame

The conservation equations may be rewritten in the center-of-mass reference frame. From the definition (2.6.22) of $\boldsymbol{v}$, the heavy-species velocity reads

$$\boldsymbol{v}_h = \boldsymbol{v} - Y_e\boldsymbol{\mathcal{V}}_e, \tag{2.7.1}$$

where $Y_e = \rho_e/\rho$ is the electron mass fraction. Equations (2.6.1) and (2.6.3) expressing the mass conservation of the respective species thus read in the center-of-mass reference frame

$$\partial_t\rho_e + \boldsymbol{\partial}_{\boldsymbol{x}}\cdot\big(\rho_e\boldsymbol{v} + \rho_e\boldsymbol{\mathcal{V}}^{\boldsymbol{v}}_e\big) = \mathfrak{m}_e\mathfrak{w}_e, \tag{2.7.2}$$

$$\partial_t\rho_i + \boldsymbol{\partial}_{\boldsymbol{x}}\cdot\big(\rho_i\boldsymbol{v} + \rho_i\boldsymbol{\mathcal{V}}^{\boldsymbol{v}}_i\big) = \mathfrak{m}_i\mathfrak{w}_i, \qquad i\in\mathfrak{H}. \tag{2.7.3}$$

where $\boldsymbol{\mathcal{V}}^{\boldsymbol{v}}_e$ and $\boldsymbol{\mathcal{V}}^{\boldsymbol{v}}_i$, $i\in\mathfrak{H}$, are the species diffusion velocities in the center-of-mass reference frame:

$$\boldsymbol{\mathcal{V}}^{\boldsymbol{v}}_e = (1 - Y_e)\boldsymbol{\mathcal{V}}_e \tag{2.7.4}$$

$$\boldsymbol{\mathcal{V}}^{\boldsymbol{v}}_i = \boldsymbol{\mathcal{V}}_i - Y_e\boldsymbol{\mathcal{V}}_e, \quad i\in\mathfrak{H}. \tag{2.7.5}$$

The macroscopic equations (2.6.1)-(2.6.5) read in the center-of-mass reference frame

$$\partial_t\rho_e + \boldsymbol{\partial}_{\boldsymbol{x}}\cdot\big(\rho_e\boldsymbol{v} + \rho_e(1 - Y_e)\boldsymbol{\mathcal{V}}_e\big) = \mathfrak{m}_e\mathfrak{w}_e, \tag{2.7.6}$$

$$\begin{aligned}\partial_t\mathcal{E}_e + \boldsymbol{\partial}_{\boldsymbol{x}}\cdot\big(\mathcal{E}_e(\boldsymbol{v} - Y_e\boldsymbol{\mathcal{V}}_e)\big) =& - p_e\,\boldsymbol{\partial}_{\boldsymbol{x}}\cdot(\boldsymbol{v} - Y_e\boldsymbol{\mathcal{V}}_e) - \boldsymbol{\partial}_{\boldsymbol{x}}\cdot\boldsymbol{\mathcal{Q}}_e + \Delta E_{eh} + \boldsymbol{J}_e\cdot\mathbf{E}' \\ & + \delta_{b0}\,\boldsymbol{J}^0_e\cdot\big((\boldsymbol{v} - Y_e\boldsymbol{\mathcal{V}}_e)\wedge\mathbf{B}\big),\end{aligned} \tag{2.7.7}$$

for electrons, and

$$\partial_t\rho_i + \boldsymbol{\partial}_{\boldsymbol{x}}\cdot\big(\rho_i\boldsymbol{v} + \rho_i(\boldsymbol{\mathcal{V}}_i - Y_e\boldsymbol{\mathcal{V}}_e)\big) = \mathfrak{m}_i\mathfrak{w}_i, \qquad i\in\mathfrak{H}, \tag{2.7.8}$$

$$\begin{aligned}\partial_t\big(\rho(1 - Y_e)(\boldsymbol{v} - Y_e\boldsymbol{\mathcal{V}}_e)\big) + \boldsymbol{\partial}_{\boldsymbol{x}}\cdot\big(\rho(1 - Y_e)(\boldsymbol{v} - Y_e\boldsymbol{\mathcal{V}}_e)\otimes(\boldsymbol{v} - Y_e\boldsymbol{\mathcal{V}}_e) + p\,\mathbb{I}\big) \\ = -\,\boldsymbol{\partial}_{\boldsymbol{x}}\cdot\boldsymbol{\Pi}_h + nq\mathbf{E} + \boldsymbol{j}\wedge\mathbf{B},\end{aligned} \tag{2.7.9}$$

$$\begin{aligned}\partial_t\mathcal{E}_h + \boldsymbol{\partial}_{\boldsymbol{x}}\cdot\big(\mathcal{E}_h(\boldsymbol{v} - Y_e\boldsymbol{\mathcal{V}}_e)\big) =& -p_h\,\boldsymbol{\partial}_{\boldsymbol{x}}\cdot(\boldsymbol{v} - Y_e\boldsymbol{\mathcal{V}}_e) - \boldsymbol{\partial}_{\boldsymbol{x}}(\boldsymbol{v} - Y_e\boldsymbol{\mathcal{V}}_e) : \boldsymbol{\Pi}_h \\ & - \boldsymbol{\partial}_{\boldsymbol{x}}\cdot\boldsymbol{\mathcal{Q}}_h + \Delta E_{he} + \boldsymbol{J}_h\cdot\mathbf{E}',\end{aligned} \tag{2.7.10}$$

for the heavy species.

Given that Y_e is of order ε^2, the latter model is equivalent at first-order in ε to the following one:

$$\partial_t \rho_e + \boldsymbol{\partial_x} \cdot \big(\rho_e \boldsymbol{v} + \rho_e \boldsymbol{\mathcal{V}}_e^{\boldsymbol{v}}\big) = \mathfrak{m}_e \mathfrak{w}_e, \tag{2.7.11}$$

$$\partial_t \mathcal{E}_e + \boldsymbol{\partial_x} \cdot (\mathcal{E}_e \boldsymbol{v}) = -\, p_e\, \boldsymbol{\partial_x} \cdot \boldsymbol{v} - \boldsymbol{\partial_x} \cdot \boldsymbol{\mathcal{Q}}_e^{\boldsymbol{v}} + \Delta E_{eh} + \boldsymbol{J}_e^{\boldsymbol{v}} \cdot \mathbf{E}' + \, \delta_{b0}\, \boldsymbol{J}_e^0 \cdot (\boldsymbol{v} \wedge \mathbf{B}), \tag{2.7.12}$$

$$\partial_t \rho_i + \boldsymbol{\partial_x} \cdot \big(\rho_i \boldsymbol{v} + \rho_i \boldsymbol{\mathcal{V}}_i^{\boldsymbol{v}}\big) = \mathfrak{m}_i \mathfrak{w}_i, \qquad i \in \mathfrak{H}, \tag{2.7.13}$$

$$\partial_t (\rho \boldsymbol{v}) + \boldsymbol{\partial_x} \cdot (\rho \boldsymbol{v} \otimes \boldsymbol{v} + p\, \mathbb{I}) = -\, \boldsymbol{\partial_x} \cdot \boldsymbol{\Pi} + nq\mathbf{E} + \boldsymbol{j} \wedge \mathbf{B}, \tag{2.7.14}$$

$$\partial_t \mathcal{E}_h + \boldsymbol{\partial_x} \cdot (\mathcal{E}_h \boldsymbol{v}) = -p_h\, \boldsymbol{\partial_x} \cdot \boldsymbol{v} - \boldsymbol{\partial_x} \boldsymbol{v} : \boldsymbol{\Pi} - \, \boldsymbol{\partial_x} \cdot \boldsymbol{\mathcal{Q}}_h^{\boldsymbol{v}} + \Delta E_{he} + \boldsymbol{J}_h \cdot \mathbf{E}', \tag{2.7.15}$$

where the species diffusion velocities in the center-of-mass reference frame have been taken such as to satisfy the mass conservation constraint

$$\sum_{k \in \mathfrak{S}} \rho_k \boldsymbol{\mathcal{V}}_k^{\boldsymbol{v}} = \rho_e \boldsymbol{\mathcal{V}}_e^{\boldsymbol{v}} + \sum_{i \in \mathfrak{H}} \rho_i \boldsymbol{\mathcal{V}}_i^{\boldsymbol{v}} = 0. \tag{2.7.16}$$

The viscous tensor may be written in the form

$$\boldsymbol{\Pi} = -\eta_h \Big(\boldsymbol{\partial_x} \boldsymbol{v} + (\boldsymbol{\partial_x} \boldsymbol{v})^{\mathrm{T}} - \frac{2}{3} (\boldsymbol{\partial_x} \cdot \boldsymbol{v})\, \mathbb{I} \Big) - \kappa_h (\boldsymbol{\partial_x} \cdot \boldsymbol{v})\, \mathbb{I} - \zeta (T_e - T_h)\, \mathbb{I}, \tag{2.7.17}$$

the electron diffusion velocity and heat flux in the center-of-mass reference frame in the form

$$\begin{aligned} \boldsymbol{\mathcal{V}}_e^{\boldsymbol{v}} = &- D_{ee}^{\boldsymbol{v}} \hat{\boldsymbol{d}}_e - \sum_{i \in \mathfrak{H}} D_{ei}^{\boldsymbol{v}} \hat{\boldsymbol{d}}_i - \theta_{ee}^{\boldsymbol{v}} \boldsymbol{\partial_x} \ln T_e - \theta_{eh}^{\boldsymbol{v}} \boldsymbol{\partial_x} \ln T_h \\ &- (1 - Y_e) \big[D_{ee}^{\kappa_h}\, (\boldsymbol{\partial_x} \cdot \boldsymbol{v}) + D_{ee}^{\Theta}\, (T_e - T_h) \big]\, \hat{\boldsymbol{d}}_e \\ &- (1 - Y_e) \big[\theta_{ee}^{\kappa_h}\, (\boldsymbol{\partial_x} \cdot \boldsymbol{v}) + \theta_{ee}^{\Theta}\, (T_e - T_h) \big]\, \boldsymbol{\partial_x} \ln T_e \\ &- \delta_{b0} (1 - Y_e) \frac{n_e q_e |\mathbf{B}|}{p} D_{ee}^0\, \boldsymbol{\mathcal{B}} \wedge \boldsymbol{v} - \delta_{b0} (1 - Y_e) D_{ee}^{\odot}\, \boldsymbol{\mathcal{B}} \wedge \hat{\boldsymbol{d}}_e \\ &- \delta_{b0} (1 - Y_e) \theta_{ee}^{\odot}\, \boldsymbol{\mathcal{B}} \wedge \boldsymbol{\partial_x} \ln T_e, \end{aligned} \tag{2.7.18}$$

$$\begin{aligned} \boldsymbol{\mathcal{Q}}_e^{\boldsymbol{v}} = &- p \theta_{ee}^{\boldsymbol{v}} \hat{\boldsymbol{d}}_e - p \sum_{i \in \mathfrak{H}} \theta_{ei}^{\boldsymbol{v}} \hat{\boldsymbol{d}}_i - \hat{\lambda}_{ee} \boldsymbol{\partial_x} T_e - \hat{\lambda}_{eh} \boldsymbol{\partial_x} T_h + n_e \Big(\frac{5}{2} k_{\mathrm{B}} T_e \Big) \boldsymbol{\mathcal{V}}_e^{\boldsymbol{v}} \\ &- p \big[\theta_{ee}^{\kappa_h}\, (\boldsymbol{\partial_x} \cdot \boldsymbol{v}) + \theta_{ee}^{\Theta}\, (T_e - T_h) \big]\, \hat{\boldsymbol{d}}_e - \big[\hat{\lambda}_{ee}^{\kappa_h}\, (\boldsymbol{\partial_x} \cdot \boldsymbol{v}) + \hat{\lambda}_{ee}^{\Theta}\, (T_e - T_h) \big]\, \boldsymbol{\partial_x} T_e \\ &- \delta_{b0} n_e q_e |\mathbf{B}| \theta_{ee}^0\, \boldsymbol{\mathcal{B}} \wedge \boldsymbol{v} - \delta_{b0} p \theta_{ee}^{\odot}\, \boldsymbol{\mathcal{B}} \wedge \hat{\boldsymbol{d}}_e - \delta_{b0} \hat{\lambda}_e^{\odot}\, \boldsymbol{\mathcal{B}} \wedge \boldsymbol{\partial_x} T_e, \end{aligned} \tag{2.7.19}$$

respectively, and the heavy-species diffusion velocities and heat flux in the form

$$\begin{aligned} \boldsymbol{\mathcal{V}}_i^{\boldsymbol{v}} = &- \sum_{j \in \mathfrak{H}} D_{ij}^{\boldsymbol{v}} \hat{\boldsymbol{d}}_j - D_{ie}^{\boldsymbol{v}} \hat{\boldsymbol{d}}_e - \theta_{ih}^{\boldsymbol{v}} \boldsymbol{\partial_x} \ln T_h - \theta_{ie}^{\boldsymbol{v}} \boldsymbol{\partial_x} \ln T_e, \\ &+ Y_e \big[D_{ee}^{\kappa_h}\, (\boldsymbol{\partial_x} \cdot \boldsymbol{v}) + D_{ee}^{\Theta}\, (T_e - T_h) \big]\, \hat{\boldsymbol{d}}_e + Y_e \big[\theta_{ee}^{\kappa_h}\, (\boldsymbol{\partial_x} \cdot \boldsymbol{v}) + \theta_{ee}^{\Theta}\, (T_e - T_h) \big]\, \boldsymbol{\partial_x} \ln T_e \\ &+ \delta_{b0} Y_e \frac{n_e q_e |\mathbf{B}|}{p} D_{ee}^0\, \boldsymbol{\mathcal{B}} \wedge \boldsymbol{v} + \delta_{b0} Y_e D_{ee}^{\odot}\, \boldsymbol{\mathcal{B}} \wedge \hat{\boldsymbol{d}}_e + \delta_{b0} Y_e \theta_{ee}^{\odot}\, \boldsymbol{\mathcal{B}} \wedge \boldsymbol{\partial_x} \ln T_e, \quad i \in \mathfrak{H}, \end{aligned} \tag{2.7.20}$$

$$\boldsymbol{\mathcal{Q}}_h^{\boldsymbol{v}} = -p \sum_{j \in \mathfrak{H}} \theta_{hj}^{\boldsymbol{v}} \hat{\boldsymbol{d}}_j - p \theta_{he}^{\boldsymbol{v}} \hat{\boldsymbol{d}}_e - \hat{\lambda}_{hh} \boldsymbol{\partial_x} T_h - \hat{\lambda}_{he} \boldsymbol{\partial_x} T_e + \sum_{j \in \mathfrak{H}} \big(\frac{5}{2} k_{\mathrm{B}} T_h + \overline{E}_j \big) n_j \boldsymbol{\mathcal{V}}_j^{\boldsymbol{v}}. \tag{2.7.21}$$

The electron conduction current density in the center-of-mass reference frame may be written in the form

$$\boldsymbol{J}_e^{\boldsymbol{v}} = n_e q_e \boldsymbol{\mathcal{V}}_e^{\boldsymbol{v}}, \tag{2.7.22}$$

and the current density in the form

$$\boldsymbol{j} = \delta_{b0}\boldsymbol{j}^0 + \delta_{b1}\boldsymbol{j}^1, \tag{2.7.23}$$

where

$$\boldsymbol{j}^0 = nq\boldsymbol{v} + n_e q_e \boldsymbol{\mathcal{V}}_e^0, \tag{2.7.24}$$

$$\boldsymbol{j}^1 = nq\boldsymbol{v} + n_e q_e \boldsymbol{\mathcal{V}}_e^{\boldsymbol{v}} + \sum_{i\in\mathfrak{H}} n_i q_i \boldsymbol{\mathcal{V}}_i^{\boldsymbol{v}}. \tag{2.7.25}$$

The diffusion coefficients $D_{ee}^{\boldsymbol{v}}$, $D_{ei}^{\boldsymbol{v}}$, $i \in \mathfrak{H}$, $D_{ie}^{\boldsymbol{v}}$, $i \in \mathfrak{H}$, and $D_{ij}^{\boldsymbol{v}}$, $i, j \in \mathfrak{H}$, may be expressed in the form

$$D_{ee}^{\boldsymbol{v}} = (1 - Y_e)D_{ee}, \tag{2.7.26}$$

$$D_{ei}^{\boldsymbol{v}} = (1 - Y_e)D_{ei}, \quad i \in \mathfrak{H}, \tag{2.7.27}$$

$$D_{ie}^{\boldsymbol{v}} = D_{ie} - Y_e D_{ee}, \quad i \in \mathfrak{H}, \tag{2.7.28}$$

$$D_{ij}^{\boldsymbol{v}} = D_{ij} - Y_e D_{ej}, \quad i, j \in \mathfrak{H}, \tag{2.7.29}$$

and the thermal diffusion coefficients $\theta_{ee}^{\boldsymbol{v}}$, $\theta_{eh}^{\boldsymbol{v}}$, $\theta_{ie}^{\boldsymbol{v}}$, $i \in \mathfrak{H}$, $\theta_{ih}^{\boldsymbol{v}}$, $i \in \mathfrak{H}$, may be expressed in the form

$$\theta_{ee}^{\boldsymbol{v}} = (1 - Y_e)\theta_{ee}, \tag{2.7.30}$$

$$\theta_{eh}^{\boldsymbol{v}} = \theta_{he}^{\boldsymbol{v}} = (1 - Y_e)\theta_{eh}, \tag{2.7.31}$$

$$\theta_{ie}^{\boldsymbol{v}} = \theta_{ei}^{\boldsymbol{v}} = \theta_{ie} - Y_e\theta_{ee}, \quad i \in \mathfrak{H}, \tag{2.7.32}$$

$$\theta_{ih}^{\boldsymbol{v}} = \theta_{hi}^{\boldsymbol{v}} = \theta_{ih} - Y_e\theta_{eh}, \quad i \in \mathfrak{H}. \tag{2.7.33}$$

However, one can see from expressions (2.7.26)-(2.7.29) that the diffusion matrix associated with the center-of-mass reference frame $(D_{kl}^{\boldsymbol{v}})_{k,l\in\mathfrak{S}}$ is not symmetric, and neither is the heavy-species diffusion matrix $(D_{ij}^{\boldsymbol{v}})_{i,j\in\mathfrak{H}}$. This confirms that the center-of-mass reference frame is not adapted to the study of non-thermal multicomponent plasmas [GMM09].

2.8 Conclusion

We have derived from the kinetic theory a unified multicomponent fluid model for non-thermal, partially ionized, polyatomic, chemically reactive plasmas. We have applied the classical Chapman-Enskog procedure, upon expanding the species distribution functions in powers of ε, where the ratio ε of characteristic masses was assumed to be proportional to the Knudsen number. For the scaling adopted here, the equilibrium distribution functions are shown to be Maxwellian, with a different temperature for electrons and heavy species. We retrieve the zeroth-order and first-order drift-diffusion equations for the electrons, while the macroscopic equations for the heavy species are the Euler equations at order zero, and the Navier-Stokes-Fourier equations at order one. Those equations involve transport fluxes, which are expressed in terms of macroscopic variable gradients and source terms, by means of transport coefficients.

The inelastic scattering cross-section between electrons and heavy species was assumed to be two order of magnitude lower than other relevant scattering cross-sections: $\sigma_h^{\mathrm{in},0} = \varepsilon^2\sigma^0$. Other things being equal, it was shown that this assumption is necessary to ensure that the electron and heavy-species respective temperatures, T_e and T_h, are distinct. In a future study, an alternative scaling will be investigated where the assumptions over the inelastic scattering cross-section between electrons and heavy species are relaxed. For such a new scaling, we expect some of the internal energy states,

or internal modes, of the heavy species to thermalize at T_e, while the others will thermalize at T_h. The Chapman-Enskog expansion will thus require a splitting between the internal energy modes of the heavy-species. Typically, we may assume that vibrational modes are at equilibrium between them at $T_{\text{vib}} = T_e$, while rotational and translational modes thermalize at $T_{\text{rot}} = T_h$.

The expressions of the transport fluxes for polyatomic plasmas have been derived in the weakly-magnetized case. The structure of the macroscopic "Navier-Stokes type" equations and associated transport fluxes are similar to the monoatomic case treated in [GMM09], though expressions of transport coefficients now involve summations over the internal energy states of the heavy species. Additional terms in the electron second-order transport fluxes have been derived, associated with the interaction between the thermal non-equilibrium and the volume viscosity with the electron diffusion driving force and the electron temperature gradient. In the weakly-magnetized regime, the electron diffusion velocity and heat flux involve transverse driving forces. In a future study, the strongly-magnetized case will be investigated. In this regime, the electron transport fluxes exhibit an anisotropic behaviour with respect to the direction of the magnetic field [GG09] [GGMM10].

The derivation should also be completed with the investigation of the mathematical structure of the macroscopic equations and of the transport linear systems obtained. In particular, the entropy conservation equation must be derived, and the sign of the entropy production rate must be ascertained. Indeed, a positive entropy structure is desirable for numerical stability [Bob82] [Tor16]. Besides, the numerical computation of the transport coefficients derived above, in particular of the electron zeroth-order and first-order diffusion coefficients, should be carried out and compared to both experimental and numerical values, when accessible [EG94] [GGMM10]. Such a calculation will require data for the various collision integrals involved.

The set of equations derived in this chapter, and associated expressions for transport fluxes, are a sound basis for the numerical modeling of non-thermal plasmas. Indeed, the first-order Chapman-Enskog expansion for multicomponent gas mixtures is retrieved in the limit where $T_e = T_h$ [GGMM10]. Also, as will be seen in Chapter 4, the model derived above from the kinetic theory encompasses almost all previously existing fluid radio-frequency plasma models.

Bibliography

[ACG94] B. V. Alexeev, A. Chikhaoui, and I. T. Grushin. Application of the generalized Chapman-Enskog method to the transport-coefficient calculation in a reacting gas mixture. *Physical Review E*, 49(4):2809–2825, 1994. 11, 14, 15, 17, 18

[Bob82] A. V. Bobylev. The chapman-enskog and grad methods for solving the boltzmann equation. *Sov. Phys. Dokl.*, 27:29–31, 1982. 11, 69

[CC70] S. Chapman and T. G. Cowling. *The Mathematical Theory of Non-Uniform Gases.* Cambridge University Press, Cambridge, 1970. 5, 11, 12, 14, 18, 20, 21, 32, 33, 47, 82, 88, 111, 118, 145, 153

[CH49] C. F. Curtiss and J. O. Hirschfelder. Transport properties of multicomponent gas mixtures. *The Journal of Chemical Physics*, 17(6):550–555, 1949. 11

[Cha16] S. Chapman. The kinetic theory of simple and composite monoatomic gases: Viscosity, thermal conduction, and diffusion. *Proceedings of the Royal Society A*, 93(646):1–20, 1916. 11

[Deg07] P. Degond. Asymptotic continuum models for plasmas and disparate mass gaseous binary mixtures. In *Material Substructures in Complex Bodies: from Atomic Level to Continuum*, chapter 1, pages 1–62. Elsevier, 2007. 12

[DLD96] P. Degond and B. Lucquin-Desreux. Transport coefficients of plasmas and disparate mass binary gases. *Transport Theory and Statistical Physics*, 25(6):595–633, 1996. 12, 32

[DP75] J.-S. Darrozes and J.-P. Petit. Une nouvelle formulation des équations du mouvement d'un gaz ionisé dans un régime dominé par les collisions. *J. Méc*, 14(745), 1975. 5, 12, 20, 21

[EG94] A. Ern and V. Giovangigli. *Multicomponent Transport Algorithms*, volume m24 of *Lecture Notes in Physics Monographs*. Springer-Verlag, Berlin, 1994. 11, 17, 19, 69, 75, 79, 80, 82, 83, 88, 89, 90, 91, 110

[Ens17] D. Enskog. *Kinetische Theorie der Vorgänge in mässig verdünnten Gasen*. PhD thesis, University of Uppsala, Sweden, 1917. 11

[FK72] J. H. Ferziger and H. G. Kaper. *Mathematical Theory of Transport Processes in Gases.* North-Holland Publishing Company, 1972. 11, 12, 14, 18, 20, 21, 32, 33, 47, 59, 82, 88, 118, 153

[GC02] D. Giordano and M. Capitelli. Nonuniqueness of the two-temperature Saha equation and related considerations. *Physical Review E.*, 65:016401, 2002. 51

[GG95] C. P. Grünfeld and E. Georgescu. On a class of kinetic equations for reacting gas mixtures. *Mat. Fiz., Analiz., Geom.*, 2:408–435, 1995. 11, 14, 15, 17, 18

[GG03] V. Giovangigli and B. Graille. Kinetic theory of partially ionized reactive gas mixtures. *Physica A*, 327:313–348, 2003. 5, 12, 40

[GG09] V. Giovangigli and B. Graille. The kinetic theory of partially ionized reactive gas mixtures II. *J. Phys. A: Math. Theor.*, 42, 2009. 12, 39, 52, 61, 69

[GGMM10] V. Giovangigli, B. Graille, T. E. Magin, and M. Massot. Multicomponent transport in weakly ionized mixtures. *Plasma Sources Sci. Technol.*, 19(3):034003, 2010. 5, 59, 69, 73

[Gio99] V. Giovangigli. *Multicomponent Flow Modeling*. MESST Series. Birkhauser, Boston, 1999. 5, 6, 13, 14, 15, 17, 18, 20, 32, 33, 47, 59, 73, 75, 76, 77, 79, 80, 82, 84, 85, 88, 89, 90, 92, 110, 111

[GMM08] B. Graille, T. E. Magin, and M. Massot. Modeling of reactive plasmas for atmospheric entry flows based on kinetic theory. In *Center for Turbulence Research: Proceedings of the 2008 Summer Program*, pages 17–28. Stanford University, 2008. 12, 51, 52

[GMM09] B. Graille, T. E. Magin, and M. Massot. Kinetic theory of plasmas: Translational energy. *M3AS*, 19(4):527–599, 2009. 5, 6, 12, 14, 15, 19, 20, 21, 22, 24, 28, 32, 33, 35, 40, 47, 52, 56, 59, 61, 62, 68, 69

[Gra58] H. Grad. Principles of the kinetic theory of gases. In *Handbuch der Physik*, volume 12, pages 205–294. Springer-Verlag, Berlin, S. Flügge edition, 1958. 11

[Gra04] B. Graille. *Modélisation de mélanges gazeux réactifs ionisés dissipatifs*. PhD thesis, Ecole Polytechnique, 2004. 19, 35, 39, 40, 55, 61

[Hag16a] G. J. M. Hagelaar. Coulomb collisions in the boltzmann equation for electrons in low-temperature gas discharge plasmas. *Plasma Sources Science and Technology*, 25:015015, 2016. 22

[Hag16b] G. J. M. Hagelaar. *Documentation of BOLSIG+*. Laboratoire Plasma et Conversion d'Energie (LAPLACE), Université Paul Sabatier, March 2016. 52, 111, 112

[HCB64] J. H. Hirschfelder, C. F. Curtiss, and R. B. Bird. *Molecular Theory of Gases and Liquids*. John Wiley and Sons, New York, 1964. corrected, with note added. 11

[Hel40] E. J. Hellund. Generalized theory of diffusion. *Physical Review*, 57(4):319, 1940. 11

[KA61] Yu. Kagan and A. M. Afanas'ev. On the kinetic theory of gases with rotational degrees of freedom. *J. Exptl. Theoret. Phys.*, 41:1536–1545, 1961. 19

[KNF+04] B. Kalache, T. Novikova, A. Fontcuberta i Morral, P. Roca i Cabarrocas, W. Morscheidt, and K. Hassouni. Investigation of coupling between chemistry and discharge dynamics in radio frequency hydrogen plasmas in the Torr regime. *Journal of Physics D: Applied Physics*, 37:1765–1773, 2004. 52, 114, 115, 116, 119

[Kol74] A. F. Kolesnikov. The equations of motion of a multicomponent partially ionized two-temperature mixture of gases in an electromagnetic field with transport coefficients in higher approximations. Technical Report 1556, Institute of Mechanics, Moscow State University, 1974. in Russian. 56, 62

[Kuš91] I. Kuščer. Dissociation and recombination in an inhomogeneous gas. *Physica A*, 176(3):542–556, 1991. 15

[LH60] G. Ludwig and M. Heil. Boundary layer theory with dissociation and ionization. In *Advances in Applied Mechanics*, volume 6, pages 39–118. Academic Press, New York, 1960. 11, 14, 17, 18

[Lor05] H. A. Lorentz. The motion of electrons in metallic bodies. In *Proc. Roy. Acad. Amsterdam*, volume 7, pages 438–453, 585–593, 684–691, 1905. 12, 111

[MD04] T. E. Magin and G. Degrez. Transport properties of partially ionized and unmagnetized plasmas. *Physical Review E*, 70(046412), 2004. 5, 12

[MGM09] T. E. Magin, B. Graille, and M. Massot. Thermo-chemical dynamics and chemical quasi-equilibrium of plasmas in thermal non-equilibrium. In *Center for Turbulence Research Annual Research Briefs*, pages 71–82. Stanford University, 2009. 12

[MYM63] L. Monchick, K. S. Yun, and E. A. Mason. Formal kinetic theory of transport phenomena in polyatomic gas mixtures. *Journal of Chemical Physics*, 39(3):654–669, 1963. 5, 11, 75, 90

[Nie98] J. Nienhuis. *Plasma Models for Silicon Deposition.* PhD thesis, FOM Institute for Plasma Physics Rijnhuizen, 1998. 52, 104, 116

[PX49] I. Prigogine and E. Xhrouet. On the perturbation of Maxwell distribution function by chemical reactions in gases. *Physica*, 15:913–932, 1949. 11

[Rax05] J.-M. Rax. *Physique des plasmas.* Dunod, Paris, 2005. 24

[ST07] H. Struchtrup and M. Torrilhon. H theorem, regularization, and boundary conditions for linearized 13 moment equations. *Physical Review Letters*, 99:014502, 2007. 11

[Str05] H. Struchtrup. *Macroscopic Transport Equations for Rarefied Gas Flows.* Springer-Verlag, Berlin, 2005. 11

[Tor12] M. Torrilhon. H-theorem for nonlinear regularized 13-moment equations in kinetic gas theory. *Kinetic and Related Models*, 5(1):185–201, 2012. 11

[Tor16] M. Torrilhon. Modeling nonequilibrium gas flow based on moment equations. *Annu. Rev. Fluid Mech.*, 48:429âĂŞ458, 2016. 11, 69

[TS04] M. Torrilhon and H. Struchtrup. Regularized 13-moment-equations: Shock structure calculations and comparison to Burnett models. *J. Fluid Mech.*, 513:171–198, 2004. 11

[vdSSP+89] M. C. M. van de Sanden, P. P. J. M. Schram, A. G. Peeters, J. A. M. van der Mullen, and G. M. W. Kroesen. Thermodynamic generalization of the Saha equation for a two-temperature plasma. *Physical Review A*, 40(9):5273–5276, November 1989. 51

[Wal58] L. Waldmann. Transporterscheinungen in Gasen von mittlerem Druck. In *Handbuch der Physik*, volume 12, pages 295–514. Springer-Verlag, Berlin, S. Flügge edition, 1958. 11, 13, 17, 18, 20, 39

[WCU51] C.S. Wang Chang and G.E. Uhlenbeck. Transport phenomena in polyatomic gases. Technical report, University of Michigan Engineering Research Institute, 1951. 11

[WT62] L. Waldmann and E. Trübenbacher. Formale kinetische Theorie von Gasgemischen aus anregbaren Molekülen. *Zeitschr. Naturforschg.*, 17a:363–376, 1962. 5, 11, 13, 17, 18, 75, 82

[Zhd02] V. M. Zhdanov. *Transport Processes in Multicomponent Plasma.* Taylor & Francis, 2002. 11

Chapter 3

Numerical Simulation of Silicon Chemical Vapor Deposition

3.1 Introduction

Numerical modeling of neutral chemically reacting flows in the laminar regime is now well understood and routinely employed in the study of several applications, among which stand out combustion and materials processing [KCG03]. Both fields share indeed many similarities in their formulation and numerical treatment, involving in particular complex chemistry, multicomponent transport processes, and fluid flow, with often strong couplings between them. A detailed presentation of possible applications and historical developments can be found in [Kle95] [KCG03] [PV05] [Smo13].

In this chapter, a fully coupled numerical model for silicon epitaxy by chemical vapor deposition (CVD) is implemented in a software and tested. We solve the equations describing a chemically reacting neutral gas mixture in an axisymmetric finite-gap stagnation flow configuration. The gas phase chemistry is fully coupled to the flow and transport properties of the mixture. An heterogeneous reaction mechanism accounts for the deposition process at the substrate boundary.

The primary goal of this chapter is notably to compare the numerical results obtained with the software to that of the literature in order to demonstrate the correctness of the numerical solution. Epitaxy by chemical vapor deposition (CVD) indeed provides a good benchmark model for this purpose. As can be seen from the results of Chapter 2, the fluid equations for a non-thermal multicomponent plasma exhibit the same structure as standard models of multicomponent reacting flows [Gio99] [KCG03] [GGMM10]. Besides, an axisymmetric geometry is commonly used for both kind of processes. In such a configuration, the process flow is a low Mach number laminar stagnation strained flow, and the corresponding equations can be simplified by a "boundary-layer-type" approximation.

The software is tested against the benchmark model developed by C. R. Kleijn [Kle00] for validation. The results obtained are in close agreement with this benchmark and the software is thus validated. This software will be enriched in Chapter 4 in order to model an axisymmetric plasma discharge reactor.

The reacting flows model employed in this chapter has been tested and validated in a number of practical applications. For instance, C. K. Law and coworkers have presented results of numerical simulation of purely strained planar premixed flames, which they compared to experimental measurements of the temperature, the fluid velocity, and the major species mole fractions [LSYA94]. Their results show an excellent agreement between the experimental data and the numerical simulations. Such a successful comparison with experiment notably requires high quality chemical reaction mechanism and multi-component transport data, accurate boundary conditions, and a carefully designed experiment. As far as chemical vapor deposition is concerned, comparison with experimental data is also more difficult, since deposition processes involved are complex and their description is

often only approximate. In particular, the surface reaction mechanism for chemical vapor deposition of silicon used in this Chapter assumes that the conditions of thermal epitaxy are satisfied. Besides, the gas-phase silane chemistry might lead to clustering reactions, which would require to take into account a more complex chemistry and possibly the presence of nanoparticles in the CVD reactor. *Therefore, the numerical validation of the software achieved in this chapter does not prejudge any confrontation with experimental data.*

The chemical vapor deposition reactor is presented in section 3.2. In section 3.3, the general conservation equations are stated. The thermodynamic properties are described in section 3.4, the gas-phase chemical reaction mechanism is detailed in section 3.5, and the transport fluxes are stated in section 3.6. Then, the low Mach number approximation is derived in section 3.7, yielding the isobaric equations. In section 3.8, the strained flow equations are obtained as exact self similar solutions of the isobaric equations. The transport coefficients are expressed in section 3.9, the boundary conditions in section 3.10, and the surface reaction mechanism is described in section 3.11. Finally, the numerical method is described in section 3.12. Results are presented and compared with the benchmark model [Kle00] in section 3.13.

3.2 Chemical Vapor Deposition Reactor

A CVD reactor is considered, a schematic representation of which is shown in Figure 3.1. The problem is axisymmetric around the z axis, with corresponding polar coordinates r and θ. The inlet gas mixture, namely silane highly diluted in helium, is injected at atmospheric pressure through a showerhead with a velocity parallel to the normal axis. The substrate is placed at the bottom of the reactor and is heated up to temperatures in the range 1,000-1,200 K. The silane molecules approaching the substrate are thus heated by thermal conduction, and consequently dissociate into several radical species, which in turn may react with each other, diffuse toward the substrate, and diffuse backwards in the upstream direction as well. For the process considered here, the silicon radicals impinging on the substrate induce the deposition of crystalline silicon, at a deposition rate of the order of one nanometer per second.

3.3 Conservation Equations

The mixture can be considered as neutral, and the electro-magnetic field vanishes. As a consequence, there are no electrons and the mixture is made only of heavy species. There is only one relevant temperature, denoted by

$$T = T_h, \tag{3.3.1}$$

the mixture-averaged velocity coincides with the heavy-species velocity

$$\boldsymbol{v} = \boldsymbol{v}_h, \tag{3.3.2}$$

the mass density of the mixture is $\rho = \rho_h$, the heavy-species partial pressure p_h is equal to the total pressure p, and the internal energy of the mixture coincides with the heavy-species internal energy $\mathcal{E} = \mathcal{E}_h$. As well, the viscous tensor $\boldsymbol{\Pi}$ and the heat flux $\boldsymbol{\mathcal{Q}}$ can be identified with the heavy-species viscous tensor $\boldsymbol{\Pi}_h$ and the heavy-species heat flux $\boldsymbol{\mathcal{Q}}_h$, respectively.

The conservation equations (2.6.1)-(2.6.5) derived in Chapter 2 are now rewritten accordingly, expressing the conservation of total mass

$$\partial_t \rho + \boldsymbol{\partial}_{\boldsymbol{x}} \cdot (\rho \boldsymbol{v}) = 0, \tag{3.3.3}$$

momentum

$$\partial_t (\rho \boldsymbol{v}) + \boldsymbol{\partial}_{\boldsymbol{x}} \cdot (\rho \boldsymbol{v} \otimes \boldsymbol{v} + p \, \mathbb{I}) + \boldsymbol{\partial}_{\boldsymbol{x}} \cdot \boldsymbol{\Pi} = \rho \mathbf{g}, \tag{3.3.4}$$

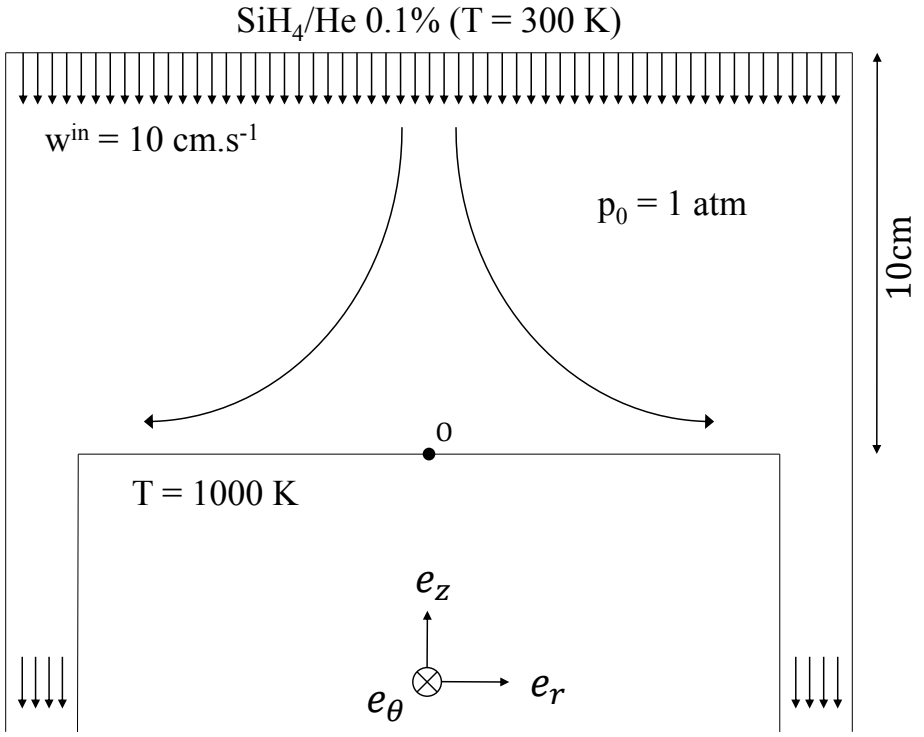

Figure 3.1 – Schematic representation of the axisymmetric chemical vapor deposition reactor.

and energy of the fluid mixture

$$\partial_t \mathcal{E} + \boldsymbol{\partial_x} \cdot (\mathcal{E}\boldsymbol{v}) + p\, \boldsymbol{\partial_x} \cdot \boldsymbol{v} + \boldsymbol{\partial_x} \boldsymbol{v} : \boldsymbol{\Pi} + \boldsymbol{\partial_x} \cdot \boldsymbol{\mathcal{Q}} = 0, \tag{3.3.5}$$

as well as the conservation of the gas phase species mass densities

$$\partial_t(\rho Y_k) + \boldsymbol{\partial_x} \cdot (\rho Y_k \boldsymbol{v} + \rho Y_k \boldsymbol{\mathcal{V}}_k) = m_k \omega_k, \qquad k \in \mathfrak{S}. \tag{3.3.6}$$

Here, ρ_k is the mass density of the k^{th} species, $\rho = \sum_{k\in\mathfrak{S}} \rho_k$ the density of the mixture, $\boldsymbol{v}$ the mass-averaged velocity, p the hydrodynamic pressure, $\boldsymbol{\Pi}$ the viscous tensor, $\mathbf{g}$ the gravity vector, neglected in (2.6.4), $\mathcal{E}$ the total energy per unit volume, $\boldsymbol{\mathcal{Q}}$ the heat flux, $Y_k = \rho_k/\rho$ is the mass fraction of the k^{th} species, $\boldsymbol{\mathcal{V}}_k$ its diffusion velocity, m_k its molar mass, and $\omega_k = \mathfrak{w}_k/\mathcal{N}_{\text{A}}$ its molar production rate due to chemical reactions. Equations (3.3.3)-(3.3.6) may also be derived from the kinetic theory of multicomponent neutral reactive gas mixtures [WT62] [MYM63] [EG94] [Gio99].

From equation (2.6.17), the species diffusion fluxes

$$\boldsymbol{\mathcal{F}}_k = \rho Y_k \boldsymbol{\mathcal{V}}_k, \qquad k \in \mathfrak{S}, \tag{3.3.7}$$

satisfy the constraints

$$\sum_{k\in\mathfrak{S}} \boldsymbol{\mathcal{F}}_k = \sum_{k\in\mathfrak{S}} \rho Y_k \boldsymbol{\mathcal{V}}_k = \mathbf{0}, \tag{3.3.8}$$

and from equation (2.4.163) the molar production rates ω_k, $k \in \mathfrak{S}$, are such that

$$\sum_{k\in\mathfrak{S}} m_k \omega_k = 0. \tag{3.3.9}$$

Equations (3.3.8) and (3.3.9) ensure total mass conservation (3.3.3). By definition, the species mass fractions satisfy the relation

$$\sum_{k\in\mathfrak{S}} Y_k = 1. \tag{3.3.10}$$

However, as is classical for complex chemistry flows, we may also consider that the variables Y_k, $k \in \mathfrak{S}$, are formally independent unknowns, so that the mass conservation relation (3.3.10) is a consequence of equations (3.3.3) and (3.3.6) rather than an a priori assumption [Gio99].

Equations (3.3.3)-(3.3.6) must be completed with expressions for the thermodynamic properties of the mixture, the transport fluxes, the chemistry source terms, and the boundary conditions.

3.4 Thermodynamics

The model requires the evaluation of the thermodynamic properties of the mixture as a function of the state variables T, p, ρ, Y_k, $k \in \mathfrak{S}$, at any time and any point of the reactor.

3.4.1 State law and mixture variables

The perfect gas law has been derived in (2.4.45), and may also be obtained from the standard kinetic theory of neutral gas mixtures [Gio99]

$$p = \frac{\rho R T}{\overline{m}}, \tag{3.4.1}$$

where T is the mixture temperature, and $\overline{m}$ is the mean molar mass of the mixture

$$\frac{1}{\overline{m}} = \sum_{k \in \mathfrak{S}} \frac{Y_k}{m_k}. \tag{3.4.2}$$

For convenience, we also introduce here various mixture variables, namely the species mole fractions

$$X_k = \frac{\overline{m}}{m_k} Y_k, \qquad k \in \mathfrak{S}, \tag{3.4.3}$$

the species partial pressures

$$p_k = \frac{\rho_k R T}{m_k} = p X_k, \qquad k \in \mathfrak{S}, \tag{3.4.4}$$

and the species molar concentrations

$$\gamma_k = \frac{p_k}{RT} = \frac{\rho Y_k}{m_k}, \qquad k \in \mathfrak{S}. \tag{3.4.5}$$

All these variables may be used to describe the state of the mixture.

3.4.2 Enthalpy and entropy

The mixture enthalpy $\mathcal{H}$ is given by

$$\mathcal{H} = \mathcal{E} + p, \tag{3.4.6}$$

and the enthalpy per unit mass, or "specific enthalpy" of the mixture h is such that

$$\rho h = \mathcal{H}. \tag{3.4.7}$$

From equation (2.4.42) and the perfect gas law (3.4.1), the mixture specific enthalpy can be decomposed into [Gio99]

$$\rho h = \sum_{k \in \mathfrak{S}} \rho_k h_k, \tag{3.4.8}$$

where h_k is the specific enthalpy of the k^{th} species

$$h_k = h_k^{\text{st}} + \int_{T^{\text{st}}}^{T} c_{pk}(T')\, \mathrm{d}T', \tag{3.4.9}$$

and h_k^{st} is the formation enthalpy of the k^{th} species at the standard temperature T^{st}, and c_{pk} is the constant pressure specific heat of the k^{th} species. The constant pressure specific heat of the mixture is given by

$$\rho c_p = \sum_{k\in\mathfrak{S}} \rho_k c_{pk}, \tag{3.4.10}$$

and is related to the constant volume specific heat of the mixture c_v given in equation (2.5.32) by

$$c_p = c_v + \frac{R}{\overline{m}}. \tag{3.4.11}$$

Similarly, the entropy of the mixture is given by [Gio99]

$$\rho s = \sum_{k\in\mathfrak{S}} \rho_k s_k, \tag{3.4.12}$$

where s_k is the specific entropy of the k^{th} species

$$s_k = s_k^{\mathrm{st}} + \int_{T^{\mathrm{st}}}^{T} \frac{c_{pk}(T')}{T'}\,\mathrm{d}T' - \frac{R}{m_k}\ln\left(\frac{p_k}{p^{\mathrm{st}}}\right), \tag{3.4.13}$$

and $s_k^{\mathrm{st}} = s_k(T^{\mathrm{st}}, p^{\mathrm{st}})$ is the formation entropy of the k^{th} species at the standard temperature T^{st} and standard atmospheric pressure $p^{\mathrm{st}} = p^{\mathrm{atm}}$, and $p_k = \rho_k RT/m_k$ is the partial pressure of the k^{th} species. Alternatively

$$s_k = s_k^{\mathrm{atm}} - \frac{R}{m_k}\ln\left(\frac{p_k}{p^{\mathrm{st}}}\right), \tag{3.4.14}$$

where $s_k^{\mathrm{atm}} = s_k^{\mathrm{atm}}(T)$ is the specific entropy of the k^{th} species at atmospheric pressure $p_k = p^{\mathrm{st}} = p^{\mathrm{atm}}$

$$s_k^{\mathrm{atm}} = s_k^{\mathrm{st}} + \int_{T^{\mathrm{st}}}^{T} \frac{c_{pk}(T')}{T'}\,\mathrm{d}T'. \tag{3.4.15}$$

The specific entropies s_k, $k \in \mathfrak{S}$, appear in the equilibrium constants for chemical reactions and are thus required in the model.

3.4.3 Enthalpy and temperature equations

The energy conservation equation (3.3.5) can also be expressed in terms of the enthalpy or in terms of the temperature. From the definition of the mixture enthalpy (3.4.6) and the energy conservation equation (3.3.5), the enthalpy balance equation is in the form

$$\partial_t(\rho h) + \boldsymbol{\partial}_{\boldsymbol{x}}\cdot(\rho h\boldsymbol{v}) + \boldsymbol{\partial}_{\boldsymbol{x}}\cdot\boldsymbol{\mathcal{Q}} = \partial_t p + \boldsymbol{\partial}_{\boldsymbol{x}} p\cdot\boldsymbol{v} - \boldsymbol{\partial}_{\boldsymbol{x}}\boldsymbol{v} : \boldsymbol{\Pi}. \tag{3.4.16}$$

On the other hand, from (3.3.3) the enthalpy derivatives read

$$\begin{aligned}
\partial_t(\rho h) + \boldsymbol{\partial}_{\boldsymbol{x}}\cdot(\rho h\boldsymbol{v}) &= \rho\partial_t h + \rho\boldsymbol{v}\cdot\boldsymbol{\partial}_{\boldsymbol{x}} h \\
&= \rho\sum_{k\in\mathfrak{S}}\partial_t(Y_k h_k) + \sum_{k\in\mathfrak{S}}\rho\boldsymbol{v}\cdot\boldsymbol{\partial}_{\boldsymbol{x}}(Y_k h_k) \\
&= \rho\sum_{k\in\mathfrak{S}} Y_k c_{pk}\partial_t T + \sum_{k\in\mathfrak{S}}\rho\boldsymbol{v}\cdot Y_k c_{pk}\boldsymbol{\partial}_{\boldsymbol{x}} T + \sum_{k\in\mathfrak{S}} h_k(\rho\partial_t Y_k + \rho\boldsymbol{v}\cdot\boldsymbol{\partial}_{\boldsymbol{x}} Y_k) \\
&= \rho c_p\partial_t T + \rho c_p\boldsymbol{v}\cdot\boldsymbol{\partial}_{\boldsymbol{x}} T + \sum_{k\in\mathfrak{S}} h_k(\rho\partial_t Y_k + \rho\boldsymbol{v}\cdot\boldsymbol{\partial}_{\boldsymbol{x}} Y_k).
\end{aligned}$$

Since by (3.3.6) and (3.3.3)

$$\rho\partial_t Y_k + \rho\boldsymbol{v}\cdot\boldsymbol{\partial_x} Y_k = m_k\omega_k - \boldsymbol{\partial_x}\cdot\boldsymbol{\mathcal{F}}_k,$$

and

$$\sum_{k\in\mathfrak{S}} h_k\,\boldsymbol{\partial_x}\cdot\boldsymbol{\mathcal{F}}_k = \boldsymbol{\partial_x}\cdot\Big(\sum_{k\in\mathfrak{S}} h_k\boldsymbol{\mathcal{F}}_k\Big) - \Big(\sum_{k\in\mathfrak{S}} c_{pk}\boldsymbol{\mathcal{F}}_k\Big)\cdot\boldsymbol{\partial_x} T,$$

the evolution equation for the temperature is found in the form

$$\begin{aligned}\rho c_p\partial_t T + \rho c_p\boldsymbol{v}\cdot\boldsymbol{\partial_x} T + \boldsymbol{\partial_x}\cdot\Big(\boldsymbol{\mathcal{Q}} - \sum_{k\in\mathfrak{S}} h_k\boldsymbol{\mathcal{F}}_k\Big) = &-\boldsymbol{\Pi}:\boldsymbol{\partial_x}\boldsymbol{v} + \partial_t p + \boldsymbol{\partial_x} p\cdot\boldsymbol{v} \\ &-\Big(\sum_{k\in\mathfrak{S}} c_{pk}\boldsymbol{\mathcal{F}}_k\Big)\cdot\boldsymbol{\partial_x} T - \sum_{k\in\mathfrak{S}} h_k m_k\omega_k.\end{aligned} \tag{3.4.17}$$

The term $-\sum_{k\in\mathfrak{S}} h_k m_k\omega_k$ notably represents the heat release due to chemical reactions.

3.4.4 Thermodynamic data

The enthalpy of the mixture can be computed by (3.4.8) from the knowledge of the species specific enthalpies h_k, $k\in\mathfrak{S}$, and the entropy of the mixture can be computed by (3.4.12) from the knowledge of the species specific entropies s_k, $k\in\mathfrak{S}$. Thus, thermodynamic data needed are the species constant pressure specific heats $c_{pk}(T)$, $k\in\mathfrak{S}$, the species specific enthalpies $h_k(T)$, $k\in\mathfrak{S}$, and the species specific entropies at atmospheric pressure $s_k^{\mathrm{atm}}(T)$, $k\in\mathfrak{S}$. In general, these quantities are evaluated from their molar counterparts

$$C_{pk}(T) = m_k c_{pk}(T), \qquad H_k(T) = m_k h_k(T), \qquad S_k^{\mathrm{atm}}(T) = m_k s_k^{\mathrm{atm}}(T). \tag{3.4.18}$$

From expressions (3.4.9) and (3.4.15), the species molar specific heats $C_{pk}(T)$, $k\in\mathfrak{S}$, the species molar specific enthalpies $H_k(T)$, $k\in\mathfrak{S}$, and the species molar specific entropies at atmospheric pressure $S_k^{\mathrm{atm}}(T)$, $k\in\mathfrak{S}$, are related by the following relations

$$H_k(T) = H_k^{\mathrm{st}} + \int_{T^{\mathrm{st}}}^{T} c_{pk}(T')\,\mathrm{d}T', \tag{3.4.19}$$

$$S_k^{\mathrm{atm}}(T) = S_k^{\mathrm{st}} + \int_{T^{\mathrm{st}}}^{T} \frac{c_{pk}(T')}{T'}\,\mathrm{d}T'. \tag{3.4.20}$$

The molar specific heats $C_{pk}(T)$, $k\in\mathfrak{S}$, are generally evaluated from polynomial approximations. The corresponding absolute thermodynamic data can be found in the JANAF Tables [SP71] [CDD+85] [Cha98].

In this work, fourth-order NASA / SANDIA polynomials defined over two temperature intervals have been used

$$\frac{C_{pk}(T)}{R} = \begin{cases} a_{1k} + a_{2k}T + a_{3k}T^2 + a_{4k}T^3 + a_{5k}T^4, & T_k^{\mathrm{inf}} \le T \le T_k^{\mathrm{mid}}, \\ a'_{1k} + a'_{2k}T + a'_{3k}T^2 + a'_{4k}T^3 + a'_{5k}T^4, & T_k^{\mathrm{mid}} \le T \le T_k^{\mathrm{sup}}, \end{cases} \tag{3.4.21}$$

where T_k^{inf} is the temperature lower bound, T_k^{sup} the temperature upper bound, and T_k^{mid} an intermediate temperature. Two ranges of temperatures are used for a better precision over $c_{pk}(T)$. The molar specific enthalpies and the molar specific entropies at atmospheric pressure then read from (3.4.19) and (3.4.20), respectively

$$\frac{H_k(T)}{RT} = \begin{cases} a_{1k} + a_{2k}T/2 + a_{3k}T^2/3 + a_{4k}T^3/4 + a_{5k}T^4/5 + a_{6k}/T, & T_k^{\mathrm{inf}} \le T \le T_k^{\mathrm{mid}}, \\ a'_{1k} + a'_{2k}T/2 + a'_{3k}T^2/3 + a'_{4k}T^3/4 + a'_{5k}T^4/5 + a'_{6k}/T, & T_k^{\mathrm{mid}} \le T \le T_k^{\mathrm{sup}}, \end{cases} \tag{3.4.22}$$

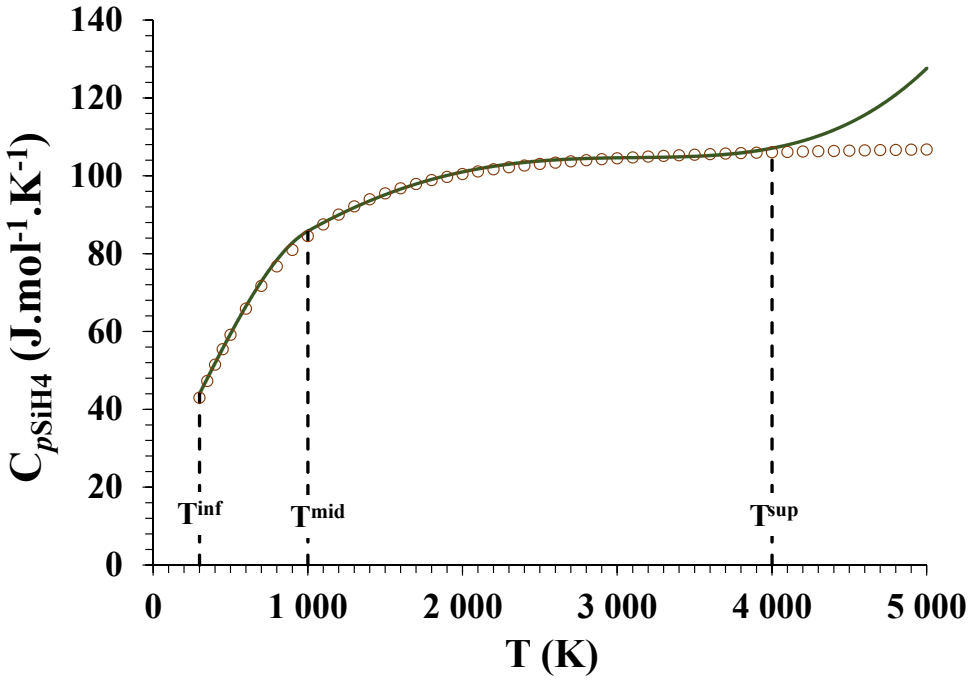

Figure 3.2 – Comparison of the polynomial fits for $C_{p\,\mathrm{SiH_4}}$ (continuous line) obtained from the Chemkin Thermodynamic Database [KRM90] and valid over the ranges $[T^{\mathrm{inf}}, T^{\mathrm{mid}}]$ and $[T^{\mathrm{mid}}, T^{\mathrm{sup}}]$, where $T^{\mathrm{inf}} = 300$ K, $T^{\mathrm{mid}} = 1000$ K and $T^{\mathrm{sup}} = 4000$ K, with absolute data (circles) from the JANAF Thermochemical Tables [Cha98].

$$\frac{S_k^{\mathrm{atm}}(T)}{R} = \begin{cases} a_{1k}\ln T + a_{2k}T + a_{3k}T^2/2 + a_{4k}T^3/3 + a_{5k}T^4/4 + a_{7k}, & T_k^{\mathrm{inf}} \le T \le T_k^{\mathrm{mid}}, \\ a'_{1k}\ln T + a'_{2k}T + a'_{3k}T^2/2 + a'_{4k}T^3/3 + a'_{5k}T^4/4 + a'_{7k}, & T_k^{\mathrm{mid}} \le T \le T_k^{\mathrm{sup}}, \end{cases} \tag{3.4.23}$$

where the coefficients a_{1k}, a'_{1k} are related in particular to H_k^{st} and a_{7k}, a'_{7k} to S_k^{st}.

The polynomial expansion coefficients have been taken from the Chemkin Thermodynamic Database [KRM90]. For each species $k \in \mathfrak{S}$, the tables give the temperatures T_k^{inf}, T_k^{mid} and T_k^{sup}, and the two sets of coefficients $a_{1k}, \ldots, a_{7k}$, and $a'_{1k}, \ldots, a'_{7k}$ corresponding to the respective temperature ranges $[T_k^{\mathrm{inf}}, T_k^{\mathrm{mid}}]$ and $[T_k^{\mathrm{mid}}, T_k^{\mathrm{sup}}]$. As an example, Figure 3.2 shows a comparison of the polynomial fits obtained for the silane molar constant pressure specific heat $C_{p\,\mathrm{SiH_4}}$, valid over the temperature ranges 300-1000 K and 1000-4000 K, with the absolute data from the JANAF Thermochemical Tables [Cha98]. As can be seen on the figure, the polynomial fit is consistent with absolute thermodynamic data over the prescribed range of temperatures $[T_{\mathrm{SiH_4}}^{\mathrm{inf}}, T_{\mathrm{SiH_4}}^{\mathrm{sup}}]$.

3.5 Chemistry

We consider a set of n^r chemical reactions, which can be written in the form

$$\sum_{k\in\mathfrak{S}} \nu_k^{r\mathrm{f}}\,\mathfrak{M}_k \rightleftharpoons \sum_{k\in\mathfrak{S}} \nu_k^{r\mathrm{b}}\,\mathfrak{M}_k, \quad r \in \mathscr{R}, \tag{3.5.1}$$

where $\mathscr{R} = \{1, \ldots, n^r\}$ is the set of reaction indices, $\mathfrak{M}_k$ denotes the chemical symbol of the k^{th} species, and where $\nu_k^{r\mathrm{f}}$, respectively $\nu_k^{r\mathrm{b}}$, denotes the forward, respectively the backward, stoichiometric coefficient of the k^{th} species in the r^{th} reaction. According to the kinetic theory [EG94] [Gio99], the molar production rate of the k^{th} species can be decomposed into the different contributions from

each reaction

$$\omega_k = \sum_{r \in \mathscr{R}} \nu_k^r \tau_r, \tag{3.5.2}$$

where τ_r is the rate of progress of the r^{th} reaction, and

$$\nu_k^r = \nu_k^{r\text{f}} - \nu_k^{r\text{b}} \tag{3.5.3}$$

is the net stoichiometric coefficient of the k^{th} species in the r^{th} reaction. The stoichiometric coefficients satisfy the relation (2.2.38) for conservation of mass [EG94] [Gio99]

$$\sum_{k \in \mathfrak{S}} \nu_k^{r\text{f}} m_k = \sum_{k \in \mathfrak{S}} \nu_k^{r\text{b}} m_k, \qquad r \in \mathscr{R}, \tag{3.5.4}$$

which in turn yields the total mass conservation equation for chemical reactions (3.3.9).

Table 3.1 – List of gas phase reactions with corresponding Arrhenius parameters.

r	**Reaction**	A_r **(mol,cm^3,s)**	β_r	$\mathfrak{E}_r$ **(cal.mol^{-1})**
1	$SiH_4 = SiH_2 + H_2$	1.09×10^{25}	-3.37	61,200
2	$SiH_4 = SiH_3 + H$	3.69×10^{15}	0.0	93,000
3	$Si_2H_6 = SiH_4 + SiH_2$	3.24×10^{29}	-4.24	58,000
4	$SiH_4 + H = SiH_3 + H_2$	1.46×10^{13}	0.0	2,500
5	$SiH_4 + SiH_3 = Si_2H_5 + H_2$	1.77×10^{12}	0.0	4,400
6	$SiH_4 + SiH = Si_2H_3 + H_2$	1.45×10^{12}	0.0	2,000
7	$SiH_4 + SiH = Si_2H_5$	1.43×10^{13}	0.0	2,000
8	$SiH_2 = Si + H_2$	1.06×10^{14}	-0.88	4,500
9	$SiH_2 + H = SiH + H_2$	1.39×10^{13}	0.0	2,000
10	$SiH_2 + H = SiH_3$	3.81×10^{13}	0.0	2,000
11	$SiH_2 + SiH_3 = Si_2H_5$	6.58×10^{12}	0.0	2,000
12	$SiH_2 + Si_2 = Si_3 + H_2$	3.55×10^{11}	0.0	2,000
13	$SiH_2 + Si_3 = Si_2H_2 + Si_2$	1.43×10^{11}	0.0	16,200
14	$H_2SiSiH_2 = Si_2H_2 + H_2$	3.16×10^{14}	0.0	53,000
15	$Si_2H_6 = H_3SiSiH + H_2$	7.94×10^{15}	0.0	56,400
16	$H_2 + SiH = SiH_3$	3.45×10^{13}	0.0	2,000
17	$H_2 + Si_2 = Si_2H_2$	1.54×10^{13}	0.0	2,000
18	$H_2 + Si_2 = SiH + SiH$	1.54×10^{13}	0.0	40,000
19	$H_2 + Si_3 = Si + Si_2H_2$	9.79×10^{12}	0.0	47,200
20	$Si_2H_5 = Si_2H_3 + H_2$	3.16×10^{14}	0.0	53,000
21	$Si_2H_2 + H = Si_2H_3$	8.63×10^{14}	0.0	2,000
22	$H + Si_2 = SiH + Si$	5.15×10^{13}	0.0	5,300
23	$SiH_4 + H_3SiSiH = Si_3H_8$	6.02×10^{13}	0.0	0
24	$SiH_2 + Si_2H_6 = Si_3H_8$	1.81×10^{14}	0.0	0
25	$SiH_3 + Si_2H_5 = Si_3H_8$	3.31×10^{13}	0.0	0
26	$H_3SiSiH = H_2SiSiH_2$	1.15×10^{20}	-3.06	6,630

The rate of progress (2.4.160) reads

$$\tau_r = \mathcal{K}_r^{\text{f}} \prod_{k \in \mathfrak{S}} \gamma_k^{\nu_k^{r\text{f}}} - \mathcal{K}_r^{\text{b}} \prod_{k \in \mathfrak{S}} \gamma_k^{\nu_k^{r\text{b}}}, \tag{3.5.5}$$

where $\gamma_k = \rho Y_k / m_k$ is the molar concentration of the k^{th} species, and $\mathcal{K}_r^{\text{f}}$ and $\mathcal{K}_r^{\text{b}}$ are the forward and backward rate constants of the r^{th} reaction. As a consequence of detailed balancing and reciprocity relations (2.2.36), the ratio of the rate constants $\mathcal{K}_r^{\text{f}}$ and $\mathcal{K}_r^{\text{b}}$ is the equilibrium constant of the r^{th} reaction, as already stated in (2.4.169)

$$\mathcal{K}_r^{\text{e}}(T) = \frac{\mathcal{K}_r^{\text{f}}(T)}{\mathcal{K}_r^{\text{b}}(T)}. \tag{3.5.6}$$

The equilibrium constant also corresponds to the chemical equilibrium proportions, as described by statistical mechanics [Tol38], as well as classical thermochemistry [SS65] [Kra70], and is given by (2.4.168)

$$\ln \mathcal{K}_r^{\text{e}}(T) = -\sum_{k\in\mathfrak{S}} \frac{\nu_k^r m_k}{RT}\Big(g_k^{\text{atm}}(T) - \frac{RT}{m_k}\ln\big(\frac{p^{\text{atm}}}{RT}\big)\Big), \tag{3.5.7}$$

where g_k^{atm}, $k \in \mathfrak{S}$, denote the species specific Gibbs functions at atmospheric pressure

$$g_k^{\text{atm}}(T) = h_k(T) - T s_k^{\text{atm}}(T), \quad k \in \mathfrak{S}. \tag{3.5.8}$$

In general, the forward rate constant is approximated by a generalized Arrhenius empirical relation of the form

$$\mathcal{K}_r^{\text{f}}(T) = A_r T^{\beta_r} \exp\Big(-\frac{\mathfrak{E}_r}{RT}\Big), \tag{3.5.9}$$

where A_r is the pre-exponential factor, β_r the pre-exponential exponent and $\mathfrak{E}_r \geq 0$ the activation energy of the r^{th} reaction. The backward rate constant is then deduced from the forward rate constant (3.5.9) and the equilibrium constant (3.5.7) by applying the law of mass action (3.5.6).

The gas phase reaction mechanism adopted for the present model has been developed by Coltrin and coworkers [CKE89], as described in [Kle00]. The $n^r = 26$ reversible chemical reactions and associated Arrhenius parameters are listed in Table 3.1. The gas phase chemical kinetics are driven by the decomposition of SiH_4 into SiH_2 and H_2 in the hot gas region above the susceptor surface. This initiates a chain of homogeneous reactions, leading to the formation of many silicon containing species. Each of these species may diffuse to and react at the surface to form crystalline silicon. The gas phase chemistry mechanism is implemented within a highly vectorized version [GD88] of the Chemkin-II FORTRAN software [KRM89].

3.6 Transport Fluxes

The transport fluxes derived in Chapter 2 are now rewritten in the case of a neutral gas mixture. The electro-magnetic field vanishes and in the absence of electrons the viscous tensor $\mathbf{\Pi}$ and the heat flux $\boldsymbol{\mathcal{Q}}$ are identified with the heavy-species viscous tensor $\mathbf{\Pi}_h$ and the heavy-species heat flux $\boldsymbol{\mathcal{Q}}_h$, respectively. From equations (2.6.34)-(2.6.36), the transport fluxes read

$$\mathbf{\Pi} = -(\kappa - \tfrac{2}{3}\eta)(\boldsymbol{\partial}_{\boldsymbol{x}} \cdot \boldsymbol{v})\,\mathbb{I} - \eta\,(\boldsymbol{\partial}_{\boldsymbol{x}}\boldsymbol{v} + \boldsymbol{\partial}_{\boldsymbol{x}}\boldsymbol{v}^{\text{T}}), \tag{3.6.1}$$

$$\boldsymbol{\mathcal{V}}_k = -\sum_{l\in\mathfrak{S}} D_{kl}\hat{\boldsymbol{d}}_l - \theta_k \boldsymbol{\partial}_{\boldsymbol{x}} \ln T, \qquad k \in \mathfrak{S}, \tag{3.6.2}$$

$$\boldsymbol{\mathcal{Q}} = \sum_{k\in\mathfrak{S}} h_k \boldsymbol{\mathcal{F}}_k - \hat{\lambda}\boldsymbol{\partial}_{\boldsymbol{x}} T - p\sum_{k\in\mathfrak{S}} \theta_k \hat{\boldsymbol{d}}_k, \tag{3.6.3}$$

where $\kappa = \kappa_h$ denotes the volume viscosity, $\eta = \eta_h$ the shear viscosity, $^{\text{T}}$ the transposition operator, D_{kl}, $k, l \in \mathfrak{S}$ the multicomponent diffusion coefficients, $\hat{\boldsymbol{d}}_k$ the unconstrained diffusion driving force

of the k^{th} species, $\theta_k = \theta_{kh}$ the thermal diffusion coefficient of the k^{th} species and $\hat{\lambda} = \hat{\lambda}_{hh}$ the partial thermal conductivity. The species diffusion driving forces read

$$\hat{\boldsymbol{d}}_k = \frac{1}{p}\boldsymbol{\partial}_{\boldsymbol{x}} p_k = X_k\, \boldsymbol{\partial}_{\boldsymbol{x}} \ln p + \boldsymbol{\partial}_{\boldsymbol{x}} X_k, \qquad k \in \mathfrak{S}. \tag{3.6.4}$$

The first term in the expression (3.6.2) of the diffusion velocity $\boldsymbol{\mathcal{V}}_k$ incorporates diffusion effects due to partial pressure gradients and specific external forces. The second term represents diffusion due to temperature gradients and is called the Soret effect. The first term in the expression (3.6.3) of the heat flux $\boldsymbol{\mathcal{Q}}$ represents the transfer of energy accompanying species molecular diffusion, whereas the second term corresponds to Fourier's law. The third term stands for thermal diffusion due to concentration gradients, and is referred to as the Dufour effect, which is the symmetric of the Soret effect. Expressions (3.6.1)-(3.6.3) for transport fluxes may also be derived from the kinetic theory of multicomponent neutral gas mixtures [WT62] [CC70] [FK72] [EG94] [Gio99].

From the relations (2.5.61)-(2.5.63) and (2.5.67), the diffusion matrix $D = (D_{kl})_{k,l\in\mathfrak{S}}$, which coincides with the heavy-species diffusion matrix D_h when $Y_e = 0$, exhibits the following mathematical properties

$$D = D^{\mathrm{T}}, \tag{3.6.5}$$

$$N(D) = \mathbb{R}Y, \tag{3.6.6}$$

$$R(D) = Y^{\perp}, \tag{3.6.7}$$

$$D \text{ is nonnegative}, \tag{3.6.8}$$

i.e., D is symmetric, nonnegative, its kernel is the one-dimensional space spanned by the vector $Y = (Y_k)_{k\in\mathfrak{S}}$, and its range is the orthogonal complement to $\mathbb{R}Y$. From the preceding relations (3.6.5) and (3.6.7), or from (2.5.67), the diffusion matrix D satisfies the relation

$$\sum_{k\in\mathfrak{S}} Y_k D_{kl} = 0, \quad l \in \mathfrak{S}, \tag{3.6.9}$$

and as well from (2.5.69) the thermal diffusion vector $\theta = (\theta_k)_{k\in\mathfrak{S}}$ satisfies the relation

$$\sum_{k\in\mathfrak{S}} Y_k \theta_k = 0, \tag{3.6.10}$$

i.e., it is orthogonal to the space $\mathbb{R}Y$.

It is often more practical [CC70] [FK72] [Gio99] to use the constrained diffusion driving forces

$$\boldsymbol{d}_k = \boldsymbol{\partial}_{\boldsymbol{x}} X_k + (X_k - Y_k)\, \boldsymbol{\partial}_{\boldsymbol{x}} \ln p, \qquad k \in \mathfrak{S}, \tag{3.6.11}$$

where $X_k = p_k/p$ and $Y_k = \rho_k/\rho$ are the respective mole and mass fractions of the k^{th} species, in place of the unconstrained diffusion driving forces $\hat{\boldsymbol{d}}_k$, $k \in \mathfrak{S}$, in expressions (3.6.2) and (3.6.3) for the species diffusion velocities and heat flux

$$\boldsymbol{\mathcal{V}}_k = -\sum_{l\in\mathfrak{S}} D_{kl}\boldsymbol{d}_l - \theta_k \boldsymbol{\partial}_{\boldsymbol{x}} \ln T, \qquad k \in \mathfrak{S}, \tag{3.6.12}$$

$$\boldsymbol{\mathcal{Q}} = \sum_{k\in\mathfrak{S}} h_k \boldsymbol{\mathcal{F}}_k - \hat{\lambda}\boldsymbol{\partial}_{\boldsymbol{x}} T - p\sum_{k\in\mathfrak{S}} \theta_k \boldsymbol{d}_k. \tag{3.6.13}$$

Both formulations are indeed equivalent, since

$$\boldsymbol{d}_k = \hat{\boldsymbol{d}}_k - Y_k \sum_{l\in\mathfrak{S}} \hat{\boldsymbol{d}}_l, \tag{3.6.14}$$

$Y \in N(D)$ and $\langle Y, \theta \rangle = 0$ by (3.6.9) and (3.6.10). The mass conservation constraint (3.3.8) over the species diffusion velocities is also a consequence of (3.6.9) and (3.6.10). Correspondingly, the constrained diffusion driving forces are by definition linearly dependent

$$\sum_{k \in \mathfrak{S}} \boldsymbol{d}_k = 0, \tag{3.6.15}$$

as are the species diffusion fluxes $\boldsymbol{\mathcal{F}}_k = \rho Y_k \boldsymbol{\mathcal{V}}_k$, $k \in \mathfrak{S}$.

Finally, the diffusion velocities $\boldsymbol{\mathcal{V}}_k$, $k \in \mathfrak{S}$, and the heat flux $\boldsymbol{\mathcal{Q}}$ may be expressed in terms of the thermal diffusion ratios χ_k, $k \in \mathfrak{S}$, and the thermal conductivity λ, instead of the partial thermal conductivity $\hat{\lambda}$ and the thermal diffusion coefficients θ_k, $k \in \mathfrak{S}$. The species thermal diffusion ratios are the solution to the following constrained linear system

$$\begin{cases} D\chi = \theta, \\ \displaystyle\sum_{k \in \mathfrak{S}} \chi_k = 0, \end{cases} \tag{3.6.16}$$

where $\chi = (\chi_k)_{k \in \mathfrak{S}}$ and $\theta = (\theta_k)_{k \in \mathfrak{S}}$. The system (3.6.16) is well-posed since D is positive definite over the space $\mathcal{U}^{\perp}$, where $\mathcal{U} = (1)_{k \in \mathfrak{S}}$ is the unit vector [EG94]. The thermal conductivity is then given by

$$\lambda = \hat{\lambda} - \frac{p}{T} \sum_{k \in \mathfrak{S}} \theta_k \chi_k. \tag{3.6.17}$$

Expressions (3.6.12) and (3.6.13) for the diffusion velocities and heat flux may then be replaced with the following alternative expressions

$$\boldsymbol{\mathcal{V}}_k = -\sum_{l \in \mathfrak{S}} D_{kl} (\boldsymbol{d}_l + \chi_l \boldsymbol{\partial}_{\boldsymbol{x}} \ln T), \qquad k \in \mathfrak{S}, \tag{3.6.18}$$

$$\boldsymbol{\mathcal{Q}} = \sum_{k \in \mathfrak{S}} h_k \boldsymbol{\mathcal{F}}_k - \lambda \boldsymbol{\partial}_{\boldsymbol{x}} T + p \sum_{k \in \mathfrak{S}} \chi_k \boldsymbol{\mathcal{V}}_k. \tag{3.6.19}$$

3.7 Low Mach Number Flow

In the chemical vapor deposition process considered in this Chapter, the macroscopic fluid velocity v is usually negligible in comparison with the sound speed. In other words, the Mach number, which is the ratio of a characteristic macroscopic velocity v^0 over a characteristic sound speed $\mathfrak{c}_s^0$, is small compared to one

$$\epsilon = \frac{v^0}{\mathfrak{c}_s^0} \ll 1. \tag{3.7.1}$$

For an ideal gas mixture, a characteristic sound velocity may be taken as

$$\mathfrak{c}_s^0 = \sqrt{\frac{p^0}{\rho^0}}, \tag{3.7.2}$$

where p^0 and ρ^0 denote a characteristic pressure and a characteristic mass density of the fluid, respectively. The characteristic (volume or shear) viscosity is denoted by η^0 and the typical hydrodynamic length L^0 is a viscous length, i.e., a length such that the Reynolds number is of order unity

$$L^0 = \frac{\eta^0}{\rho^0 v^0}, \tag{3.7.3}$$

and the corresponding characteristic time is $t^0 = L^0/v^0$. As stated above, the only external force acting on the species is gravity. We assume that the associated Froude number is of order unity or larger

$$\frac{(v^0)^2}{L^0 \mathrm{g}^0} \gtrsim 1, \tag{3.7.4}$$

where g^0 is the order of magnitude of the gravitational acceleration.

3.7.1 Momentum equation and pressure splitting

The scaling introduced above is applied to the momentum equation (3.3.4). The scaled ratio associated with quantity ϕ is denoted by $\hat{\phi} = \phi/\phi^0$. The following momentum equation is obtained after a little algebra [Gio99]

$$\epsilon^2\big(\partial_{\hat{t}}(\widehat{\rho}\widehat{\boldsymbol{v}}) + \boldsymbol{\partial}_{\widehat{\boldsymbol{x}}} \cdot (\widehat{\rho}\widehat{\boldsymbol{v}} \otimes \widehat{\boldsymbol{v}}) + \boldsymbol{\partial}_{\widehat{\boldsymbol{x}}} \cdot \widehat{\boldsymbol{\Pi}} - \widehat{\rho}\widehat{\mathbf{g}}\big) = -\,\boldsymbol{\partial}_{\widehat{\boldsymbol{x}}}\hat{p}. \tag{3.7.5}$$

From (3.7.5) we deduce that the pressure spatial gradient is of order $O(\epsilon^2)$, so that the pressure can be decomposed into

$$\widehat{p}(\hat{t}, \widehat{\boldsymbol{x}}) = \widehat{p}_0(\hat{t}) + \epsilon^2 \widehat{p}_2(\hat{t}, \widehat{\boldsymbol{x}}). \tag{3.7.6}$$

In terms of the original variables, this yields the classical splitting [Gio99]

$$p(t, \boldsymbol{x}) = p_0(t) + \epsilon^2 \tilde{p}(t, \boldsymbol{x}), \tag{3.7.7}$$

where p_0 is a spatially uniform pressure and $\tilde{p}$ is the fluid hydrodynamic perturbation.

Upon introducing this pressure splitting in equation (3.7.5), the following simplified momentum conservation equation is obtained [Gio99] in terms of the original variables

$$\partial_t(\rho \boldsymbol{v}) + \boldsymbol{\partial}_{\boldsymbol{x}} \cdot (\rho \boldsymbol{v} \otimes \boldsymbol{v}) + \boldsymbol{\partial}_{\boldsymbol{x}} \tilde{p} + \boldsymbol{\partial}_{\boldsymbol{x}} \cdot \boldsymbol{\Pi} = \rho \mathbf{g}. \tag{3.7.8}$$

As well, the following simplified state law [Gio99] is obtained from (3.4.1)

$$\rho = \frac{p_0 \overline{m}}{RT}, \tag{3.7.9}$$

where terms of order two or larger in ϵ have been omitted. With such a simplified state law and momentum equation, acoustic waves are notably filtered out.

3.7.2 Temperature equation

In the low Mach number limit, the temperature evolution equation (3.4.17) may also be simplified. The internal energy is associated with molecular velocity fluctuations, so that

$$c_p^0 T^0 = (\mathfrak{c}_s^0)^2, \tag{3.7.10}$$

where c_p^0 and T^0 are the respective orders of magnitude of the constant pressure specific heat and temperature. Furthermore, the characteristic thermal conductivity scales as

$$\lambda^0 = \eta^0 c_p^0, \tag{3.7.11}$$

i.e., the Prandtl number is of order one, and the order of magnitude of the diffusion coefficients D^0 is such that the Schmidt number is of order one, namely

$$\eta^0 = \rho^0 D^0. \tag{3.7.12}$$

Taking into account these orders of magnitude, the following scaled evolution equation for the temperature is obtained after some algebra

$$\widehat{\rho}\widehat{c_p}\partial_{\widehat{t}}\widehat{T} + \widehat{\rho}\widehat{c_p}\widehat{\boldsymbol{v}}\cdot\boldsymbol{\partial}_{\widehat{\boldsymbol{x}}}\widehat{T} + \boldsymbol{\partial}_{\widehat{\boldsymbol{x}}}\cdot\Big(\widehat{\boldsymbol{\mathcal{Q}}} - \sum_{k\in\mathfrak{S}}\widehat{h}_k\widehat{\boldsymbol{\mathcal{F}}}_k\Big) = \partial_{\widehat{t}}\widehat{p}_0 + \epsilon^2\Big(\partial_{\widehat{t}}\widehat{p}_2 + \boldsymbol{\partial}_{\widehat{\boldsymbol{x}}}\widehat{p}_2\cdot\widehat{\boldsymbol{v}} - \widehat{\boldsymbol{\Pi}} : \boldsymbol{\partial}_{\widehat{\boldsymbol{x}}}\widehat{\boldsymbol{v}}\Big)$$
$$-\Big(\sum_{k\in\mathfrak{S}}\widehat{c}_{pk}\widehat{\boldsymbol{\mathcal{F}}}_k\Big)\cdot\boldsymbol{\partial}_{\widehat{\boldsymbol{x}}}\widehat{T} - \sum_{k\in\mathfrak{S}}\widehat{h}_k\widehat{m}_k\widehat{\omega}_k. \tag{3.7.13}$$

Finally, expanding equation (3.7.13) at order zero in ϵ^2 yields the following temperature equation in the low Mach number limit [Gio99], written in terms of the original variables

$$\rho c_p\partial_t T + \rho c_p\boldsymbol{v}\cdot\boldsymbol{\partial}_{\boldsymbol{x}}T + \boldsymbol{\partial}_{\boldsymbol{x}}\cdot\Big(\boldsymbol{\mathcal{Q}} - \sum_{k\in\mathfrak{S}}h_k\boldsymbol{\mathcal{F}}_k\Big) = -\Big(\sum_{k\in\mathfrak{S}}c_{pk}\boldsymbol{\mathcal{F}}_k\Big)\cdot\boldsymbol{\partial}_{\boldsymbol{x}}T - \sum_{k\in\mathfrak{S}}h_k m_k\omega_k. \tag{3.7.14}$$

Note that the uniform pressure in the CVD reactor p_0 is independent of time, so that $\partial_t p_0 = 0$. Equation (3.7.14) merely expresses energy balance.

3.7.3 Isobaric equations

The low Mach number scaling, when applied to the species mass conservation equations (3.3.6) and the total mass conservation equation (3.3.3), does not yield any further simplification. Upon assuming that the spatially uniform pressure p_0 is independent of time, we obtain the so-called "isobaric equations" (3.3.3), (3.3.6), (3.7.8) and (3.7.14) [Gio99]

$$\partial_t\rho + \boldsymbol{\partial}_{\boldsymbol{x}}\cdot(\rho\boldsymbol{v}) = 0, \tag{3.7.15}$$

$$\partial_t(\rho Y_k) + \boldsymbol{\partial}_{\boldsymbol{x}}\cdot(\rho Y_k\boldsymbol{v} + \boldsymbol{\mathcal{F}}_k) = m_k\omega_k, \qquad k\in\mathfrak{S}, \tag{3.7.16}$$

$$\partial_t(\rho\boldsymbol{v}) + \boldsymbol{\partial}_{\boldsymbol{x}}\cdot(\rho\boldsymbol{v}\otimes\boldsymbol{v}) + \boldsymbol{\partial}_{\boldsymbol{x}}\tilde{p} + \boldsymbol{\partial}_{\boldsymbol{x}}\cdot\boldsymbol{\Pi} = \rho\mathbf{g}, \tag{3.7.17}$$

$$\rho c_p\partial_t T + \rho c_p\boldsymbol{v}\cdot\boldsymbol{\partial}_{\boldsymbol{x}}T + \boldsymbol{\partial}_{\boldsymbol{x}}\cdot\Big(\boldsymbol{\mathcal{Q}} - \sum_{k\in\mathfrak{S}}h_k\boldsymbol{\mathcal{F}}_k\Big) = -\sum_{k\in\mathfrak{S}}c_{pk}\,\boldsymbol{\mathcal{F}}_k\cdot\boldsymbol{\partial}_{\boldsymbol{x}}T - \sum_{k\in\mathfrak{S}}h_k m_k\omega_k. \tag{3.7.18}$$

In the next section, we seek for self similar solutions of such isobaric equations (3.7.15)-(3.7.18) in axisymmetric geometry.

3.8 Strained Flow

The chemical vapor deposition process flow considered in this study is a particular case of strained flows. Strained flows may be obtained by directing two impinging jets one on each other or against a flat plate. The corresponding equations are usually derived from a boundary layer approximation. However, in planar or cylindrincal geometries, the strained flow equations may be obtained as *exact* solutions [Gio88] [KMEDL88] [Gio99] of the isobaric equations (3.7.15)-(3.7.18).

3.8.1 Self similar solution

We recall that the cylindrical coordinates (r,θ,z), with corresponding unit vectors $\boldsymbol{e}_r$, $\boldsymbol{e}_\theta$ and $\boldsymbol{e}_z$, are such that $\boldsymbol{e}_z$ is normal to the stagnation plane $(O,\boldsymbol{e}_r,\boldsymbol{e}_\theta)$, where O is the origin located at the centre of the substrate (see Figure 3.1). Because of the axial symmetry, the average velocity may be written in the cylindrical coordinates $\boldsymbol{v} = (u,0,w)$. We also assume that gravity is either oriented

in the normal direction, namely $\mathbf{g} = (0, 0, \mathrm{g})$, or negligible. In this framework, we seek for a self similar solution of the isobaric equations (3.7.15)-(3.7.18), of the form

$$\rho = \rho(t, z) \tag{3.8.1}$$
$$u = r\hat{u}(t, z) \tag{3.8.2}$$
$$w = w(t, z) \tag{3.8.3}$$
$$\tilde{p} = -J(t)\frac{r^2}{2} + \hat{p}(t, z) \tag{3.8.4}$$
$$T = T(t, z) \tag{3.8.5}$$
$$Y_k = Y_k(t, z), \qquad k \in \mathfrak{S}, \tag{3.8.6}$$

where $J(t)$ denotes the pressure curvature in the tangential direction.

From expressions (3.6.18) and (3.6.19), the diffusion velocities and heat flux can be expressed in the form

$$\boldsymbol{\mathcal{V}}_k = \big(0, 0, \mathcal{V}_k(t, z)\big), \qquad k \in \mathfrak{S}, \tag{3.8.7}$$
$$\boldsymbol{\mathcal{Q}} = \big(0, 0, \mathcal{Q}(t, z)\big). \tag{3.8.8}$$

Upon substituting (3.8.1)-(3.8.6) into the isobaric equations (3.7.15)-(3.7.18), the fluid equations may be written in the form

$$\partial_t \rho + 2\rho\hat{u} + \partial_z(\rho w) = 0, \tag{3.8.9}$$

$$\rho\partial_t Y_k + \rho w\partial_z Y_k = m_k\omega_k - \partial_z\mathcal{F}_k, \qquad k \in \mathfrak{S}, \tag{3.8.10}$$

$$\rho r\partial_t\hat{u} + \rho\hat{u}^2 r + \rho r w\partial_z\hat{u} = Jr + \partial_z(\eta\partial_z\hat{u})r, \tag{3.8.11}$$

$$\rho\partial_t w + \rho w\partial_z w = -\partial_z\hat{p} + 2\eta\partial_z\hat{u} + 2\partial_z\Big((\kappa - \frac{2}{3}\eta)\hat{u}\Big) + \partial_z\Big((\kappa + \frac{4}{3}\eta)\partial_z w\Big) + \rho\mathrm{g}, \tag{3.8.12}$$

$$\rho c_p\partial_t T + \rho c_p w\partial_z T = \partial_z\Big(\lambda\partial_z T - p\sum_{k\in\mathfrak{S}}\chi_k\mathcal{V}_k\Big) - \sum_{k\in\mathfrak{S}} c_{pk}\mathcal{F}_k\partial_z T - \sum_{k\in\mathfrak{S}} h_k m_k\omega_k, \tag{3.8.13}$$

where $\mathcal{F}_k = \rho Y_k\mathcal{V}_k$ is the normal coordinate of the k^{th}-species diffusion flux, so that for all $k \in \mathfrak{S}$, $\boldsymbol{\mathcal{F}}_k = (0, 0, \mathcal{F}_k)$. The first two equations are the conservation equations for the fluid density and the species mass fractions, respectively, the third and fourth equations are the conservation equations for the tangential and normal velocity components, $\hat{u}$ and w, respectively, and the fifth equation is the evolution equation for the temperature.

Equation (3.8.12) for the normal momentum uncouples from the remaining governing equations, and is usually discarded though it may be used to determine the pressure correction $\hat{p}$. The equation for tangential momentum is divided by r, and the system of equations to be solved finally reads

$$\partial_t \rho + 2\rho\hat{u} + \partial_z(\rho w) = 0, \tag{3.8.14}$$

$$\rho\partial_t Y_k + \rho w\partial_z Y_k = m_k\omega_k - \partial_z\mathcal{F}_k, \qquad k \in \mathfrak{S}, \tag{3.8.15}$$

$$\rho\partial_t\hat{u} + \rho\hat{u}^2 + \rho w\partial_z\hat{u} = J + \partial_z(\eta\partial_z\hat{u}), \tag{3.8.16}$$

$$\rho c_p\partial_t T + \rho c_p w\partial_z T = \partial_z\Big(\lambda\partial_z T - p\sum_{k\in\mathfrak{S}}\chi_k\mathcal{V}_k\Big) - \sum_{k\in\mathfrak{S}} c_{pk}\mathcal{F}_k\partial_z T - \sum_{k\in\mathfrak{S}} h_k m_k\omega_k. \tag{3.8.17}$$

Since p_0 is a known parameter, ρ is obtained from the perfect gas law (3.7.9), provided the mass fractions Y_k, $k \in \mathfrak{S}$, and temperature T are known. Thus, we are left with n^s+3 formally independent unknowns, namely the temperature T, the species mass fractions Y_k, $k \in \mathfrak{S}$, the so-called tangential velocity $\hat{u}$, and the normal velocity w. Equation (3.8.14) determines the normal velocity, equation (3.8.15) the species mass fractions, equation (3.8.16) the tangential velocity, and equation (3.8.17) the temperature.

The system of equations (3.8.14)-(3.4.17) is valid provided boundary conditions are compatible with the self-similarity assumptions (3.8.1)-(3.8.6). The method is easily extended to the case of a rotating disk reactor. The convection velocity is then taken in the form $\boldsymbol{v} = (ru(z,t), rv(z,t), w(z,t))$ [KCG03].

3.8.2 Traditional variables

The pressure curvature J is a natural parameter of the laminar flow process that is generally independent of time and that is usually specified through the strain rate

$$\alpha = \sqrt{\frac{J}{\rho^{\text{in}}}}. \tag{3.8.18}$$

The injected mixture macroscopic properties T^{in}, p^{in}, ρ^{in}, $(Y_k^{\text{in}})_{k\in\mathfrak{S}}$, are also such that

$$\rho^{\text{in}} = \frac{p^{\text{in}}\overline{m}^{\text{in}}}{RT^{\text{in}}}, \tag{3.8.19}$$

where $1/\overline{m}^{\text{in}} = \sum_{k\in\mathfrak{S}} Y_k^{\text{in}}/m_k$ and the inlet mass fractions must sum up to unity, i.e., $\sum_{k\in\mathfrak{S}} Y_k^{\text{in}} = 1$.

It is traditional for strained flows to introduce the auxiliary variables

$$\tilde{u} = \frac{\hat{u}}{\alpha} = \frac{u}{\alpha r}, \tag{3.8.20}$$

$$\tilde{w} = \rho w. \tag{3.8.21}$$

The strained flow isobaric equations (3.8.14)-(3.8.17) then read

$$\partial_t \rho + 2\rho\alpha\tilde{u} + \partial_z \tilde{w} = 0, \tag{3.8.22}$$

$$\rho\partial_t Y_k + \tilde{w}\partial_z Y_k = m_k\omega_k - \partial_z \mathcal{F}_k, \qquad k \in \mathfrak{S}, \tag{3.8.23}$$

$$\rho\partial_t \tilde{u} + \tilde{w}\partial_z \tilde{u} = \alpha(\rho^{\text{in}} - \rho\tilde{u}^2) + \partial_z(\eta\partial_z\tilde{u}), \tag{3.8.24}$$

$$\rho c_p \partial_t T + c_p\tilde{w}\partial_z T = \partial_z\Big(\lambda\partial_z T - p\sum_{k\in\mathfrak{S}}\chi_k\mathcal{V}_k\Big) - \sum_{k\in\mathfrak{S}} c_{pk}\mathcal{F}_k\partial_z T - \sum_{k\in\mathfrak{S}} h_k m_k\omega_k. \tag{3.8.25}$$

The transport fluxes, namely the species diffusion velocities $\boldsymbol{\mathcal{V}}_k = \mathcal{V}_k(t,z)\boldsymbol{e}_z$, $k \in \mathfrak{S}$, the heat flux $\boldsymbol{\mathcal{Q}} = \mathcal{Q}(t,z)\boldsymbol{e}_z$, the viscous tensor $\boldsymbol{\Pi} = \Pi(t,z)\boldsymbol{e}_z$, have been expressed in section 3.6 in terms of transport coefficients, whose expressions are given in the following section.

3.9 Transport Coefficients

Transport coefficients have been calculated by means of the multicomponent transport library "EGLIB" developed by Ern and Giovangigli [EG96a]. In this section, the approximations chosen for

each transport coefficient are described and compared to those of the benchmark model [Kle00]. For a thorough description of the mathematical theory of multicomponent transport property evaluation, the reader is referred to [EG94] [Gio99].

Transport coefficients generally depend on the temperature T, the pressure p, and the species mass fractions Y_k, $k \in \mathfrak{S}$. In the low Mach number limit, the transport coefficients depend only on the spatially uniform pressure p_0.

3.9.1 Molecular parameters and collision integrals

The practical calculation of transport coefficients requires the choice of the interaction potentials φ_{kl} between molecule species pairs (k,l), $k,l \in \mathfrak{S}$. Generally the Lennard-Jones interaction potentials are used

$$\varphi_{kl} = 4\epsilon_{kl}\Big[\big(\frac{\sigma_{kl}}{r}\big)^{12} - \big(\frac{\sigma_{kl}}{r}\big)^{6}\Big], \tag{3.9.1}$$

where σ_{kl} denotes the collision diameter, ϵ_{kl} the potential well depth, and r the distance between the molecules. Molecular parameters ϵ_{kl} and σ_{kl}, for $k,l \in \mathfrak{S}$, are usually expressed in terms of pure species parameters ϵ_k and σ_k, for $k \in \mathfrak{S}$. The mixture contains exclusively non polar molecules and for such molecules, the collision diameter and the potential well depth read

$$\frac{\epsilon_{kl}}{k_{\mathrm{B}}} = \sqrt{\big(\frac{\epsilon_k}{k_{\mathrm{B}}}\big)\big(\frac{\epsilon_l}{k_{\mathrm{B}}}\big)}, \tag{3.9.2}$$

$$\sigma_{kl} = \frac{1}{2}(\sigma_k + \sigma_l). \tag{3.9.3}$$

The transport linear systems are generally expressed in terms of collision integrals which are functions of the state variables and of molecular parameters. These quantities are integrals along collision paths between pairs of molecules which naturally appear in the expression of transport linear systems and which depend on the dynamics of intermolecular collisions and thus on species pairs [CC70] [FK72] [EG94]. The species collision numbers ξ_k^{int} at 298 K, $k \in \mathcal{P}$, where $\mathcal{P}$ denotes the set of polyatomic species, are also required for the evaluation of transport coefficients [EG94]. These collision numbers are associated with energy transfer either between translational degrees of freedom and internal degrees of freedom or between internal degrees of freedom [EG94] [Gio99], and arise under the common assumption that complex collisions, i.e., collisions in which there are more than one quantum jumps, may be neglected [MM62] [MPM65] [EG94].

In this work, the pure species transport properties and the collision integrals needed were calculated using approximation formulas and a software written at the SANDIA National Laboratories [KDLW$^+$86]. Lennard-Jones interaction potentials are used as in the benchmark model by Kleijn [Kle00]. The molecular species parameters have been taken from [KDLW$^+$98], and are listed in Table 3.2.

The different approximations chosen for each transport coefficient are detailed in the remaining of this section.

3.9.2 Shear viscosity

In the benchmark model by Kleijn [Kle00], the shear viscosity η is evaluated from Wilke's empirical formula [Wil50] [KDLW$^+$98]

$$\eta^{\mathrm{Wilke}} = \sqrt{8}\sum_{k\in\mathfrak{S}} \frac{X_k\eta_k}{\sum_{l\in\mathfrak{S}} X_l(1+\mathfrak{m}_k/\mathfrak{m}_l)^{-1/2}\big(1+(\eta_k/\eta_l)^{1/2}(\mathfrak{m}_l/\mathfrak{m}_k)^{1/4}\big)^2}, \tag{3.9.4}$$

where η_k, $k \in \mathfrak{S}$, denote the pure species shear viscosities.

Table 3.2 – Molecular parameters adopted for the present model.

k	Species	ϵ_k/k_B (K)	σ_k (Å)	ξ_k^{int}(298 K)
1	H	145.0	2.050	
2	H_2	38.0	2.920	280.0
3	Si	3,036.0	2.910	
4	Si_2	3,036.0	3.280	1.0
5	Si_3	3,036.0	3.550	1.0
6	SiH	95.8	3.662	1.0
7	SiH_2	133.1	3.803	1.0
8	SiH_3	170.3	3.943	1.0
9	SiH_4	207.6	4.084	1.0
10	Si_2H_2	323.8	4.383	1.0
11	Si_2H_3	318.2	4.494	1.0
12	H_3SiSiH	312.6	4.601	1.0
13	H_2SiSiH_2	312.6	4.601	1.0
14	Si_2H_5	306.9	4.717	1.0
15	Si_2H_6	301.3	4.828	1.0
16	Si_3H_8	331.2	5.562	1.0
17	He	10.2	2.576	

However, as shown by Ern and Giovangigli [EG96b] [Gio99], even a direct resolution of the symmetric linear system associated with the first "natural" variational space for the shear viscosity, namely the space of size n^s spanned by the basis functions

$$\phi^{2000k} = \big((\boldsymbol{w}_k \otimes \boldsymbol{w}_k - \frac{1}{3}\boldsymbol{w}_k \cdot \boldsymbol{w}_k \, \mathbb{I})\delta_{kl}\big)_{l\in\mathfrak{S}}, \qquad k \in \mathfrak{S}, \tag{3.9.5}$$

is less computationally expensive than Wilke's formula which involves fourth order roots. Thus, we prefer applying one step of the conjugate gradient method to the corresponding linear system, which is faster than a direct numerical inversion, while still ten times more accurate than Wilke's formula [EG94] [EG95a] [EG96a].

3.9.3 Diffusion coefficients

The diffusion coefficients are approximated by the first order diffusion coefficients [Gio91] [EG94] [Gio99]

$$D = D^{[0]},$$

associated with the projection of the perturbed distribution functions $\boldsymbol{\Phi}^{D_i}$, $i \in \mathfrak{S}$, on the variational space of size n^s spanned by the functions

$$\phi^{1000k} = \big(\boldsymbol{w}_k \delta_{kl}\big)_{l\in\mathfrak{S}}, \qquad k \in \mathfrak{S}. \tag{3.9.6}$$

The corresponding transport linear system is made of n^s systems of order n^s indexed by $i \in \mathfrak{S}$, of the form

$$\Delta\alpha^{D_i} = \beta^{D_i} \tag{3.9.7}$$

$$\alpha^{D_i} \in Y^{\perp}, \tag{3.9.8}$$

where $Y = (Y_k)_{k\in\mathfrak{S}}$ is the mass fraction vector. The system matrix Δ is common to the n^s linear systems, and is given by

$$\Delta_{kk} = \sum_{\substack{l\in\mathfrak{S}\\ l\neq k}} \frac{X_k X_l}{\mathcal{D}^{\text{bin}}_{k,l}}, \qquad k \in \mathfrak{S}, \tag{3.9.9}$$

$$\Delta_{kl} = -\frac{X_k X_l}{\mathcal{D}^{\text{bin}}_{k,l}}, \qquad k,l \in \mathfrak{S}, \quad k \neq l, \tag{3.9.10}$$

where $\mathcal{D}^{\text{bin}}_{k,l}$ is the binary diffusion coefficient for species pair (k,l), which only depends on T and p. The right hand terms of (3.9.7) are given by

$$\beta_k^{D_i} = \delta_{ki} - \frac{Y_k}{\sum_{j\in\mathfrak{S}} Y_j}, \qquad k \in \mathfrak{S}. \tag{3.9.11}$$

Finally, the approximate diffusion coefficients are evaluated from the following expressions [EG94] [Gio99]

$$D^{[0]}_{ij} = \langle \alpha^{D_i}, \beta^{D_j} \rangle = \langle \alpha^{D_j}, \beta^{D_i} \rangle = \alpha_j^{D_i} = \alpha_i^{D_j}, \qquad i,j \in \mathfrak{S}. \tag{3.9.12}$$

From the preceding relations, and from equation (3.6.18), where D has been replaced by $D^{[0]}$, the classical Stefan-Maxwell [Wil58] [DL68] [Gio90] equations are retrieved

$$\boldsymbol{d}_k + \chi_k \boldsymbol{\partial}_{\boldsymbol{x}} \ln T = \sum_{\substack{l\in\mathfrak{S}\\ l\neq k}} \frac{X_k X_l}{\mathcal{D}^{\text{bin}}_{k,l}} \boldsymbol{\mathcal{V}}_l - \Big(\sum_{\substack{l\in\mathfrak{S}\\ l\neq k}} \frac{X_k X_l}{\mathcal{D}^{\text{bin}}_{k,l}} \Big) \boldsymbol{\mathcal{V}}_k, \qquad k \in \mathfrak{S}, \tag{3.9.13}$$

$$\sum_{l\in\mathfrak{S}} Y_l \boldsymbol{\mathcal{V}}_l = \boldsymbol{0}. \tag{3.9.14}$$

Thus, evaluation of the first order transport coefficients $D^{[0]}$ is equivalent to solving the constrained linear system (3.9.7)-(3.9.8) or, equivalently, to inverting the Stefan-Maxwell equations (3.9.13)-(3.9.14) for the diffusion velocities. A more precise description of the mathematical properties associated with the Stefan-Maxwell equations may be found in [Gio90] [Gio91] [EG94].

Kleijn [Kle00] also considers the Stefan-Maxwell equations corresponding to the first order diffusion coefficients $D^{[0]}$, and proceeds by a direct inversion of a nonsymmetric form of the corresponding linear system [KDLW$^+$98]. Conversely, we have applied two steps of a projected standard iterative method to approximate the diffusion coefficients [EG96a], which is ten times to hundred times faster [EG96b] and should remain within tenths of a percent accuracy with respect to the exact solution [EG94].

3.9.4 Thermal conductivity and thermal diffusion ratios

It is worth noting that in reference [Kle00] the so-called "thermal conductivity λ" actually refers to the *partial* thermal conductivity defined above as $\hat{\lambda}$. This difference of nomenclature is also observable in the Chemkin Transport Package [KDLW$^+$98], which is the reference cited by Kleijn, where the quantity "λ_0" is called the "thermal conductivity", but actually stands for the *partial* thermal conductivity. The original papers by Monchick, Yun and Mason [MYM63] and Dixon-Lewis [DL68], however, make a clear distinction between the partial thermal conductivity, denoted by "λ_0", and the thermal conductivity, denoted by "λ_∞". As well, the thermal diffusion coefficients D^{T}_k defined by Kleijn [Kle00] following [MYM63] [DL68] [KDLW$^+$98] differ from our definition by the factor ρY_k

$$D^{\text{T}}_k = \rho Y_k \theta_k, \qquad k \in \mathfrak{S}, \tag{3.9.15}$$

as shown in [EG94]. Having this in mind, we conserve in the following the notations and terminology adopted in the preceding sections.

We denote by $\hat{\lambda}^{[1]}$, $\theta^{[1]}$, $D^{[1]}$ the first-order partial thermal conductivity, thermal diffusion vector, and diffusion matrix derived from the resolution of the constrained linear system arising from the projection of the perturbed distribution functions $\mathbf{\Phi}^{\hat{\lambda}}$, and $\mathbf{\Phi}^{D_l}$, $l \in \mathfrak{S}$, on the variational space [EG94]

$$\mathcal{A}^D = \mathcal{A}^{\hat{\lambda}} = \mathrm{Span}\big(\phi^{1000\mathrm{k}},\, \mathrm{k} \in \mathfrak{S}, \quad \phi^{1010\mathrm{k}},\, \mathrm{k} \in \mathfrak{S}, \quad \phi^{1001\mathrm{k}},\, \mathrm{k} \in \mathcal{P}\big),$$

where the ϕ^{1000k}, $k \in \mathfrak{S}$, were given in (3.9.6), and where

$$\phi^{1010k} = \big((\frac{5}{2} - \boldsymbol{w}_k \cdot \boldsymbol{w}_k)\boldsymbol{w}_k \delta_{kl}\big)_{l\in\mathfrak{S}}, \qquad k \in \mathfrak{S} \tag{3.9.16}$$

$$\phi^{1001k} = \big((\overline{\epsilon}_k - \epsilon_{k\mathrm{K}})\boldsymbol{w}_k \delta_{kl}\big)_{l\in\mathfrak{S}}, \qquad k \in \mathcal{P}. \tag{3.9.17}$$

The set $\mathcal{P}$ is the indexing set for polyatomic molecules, $n^{\mathcal{P}}$ the number of polyatomic molecules, and $\overline{\epsilon}_k = \overline{E}_k / k_{\mathrm{B}} T$, $k \in \mathcal{P}$. In particular, $D^{[1]}$ is a higher order of approximation than $D^{[0]}$ for the multicomponent diffusion matrix D.

In the benchmark model [Kle00], the partial thermal conductivity $\hat{\lambda}$ and the thermal diffusion vector $\theta = (\theta_k)_{k\in\mathfrak{S}}$ are evaluated through the direct matrix inversion of the first-order linear system of size $2n^s + n^{\mathcal{P}}$ associated with the variational space $\mathcal{A}^{\hat{\lambda}}$ described above, while D is approximated by $D^{[0]}$ instead of $D^{[1]}$.

The space $\mathcal{A}^{\hat{\lambda}}$ can be decomposed into

$$\mathcal{A}^{\hat{\lambda}} = \mathrm{Span}\big(\phi^{1000\mathrm{k}},\, \mathrm{k} \in \mathfrak{S}\big) \oplus \mathcal{A}^{\lambda}, \tag{3.9.18}$$

where

$$\mathcal{A}^{\lambda} = \mathrm{Span}\big(\phi^{1010\mathrm{k}},\, \mathrm{k} \in \mathfrak{S}, \quad \phi^{1001\mathrm{k}},\, \mathrm{k} \in \mathcal{P}\big). \tag{3.9.19}$$

Ern and Giovangigli [EG95b] have shown that approximating $\hat{\lambda}$, θ, D by $\hat{\lambda}^{[1]}$, $\theta^{[1]}$, $D^{[1]}$, respectively, and defining the approximate thermal conductivity $\lambda^{[1]}$ and thermal diffusion ratios $\chi_k^{[1]}$, $k \in \mathfrak{S}$, by

$$\begin{cases} D^{[1]}\chi^{[1]} = \theta^{[1]}, \\ \displaystyle\sum_{k\in\mathfrak{S}} \chi_k^{[1]} = 0, \end{cases} \tag{3.9.20}$$

$$\lambda^{[1]} = \hat{\lambda}^{[1]} - \frac{p}{T} \sum_{k\in\mathfrak{S}} \theta_k^{[1]} \chi_k^{[1]}, \tag{3.9.21}$$

is actually equivalent to approximating D by $D^{[1]}$, and λ and χ from the projection of the perturbed distribution function on the variational space $\mathcal{A}^{\lambda}$ of size $n^s + n^{\mathcal{P}}$.

In other words, the variational space associated with the evaluation of λ and χ uncouples from the variational space for D. Therefore, we have kept the approximation $D = D^{[0]}$ as in [Kle00] for the diffusion matrix, but we have chosen the first-order expression for the thermal conductivity and thermal diffusion ratios

$$\lambda = \lambda^{[1]} \tag{3.9.22}$$

$$\chi_k = \chi_k^{[1]}, \qquad k \in \mathfrak{S}, \tag{3.9.23}$$

instead of approximating the partial thermal conductivity and thermal diffusion vector by expressions $\hat{\lambda}^{[1]}$ and $\theta^{[1]}$, as in the benchmark model [Kle00]. Indeed, there is no reason for neglecting the translational and internal energy when expanding $\mathbf{\Phi}^{D_l}$ for the calculation of the diffusion coefficients, but not neglecting it for the calculation of $\hat{\lambda}$ and θ.

3.10 Boundary Conditions

We consider now the CVD reactor model illustrated in Figure 3.1 for which we specify relevant boundary conditions compatible with the self similar formulation. The substrate is at $z = 0$, while $z = L$ corresponds to the injection plane.

The temperature at the substrate boundary is assumed constant and equal to

$$T|_{t,0} = T^{\mathrm{s}}, \tag{3.10.1}$$

and the temperature at the inlet boundary is equal to the temperature of the inlet gas mixture

$$T|_{t,L} = T^{\mathrm{in}}. \tag{3.10.2}$$

The inlet flux is assumed to be perfectly normal, since the gas mixture is injected through a showerhead. Besides, the condition of adherence on the substrate can reasonably be assumed for such atmospheric pressure flows with convection velocities around 10 cm.s^{-1}. Thus the boundary conditions for the tangential velocity read

$$\tilde{u}|_{t,0} = 0, \tag{3.10.3}$$
$$\tilde{u}|_{t,L} = 0. \tag{3.10.4}$$

The inlet boundary conditions for the species mass fractions are those of a porous wall

$$\big(Y_k\tilde{w} + \mathcal{F}_k\big)\big|_{t,L} = Y_k^{\mathrm{in}}\tilde{w}^{\mathrm{in}}, \qquad k \in \mathfrak{S}, \tag{3.10.5}$$

where $\tilde{w}^{\mathrm{in}} = \tilde{w}|_{t,L}$ is the inlet mass flow, assumed continuous at the interface and Y_k^{in}, $k \in \mathfrak{S}$ are the species mass fractions in the injected mixture.

The boundary conditions for the species mass fractions at the substrate are those of a catalytic plate

$$\big(Y_k\tilde{w} + \mathcal{F}_k\big)\big|_{t,0} = m_k\widehat{\omega}_k, \qquad k \in \mathfrak{S}, \tag{3.10.6}$$

where $\widehat{\omega}_k$ is the surface molar production rate of the k^{th} species.

Physically speaking, the normal velocity is constrained at both ends of the reactor, inlet and substrate. Indeed, if we neglect the slight variation of the substrate position along the z axis due to surface growth, the normal velocity at the substrate must be zero or equal to the Stefan flux

$$\tilde{w}|_{t,0} = \sum_{k\in\mathfrak{S}} m_k\widehat{\omega}_k \tag{3.10.7}$$

associated with surface deposition [Gio99] [Kle00] [KCG03]. On the other hand, the inlet velocity is imposed by the experimentator. Thus, two boundary conditions are specified for the normal velocity equation (3.8.22), which is only of order one in $\tilde{w}$. The excess boundary condition actually determines the scalar α. Two methods are then possible in practice. As a first method, the normal velocity is specified at both ends of the reactor, while the strain rate α is treated as an eigenvalue of the boundary-value problem [KCG03]. Alternatively, the normal mass flux at the substrate is set equal to the Stefan flux (3.10.7), and the strain rate α is given as an input parameter to the numerical solver, while the inlet normal velocity is left unkown. Several numerical simulations are then run for different values of α until the steady-state normal velocity at the upper boundary approaches the specified value $\tilde{w}|_{t,L} = \tilde{w}^{\mathrm{in}}$. The latter method is the method used in this work.

3.11 Surface Chemistry

The computation of the molar deposition rates $\widehat{\omega}_k$, $k \in \mathfrak{S}$, appearing in the substrate boundary condition (3.10.6) requires the choice of a surface reaction mechanism.

We consider a set $\widehat{\mathscr{R}}$ of heterogeneous reactions describing the deposition process, in the form

$$\sum_{l \in \mathfrak{S} \cup \widehat{\mathfrak{S}}} \widehat{\nu}_l^{\mathrm{rf}}\, \mathfrak{M}_l \rightleftharpoons \sum_{l \in \mathfrak{S} \cup \widehat{\mathfrak{S}}} \widehat{\nu}_l^{\mathrm{rb}}\, \mathfrak{M}_l, \quad r \in \widehat{\mathscr{R}}, \tag{3.11.1}$$

where $\widehat{\mathfrak{S}}$ denotes the set of surface species, and $\widehat{\nu}_l^{\mathrm{rf}}$ and $\widehat{\nu}_l^{\mathrm{rb}}$ denote the forward and backward stoichiometric coefficients of the l^{th} species in the r^{th} surface reaction, respectively. The molar surface production rate is then computed from the rates of progress $\widehat{\tau}_r$, $r \in \widehat{\mathscr{R}}$

$$\widehat{\omega}_k = \sum_{r \in \widehat{\mathscr{R}}} (\widehat{\nu}_k^{\mathrm{rf}} - \widehat{\nu}_k^{\mathrm{rb}})\, \widehat{\tau}_r, \qquad k \in \mathfrak{S} \cup \widehat{\mathfrak{S}}. \tag{3.11.2}$$

Table 3.3 – Heterogeneous reaction mechanism adopted for the present model and corresponding sticking probabilities [CKM86] [Kle00].

r	k_r	**Surface reaction**	s_{k_r}
1	3	$Si(g) \longrightarrow Si(s)$	1.0
2	6	$SiH(g) \longrightarrow Si(s) + H(g)$	1.0
3	7	$SiH_2(g) \longrightarrow Si(s) + H_2(g)$	1.0
4	8	$SiH_3(g) \longrightarrow Si(s) + H_2(g) + H(g)$	1.0
5	9	$SiH_4(g) \longrightarrow Si(s) + 2H_2(g)$	4.44×10^{-6}
6	4	$Si_2(g) \longrightarrow 2Si(s)$	1.0
7	10	$Si_2H_2(g) \longrightarrow 2Si(s) + H_2(g)$	1.0
8	11	$Si_2H_3(g) \longrightarrow 2Si(s) + H_2(g) + H(g)$	1.0
9	12	$H_3SiSiH(g) \longrightarrow 2Si(s) + 2H_2(g)$	1.0
10	13	$H_2SiSiH_2(g) \longrightarrow 2Si(s) + 2H_2(g)$	1.0
11	14	$Si_2H_5(g) \longrightarrow 2Si(s) + 2H_2(g) + H(g)$	1.0
12	15	$Si_2H_6(g) \longrightarrow 2Si(s) + 3H_2(g)$	4.44×10^{-5}
13	5	$Si_3(g) \longrightarrow 3Si(s)$	1.0
14	16	$Si_3H_8(g) \longrightarrow 3Si(s) + 4H_2(g)$	0.0

The reactions considered are assumed to be irreversible, in the form

$$Si_nH_{2m}(g) \longrightarrow nSi(s) + mH_2(g), \tag{3.11.3}$$

$$Si_nH_{2m+1}(g) \longrightarrow nSi(s) + mH_2(g) + H(g). \tag{3.11.4}$$

Thus, each surface reaction $r \in \widehat{\mathscr{R}}$ is associated with a unique gas-phase reactant species $k_r \in \mathfrak{S}$. The rate of progress of reaction $r \in \widehat{\mathscr{R}}$ is simply the consumption rate of species number k_r at the surface, expressed as its thermal flux towards the wall [MW60] [McD64] [CKM86] [Kle00]

$$\widehat{\tau}_r = \frac{s_{k_r}}{1 - \frac{s_{k_r}}{2}} \gamma_{k_r} \sqrt{\frac{RT}{2\pi m_{k_r}}}, \qquad r \in \widehat{\mathscr{R}}, \tag{3.11.5}$$

where $\gamma_{k_r} = \rho Y_{k_r}/m_{k_r}$ is the molar concentration of the depositing species, and s_{k_r} is its sticking coefficient. The reactive probability s_{k_r} is adjusted by the factor $1 - s_{k_r}/2$ in order to remain valid

in the limit $s_{k_r} \to 1$, where nearly all the molecules of species k_r stick to the wall without being reflected [MW60] [KCG03].

The silicon deposition rate associated with each surface reaction $r \in \widehat{\mathscr{R}}$ is then given by

$$w^r_{\mathrm{Si(s)}} = \mathrm{V}^{\mathrm{Si}}_{\mathrm{m}}\, \widehat{\nu}^{r\mathrm{b}}_{\mathrm{Si(s)}} \widehat{\tau}_r, \tag{3.11.6}$$

where $\widehat{\nu}^{r\mathrm{b}}_{\mathrm{Si(s)}}$ is the backward stoichiometric coefficient of Si(s) in the r^{th} surface reaction, and $\mathrm{V}^{\mathrm{Si}}_{\mathrm{m}}$ is the molar volume of crystalline silicon

$$\mathrm{V}^{\mathrm{Si}}_{\mathrm{m}} \simeq 12.06 \text{ cm}^3.\text{mol}^{-1}, \tag{3.11.7}$$

and, consequently, the total silicon deposition rate reads

$$w_{\mathrm{Si(s)}} = \sum_{r \in \widehat{\mathscr{R}}} w^r_{\mathrm{Si(s)}} = \mathrm{V}^{\mathrm{Si}}_{\mathrm{m}}\, \widehat{\omega}_{\mathrm{Si(s)}}. \tag{3.11.8}$$

The sticking coefficients have been taken from [CKM86], as described in the benchmark model [Kle00]. The list of surface reactions and the corresponding sticking coefficients are given in Table 3.3. The values correspond to a substrate temperature of $T^{\mathrm{s}} = 1000$ K.

The surface reaction mechanism can be very complex and include adsorption, desorption, complex surface reactions between surface species only or involving also gas-phase species. The accurate description of surface deposition requires an appropriate surface reaction scheme, along with the corresponding thermodynamic and reaction data [KCG03]. The present surface reaction mechanism is thus a first step towards a more consistent numerical modeling of the deposition process.

3.12 Numerical Method

Equations (3.8.22)-(3.8.25) are discretized over a grid along the z axis of the form

$$Z = \{0 = z_1 < z_2 < \cdots < z_N = L\}, \tag{3.12.1}$$

where N is the number of grid points. We denote by $n^c = n^s + 3$ the number of unknowns. The solution vector is denoted by

$$\Xi = (\Xi_l)_{1 \le l \le n^c} = (T, \tilde{u}, \tilde{v}, Y_1, \ldots, Y_{n^s}), \tag{3.12.2}$$

and the discretized solution vector is denoted by

$$\Xi_Z = (\Xi_{l,i})_{1 \le l \le n^c, 1 \le i \le N}, \tag{3.12.3}$$

where $\Xi_{l,i} = \Xi_l(z_i)$. The discretized equations are obtained from a three-point finite difference scheme. The time derivatives are discretized in a fully implicit manner. The convective terms appearing in the equations for the tangential velocity, the species mass fractions, and the temperature, are treated by means of an upwind scheme [Pat80].

The steady discretized equations consist in a system of $N \times (n^s + 3)$ nonlinear algebraic equations, of the form

$$F_Z(\Xi_Z) = 0. \tag{3.12.4}$$

A modified Newton method is applied to the latter system of discretized equations. The corresponding iterates are given as

$$J(\Xi^k_Z)(\Xi^{k+1}_Z - \Xi^k_Z) = -\lambda_k F_Z(\Xi^k_Z), \qquad k = 0, 1, 2 \ldots, \tag{3.12.5}$$

where Ξ_Z^k is the k^{th} Newton iteration, λ_k the k^{th} damping parameter calculated according to the method of Deuflhard [Deu74], and where

$$J(\Xi_Z^k) = \frac{\partial F_Z}{\partial \Xi_Z}(\Xi_Z^k) \tag{3.12.6}$$

denotes the Jacobian matrix evaluated at Ξ_Z^k.

The Jacobian matrix is obtained from the evaluation of the finite differences of F_Z

$$J(\Xi_Z)U = \frac{F_Z(\Xi_Z + \delta U) - F_Z(\Xi_Z)}{\delta} \tag{3.12.7}$$

along vectors of the form $U = U^{k_0,n_0}$, indexed by $k_0 \in \{1,\dots,n^c\}$ and $n_0 \in \{1,2,3\}$. For each $k_0 \in \{1,\dots,n^c\}$ and $n_0 \in \{1,2,3\}$, the vector $U^{k_0,n_0} = (U_{ln})_{k\in\{1,\dots,n^c\},n\in\{1,\dots,N\}}$ is taken such that its only nonzero components U_{ln} are those for which $k = k_0$ and $n \equiv n_0 \pmod 3$. Consequently, the evaluation of the Jacobian matrix requires merely $3n^c + 1$ evaluations of F_Z. Furthermore, the thermochemical properties, namely the molar production rates and transport coefficients, need only be evaluated every three points when evaluating the perturbed terms $F_Z(\Xi_Z + \delta U)$, provided that $F_Z(\Xi_Z)$ has been evaluated first.

Also, due to the use of a three-point discretization scheme, the numerical Jacobian is banded, that is the Jacobian matrix consists in blocks whose nonzero elements appear only in the first three diagonals. The numerical inversion of such a matrix can be considerably simplified by using an appropriate decomposition method given by linear algebra.

The steady equations (3.12.4) are solved by the Newton method after a specified number of non-stationary iterations, provided the non-stationary solution has approached sufficiently the domain of convergence of the steady equations. The non-stationary equations for the n^{th} iteration at time t may be written in the form

$$A(\Xi_Z^n)\,\partial_t \Xi_Z^n + F_Z(\Xi_Z^n) = 0, \tag{3.12.8}$$

were Ξ_Z^n denotes the n^{th} iterate over the grid Z, $A(\Xi_Z^n)$ is a bloc diagonal matrix, and

$$\partial_t \Xi_Z^n = \frac{\Xi_Z^n - \Xi_Z^{n-1}}{t^n - t^{n-1}} \tag{3.12.9}$$

is the discretized time derivative at time t^n. These implicit non-stationary equations are solved by the Newton method, making use of the following Euler predictor

$$\widetilde{\Xi}_Z^n = \Xi_Z^{n-1} + \Delta t^n\, \partial_t \Xi_Z^{n-1}. \tag{3.12.10}$$

Accordingly, the time step at iteration n, $\Delta t^n = t^n - t^{n-1}$, is chosen such that

$$\left\| \Xi_Z^n - \widetilde{\Xi}_Z^n \right\| \simeq \left\| \frac{1}{2}(\Delta t^n)^2\, \frac{\partial_t \Xi_Z^{n-1} - \partial_t \Xi_Z^{n-2}}{t^{n-1} - t^{n-2}} \right\| \leq \varepsilon, \tag{3.12.11}$$

where ε is taken smaller than 1.

3.13 Results and Discussion

The governing equations (3.8.22)-(3.8.25) for the axisymmetric strained CVD reactor are solved for the configuration presented in Figure 3.1. The inlet mixture is composed of 0.1 % silane diluted in helium, namely $X_{\text{SiH}_4} = 0.1$ % and $X_{\text{He}} = 99.9$ %. The pressure is constant and equal to $p_0 = 1$ atm. The inlet temperature is $T^{\text{in}} = 300$ K and the inlet normal velocity is $w^{\text{in}} = 10$ cm.s^{-1}. The strain rate α has been varied over several numerical simulation in order to obtain the specified normal

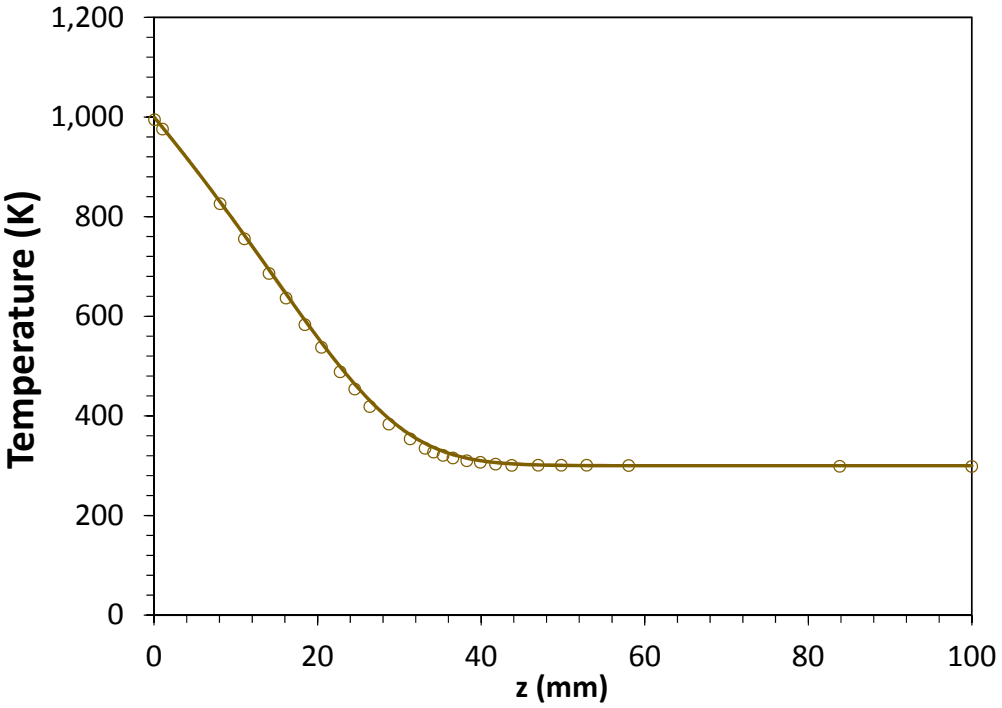

Figure 3.3 – Temperature profile along the axis of symmetry of the reactor. Continuous line, this work. Circles, simulations by Kleijn [Kle00].

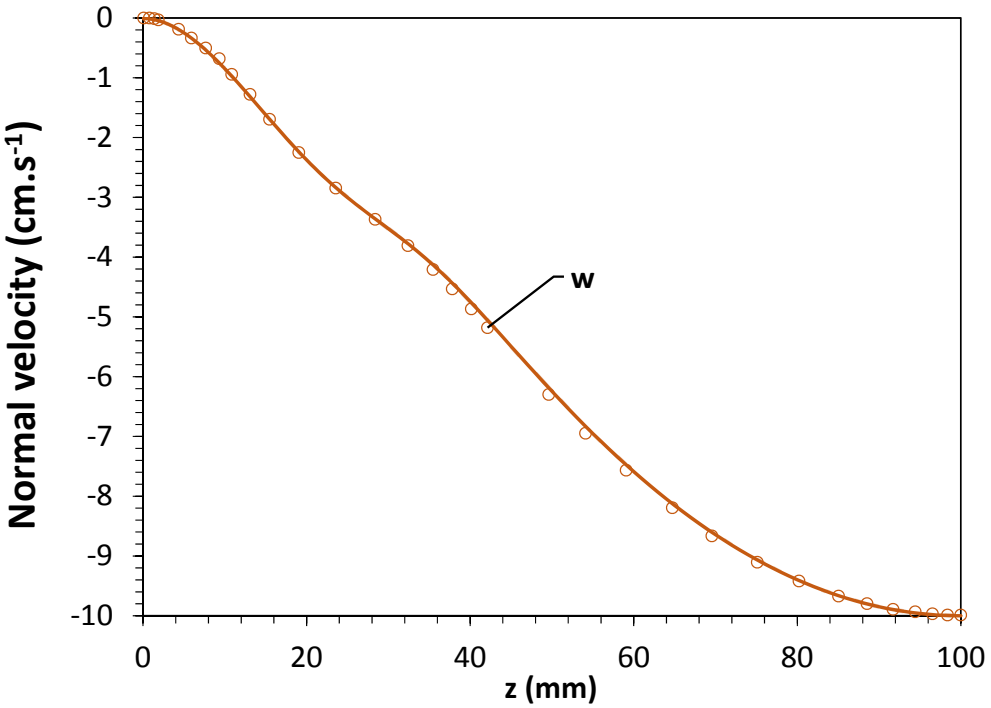

Figure 3.4 – Normal velocity profile along the z axis. Continuous line, this work. Circles, simulations by Kleijn [Kle00].

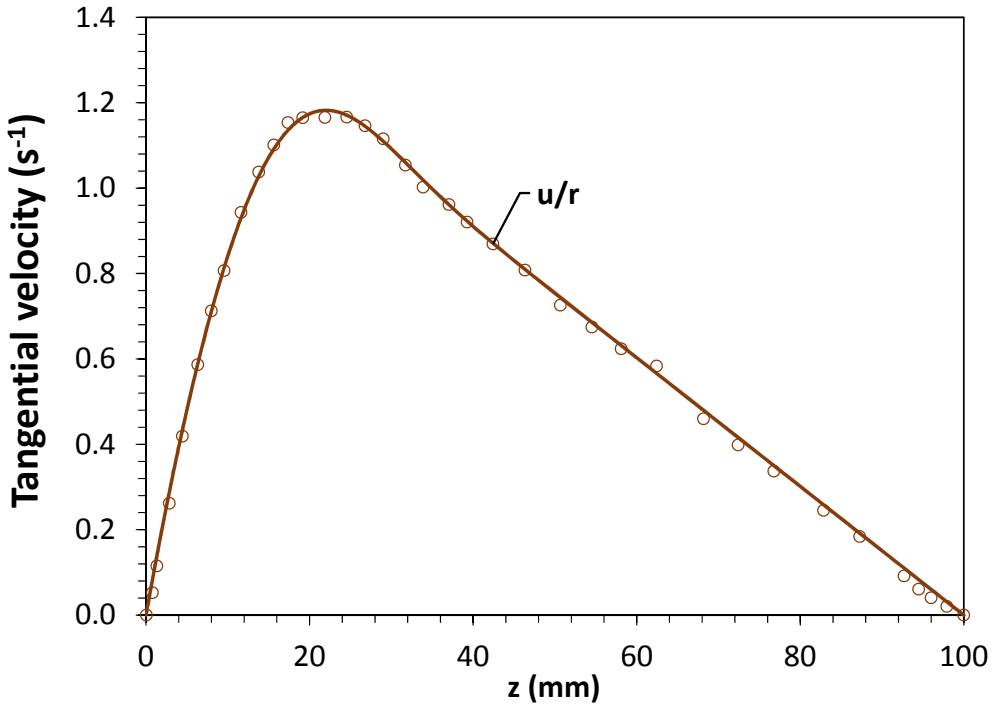

Figure 3.5 – Tangential velocity profile along the z axis. Continuous line, this work. Circles, simulations by Kleijn [Kle00].

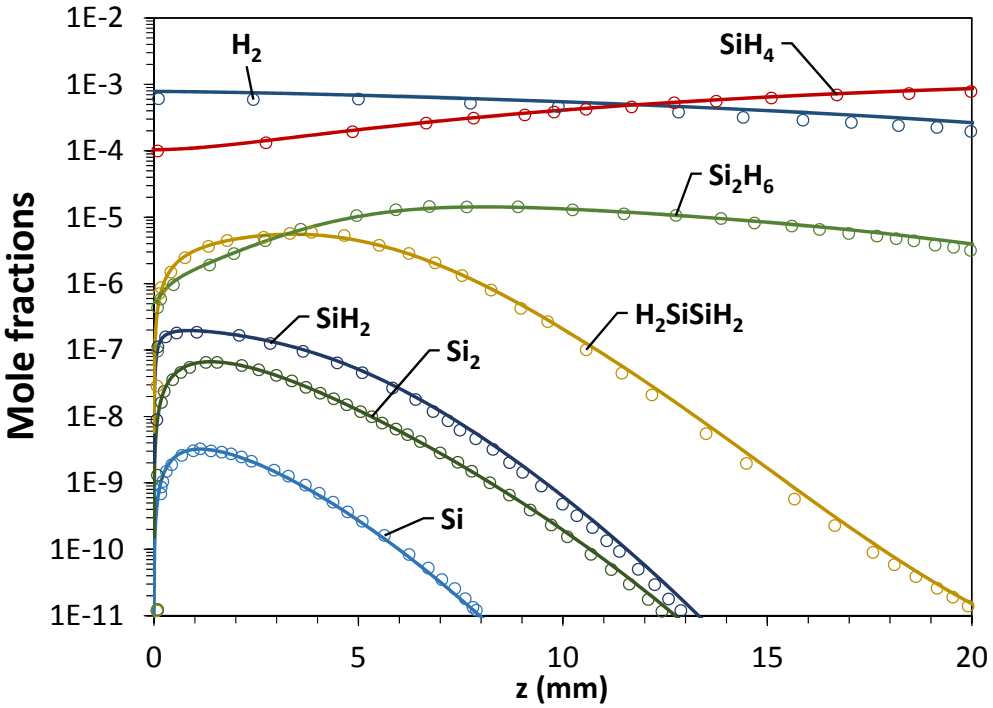

Figure 3.6 – Axial concentration profiles for some selected species. Continuous line, this work. Circles, simulations by Kleijn [Kle00].

inlet velocity of 10 cm.s^{-1}. The corresponding value is $\alpha = 1.22775$ s^{-1}. The substrate temperature is set at $T^{\mathrm{s}} = 1000$ K.

The axial profiles obtained for the temperature, the normal velocity, the tangential velocity, and the species mole fractions are compared to the results of the benchmark model presented in [Kle00]. The temperature profile along the axis of symmetry of the reactor is shown in Figure 3.3. Figures 3.4 and 3.5 show the normal and tangential velocity profiles, respectively. Finally, Figure 3.6 represents the mole fractions of several selected species close to the substrate.

The temperature profile shows a strong gradient in the vicinity of the substrate, associated with thermal conduction. Therefore, chemical reactions occur exclusively in a localized zone close to the substrate, where the temperature is sufficiently high to initiate silane dissociation. This is confirmed by the study of the species concentration profiles. Most of the silane dissociation occurs between $z = 0$ cm and $z = 0.2$ cm, and a significant silane depletion can be observed in this region. The deposition of the radicals on the substrate explains the very sharp gradients observed at the boundary. The radicals also diffuse backwards in the upstream direction, depending on their diffusion length.

The profiles in Figures 3.3-3.6 show an excellent agreement with the simulations of Kleijn [Kle00]. Also, the total deposition rate computed does not differ by more than 1 % from [Kle00]. The slight differences observed might be explained by different choices for approximation of transport coefficients, formulation of inlet boundary conditions, or discretization schemes. This validates the sofware developed against standard models for multicomponent reactive gas flows.

3.14 Conclusion

We have implemented a self-consistent model for chemical vapor deposition of crystalline silicon in an axisymmetric reactor. The equations for multicomponent reacting neutral gas flows have been stated, along with thermodynamic properties, chemistry mechanism and transport fluxes. Equations have then been expanded using the low Mach number approximation, and the strained flow equations have subsequently been derived as an exact self similar solution of the isobaric equations in axisymmetric coordinates. The expressions of transport coefficients have been recalled in section 3.9, and have been calculated by means of the library EGLIB [EG96a] using approximations similar to those made in the benchmark model [Kle00]. The boundary conditions have also been detailed in section 3.10, and the heterogeneous reactions mechanism has been taken from [Kle00]. The numerical methods presented in section 3.12 are slightly different from those used in the benchmark model [Kle00]. All equations are indeed coupled and discretized implicitly. A modified Newton method has been used for the resolution of the discretized equations.

The results of our numerical simulations are fully consistent with the benchmark model [Kle00] as well as with the standard SPIN software [CKE$^+$91], with an accuracy within a few percents. The species density profiles in the vicinity of the substrate are very close to the benchmark profiles. The maximum mole fraction of main species are also very close, as well as the deposition rate computed from surface fluxes on the substrate. This validates the software implemented in this chapter.

Chemical vapor deposition of silicon in general might be more complex than the process described in this chapter. In particular, we have restrained ourselves to the deposition of crystalline silicon for the purpose of software validation against the benchmark model [Kle00]. Besides, the nucleation of silicon nanoparticles might also occur under specific conditions, inducing thereby a drastic modification of the process properties.

In the next chapter, the software will be enriched and applied to the modeling of silane plasma discharges. This will require the incorporation of charged species, including electrons, which will be coupled to the electric field specified by Poisson's equation, as well as to the electron temperature equation. The set of species and the set of gas-phase chemical reactions will also be adapted to the plasma regime, where the gas temperature is in the range 300-500 K, while the electron temperature is of the order of a few electronvolts. Boundary conditions for charged species will also be taken into account with care, since the drift induced by the electric field might exceed by one order of magnitude the diffusion velocity.

Apart from these difficulties specific to plasma discharge modeling, the framework adopted in this Chapter, the general formulation of the model equations, including transport fluxes, chemistry mechanism, thermodynamic properties and boundary conditions, as well as the self similar formulation of strained flow equations, will remain unchanged. Also, the numerical methods employed in this Chapter are sufficiently robust and optimized to be used for the study of an industrial plasma reactor.

Bibliography

[CC70] S. Chapman and T. G. Cowling. *The Mathematical Theory of Non-Uniform Gases.* Cambridge University Press, Cambridge, 1970. 5, 11, 12, 14, 18, 20, 21, 32, 33, 47, 82, 88, 111, 118, 145, 153

[CDD+85] M. W. Chase, Jr., C. A. Davies, J. R. Downey, Jr., D. J. Frurip, R. A. McDonald, and A. N. Syverud. JANAF thermochemical tables: Third edition. *J. Phys. Chem. Ref. Data*, 14(Suppl. 1), 1985. 78

[Cha98] M. W. Chase, Jr. NIST-JANAF thermochemical tables: Fourth edition. *J. Phys. Chem. Ref. Data*, Monograph No. 9, 1998. 78, 79

[CKE89] M. E. Coltrin, R. J. Kee, and G. H. Evans. A mathematical model of the fluid mechanics and gas-phase chemistry in a rotating disk chemical vapor deposition. *J. Electrochem. Soc.*, 136(3):819–829, 1989. 81, 119

[CKE+91] M.E. Coltrin, R.J. Kee, G.H. Evans, E. Meeks, F.M. Rupley, and J.F. Grcar. A FORTRAN program for modeling one-dimensional rotating-disk/stagnation-flow chemical vapor deposition reactors. Technical Report SAND91-8003, SANDIA National Laboratories, 1991. 99

[CKM86] M. E. Coltrin, R. J. Kee, and J. A. Miller. A mathematical model of silicon chemical vapor deposition. *J. Electrochem. Soc.*, 133(6):1206–1213, 1986. 93, 94, 119

[Deu74] P. Deuflhard. A modified newton method for the solution of ill-conditioned systems of nonlinear equations with application to multiple shooting. *Numer. Math.*, 22(4):289–315, 1974. 95

[DL68] G. Dixon-Lewis. Flame structure and flame reaction kinetics: II. Transport phenomena in multicomponent systems. *Proc. Roy. Soc. A*, 307:111–135, 1968. 90

[EG94] A. Ern and V. Giovangigli. *Multicomponent Transport Algorithms*, volume m24 of *Lecture Notes in Physics Monographs*. Springer-Verlag, Berlin, 1994. 11, 17, 19, 69, 75, 79, 80, 82, 83, 88, 89, 90, 91, 110

[EG95a] A. Ern and V. Giovangigli. Fast and accurate multicomponent property evaluations. *J. Comp. Phys.*, 120(1):105–116, August 1995. 89

[EG95b] A. Ern and V. Giovangigli. Thermal conduction and thermal diffusion in dilute polyatomic gas mixtures. *Physica A*, 214(4):526–546, April 1995. 91

[EG96a] A. Ern and V. Giovangigli. EGLIB server and user's manual. http://www.cmap.polytechnique.fr/www.eglib/, 1996. 87, 89, 90, 99

[EG96b] A. Ern and V. Giovangigli. Optimized transport algorithms for flame codes. *Comb. Sci. Tech.*, 118:387–395, 1996. 89, 90

[FK72] J. H. Ferziger and H. G. Kaper. *Mathematical Theory of Transport Processes in Gases.* North-Holland Publishing Company, 1972. 11, 12, 14, 18, 20, 21, 32, 33, 47, 59, 82, 88, 118, 153

[GD88] V. Giovangigli and N. Darabiha. Vector computers and complex chemistry combustion. In C. Schmidt-Lainé C.-M. Brauner, editor, *Mathematical Modeling in Combustion and Related Topics*, volume 140 of *NATO ASI Series, Series E: Applied Sciences*, pages 491–503. Martinus Nijhoff Publishers, 1988. 81

[GGMM10] V. Giovangigli, B. Graille, T. E. Magin, and M. Massot. Multicomponent transport in weakly ionized mixtures. *Plasma Sources Sci. Technol.*, 19(3):034003, 2010. 5, 59, 69, 73

[Gio88] V. Giovangigli. Structure et extinction de flammes laminaires prémélangées. Doctorat ès Sciences, Université Paris 6, 1988. 85

[Gio90] V. Giovangigli. Mass conservation and singular multicomponent diffusion algorithms. *IMPACT Comput. Sci. Eng.*, 2(1):73–97, 1990. 90, 110

[Gio91] V. Giovangigli. Convergent iterative methods for multicomponent diffusion. *IMPACT Comput. Sci. Eng.*, 3(3):244–276, 1991. 89, 90

[Gio99] V. Giovangigli. *Multicomponent Flow Modeling*. MESST Series. Birkhauser, Boston, 1999. 5, 6, 13, 14, 15, 17, 18, 20, 32, 33, 47, 59, 73, 75, 76, 77, 79, 80, 82, 84, 85, 88, 89, 90, 92, 110, 111

[KCG03] R. J. Kee, M. E. Coltrin, and P. Glarborg. *Chemically Reacting Flow: Theory and Practice*. Wiley, 2003. 73, 87, 92, 94, 119

[KDLW+86] R. J. Kee, G. Dixon-Lewis, J. Warnatz, M. E. Coltrin, and J. A. Miller. A FORTRAN computer code package for the evaluation of gas-phase multicomponent transport properties. Technical Report SAND86–8246, SANDIA National Laboratories, 1986. 88, 111

[KDLW+98] R. J. Kee, G. Dixon-Lewis, J. Warnatz, M. E. Coltrin, J. A. Miller, and H. K. Moffat. A FORTRAN computer code package for the evaluation of gas-phase, multicomponent transport properties. Technical Report SAND86-8246B, SANDIA National Laboratories, 1998. 88, 90

[Kle95] C. R. Kleijn. *Computational Modeling in Semiconductor Processing*, chapter Chemical Vapor Deposition Processes, pages 97–216. Artech House, Boston, 1995. 73

[Kle00] C. R. Kleijn. Computational modeling of transport phenomena and detailed chemistry in chemical vapor deposition – a benchmark solution. *Thin Solid Films*, 365(2):294–306, 2000. 73, 74, 81, 88, 90, 91, 92, 93, 94, 96, 97, 98, 99

[KMEDL88] R. J. Kee, J. A. Miller, G. H. Evans, and G. Dixon-Lewis. A computational model of the structure and extinction of strained, opposed flow, premixed methane-air flames. In *Twenty-Second Symposium (International) on Combustion*, pages 179–1494. The Combustion Institute, 1988. 85

[Kra70] F. J. Krambeck. The mathematical structure of chemical kinetics. *Arch. Rational Mech. Anal.*, 38:317–347, 1970. 81

[KRM89] R. J. Kee, F. M. Rupley, and J. A. Miller. Chemkin-II: A FORTRAN chemical kinetics package for the analysis of gas-phase chemical kinetics. Technical Report SAND89-8009, SANDIA National Laboratories, 1989. 81

[KRM90] R. J. Kee, F. M. Rupley, and J. A. Miller. The Chemkin thermodynamic data base. Technical Report SAND87-8215B, SANDIA National Laboratories, 1990. 79

[LSYA94] C. K. Law, G. Sung, G. Yu, and R. L. Axelbaum. On the structural sensitivity of purely strained planar premixed flames to strain rate variations. *Combustion and Flame*, 98:139–154, 1994. 73

[McD64] E. W. McDaniel. *Collision Phenomena in Ionized Gases*. Wiley, 1964. 93, 118

[MM62] E. A. Mason and L. Monchick. Heat conductivity of polyatomic and polar gases. *J. Chem Phys.*, 36(6):1622–1639, 1962. 88

[MPM65] L. Monchick, A. N. G. Pereira, and E. A. Mason. Heat conductivity of polyatomic and polar gases and gas mixtures. *J. Chem. Phys.*, 42(9):3241–3256, 1965. 88

[MW60] H. Motz and H. Wise. Diffusion and heterogeneous reaction. III. Atom recombination at a catalytic boundary. *J. Chem. Phys.*, 32(6):1893–1894, 1960. 93, 94, 118, 119

[MYM63] L. Monchick, K. S. Yun, and E. A. Mason. Formal kinetic theory of transport phenomena in polyatomic gas mixtures. *Journal of Chemical Physics*, 39(3):654–669, 1963. 5, 11, 75, 90

[Pat80] S. V. Patankar. *Numerical Heat Transfer and Fluid Flow*. Series in Computational Methods in Mechanics and Thermal Sciences. McGraw-Hill, 1980. 94, 123, 124

[PV05] T. Poinsot and D. Veynante. *Theoretical and Numerical Combustion*. R. T. Edwards, 2nd edition, 2005. 73

[Smo13] M. D. Smooke. The computation of laminar flames. *Proceedings of the Combustion Institute*, 34(1):65–98, 2013. 73

[SP71] D. R. Stull and H. Prophet. *JANAF Thermochemical Tables: Second Edition*, volume NSRDS-NBS37. National Bureau of Standards, Washington, 1971. 78

[SS65] N. Z. Shapiro and L. S. Shapley. Mass action law and the gibbs free energy function. *SIAM J. Appl. Math.*, 13:353–375, 1965. 81

[Tol38] R. C. Tolman. *The Principles of Statistical Mechanics*. Oxford University Press, 1938. 81, 113

[Wil50] C. R. Wilke. A viscosity equation for gas mixtures. *J. Chem. Phys.*, 18(4):517–519, 1950. 88

[Wil58] F. A. Williams. Elementary derivation of the multicomponent diffusion equation. *Am. J. Phys.*, 26(7):467–469, 1958. 90

[WT62] L. Waldmann and E. Trübenbacher. Formale kinetische Theorie von Gasgemischen aus anregbaren Molekülen. *Zeitschr. Naturforschg.*, 17a:363–376, 1962. 5, 11, 13, 17, 18, 75, 82

Chapter 4

Simulation of a Silane-Hydrogen Radio-Frequency Plasma Discharge

4.1 Introduction

Plasma enhanced chemical vapor deposition, or "PECVD", is a low-temperature process which is routinely used to process high quality materials with various optical and electrical properties. The quality of the deposited material generally depends on the process parameters and the type of substrate used, and ranges from amorphous silicon to crystalline silicon, passing by microcrystalline, or so-called "polymorphous silicon" [RiCNTD$^+$07].

Self-consistent modeling of radio-frequency plasma discharges is crucial for the understanding and optimization of PECVD processes commonly employed in the fabrication of photovoltaic solar cells. As standard CVD, PECVD is a complex process involving many parameters, such as pressure, gas flow rates, or applied potential, which in turn drive many coupled physical quantities, several of which may be difficult to assess experimentally. The PECVD process is also more complex than the chemical vapor deposition process, because of the thermal non-equilibrium between electrons and heavy-species, the sharp potential barrier and the sharp electron temperature peaks accross the plasma sheaths, the strong coupling between charged-species diffusion and electric drift, and the strong coupling between the charged species and electric potential imposed by Poisson's equation. Due to this extreme complexity, and because experimental data on discharges under practical deposition conditions remain scarce, numerical simulation is highly desirable for the optimization of silane-hydrogen plasma discharges. In this chapter, we will consider a discharge in which nanoparticles are absent. The modeling of the nanoparticle dynamics and their coupling to other plasma parameters will be addressed in Chapter 5.

The numerical modeling of radio-frequency plasma discharges has been extensively studied over the last thirty years [BL04]. Two main methods are generally employed. For low pressures, due to the strong departure from local thermal equilibrium the resolution of the Boltzmann equation is necessary. In general, "particle in cell" or Monte Carlo methods are used. Conversely, when the pressure is too high, the Boltzmann equation becomes impractical due to the high species densities and collision frequencies, and a fluid model is required. Fluid models are generally valid for pressures above 500 mTorr [GJ86], which is the case of the process considered here.

One of the first fluid numerical model of radio-frequency discharge was developed by Graves and Jensen [GJ86], for a discharge containing two species, namely electrons and positive ions. The model solved the species continuity equations, coupled to the Poisson's equation for the electric potential, and the electron temperature equation, and was followed by many similar models for both electropositive and electronegative discharges [RTS87] [Boe87] [PE90].

Silane hydrogen mixtures are very reactive and produce many different radicals and species. Models taking into account such a complex chemistry have also been developed and implemented

numerically. For pure H_2 plasma a very detailed description of chemical kinetics can be obtained, including vibrational kinetics of H_2 [GCC+92], negative ion H^- and H atom kinetics, and a good agreement with experiments has been obtained [HGG99] [DEL+14]. Concerning silane discharges, due to the production of H_2 occurring from the dissociation of SiH_4, a correct chemical mechanism must include H_2 plasma chemistry. However, due to the large number of different molecules and ions appearing in silane discharges, the chemical kinetics are generally simplified compared to pure H_2 discharges. Several models have been proposed and some of them have been compared to experiments [Nie98] [dBGG04] [LAM06].

In this chapter, the model for non-thermal reactive plasma derived in Chapter 2 is simplified in order to describe silane-hydrogen radio-frequency plasma discharge in the Torr regime. The model includes thermal non-equilibrium, two-temperature chemistry, and coupling between charged species and electric potential. The model is then implemented numerically. The chemical vapor deposition software validated in Chapter 3 is enriched in order to model a radio-frequency silane-hydrogen plasma discharge. The fluid plasma equations are solved in axisymmetric geometry using a self similar model, taking into account a two-temperature hydrogen-silane plasma chemistry, including electron collision reactions and heavy-species reactions. The deposition process is also described by a simplified surface reaction mechanism. Results are presented for typical conditions used in low-temperature silicon epitaxy [RCL12]. A self-consistent computation of the DC bias potential is also implemented, allowing to study the effect of asymmetric excitation on silane-hydrogen capacitively coupled plasma discharges.

The radio-frequency process is described in section 4.2. In section 4.3, the governing equations are stated, along with expressions for the transport fluxes. In section 4.4, the model is simplified and a self similar formulation is derived. Transport coefficients are described in section 4.5, the chemistry mechanism in section 4.6, and the electron heavy-species energy exchange term in section 4.7. The boundary conditions are given in section 4.8, and the numerical method is presented in section 4.10. Results are presented in section 4.11.

4.2 Radio-Frequency Reactor

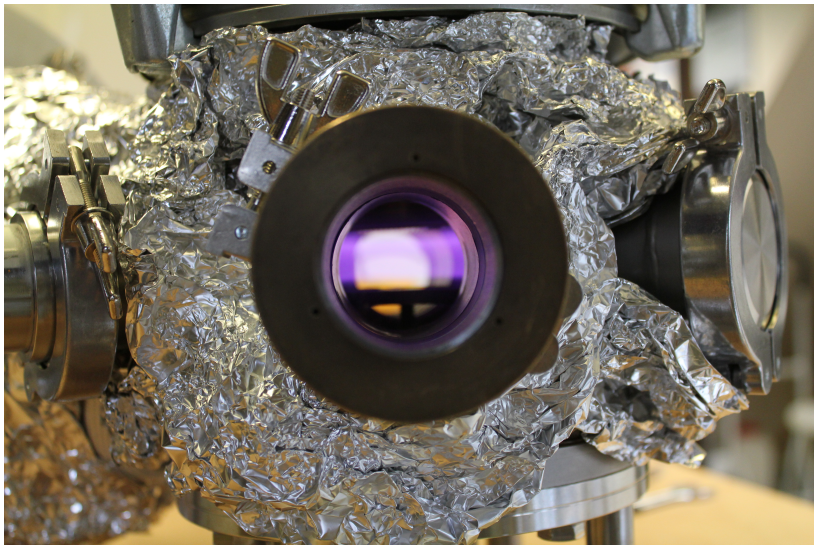

Figure 4.1 – Parallel plate radio-frequency plasma reactor from the GREMI laboratory, in Université d'Orléans.

A schematic representation of the radio-frequency reactor is shown in Figure 4.2. The reactor is

axisymmetric around the z axis, with corresponding polar coordinates r and θ. A silane-hydrogen gas mixture is injected through a showerhead with a normal inlet velocity. The lower electrode is grounded, while the upper electrode is driven by a periodic applied potential at a frequency of $f = 13.56$ MHz, which is the standard frequency used in industrial radio-frequency reactors.

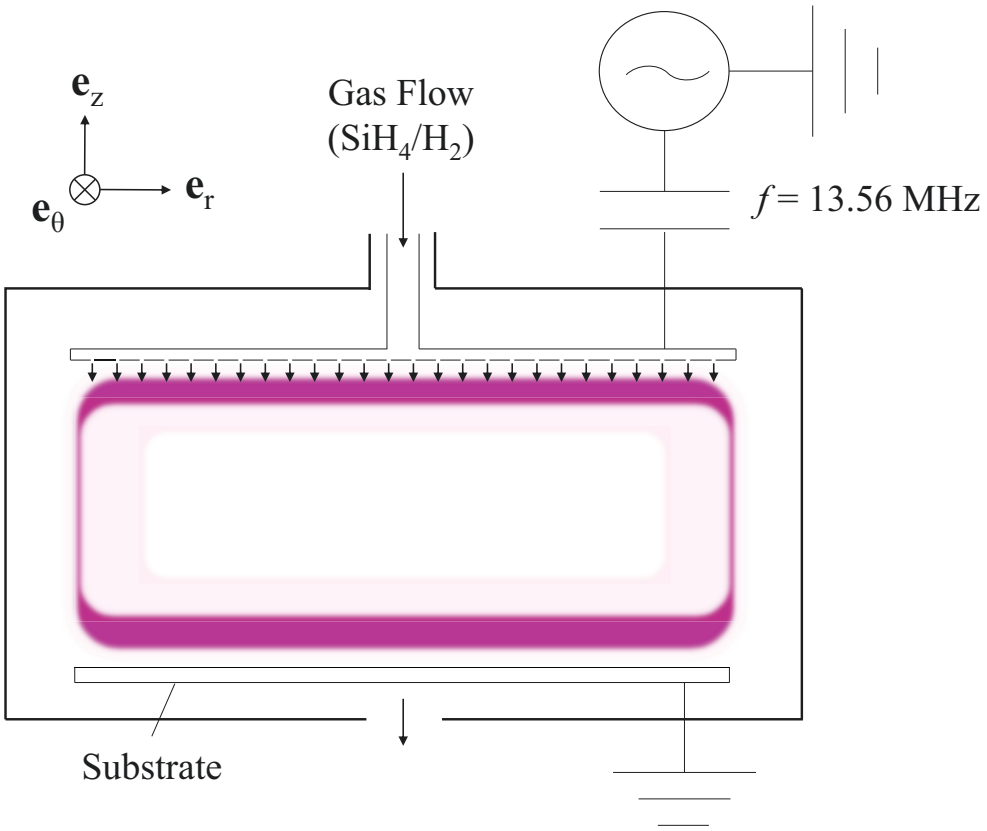

Figure 4.2 – Schematic representation of the axisymmetric radio-frequency reactor.

Before the plasma is ignited, a steady flow is established in the reactor with a prescribed uniform pressure. After ignition, the oscillating potential induces an oscillating electric field in the plasma region located near the electrodes, commonly referred to as the "plasma sheath". Conversely, the central region of the discharge, called the plasma bulk, is quasi-neutral. The oscillating electric field accelerates the electrons in the plasma sheaths, which collide with the heavier neutral carrier gases, inducing in turn ionization, dissociation, or attachment to the carrier gas. The mixture thus becomes weakly ionized, and subsequent chemical reactions produce radicals and silicon containing species, which may depose on the reactor walls.

4.3 General Equations for a Multicomponent Plasma

4.3.1 Conservation equations

The governing equations (2.6.1)-(2.6.5) for a non-thermal multicomponent plasma derived in section 2.6 may be written in the form

$$\partial_t(\rho Y_k) + \boldsymbol{\partial_x} \cdot (\rho Y_k \boldsymbol{v}_h + \rho Y_k \boldsymbol{\mathcal{V}}_k) = m_k \omega_k, \qquad k \in \mathfrak{S}, \tag{4.3.1}$$

$$\partial_t (\rho_h \boldsymbol{v}_h) + \boldsymbol{\partial_x} \cdot (\rho_h \boldsymbol{v}_h \otimes \boldsymbol{v}_h + p\, \mathbb{I}) + \boldsymbol{\partial_x} \cdot \boldsymbol{\Pi}_h = \rho \mathbf{g} + nq\mathbf{E}, \tag{4.3.2}$$

$$\partial_t \mathcal{E}_e + \boldsymbol{\partial_x} \cdot (\mathcal{E}_e \boldsymbol{v}_h) + p_e\, \boldsymbol{\partial_x} \cdot \boldsymbol{v}_h + \boldsymbol{\partial_x} \cdot \boldsymbol{\mathcal{Q}}_e = \boldsymbol{J}_e \cdot \mathbf{E} + \Delta E_{eh}, \tag{4.3.3}$$

$$\partial_t \mathcal{E}_h + \boldsymbol{\partial_x} \cdot (\mathcal{E}_h \boldsymbol{v}_h) + p_h\, \boldsymbol{\partial_x} \cdot \boldsymbol{v}_h + \boldsymbol{\partial_x} \boldsymbol{v}_h : \boldsymbol{\Pi}_h + \boldsymbol{\partial_x} \cdot \boldsymbol{\mathcal{Q}}_h = \boldsymbol{J}_h \cdot \mathbf{E} + \Delta E_{he}, \tag{4.3.4}$$

where as in the preceding chapter ρ_k denotes the mass density, $Y_k = \rho_k/\rho$ the mass fraction, and $n_k = \rho_k/\mathfrak{m}_k$ the density of the k^{th} species, while $\rho = \sum_{k\in\mathfrak{S}} \rho_k$ denotes the mass density of the fluid mixture, and $\boldsymbol{v}_h$ the heavy-species mass-averaged velocity. For $k \in \mathfrak{S}$, $\boldsymbol{\mathcal{V}}_k$ denotes the diffusion velocity of the k^{th} species in the mass-averaged velocity reference frame, $m_k = \mathcal{N}_{\text{A}}\mathfrak{m}_k$ its molar mass, and ω_k its molar production rate. Besides, p_e, p_h and $p = p_e + p_h$ denote the electron partial pressure, the heavy-species partial pressure, and the total pressure, respectively, where $n_h = \sum_{i\in\mathfrak{H}} n_i$. The vector $\mathbf{g}$ is the gravity vector, $\mathbf{E}$ is the electric field, and q is the average charge of the mixture

$$nq = \sum_{k\in\mathfrak{S}} n_k q_k, \tag{4.3.5}$$

where $n = \sum_{k\in\mathfrak{S}} n_k = n_e + n_h$. Also, $\boldsymbol{\Pi}_h$ denotes the viscous tensor, $\mathcal{E}_e$ and $\mathcal{E}_h$ denote the electron and heavy-species energy per unit volume, respectively, $\boldsymbol{\mathcal{Q}}_e$ and $\boldsymbol{\mathcal{Q}}_h$ denote the electron and heavy-species heat flux, respectively, and $\boldsymbol{J}_e = n_e q_e \boldsymbol{\mathcal{V}}_e$, respectively $\boldsymbol{J}_h = \sum_{i\in\mathfrak{H}} n_i q_i \boldsymbol{\mathcal{V}}_i$, is the electron, respectively the heavy-species, conduction current density. Finally, $\Delta E_{eh} = -\Delta E_{he}$ is the energy exchange rate between electrons and heavy species due to nonreactive or reactive collisions.

The electric potential φ is solution of the Poisson's equation

$$\partial^2_{\boldsymbol{x}}\varphi = -\frac{nq}{\varepsilon_0}, \tag{4.3.6}$$

where ε_0 is the vacuum dielectric permittivity, and the electric field reads

$$\mathbf{E} = -\boldsymbol{\partial}_{\boldsymbol{x}}\varphi. \tag{4.3.7}$$

The magnetic field has been neglected, as the typical discharge dimensions are sufficiently small to avoid the generation of magnetic waves [CB11].

4.3.2 Thermodynamics

The perfect gas laws (2.4.31) and (2.4.45) derived from the kinetic theory read

$$\rho_e = \frac{p_e m_e}{RT_e}, \tag{4.3.8}$$

$$\rho_h = \frac{p_h \overline{m}_h}{RT_h}, \tag{4.3.9}$$

where T_h and T_e are the heavy-species and electron temperature, respectively, and $\overline{m}_h$ is the mean heavy-species molar mass

$$\frac{\rho_h}{\overline{m}_h} = \sum_{i\in\mathfrak{H}} \frac{\rho_i}{m_i}. \tag{4.3.10}$$

The energy conservation equations (4.3.3), (4.3.4) can also be expressed in terms of the temperatures T_e, T_h. The heavy-species and electron enthalpies per unit mass, h_h and h_e, respectively, are given by

$$\rho_h h_h = \mathcal{E}_h + p_h, \tag{4.3.11}$$

$$\rho_e h_e = \mathcal{E}_e + p_e. \tag{4.3.12}$$

The heavy-species enthalpy can be decomposed into

$$\rho_h h_h = \sum_{i\in\mathfrak{H}} \rho_i h_i, \tag{4.3.13}$$

where h_i is the specific enthalpy of the i^{th} heavy species already given in (3.4.9)

$$h_i = h_i^{st} + \int_{T^{st}}^{T} c_{pi}(T')\,\mathrm{d}T', \quad i \in \mathfrak{H}. \tag{4.3.14}$$

Similarly, we introduce the heavy-species constant pressure specific heat c_{ph}, defined by

$$\rho_h c_{ph} = \sum_{i\in\mathfrak{H}} \rho_i c_{pi}. \tag{4.3.15}$$

From the definition of the heavy-species enthalpy (4.3.11) and the heavy-species energy conservation equation (4.3.4), the following enthalpy balance equation is obtained

$$\partial_t(\rho_h h_h) + \boldsymbol{\partial_x}\cdot(\rho_h h_h \boldsymbol{v}_h) + \boldsymbol{\partial_x}\cdot\boldsymbol{\mathcal{Q}}_h = \partial_t p_h + \boldsymbol{\partial_x} p_h\cdot\boldsymbol{v}_h - \boldsymbol{\partial_x}\boldsymbol{v}_h : \boldsymbol{\Pi}_h + \boldsymbol{J}_h\cdot\mathbf{E} + \Delta E_{he}. \tag{4.3.16}$$

On the other hand, the enthalpy derivatives may be expressed as

$$\begin{aligned}\partial_t(\rho_h h_h) + \boldsymbol{\partial_x}\cdot(\rho_h h_h \boldsymbol{v}_h) &= \sum_{i\in\mathfrak{H}} \rho_i \partial_t h_i + \sum_{i\in\mathfrak{H}} \rho_i \boldsymbol{v}_h\cdot\boldsymbol{\partial_x} h_i + \sum_{i\in\mathfrak{H}} h_i(\partial_t\rho_i + \boldsymbol{\partial_x}\cdot(\rho_i\boldsymbol{v}_h))\\ &= \rho_h c_{ph}\partial_t T_h + \rho_h c_{ph}\boldsymbol{v}_h\cdot\boldsymbol{\partial_x} T_h - \boldsymbol{\partial_x}\cdot\Big(\sum_{i\in\mathfrak{H}} h_i\boldsymbol{\mathcal{F}}_i\Big)\\ &\quad + \sum_{i\in\mathfrak{H}} c_{pi}\,\boldsymbol{\mathcal{F}}_i\cdot\boldsymbol{\partial_x} T_h + \sum_{i\in\mathfrak{H}} h_i m_i\omega_i,\end{aligned}$$

where $\boldsymbol{\mathcal{F}}_i = \rho_i\boldsymbol{\mathcal{V}}_i$, $i \in \mathfrak{H}$, are the heavy-species diffusion fluxes. The evolution equation for the heavy-species temperature T_h thus reads

$$\begin{aligned}\rho_h c_{ph}\partial_t T_h + \rho_h c_{ph}\boldsymbol{v}_h\cdot\boldsymbol{\partial_x} T_h + \boldsymbol{\partial_x}\cdot\Big(\boldsymbol{\mathcal{Q}}_h - \sum_{i\in\mathfrak{H}} h_i\boldsymbol{\mathcal{F}}_i\Big) &= \partial_t p_h + \boldsymbol{\partial_x} p_h\cdot\boldsymbol{v}_h\\ - \boldsymbol{\Pi}_h : \boldsymbol{\partial_x}\boldsymbol{v}_h - \Big(\sum_{i\in\mathfrak{H}} c_{pi}\boldsymbol{\mathcal{F}}_i\Big)\cdot\boldsymbol{\partial_x} T_h - \sum_{i\in\mathfrak{H}} h_i m_i\omega_i + \boldsymbol{J}_h\cdot\mathbf{E} + \Delta E_{he}.\end{aligned} \tag{4.3.17}$$

We proceed in a similar fashion for the electron temperature. The electron specific enthalpy per unit mass

$$h_e = h_e^{\text{st}} + \int_{T^{\text{st}}}^{T} c_{pe}(T')\,dT' \tag{4.3.18}$$

is such that

$$\rho_e h_e = \mathcal{E}_e + p_e, \tag{4.3.19}$$

and is thus solution of the following evolution equation

$$\partial_t(\rho_e h_e) + \boldsymbol{\partial_x}\cdot(\rho_e h_e \boldsymbol{v}_h) + \boldsymbol{\partial_x}\cdot\boldsymbol{\mathcal{Q}}_e = \partial_t p_e + \boldsymbol{v}_h\cdot\boldsymbol{\partial_x} p_e + \boldsymbol{J}_e\cdot\mathbf{E} + \Delta E_{eh}. \tag{4.3.20}$$

Since

$$\begin{aligned}\partial_t(\rho_e h_e) + \boldsymbol{\partial_x}\cdot(\rho_e h_e \boldsymbol{v}_h) &= \rho_e\partial_t h_e + \rho_e\boldsymbol{v}_h\cdot\boldsymbol{\partial_x} h_e + h_e(\partial_t\rho_e + \boldsymbol{\partial_x}\cdot(\rho_e\boldsymbol{v}_h))\\ &= \rho_e c_{pe}\partial_t T_e + \rho_e c_{pe}\boldsymbol{v}_h\cdot\boldsymbol{\partial_x} T_e - \boldsymbol{\partial_x}\cdot(h_e\boldsymbol{\mathcal{F}}_e)\\ &\quad + c_{pe}\,\boldsymbol{\mathcal{F}}_e\cdot\boldsymbol{\partial_x} T_e + h_e m_e\omega_e,\end{aligned}$$

the electron temperature equation finally reads

$$\begin{aligned}\rho_e c_{pe}\partial_t T_e + \rho_e c_{pe}\boldsymbol{v}_h\cdot\boldsymbol{\partial_x} T_e + \boldsymbol{\partial_x}\cdot(\boldsymbol{\mathcal{Q}}_e - h_e\boldsymbol{\mathcal{F}}_e) &= \partial_t p_e + \boldsymbol{v}_h\cdot\boldsymbol{\partial_x} p_e\\ - c_{pe}\,\boldsymbol{\mathcal{F}}_e\cdot\boldsymbol{\partial_x} T_e - h_e m_e\omega_e + \boldsymbol{J}_e\cdot\mathbf{E} + \Delta E_{eh}.\end{aligned} \tag{4.3.21}$$

4.3.3 Transport fluxes

The transport fluxes involved in the conservation equations (4.3.1)-(4.3.4) have been stated in Chapter 2. From equations (2.6.27) and (2.6.33), the electron diffusion velocity and heat flux may be expressed in the form

$$\begin{aligned}\boldsymbol{\mathcal{V}}_e =& - D_{ee}\hat{\boldsymbol{d}}_e - \sum_{i\in\mathfrak{H}} D_{ei}\hat{\boldsymbol{d}}_i - \theta_{ee}\boldsymbol{\partial}_{\boldsymbol{x}}\ln T_e - \theta_{eh}\boldsymbol{\partial}_{\boldsymbol{x}}\ln T_h \\ & - \left[D_{ee}^{\kappa_h}\left(\boldsymbol{\partial}_{\boldsymbol{x}}\cdot\boldsymbol{v}\right) + D_{ee}^{\Theta}\left(T_e - T_h\right)\right]\hat{\boldsymbol{d}}_e - \left[\theta_{ee}^{\kappa_h}\left(\boldsymbol{\partial}_{\boldsymbol{x}}\cdot\boldsymbol{v}\right) + \theta_{ee}^{\Theta}\left(T_e - T_h\right)\right]\boldsymbol{\partial}_{\boldsymbol{x}}\ln T_e,\end{aligned} \tag{4.3.22}$$

$$\begin{aligned}\boldsymbol{\mathcal{Q}}_e =& - p\theta_{ee}\hat{\boldsymbol{d}}_e - p\sum_{i\in\mathfrak{H}}\theta_{ei}\hat{\boldsymbol{d}}_i - \hat{\lambda}_{ee}\boldsymbol{\partial}_{\boldsymbol{x}}T_e - \hat{\lambda}_{eh}\boldsymbol{\partial}_{\boldsymbol{x}}T_h + n_e\Big(\frac{5}{2}k_{\text{B}}T_e\Big)\boldsymbol{\mathcal{V}}_e \\ & - p\big[\theta_{ee}^{\kappa_h}\left(\boldsymbol{\partial}_{\boldsymbol{x}}\cdot\boldsymbol{v}\right) + \theta_{ee}^{\Theta}\left(T_e - T_h\right)\big]\hat{\boldsymbol{d}}_e - \left[\hat{\lambda}_{ee}^{\kappa_h}\left(\boldsymbol{\partial}_{\boldsymbol{x}}\cdot\boldsymbol{v}\right) + \hat{\lambda}_{ee}^{\Theta}\left(T_e - T_h\right)\right]\boldsymbol{\partial}_{\boldsymbol{x}}T_e,\end{aligned} \tag{4.3.23}$$

where the unconstrained electron diffusion driving force reads

$$\hat{\boldsymbol{d}}_k = \frac{1}{p}\left(\boldsymbol{\partial}_{\boldsymbol{x}}p_k - n_k q_k\mathbf{E}\right), \quad k\in\mathfrak{S}. \tag{4.3.24}$$

The electron self-diffusion coefficient D_{ee}, the electron self-thermal-diffusion coefficient θ_{ee}, and the electron self-partial-thermal-conductivity $\hat{\lambda}_{ee}$ have been expressed in (2.6.28), (2.6.29) and (2.6.32), respectively. The electron i^{th}-heavy-species diffusion coefficient $D_{ei} = D_{ie}$, the electron heavy-temperature thermal diffusion coefficient $\theta_{eh} = \theta_{he}$, the i^{th}-heavy-species electron-temperature thermal diffusion coefficient $\theta_{ei} = \theta_{ie}$, and the electron heavy-temperature partial thermal conductivity $\hat{\lambda}_{eh}$ have been stated in (2.5.43), (2.5.54), (2.5.45), and (2.5.95), respectively. The remaining transport coefficients $D_{ee}^{\kappa_h}$, $\theta_{ee}^{\kappa_h}$, D_{ee}^{Θ}, θ_{ee}^{Θ}, $\hat{\lambda}_{ee}^{\kappa_h}$, and $\hat{\lambda}_{ee}^{\Theta}$, have been expressed in (2.5.96)-(2.5.101).

The heavy species diffusion velocities, viscous tensor and heat flux have also been derived in Chapter 2, and were expressed in equations (2.6.34)-(2.6.36) as

$$\boldsymbol{\mathcal{V}}_i = -\sum_{j\in\mathfrak{H}} D_{ij}\hat{\boldsymbol{d}}_j - D_{ie}\hat{\boldsymbol{d}}_e - \theta_{ih}\boldsymbol{\partial}_{\boldsymbol{x}}\ln T_h - \theta_{ie}\boldsymbol{\partial}_{\boldsymbol{x}}\ln T_e, \quad i\in\mathfrak{H}, \tag{4.3.25}$$

$$\boldsymbol{\Pi}_h = -\eta_h\left(\boldsymbol{\partial}_{\boldsymbol{x}}\boldsymbol{v}_h + (\boldsymbol{\partial}_{\boldsymbol{x}}\boldsymbol{v}_h)^{\text{T}} - \frac{2}{3}(\boldsymbol{\partial}_{\boldsymbol{x}}\cdot\boldsymbol{v}_h)\,\mathbb{I}\right) - \kappa_h(\boldsymbol{\partial}_{\boldsymbol{x}}\cdot\boldsymbol{v}_h)\,\mathbb{I} - \zeta(T_e - T_h)\,\mathbb{I}, \tag{4.3.26}$$

$$\boldsymbol{\mathcal{Q}}_h = -p\sum_{j\in\mathfrak{H}}\theta_{hj}\hat{\boldsymbol{d}}_j - p\theta_{he}\hat{\boldsymbol{d}}_e - \hat{\lambda}_{hh}\boldsymbol{\partial}_{\boldsymbol{x}}T_h - \hat{\lambda}_{he}\boldsymbol{\partial}_{\boldsymbol{x}}T_e + \sum_{j\in\mathfrak{H}}\big(\frac{5}{2}k_{\text{B}}T_h + \overline{E}_j\big)n_j\boldsymbol{\mathcal{V}}_j, \tag{4.3.27}$$

where the heavy-species diffusion coefficients D_{ij}, $i,j\in\mathfrak{H}$, the heavy-species heavy-temperature thermal diffusion coefficients θ_{ih}, $i\in\mathfrak{H}$, the heavy-species self-partial-thermal-conductivity $\hat{\lambda}_{hh}$, and the heavy-species electron-temperature partial thermal conductivity $\hat{\lambda}_{he}$ have been expressed in (2.5.42), (2.5.44), (2.5.52), and (2.5.53), respectively. Also, the heavy-species shear viscosity η_h and volume viscosity κ_h, and the thermal non-equilibrium viscosity ζ, were given in (2.5.48)-(2.5.50).

4.4 Simplified Model

In the case of a radio-frequency axisymmetric reactor, the general plasma model embedded in equations (4.3.1)-(4.3.2), (4.3.6), (4.3.17) and (4.3.21) can be simplified in several ways. Indeed, it is generally sufficient as a first approximation to consider the coupled evolution of charged species, electric potential and electron temperature.

4.4.1 Equations

The heavy-species convection velocity is generally neglected

$$\boldsymbol{v}_h = 0, \tag{4.4.1}$$

and the heavy-species temperature can be considered uniform as a first approximation

$$T_h(t, \boldsymbol{x}) = T_h, \tag{4.4.2}$$

where T_h independent of t and $\boldsymbol{x}$. The momentum equation (4.3.2) and the heavy-species temperature equation (4.3.17) are thus discarded, and the system (4.3.1)-(4.3.4) is reduced to a system of $n^s + 2$ equations, of the form

$$\partial_t(\rho Y_k) + \boldsymbol{\partial}_{\boldsymbol{x}} \cdot (\rho Y_k \boldsymbol{\mathcal{V}}_k) = m_k \omega_k, \ k \in \mathfrak{S}, \ k \neq \mathrm{H}_2, \qquad Y_{\mathrm{H}_2} = 1 - \sum_{k \neq \mathrm{H}_2} Y_k, \tag{4.4.3}$$

$$\partial^2_{\boldsymbol{x}} \varphi = -\frac{nq}{\varepsilon_0}, \tag{4.4.4}$$

$$\partial_t\Big(\frac{3}{2} n_e k_{\mathrm{B}} T_e\Big) + \boldsymbol{\partial}_{\boldsymbol{x}} \cdot \boldsymbol{\mathcal{Q}}_e = \boldsymbol{J}_e \cdot \mathbf{E} + \Delta E_{eh}. \tag{4.4.5}$$

The equation for the main carrier gas H_2 is taken such as to ensure the total mass conservation in the mixture, since $\sum_{k \in \mathfrak{S}} Y_k \boldsymbol{\mathcal{V}}_k = Y_e \boldsymbol{\mathcal{V}}_e \neq 0$ a priori. Also, the pressure is assumed to be uniform in the reactor

$$p(t, \boldsymbol{x}) = p_0, \tag{4.4.6}$$

where p_0 is independent of t and $\boldsymbol{x}$, in agreement with the low Mach number approximation. Equations (4.4.3) may also be written in their nonconservative form

$$\rho \partial_t Y_k + \boldsymbol{\partial}_{\boldsymbol{x}} \cdot (\rho Y_k \boldsymbol{\mathcal{V}}_k) = m_k \omega_k, \ k \in \mathfrak{S}, \ k \neq \mathrm{H}_2, \qquad Y_{\mathrm{H}_2} = 1 - \sum_{k \neq \mathrm{H}_2} Y_k, \tag{4.4.7}$$

where the time derivative of ρ, which is proportional to the time derivative of $\overline{m}$, has been neglected. Indeed, in the approximation $\boldsymbol{v}_h = 0$, the total mass conservation equation reads $\partial_t \rho = \boldsymbol{\partial}_{\boldsymbol{x}} \cdot (\rho Y_e \boldsymbol{\mathcal{V}}_e)$, which is proportional to the mass ratio ε^2 and is therefore negligible. Alternatively, the center-of-mass reference frame equations (2.7.11)-(2.7.15) could have been used, and the assumption $\boldsymbol{v}_h = 0$ would have been replaced by $\boldsymbol{v} = 0$.

4.4.2 Self similar formulation

As can be seen in Figure 4.2, the cylindrical coordinates (r, θ, z), with corresponding unit vectors $\boldsymbol{e}_r$, $\boldsymbol{e}_\theta$ and $\boldsymbol{e}_z$, are such that $\boldsymbol{e}_z$ is normal to the stagnation plane $(O, \boldsymbol{e}_r, \boldsymbol{e}_\theta)$, where O is the origin located at the centre of the substrate (see Figure 4.2). As in Chapter 3, we assume that the gravity is either oriented in the normal direction: $\mathbf{g} = (0, 0, \mathrm{g})$, either negligible. In this framework, we seek for a self similar solution of equations (4.4.7), (4.4.4) and (4.4.5), of the form

$$\rho = \rho(t, z), \tag{4.4.8}$$

$$T_e = T_e(t, z), \tag{4.4.9}$$

$$Y_k = Y_k(t, z), \ k \in \mathfrak{S}, \tag{4.4.10}$$

$$\varphi = \varphi(t, z). \tag{4.4.11}$$

From the expressions (4.4.18) and (4.4.21) where the pressure p has been replaced by the spatially uniform pressure p_0, which is valid for a low Mach number flow, the diffusion velocities and the electron heat flux can be expressed in the form

$$\boldsymbol{\mathcal{V}}_k = \big(0, 0, \mathcal{V}_k(t,z)\big),\ k \in \mathfrak{S}, \tag{4.4.12}$$

$$\boldsymbol{\mathcal{Q}}_e = \big(0, 0, \mathcal{Q}_e(t,z)\big). \tag{4.4.13}$$

Thus, equations (4.4.7), (4.4.4) and (4.4.5) are rewritten

$$\rho\partial_t Y_k + \partial_z(\rho Y_k \mathcal{V}_k) = m_k\omega_k,\ k \in \mathfrak{S},\ k \neq \mathrm{H}_2, \qquad Y_{\mathrm{H}_2} = 1 - \sum_{k\neq \mathrm{H}_2} Y_k, \tag{4.4.14}$$

$$\partial_z^2\varphi = -\frac{nq}{\varepsilon_0}, \tag{4.4.15}$$

$$\partial_t\Big(\frac{3}{2}n_e k_{\mathrm{B}} T_e\Big) + \partial_z \mathcal{Q}_e = n_e q_e \mathcal{V}_e \mathrm{E} + \Delta E_{eh}, \tag{4.4.16}$$

where

$$\mathrm{E} = -\partial_z\varphi \tag{4.4.17}$$

is the electric field.

4.4.3 Transport fluxes

As far as the transport fluxes are concerned, the heavy-species viscous tensor (4.3.26) and heat flux (4.3.27) are not required anymore since they do not appear in the simplified system (4.4.3)-(4.4.5). Also, the remaining transport fluxes (4.3.22)-(4.3.23), and (4.3.25) are simplified. The Soret effect is neglected, the species diffusion is reduced to the self-species diffusion driving terms, and the transport coefficients $D_{ee}^{\kappa_h}$, D_{ee}^{Θ}, $\theta_{ee}^{\kappa_h}$, and θ_{ee}^{Θ} are generally neglected. The species diffusion velocities are thus taken in the form

$$\boldsymbol{\mathcal{V}}_k = -D_k^* \frac{\boldsymbol{\partial}_{\boldsymbol{x}} Y_k}{Y_k} + \mu_k^* \mathbf{E}, \qquad k \in \mathfrak{S},\ k \neq \mathrm{H}_2, \tag{4.4.18}$$

where D_k^* is the self-diffusion coefficient of the k^{th} species, and the mobility coefficient μ_k^* is given by the Einstein relation

$$\mu_k^* = \frac{D_k^* q_k}{k_{\mathrm{B}} T_k}, \quad k \in \mathfrak{S}, \tag{4.4.19}$$

where T_k is the temperature of the k^{th} species

$$T_k = \begin{cases} T_e, & k = e, \\ T_h, & k \neq e. \end{cases} \tag{4.4.20}$$

Equation (4.4.18) corresponds to the first variational approximation to the first-order multicomponent diffusion coefficients (3.9.12) in a neutral gas mixture [OB81] [Gio99], commonly referred to as the "Hirschfelder-Curtiss approximation" [HC49], except the term $\boldsymbol{\partial}_{\boldsymbol{x}} X_k/X_k$ has been replaced by $\boldsymbol{\partial}_{\boldsymbol{x}} Y_k/Y_k$, where $Y_k = X_k \mathfrak{m}_k/\overline{\mathfrak{m}}$, that is the spatial derivative of $\overline{\mathfrak{m}}$ has been neglected. Also, the correction velocity [OB81] [Gio99] has been dropped since the mass conservation is ensured by the equation for H_2. Thus, the governing equation (4.4.7) for the k^{th} species depends only on the mass fraction Y_k, and not on Y_l, $l \neq k$. Such a diagonal approximation is valid when one of the species is in excess while all the other species are in trace amounts [Gio90] [EG94].

Concerning the electron heat flux, the Dufour effect is generally neglected, the heavy-species temperature gradient is zero since T_h was assumed to be constant, and the transport coefficients $\hat{\lambda}_{ee}^{\kappa_h}$, $\hat{\lambda}_{ee}^{\Theta}$, $\theta_{ee}^{\kappa_h}$, and θ_{ee}^{Θ} are generally neglected. Thus, $\mathcal{Q}_e$ can be taken in the form

$$\mathcal{Q}_e = \frac{5}{2} n_e k_{\mathrm{B}} T_e \boldsymbol{\mathcal{V}}_e - \hat{\lambda}_{ee} \boldsymbol{\partial}_{\boldsymbol{x}} T_e, \tag{4.4.21}$$

where $\hat{\lambda}_{ee}$ is the electron self-partial-thermal-conductivity.

4.5 Transport coefficients

The self-diffusion coefficients D_k^*, $k \in \mathfrak{S}$, are taken according to the "Hirschfelder-Curtiss approximation" [HC49] [OB81] [Gio99], namely

$$D_k^* = \frac{p(1-Y_k)}{\sum\limits_{\substack{l\in\mathfrak{N}\\ l\neq k}} p_l/\mathcal{D}_{k,l}^{\text{bin}}}, \qquad k \in \mathfrak{S}, \tag{4.5.1}$$

where $\mathcal{D}_{k,l}^{\text{bin}}$ is the binary diffusion coefficient for species pair (k,l), and where $\mathfrak{N} \subset \mathfrak{S}$ denotes the indexing set for neutral species. In practice, due to the lack of data on charged species binary diffusion coefficients, we consider that the charged species diffuse against H_2 and SiH_4 only. This has no influence on numerical results, since H_2 and SiH_4 are in excess and other neutral species are only present in trace amount.

The electron self-partial-thermal-conductivity is given by the following Drude-Lorentz type formula [Lor05]

$$\hat{\lambda}_{ee} = \frac{5}{2} n_e k_{\text{B}} D_e^*. \tag{4.5.2}$$

Equation (4.5.2) can be obtained from the kinetic theory of a Lorentz gas made of Maxwellian molecules, that is molecules interacting with a potential proportional to r^{-5}, where r is the intermolecular distance [CC70].

The electron binary diffusion coefficients are taken equal to

$$\mathcal{D}_{e,\text{SiH}_4}^{\text{bin}}\, p = 1.2 \cdot 10^6 \text{ cm}^2.\text{s}^{-1}.\text{Torr}, \tag{4.5.3}$$

$$\mathcal{D}_{e,\text{H}_2}^{\text{bin}}\, p = \frac{k_{\text{B}} T_e}{q_e}\, 7.5 \cdot 10^5 \text{ cm}^2.\text{s}^{-1}.\text{Torr}. \tag{4.5.4}$$

The electron mobilities are plotted as a function of T_e in Figure 4.3. The continuous lines correspond to the values obtained with the Bolsig software [HP05] [Hag16] assuming a Maxwellian electron distribution function, and the dashed lines correspond to the approximation retained in this work. The figures show a good agreement with the results of the Bolsig software, although the electron mobility in hydrogen is slightly underestimated at high electron temperatures.

The binary diffusion coefficients of ions with respect to neutral molecules are taken in the form [PLB96]

$$\mathcal{D}_{ij}^{\text{bin}}\, p = 38.7 \frac{k_{\text{B}} T_h}{|q_i|} \frac{T_h}{\sqrt{\alpha_j \mathfrak{m}_{ij}}} \text{ cm}^2.\text{s}^{-1}.\text{Torr}, \qquad i \in \mathfrak{I},\ j \in \mathfrak{N}, \tag{4.5.5}$$

where $\mathfrak{m}_{ij} = \mathfrak{m}_i \mathfrak{m}_j / (\mathfrak{m}_i + \mathfrak{m}_j)$ is the reduced mass of the species pair (i,j) in a.m.u., α_j the polarizability of the j^{th} species in Å^3 [PLB96]

$$\alpha_{\text{H}_2} = 0.805 \text{ Å}^3, \tag{4.5.6}$$

$$\alpha_{\text{SiH}_4} = 4.62 \text{ Å}^3, \tag{4.5.7}$$

and other variables are in S.I. units. Finally, the binary diffusion coefficients of neutral species are computed with the "TRANFT" fitting program [KDLW$^+$86], as in Chapter 3.

4.6 Silane-Hydrogen Plasma Chemistry

The chemical reaction mechanism is composed of a set $\mathscr{R}$ of elementary reactions, of the form

$$\sum_{k\in\mathfrak{S}} \nu_k^{\text{rf}}\, \mathfrak{M}_k \rightleftharpoons \sum_{k\in\mathfrak{S}} \nu_k^{\text{rb}}\, \mathfrak{M}_k, \quad r \in \mathscr{R}, \tag{4.6.1}$$

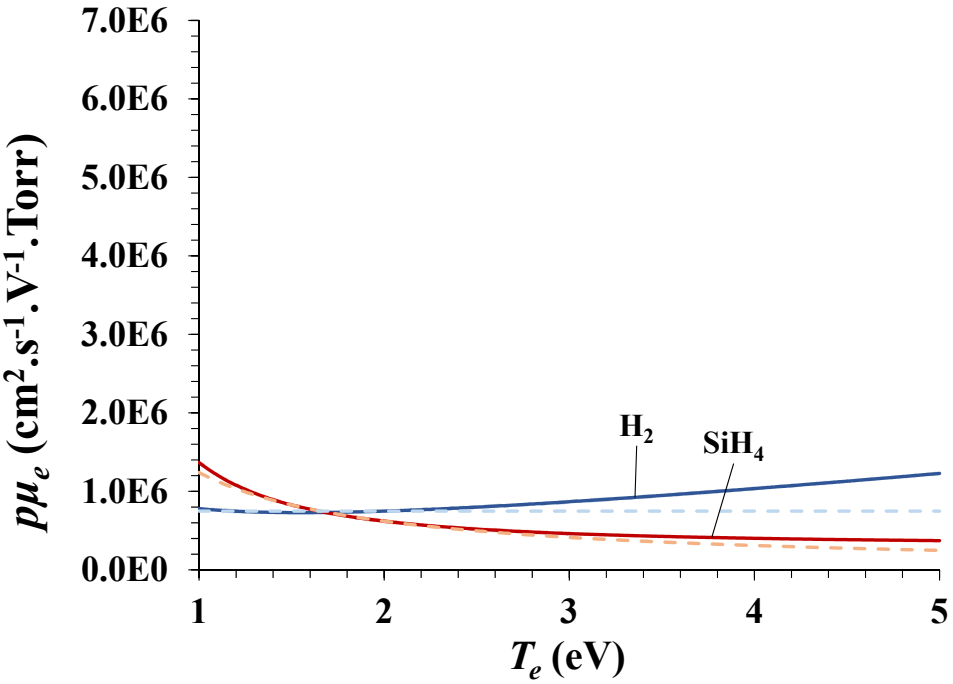

Figure 4.3 – Electron binary mobilities as a function of the electron temperature. The continuous lines correspond to the values obtained with the Bolsig software [HP05] [Hag16] assuming a Maxwellian electron distribution function, and the dashed lines correspond to the approximation retained in this work. The scattering cross-sections were taken from [IST] for H_2 and from [SIG] for SiH_4.

where $\mathfrak{M}_k$ denotes the chemical symbol of the k^{th} species, and where ν_k^{rf} and ν_k^{rb} denote the forward and backward stoichiometric coefficients of the k^{th} species in reaction r, respectively. According to expression (2.4.159) from the kinetic theory , the molar production rate of the k^{th} species can be decomposed into the different contributions from each reaction

$$\omega_k = \sum_{r \in \mathscr{R}} (\nu_k^{\text{rf}} - \nu_k^{\text{rb}}) \tau_r, \tag{4.6.2}$$

where τ_r is the rate of progress of the r^{th} reaction.

Table 4.1 – Species included in the plasma model.

Neutral Species	**Charged Species**
H, H_2, SiH_2, SiH_3, SiH_4, H_3SiSiH, Si_2H_5, Si_2H_6	e, SiH_3^+, H_3^+, H_2^+, H^+, SiH_2^-, SiH_3^-, $Si_2H_5^-$, H_3SiSiH^-

The chemistry mechanism involves two kinds of reactions: electron collision reactions on the one hand, which depend on electron temperature T_e and are assumed to be irreversible, and heavy-species reactions on the other hand, which depend on the heavy-species temperature T_h. We denote by $\mathscr{R}_e$, respectively $\mathscr{R}_h$, the set of electron collision reactions, respectively the set of heavy-species reactions, so that $\mathscr{R} = \mathscr{R}_e \cup \mathscr{R}_h$.

The rate of progress (2.4.160) of a reaction $r \in \mathscr{R}$ reads

$$\tau_r = \mathcal{K}_r^{\mathrm{f}} \prod_{k \in \mathfrak{S}} \gamma_k^{\nu_k^{r\mathrm{f}}} - \mathcal{K}_r^{\mathrm{b}} \prod_{k \in \mathfrak{S}} \gamma_k^{\nu_k^{r\mathrm{b}}}, \tag{4.6.3}$$

where $\gamma_k = \rho Y_k / m_k$ is the molar concentration of the k^{th} species, and $\mathcal{K}_r^{\mathrm{f}}$ and $\mathcal{K}_r^{\mathrm{b}}$ are the forward and backward rate constants of the r^{th} reaction.

When $r \in \mathscr{R}_h$ is a heavy-species reaction, as a consequence of detailed balancing and reciprocity relations (2.2.36), the ratio of the rate constants $\mathcal{K}_r^{\mathrm{f}}$ and $\mathcal{K}_r^{\mathrm{b}}$ is the equilibrium constant of the r^{th} reaction, as already stated in (2.4.169)

$$\mathcal{K}_r^{\mathrm{e}}(T_h) = \frac{\mathcal{K}_r^{\mathrm{f}}(T_h)}{\mathcal{K}_r^{\mathrm{b}}(T_h)}. \tag{4.6.4}$$

The reaction rate constant corresponds to the chemical equilibrium proportions, as described by statistical mechanics [Tol38], and is given by (2.4.168)

$$\ln \mathcal{K}_r^{\mathrm{e}}(T_h) = -\sum_{i \in \mathfrak{H}} \frac{\nu_i^r m_i}{R T_h} \Big(g_i^{\mathrm{atm}}(T_h) - \frac{R T_h}{m_i} \ln \big(\frac{p^{\mathrm{atm}}}{R T_h}\big) \Big), \tag{4.6.5}$$

where g_i^{atm}, $i \in \mathfrak{H}$, denote the species specific Gibbs functions at atmospheric pressure

$$g_i^{\mathrm{atm}}(T_h) = h_i(T_h) - T_h s_i^{\mathrm{atm}}(T_h), \quad i \in \mathfrak{H}. \tag{4.6.6}$$

In general, the forward rate constant is approximated by a generalized Arrhenius empirical relation, of the form

$$\mathcal{K}_r^{\mathrm{f}}(T_k) = A_r T_k^{\beta_r} \exp\Big(- \frac{\mathfrak{E}_r}{R T_k} \Big), \tag{4.6.7}$$

where T_k is the temperature of the k^{th} species, A_r is the pre-exponential factor, β_r the pre-exponential exponent and $\mathfrak{E}_r \geq 0$ the activation energy of the r^{th} reaction. Electron collision reactions are generally assumed irreversible [References]. For heavy-species reactionns, the backward rate constant is deduced from the forward rate constant and the equilibrium constant (4.6.5) by the law of mass action (4.6.4). For some of the heavy-species reactions though, both the forward and backward rate constants are specified directly in Arrhenius form.

The present model takes into account seventeen species, listed in Table 4.1. The model was adapted from the chemistry mechanism of de Bleecker and coworkers [dB06], itself originating from the work of Girshick and coworkers [Bha03] [Aga12]. We considered species containing up to 2 silicon atoms in order to lower the computation time. Previous results by Agarwal [Aga12] suggest that this is sufficient for a self-consistent calculation of overall negative ion densities and nanoparticle nucleation rate.

The set of electron collision reactions for silane-hydrogen plasma chemistry is detailed in Table 4.2. Electron collisions include ionization, dissociation, dissociative attachment, detachment, as well as recombination reactions. In particular, the formation of negative ions leading to clustering is due to the dissociative attachment reactions. The reaction rate constants have been taken in Arrhenius form, and the Arrhenius constants for silane plasma chemistry were taken from [BSGK00]. We do not consider vibrationally excited silane molecules, since vibrational effects are relatively low in the range of temperatures generally used for silicon epitaxy, i.e., around 500 K [dB06].

Heavy-species reactions are listed in Table 4.3. They comprise cluster growth reactions, neutralization reactions between positive and negative ions, neutral-neutral reactions, and additional hydrogen reactions. The cluster growth reactions are responsible for the nucleation of nanoparticles in the discharge, and are therefore of fundamental importance. The clustering rate constants were

Table 4.2 – Arrhenius parameters for electron collision reactions.

r	Electron collision	A_r (mol,cm^3,s)	β_r	$\mathfrak{E}_r$ (cal.mol^{-1})	Reference
	Ionization				
1	$SiH_4 + e \rightharpoonup SiH_3^+ + H + 2e$	1.510×10^{32}	-2.930	553,910	[BSGK00]
2	$SiH_3 + e \rightharpoonup SiH_3^+ + 2e$	1.355×10^{12}	0.900	188,396	[BSGK00]
3	$H_2 + e \rightharpoonup H_2^+ + 2e$	8.007×10^{10}	1.100	392,574	[BSGK00]
4	$H + e \rightharpoonup H^+ + 2e$	1.080×10^{16}	0.000	178,210	[SFG$^+$96]
	Dissociation				
5	$SiH_4 + e \rightharpoonup SiH_3 + H + e$	1.102×10^{21}	-1.000	245,421	[BSGK00]
6	$SiH_4 + e \rightharpoonup SiH_2 + 2H + e$	5.394×10^{21}	-1.000	245,421	[BSGK00]
7	$H_2 + e \rightharpoonup 2H + e$	1.023×10^{16}	0.000	238,347	[BSGK00]
8	$H_3^+ + e \rightharpoonup H^+ + 2H + e$	1.220×10^{17}	0.000	179,380	[SFG$^+$96]
9	$H_2^+ + e \rightharpoonup H^+ + H + e$	1.460×10^{17}	0.000	37,460	[SFG$^+$96]
	Dissociative attachment				
10	$SiH_4 + e \rightharpoonup SiH_3^- + H$	2.269×10^{21}	-1.627	190,540	[BSGK00]
11	$SiH_4 + e \rightharpoonup SiH_2^- + 2H$	2.269×10^{21}	-1.627	190,540	[BSGK00]
12	$SiH_3 + e \rightharpoonup SiH_2^- + H$	3.440×10^{15}	-0.500	44,740	[BSGK00]
	Detachment				
13	$SiH_3^- + e \rightharpoonup SiH_3 + 2e$	1.900×10^{14}	0.500	32,425	[BSGK00]
14	$SiH_2^- + e \rightharpoonup SiH_2 + 2e$	1.900×10^{14}	0.500	25,921	[BSGK00]
	Recombination and dissociative recombination				
15	$H^+ + 2e \rightharpoonup H + e$	3.630×10^{37}	-4.000	0	[SFG$^+$96]
16	$H_3^+ + e \rightharpoonup 3H$	8.000×10^{17}	-0.404	0	[SFG$^+$96], [KNF$^+$04]
17	$H_3^+ + 2e \rightharpoonup H + H_2 + e$	3.170×10^{21}	-4.500	0	[SFG$^+$96]
18	$H_2^+ + 2e \rightharpoonup 2H + e$	3.170×10^{21}	-4.500	0	[SFG$^+$96]

Table 4.3 – Arrhenius parameters for the heavy-species reactions.

r	Reaction	A_r (mol,cm^3,s)	β_r	$\mathfrak{E}_r$ (cal.mol^{-1})	Reference
	Cluster growth				
19	$SiH_3^- + SiH_4 = Si_2H_5^- + H_2$	6.020×10^{11}	0.000	0	[BSGK00]
20	$SiH_2^- + SiH_4 = H_3SiSiH^- + H_2$	6.020×10^{11}	0.000	0	[BSGK00]
	Neutralization reactions				
21	$SiH_3^- + SiH_3^+ = SiH_3 + SiH_3$	1.232×10^{18}	-0.500	0	[BSGK00]
22	$SiH_2^- + SiH_3^+ = SiH_2 + SiH_3$	1.359×10^{18}	-0.500	0	[BSGK00]
23	$Si_2H_5^- + SiH_3^+ = Si_2H_5 + SiH_3$	9.648×10^{17}	-0.500	0	[BSGK00]
24	$H_3SiSiH^- + SiH_3^+ = H_3SiSiH + SiH_3$	1.001×10^{18}	-0.500	0	[BSGK00]
	Neutral-neutral reactions				
25	$SiH_4 + H = SiH_3 + H_2$	1.510×10^{13}	0.000	2,484	[BSGK00]
26	$Si_2H_6 + H = Si_2H_5 + H_2$	9.630×10^{13}	0.000	2,484	[BSGK00]
27	$Si_2H_6 + H = SiH_3 + SiH_4$	4.820×10^{13}	0.000	2,484	[BSGK00]
28	$SiH_2 + H_2 = SiH_4$	5.260×10^{10}	0.000	0	[BSGK00]
29	$SiH_2 + SiH_4 = Si_2H_6$	3.620×10^{13}	0.000	0	[BSGK00]
30	$SiH_3 + SiH_3 = SiH_2 + SiH_4$	9.030×10^{13}	0.000	0	[BSGK00]
31	$H_2 + H_2 = 2H + H_2$	8.610×10^{17}	-0.700	52,530	[SFG$^+$96]
	Reverse rate	1.000×10^{17}	-0.600	0	[SFG$^+$96]
32	$H_2 + H = 3H$	2.700×10^{16}	-0.100	52,530	[SFG$^+$96]
	Reverse rate	3.200×10^{15}	0.000	0	[SFG$^+$96]
	Additional hydrogen reactions				
33	$H_2^+ + H = H^+ + H_2$	3.850×10^{14}	0.000	0	[SFG$^+$96], [KNF$^+$04]
	Reverse rate	1.900×10^{14}	0.000	21,902	[SFG$^+$96]
34	$H_2 + H_2^+ \rightharpoonup H_3^+ + H$	1.270×10^{15}	0.000	0	[SFG$^+$96], [KNF$^+$04]
35	$H^+ + 2\,H_2 \rightharpoonup H_3^+ + H_2$	1.950×10^{20}	-0.500	0	[SFG$^+$96], [KNF$^+$04]

computed by [Bha03] as the Langevin rates devided by 10, since the Langevin rates are known to overestimate anion-neutral reaction rates. In [dB06], this clustering reaction rate constant is divided by 100 compared to [Bha03], on the basis of experimental resuts obtained by Perrin ar al [PBEL94]. We adopted the latter value since at a temperature of 500 K the data of Perrin et al. must prevail. Negative ions remain trapped in the plasma due to the strong potential barrier, and can thus be neutralized due to electron detachment or neutralization reactions. The neutralization reactions are the main source of negative ion loss [dB06]. Finally, the H_2 plasma chemistry was also enriched compared to the work of de Bleecker, which considered pure SiH_4 chemistry, and the work of Girshick and coworkers, which considered Ar-SiH_4 chemistry. The main positive ion in H_2 plasma is indeed H_3^+, due to the fast conversion reaction [DCL05] [MJA07]

$$H_2 + H_2^+ \rightarrow H_3^+ + H. \tag{4.6.8}$$

The vibrationnally excited states of hydrogen have not been taken into account, neither the presence of H^- ion induced by the dissociative attachment on H_2 excited states [KNF$^+$04] [DCL05]. The H^- density is indeed negligible compared to silicon hydride anion densities, and H^- ions are thus expected to have a negligible influence on the plasma properties.

4.7 Energy exchange term

The energy exchange term $\Delta E_{eh} = -\Delta E_{he}$ is expressed from equations (2.6.11), (2.4.104), (2.4.137), and (2.4.139) as

$$\Delta E_{eh} = \Delta E_{eh}^{\mathrm{el}} + \Delta E_{eh}^{\mathrm{in}} + \Delta E_{eh}^{\mathrm{chem}}, \tag{4.7.1}$$

where $\Delta E_{eh}^{\mathrm{el}}$ is the energy exchange term due to elastic scattering of electrons against heavy species, $\Delta E_{eh}^{\mathrm{in}}$ the energy exchange term associated with inelastic scattering of electrons against heavy species, and $\Delta E_{eh}^{\mathrm{chem}}$ the energy exchange term due to reactive electron collisions. The elastic relaxation term is induced by the translational non-equilibrium between electrons and heavy species, and is generally reduced [LE95] to the zeroth-order term (2.4.105)

$$\Delta E_{eh}^{\mathrm{el}} = \Delta E_{eh}^{0,\mathrm{el}} = -\frac{3}{2} n_h k_{\mathrm{B}} (T_e - T_h) \frac{1}{\tau^{\mathrm{el}}}, \tag{4.7.2}$$

which is in general negligible for the process we consider [LE93] [Nie98]. As well, the energy exchange due to electron inelastic scattering against heavy species is generally approximated by the zeroth-order term (2.4.109), which can be rewritten in the form

$$\Delta E_{eh}^{\mathrm{in}} = \Delta E_{eh}^{0,\mathrm{in}} = \frac{1}{2} \sum_{i \in \mathfrak{H}} \sum_{\substack{\mathrm{I},\mathrm{I}' \in \mathfrak{Q}_i \\ \mathrm{I}' \neq \mathrm{I}}} (-\Delta E_{\mathrm{II}'}) \tau_{\mathrm{II}'}, \tag{4.7.3}$$

where $\tau_{\mathrm{II}'}$ is the rate of progress of the inelastic scattering process $(e, \mathrm{I}) \rightarrow (e, \mathrm{I}')$

$$\tau_{\mathrm{II}'} = \frac{n_i a_{i\mathrm{I}}}{Q_i^{\mathrm{int}}} \nu_{ie}^{\mathrm{II}'} \left(e^{-E_{i\mathrm{I}}/k_{\mathrm{B}}T_h} - \exp\left(\frac{\Delta E_{\mathrm{II}'}}{k_{\mathrm{B}}T_e}\right) e^{-E_{i\mathrm{I}'}/k_{\mathrm{B}}T_h} \right). \tag{4.7.4}$$

The energy exchange due to reactive electron collisions was given in (2.4.174) as

$$\Delta E_{eh}^{\mathrm{chem}} = \Delta E_{eh}^{1,\mathrm{chem}} = \sum_{r \in \mathscr{R}_e} \Delta \mathcal{E}_{er} \tau_r, \tag{4.7.5}$$

where $\Delta \mathcal{E}_{er}$ is the net average energy gained by electrons during the r^{th} electron collision reaction. Thus, from expressions (4.7.3) and (4.7.5), and noting $\mathscr{I}_e$ the indexing set for inelastic scattering of electrons against heavy species, the energy exchange term finally reads [Nie98] [KNF$^+$04]

$$\Delta E_{eh} = \sum_{r \in \mathscr{R}_e \cup \mathscr{I}_e} \Delta \mathcal{E}_{er} \tau_r, \tag{4.7.6}$$

where τ_r and $-\Delta\mathcal{E}_{er}$ are, respectively, the rate of progress and the net average electron energy loss in the r^{th} electron collision. The values adopted for the present study are specified in Table 4.4, along with the associated references.

Table 4.4 – Net average electron energy loss in reactive collisions.

r	Electron collision	$-\Delta\mathcal{E}_{er}$ (eV)	Reference
	Ionization		
1	$SiH_4 + e \rightharpoonup SiH_3^+ + H + 2e$	12.09	[BGCR87]
2	$SiH_3 + e \rightharpoonup SiH_3^+ + 2e$	8.01	[BGCR87]
3	$H_2 + e \rightharpoonup H_2^+ + 2e$	15.43	[PLB96]
4	$H + e \rightharpoonup H^+ + 2e$	13.60	[PLB96]
	Dissociation		
5	$SiH_4 + e \rightharpoonup SiH_3 + H + e$	8.00	[PSd$^+$82]
6	$SiH_4 + e \rightharpoonup SiH_2 + 2H + e$	8.00	[PSd$^+$82]
7	$H_2 + e \rightharpoonup 2H + e$	10.50	[JLEP87]
8	$H_3^+ + e \rightharpoonup H^+ + 2H + e$	14.87	[JLEP87], [CH88]
9	$H_2^+ + e \rightharpoonup H^+ + H + e$	8.67	[JLEP87], [PLB96]
	Dissociative attachment		
10	$SiH_4 + e \rightharpoonup SiH_3^- + H$	6.50	[PLB96]
11	$SiH_4 + e \rightharpoonup SiH_2^- + 2H$	8.50	[PLB96]
12	$SiH_3 + e \rightharpoonup SiH_2^- + H$	5.50	[PLB96]
	Detachment		
13	$SiH_3^- + e \rightharpoonup SiH_3 + 2e$	1.41	[PLB96]
14	$SiH_2^- + e \rightharpoonup SiH_2 + 2e$	1.12	[PLB96]
	Recombination and dissociative recombination		
15	$H^+ + 2e \rightharpoonup H + e$	−13.60	[PLB96]
16	$H_3^+ + e \rightharpoonup 3H$	1.27	[PSd$^+$82], [CH88]
17	$H_3^+ + 2e \rightharpoonup H + H_2 + e$	−9.23	[CH88]
18	$H_2^+ + 2e \rightharpoonup 2H + e$	−4.93	[JLEP87], [PLB96]

4.8 Boundary Conditions

The electron temperatures at both electrodes are specified as

$$T_e|_{t,0} = T_e^{\text{s}}, \tag{4.8.1}$$

$$T_e|_{t,L} = T_e^{\text{in}}, \tag{4.8.2}$$

where $T_e^{\text{s}} = T_e^{\text{in}} = 5000$ K $\simeq 0.43$ eV, which is representative of a secondary electron emission temperature [WG07]. Also, for the range of parameters considered here, the discharge remains in the "α-regime", in which secondary electron emission is negligible [BB90] [SG91] [dBGG04].

In the base case, the external capacitor is not taken into account. This is perfectly justified for a geometrically symmetric reactor with a sinusoidal waveform excitation. The electrode located at $z = 0$ is grounded, and a sinusoidal voltage with amplitude φ_{RF} and frequency $f = 13.56$ MHz is

imposed on the electrode located at $z = L$

$$\varphi|_{t,0} = 0, \tag{4.8.3}$$
$$\varphi|_{t,L} = \varphi_{\text{RF}} \sin(2\pi f t). \tag{4.8.4}$$

An alternative boundary condition for the potential at the driven electrode is also implemented in the following.

The boundary conditions for electrons are taken as

$$Y_e|_{t,0} = 10^{-20}, \tag{4.8.5}$$
$$Y_e|_{t,L} = 10^{-20}, \tag{4.8.6}$$

and for negative ions as

$$Y_i|_{t,0} = 0, \quad i \in \mathfrak{I}^-, \tag{4.8.7}$$
$$Y_i|_{t,L} = 0, \quad i \in \mathfrak{I}^-, \tag{4.8.8}$$

where $\mathfrak{I}^-$ denotes the set of negative ions. For positive ions, the boundary conditions at both electrodes are

$$\boldsymbol{\mathcal{F}}_i \cdot \boldsymbol{n} = \max\Big(\boldsymbol{\mathcal{F}}_i^{\text{drift}} \cdot \boldsymbol{n}, \mathcal{F}_{+,i}\Big), \quad i \in \mathfrak{I}^+, \tag{4.8.9}$$

where $\mathfrak{I}^+$ denotes the set of positive ions, $\boldsymbol{n}$ denotes the unit vector normal to the surface oriented towards the electrodes, $\boldsymbol{\mathcal{F}}_k^{\text{drift}} = \rho_k \boldsymbol{\mathcal{V}}_k^{\text{drift}}$ is the drift velocity of the k^{th} species

$$\boldsymbol{\mathcal{F}}_k^{\text{drift}} = \rho_k \mu_k^* \mathbf{E}, \quad k \in \mathfrak{S}, \tag{4.8.10}$$

and $\mathcal{F}_{+,k}$ is the average mass flux of molecules from the k^{th} species [CC70] whose velocity is directed towards the wall. This average flux is computed as that of Maxwellian molecules, that is

$$\mathcal{F}_{+,k} = \frac{1}{2} \rho_k v_{\text{th},k}, \tag{4.8.11}$$

where $v_{\text{th},k}$ is the thermal velocity of the k^{th} species, given by [CC70] [FK72]

$$v_{\text{th},k} = \left(\frac{8 k_{\text{B}} T_k}{\pi \mathfrak{m}_k} \right)^{\frac{1}{2}}, \quad k \in \mathfrak{S}. \tag{4.8.12}$$

Expression (4.8.11) actually corresponds to the surface deposition rate of neutral species as given in (3.11.5), with a sticking coefficient of 1.

The boundary condition (4.8.9) is such that when the outwards drift velocity $\boldsymbol{\mathcal{V}}_i^{\text{drift}} \cdot \boldsymbol{n}$ is large compared to the thermal velocity $v_{\text{th},i}$, the diffusion velocity at the boundary is merely equal to the drift velocity, while in the case when the drift velocity is negligible or oriented inwards, the diffusion flux at the electrode is merely the thermal flux $\rho_i v_{\text{th},i}/4$ [MW60] [McD64]. This boundary condition also ensures that the flux of positive ions is always directed outwards the reactor, since secondary ion emission is negligible for the discharge we consider.

In the dilution approximation, the boundary conditions associated wih the equation for H_2 read

$$Y_{\text{H}_2}|_{t,0} = 1 - \sum_{k \neq \text{H}_2} Y_k|_{t,0}\,, \tag{4.8.13}$$
$$Y_{\text{H}_2}|_{t,L} = 1 - \sum_{k \neq \text{H}_2} Y_k|_{t,L}\,. \tag{4.8.14}$$

For other neutral species, the boundary conditions at the upper electrode read

$$Y_n|_{t,L} = Y_n^{\text{in}}, \quad n \in \mathfrak{N}, \tag{4.8.15}$$

where Y_n^{in} is the n^{th} species inlet mass fraction, and the boundary conditions at the substrate are those of a catalytic plate

$$\big(\rho Y_n \mathcal{V}_n\big)\big|_{t,0} = m_n \widehat{\omega}_n, \quad n \in \mathfrak{N}, \tag{4.8.16}$$

where $\widehat{\omega}_n$ is the surface molar production rate of the n^{th} neutral species.

Table 4.5 – Heterogeneous reaction mechanism adopted for the present model and corresponding Arrhenius parameters.

i	**Deposition reaction**	A_i	β_i	$\mathfrak{E}_i$**(K)**	**Reference**
1	$H(g) \longrightarrow \frac{1}{2}H_2(g)$	0.01	0.0	0.0	[KNF$^+$04]
2	$SiH_2(g) \longrightarrow Si(s) + H_2(g)$	0.8	0.0	0.0	[PLB96]
4	$SiH_3(g) \longrightarrow Si(s) + H_2(g) + H(g)$	0.09	0.0	0.0	[PLB96]
5	$SiH_4(g) \longrightarrow Si(s) + 2H_2(g)$	5.37×10^{-2}	0.0	9,400	[CKM86]
6	$H_3SiSiH(g) \longrightarrow 2Si(s) + 2H_2(g)$	0.8	0.0	0.0	[PLB96]
7	$Si_2H_5(g) \longrightarrow 2Si(s) + 2H_2(g) + H(g)$	0.09	0.0	0.0	[dB06]
8	$Si_2H_6(g) \longrightarrow 2Si(s) + 3H_2(g)$	5.37×10^{-1}	0.0	9,400	[CKE89]

The molar surface production rates $\widehat{\omega}_k$, $k \in \mathfrak{S}$, are obtained from a given set $\widehat{\mathscr{R}}$ of heterogeneous reactions describing the deposition process, in the form

$$\sum_{l \in \mathfrak{S} \cup \widehat{\mathfrak{S}}} \widehat{\nu}_l^{\text{rf}}\, \mathfrak{M}_l \rightleftharpoons \sum_{l \in \mathfrak{S} \cup \widehat{\mathfrak{S}}} \widehat{\nu}_l^{\text{rb}}\, \mathfrak{M}_l, \quad r \in \widehat{\mathscr{R}}, \tag{4.8.17}$$

where $\widehat{\mathfrak{S}}$ denotes the set of surface species, and $\widehat{\nu}_l^{\text{rf}}$ and $\widehat{\nu}_l^{\text{rb}}$ denote the forward and backward stoichiometric coefficients of the l^{th} species in the r^{th} surface reaction, respectively. The molar surface production rate is then computed from the knowledge of the rates of progress $\widehat{\tau}_r$, $r \in \widehat{\mathscr{R}}$

$$\widehat{\omega}_k = \sum_{r \in \widehat{\mathscr{R}}} (\widehat{\nu}_k^{\text{rf}} - \widehat{\nu}_k^{\text{rb}})\, \widehat{\tau}_r, \qquad k \in \mathfrak{S} \cup \widehat{\mathfrak{S}}. \tag{4.8.18}$$

The surface reactions are assumed irreversible. Each surface reaction $r \in \widehat{\mathscr{R}}$ is associated with a unique gas-phase heavy-species reactant, denoted by $i_r \in \mathfrak{H}$. The rate of progress of reaction $r \in \widehat{\mathscr{R}}$ is calculated as in (3.11.5)

$$\widehat{\tau}_r = \frac{s_{i_r}}{1 - \frac{s_{i_r}}{2}} \gamma_{i_r} \sqrt{\frac{RT_h}{2\pi m_{i_r}}}, \qquad r \in \widehat{\mathscr{R}}, \tag{4.8.19}$$

where $\gamma_{i_r} = \rho Y_{i_r}/m_{i_r}$ is the molar concentration of the depositing species, and s_{i_r} is its sticking coefficient. As in (3.11.5), the reactive probability s_{i_r} is adjusted by the factor $1 - s_{i_r}/2$ in order to remain valid in the limit $s_{i_r} \to 1$, where nearly all the molecules of species i_r stick to the wall without being reflected [MW60] [KCG03].

The silicon deposition rate (in cm.s^{-1}) associated with each surface reaction r then follows

$$w_{\text{Si(s)}}^r = \mathrm{V}_{\mathrm{m}}^{\text{Si}}\, \widehat{\nu}_{\text{Si(s)}}^{\text{rb}} \widehat{\tau}_r, \tag{4.8.20}$$

where $\widehat{\nu}^{rb}_{Si(s)}$ is the backward soichiometric coefficient of Si(s) in the r^{th} surface reaction, and V^{Si}_m is the molar volume of crystalline silicon

$$V^{Si}_m \simeq 12.06 \text{ cm}^3.\text{mol}^{-1}, \tag{4.8.21}$$

and consequently the total silicon deposition rate reads

$$w_{Si(s)} = \sum_{r \in \widehat{\mathscr{R}}} w^r_{Si(s)} = V^{Si}_m \widehat{\omega}_{Si(s)}. \tag{4.8.22}$$

The heterogeneous reaction mechanism used in the present software corresponds to the deposition of amorphous silicon by low temperature PECVD. The sticking coefficients associated with the main silicon radicals have been taken from [PLB96]. They have been taken in Arrhenius form

$$\gamma_i(T_h) = A_i T_h^{\beta_i} \exp\Big(-\frac{\mathfrak{E}_i}{T_h}\Big), \quad i \in \mathfrak{H}, \tag{4.8.23}$$

where A_i is the pre-exponential factor, β_i the pre-exponential exponent and $\mathfrak{E}_i \geq 0$ the activation energy in Kelvin. The list of surface reactions and the corresponding Arrhenius parameters are given in Table 4.5.

4.9 External Circuit

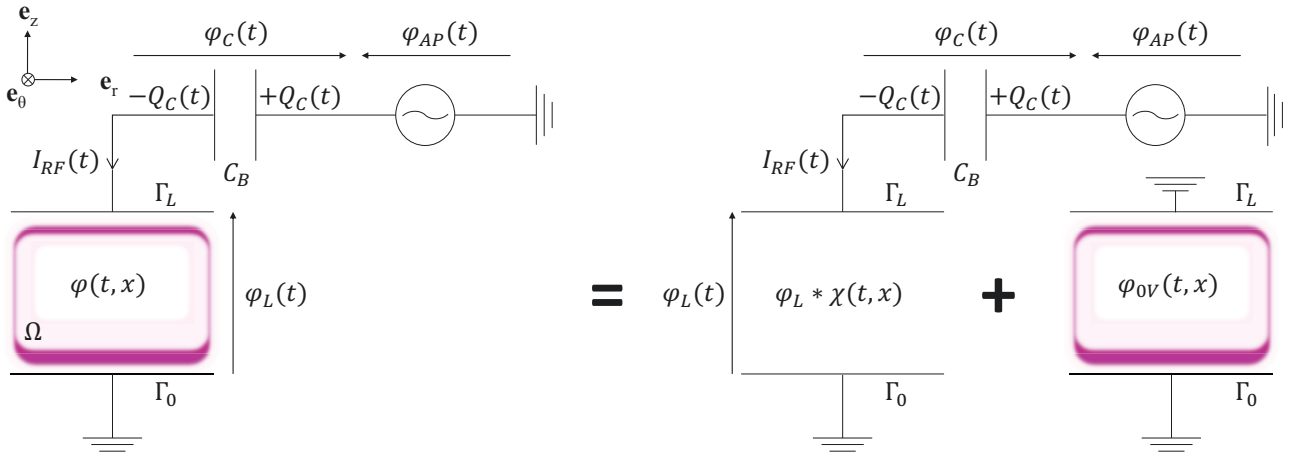

Figure 4.4 – Schematic representation of the discharge and external circuit, including the generator and blocking capacitor. The potential is decomposed in a "bare" potential $\varphi_L \chi$ and a "relaxation" potential φ_{0V}.

An alternative boundary condition for the potential at the driven electrode was also implemented. In this new formulation, the external blocking capacitor is taken into account, which will allow for the determination of the DC bias in an asymmetric discharge. A schematic representation of the discharge and external circuit is presented in Figure 4.4. For the sake of simplicity, no matching box is considered. In order to compute the potential at the driven electrode $\varphi_L(t) = \varphi(t, L)$, the potential accross the discharge is decomposed in the form

$$\varphi = \varphi_{0V} + \varphi_L \chi, \tag{4.9.1}$$

where φ_{0V} is the solution of Poisson's equation with the actual charge distribution in the reactor at time t, which can be asymmetric, and a driven potential equal to zero

$$\partial^2_{\boldsymbol{x}}\varphi_{0V} = -\sum_{k\in\mathfrak{S}} \frac{n_k q_k}{\varepsilon_0},\ \boldsymbol{x}\in\Omega, \qquad \varphi_{|\Gamma_0} = 0, \qquad \varphi_{|\Gamma_{\text{L}}} = 0, \tag{4.9.2}$$

and χ is the "bare" potential, that is the solution of the Laplace's equation accross the reactor

$$\partial^2_{\boldsymbol{x}}\chi = 0,\ \boldsymbol{x}\in\Omega, \qquad \chi_{|\Gamma_0} = 0, \qquad \chi_{|\Gamma_{\text{L}}} = 1, \tag{4.9.3}$$

which depends only on the geometry of the reactor and can be computed a priori. In the preceding equations, Γ_0 and Γ_{L} denote the respective electrode surfaces, and the walls are grounded so the potentials must vanish at the reactor walls.

The conservation of total current in the circuit can then be written in the form

$$I_{\text{RF}}(t) = \frac{dQ_{\text{C}}}{dt} = C_{\text{B}}\frac{d\varphi_{\text{C}}}{dt} = C_{\text{B}}\left(\frac{d\varphi_{\text{AP}}}{dt} - \frac{d\varphi_{\text{L}}}{dt}\right), \tag{4.9.4}$$

from which φ_{L} is solution to

$$C_{\text{B}}\frac{d\varphi_{\text{L}}}{dt} = C_{\text{B}}\frac{d\varphi_{\text{AP}}}{dt} - I_{\text{RF}}(t) \tag{4.9.5}$$

where φ_{AP} is the applied potential.

The current can be expressed in terms of the physical variables directly as

$$I_{\text{RF}}(t) = -\int_{\Gamma_{\text{L}}} (\boldsymbol{j} + \varepsilon_0\partial_t\mathbf{E})\cdot\boldsymbol{n}\, ds, \tag{4.9.6}$$

where

$$\boldsymbol{j} = \sum_{k\in\mathfrak{S}} n_k q_k \boldsymbol{v}_k \tag{4.9.7}$$

is the conduction current, and $\varepsilon_0\partial_t\mathbf{E}$ is the displacement current. Alternatively, the following expression can be obtained [Qui05]

$$I_{\text{RF}}(t) = \frac{1}{\varphi_{\text{L}}(t)}\mathcal{P} = -\int_\Omega \boldsymbol{\partial}_{\boldsymbol{x}}\chi\cdot\boldsymbol{j}\, d\omega + C_{\text{V}}\frac{d\varphi_{\text{L}}}{dt}, \tag{4.9.8}$$

where C_{V} is the "bare" capacitance of the reactor

$$C_{\text{V}} = \varepsilon_0\int_{\Gamma_{\text{L}}} \boldsymbol{\partial}_{\boldsymbol{x}}\chi\cdot\boldsymbol{n}\, ds, \tag{4.9.9}$$

which depends only on the geometry of the reactor and can be computed a priori.

Therefore, the potential φ_{L} is the solution of the following differential equation

$$(C_{\text{B}} + C_{\text{V}})\frac{d\varphi_{\text{L}}}{dt} = C_{\text{B}}\frac{d\varphi_{\text{AP}}}{dt} + \int_\Omega \boldsymbol{\partial}_{\boldsymbol{x}}\chi\cdot\boldsymbol{j}\, d\omega, \tag{4.9.10}$$

which is solved self-consistently within the software. In this work, we have preferred expression (4.9.8) to (4.9.6) since it has revealed more stable numerically. Note that in the one-dimensional approximation, equation 4.9.10 becomes

$$(C_{\text{B}} + C_{\text{V}})\frac{d\varphi_{\text{L}}}{dt} = C_{\text{B}}\frac{d\varphi_{\text{AP}}}{dt} + \frac{S}{L}\int_0^L j\, dz, \tag{4.9.11}$$

and the "bare" capacitance reads

$$C_{\text{V}} = \frac{\varepsilon_0 S}{L}, \tag{4.9.12}$$

where S is the surface of the electrodes, which is the classical expression for the capacitance of a parallel plate capacitor. In practice, the geometry of a reactor is complicated, and due to the law of electromagnetics, even a small feature in the structure of the reactor can change considerably the value of the "bare" capacitance, so that it is better to measure it experimentally. Besides, since the blocking capacitance is generally taken large before C_{v}, the actual value of C_{v} does not matter and equation (4.9.10) only depends on C_{B}.

Figure 4.5 – Picture of the ARCAM multiplasma monochamber reactor in LPICM.

4.10 Numerical Implementation

The numerical implementation follows the same framework as in section 3.12 of the preceding chapter. We denote by $n^c = n^s + 2$ the number of unknowns. The solution vector is denoted by

$$\boldsymbol{\Xi} = (\Xi_l)_{1\leq l\leq n^c} = (T_e, \varphi, Y_1, \ldots, Y_{n^s}), \tag{4.10.1}$$

The discretized equations are obtained from a three-point finite difference scheme. The time derivatives are discretized in a fully implicit manner. The discretization of the transport fluxes requires special care, for the electric field acts as a convection velocity.

4.10.1 Discretization

As in Chapter 3, equations (4.4.14)-(4.4.16) are discretized over a grid along the z axis of the form

$$Z = \{0 = z_1 < z_2 < \cdots < z_N = L\}, \tag{4.10.2}$$

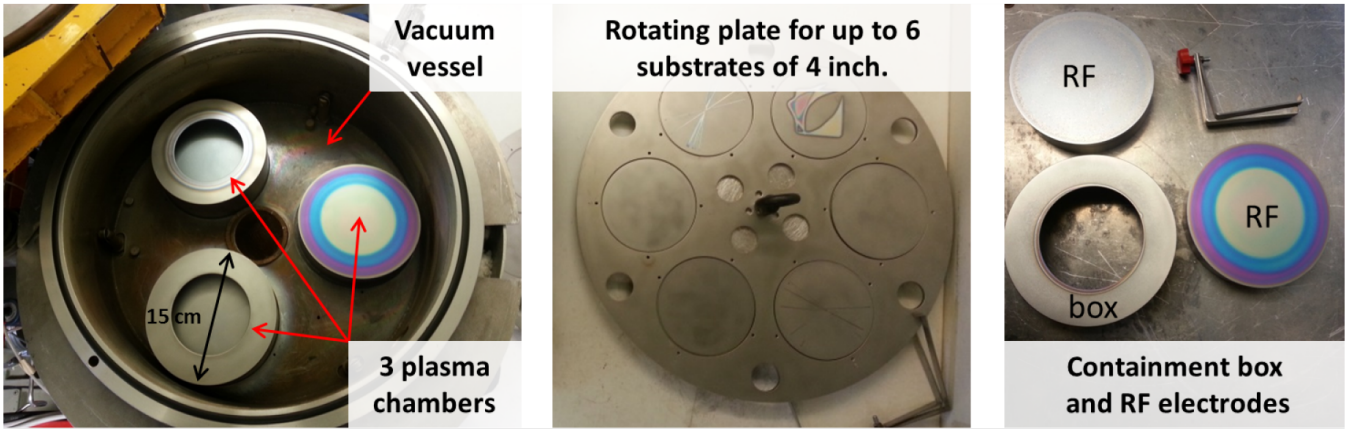

Figure 4.6 – Interior of the ARCAM reactor in LPICM (Left); grounded rotating plate (Middle); RF electrode and plasma box (Right).

where N is the number of grid points. The discretized solution vector is denoted by

$$\Xi_Z = (\Xi_{k,i})_{1\leq k\leq n^c, 1\leq i\leq N}. \tag{4.10.3}$$

Discretization of the species diffusion velocities It is known that, in the case of a neutral gas, an unproper discretization of the species diffusion flux $\rho Y_k v_h - D_k^* \partial_z Y_k$, where v_h is the convection velocity, may lead to unstable or less consistent numerical solution. For the sake of stability and consistency, the discretization must take into account the order of magnitude of the Peclet number

$$P_{k,i+1/2} = \left(\frac{\rho v_h \Delta z}{D_k^*}\right)_{i+1/2}, \quad k \in \mathfrak{S},\ 1 \leq i \leq N, \tag{4.10.4}$$

where $(\Delta z)_{i+1/2} = z_{i+1} - z_i$ is the mesh size around midpoint $z_{i+1/2} = (z_i + z_{i+1})/2$. Several schemes are possible to avoid such drift-induced instability, more or less consistent, for example the upwind discretization scheme, the "hybrid" scheme, the "power-law" scheme, or the "exact" exponential scheme [Pat80].

Similarly, in the plasma case the electric drift behaves as a convection velocity. Indeed, the species diffusion velocities, expressed in equations (4.4.18), read in the axisymmetric coordinates

$$\mathcal{V}_k = -D_k^* \frac{\partial_z Y_k}{Y_k} + \mu_k^* \mathrm{E}, \qquad k \in \mathfrak{S},\ k \neq \mathrm{H}_2. \tag{4.10.5}$$

Since the electric field in the sheaths may reach fairly large values, namely the associated Peclet number

$$P_{k,i+1/2} = \left(\frac{\mu_k^* \mathrm{E} \Delta z}{D_k^*}\right)_{i+1/2}, \quad k \in \mathfrak{S},\ 1 \leq i \leq N, \tag{4.10.6}$$

may be large compared to 1, the central difference scheme may lead to numerical instability, as for the convection-diffusion problem. In general, the exponential discretization scheme is adopted to avoid such instability, in the form

$$(Y_k \mathcal{V}_k)_{i+1/2} = \left(\frac{D_k^*}{\Delta z}\right)_{i+1/2} P_{k,i+1/2} \frac{Y_{k,i}\, e^{\frac{P_{k,i+1/2}}{2}} - Y_{k,i+1}\, e^{-\frac{P_{k,i+1/2}}{2}}}{e^{\frac{P_{k,i+1/2}}{2}} - e^{-\frac{P_{k,i+1/2}}{2}}}, \quad k \in \mathfrak{S},\ 1 \leq i \leq N, \tag{4.10.7}$$

where $Y_{k,i}$ denotes the mass fraction of the k^{th} species at grid point z_i. The exponential scheme (4.10.7) is often referred to as the "Scharfetter-Gummel" numerical scheme in the litterature [SG69] [Boe87].

Discretization of the electron heat flux Equation (4.4.16) for the electron temperature involves the electron heat flux (4.4.21), which reads in axisymmetric coordinates

$$\mathcal{Q}_e = \frac{5}{2} n_e k_{\text{B}} T_e \mathcal{V}_e - \hat{\lambda}_{ee} \partial_z T_e. \tag{4.10.8}$$

where $\hat{\lambda}_e$ was expressed in equation (4.5.2). As the species diffusion velocities, the electron heat flux can be discretized by the exponential or "Scharfetter-Gummel" numerical scheme [Pat80] [SG69]. This yields

$$(\mathcal{Q}_e)_{i+1/2} = \Big(\frac{\hat{\lambda}_{ee}}{\Delta z}\Big)_{i+1/2} P_{\mathcal{Q}_e,i+1/2} \, \frac{T_{e,i}\, e^{\frac{P_{\mathcal{Q}_e,i+1/2}}{2}} - T_{e,i+1}\, e^{-\frac{P_{\mathcal{Q}_e,i+1/2}}{2}}}{e^{\frac{P_{\mathcal{Q}_e,i+1/2}}{2}} - e^{-\frac{P_{\mathcal{Q}_e,i+1/2}}{2}}}, \quad 1 \le i \le N, \tag{4.10.9}$$

where $P_{\mathcal{Q}_e,i+1/2}$ is the corresponding Peclet number

$$P_{\mathcal{Q}_e,i+1/2} = \Big(\frac{\frac{5}{2} k_{\text{B}} n_e \mathcal{V}_e \Delta z}{\hat{\lambda}_{ee}}\Big)_{i+1/2}, \quad 1 \le i \le N. \tag{4.10.10}$$

4.10.2 Resolution

Contrarily to the chemical vapor deposition process described in Chapter 3, the radio-frequency discharge problem is fully non-stationary, since the potential imposed on the RF electrode depends on time. Yet, the applied signal being periodic, after a few cycles the process reaches a pseudo-stationary state, in which the relevant physical variables, namely the electron temperature T_e, the electric potential φ and the species mass fractions Y_k, $k \in \mathfrak{S}$, are periodic with the same period as the RF signal.

As in Chapter 3, the equations for the n^{th} iteration at time t may be written in the form

$$\boldsymbol{A}(\boldsymbol{\Xi}_Z^n)\, \partial_t \boldsymbol{\Xi}_Z^n + \boldsymbol{F}_Z(\boldsymbol{\Xi}_Z^n) = 0, \tag{4.10.11}$$

were $\boldsymbol{\Xi}_Z^n$ denotes the n^{th} iterate over the grid Z, $\boldsymbol{A}(\boldsymbol{\Xi}_Z^n)$ is a bloc diagonal matrix, and

$$\partial_t \boldsymbol{\Xi}_Z^n = \frac{\boldsymbol{\Xi}_Z^n - \boldsymbol{\Xi}_Z^{n-1}}{t^n - t^{n-1}} \tag{4.10.12}$$

is the discretized time derivative at time t^n. These implicit non-stationary equations are solved by the modified Newton method already described in section 3.12.

4.11 Results and Discussion

Simulations have been carried out under typical conditions for plasma enhanced low-temperature epitaxy of silicon [RCL12]. The geometry is that of Figure 4.2. The interelectrode distance is set equal to 2 cm. For the base case, the inlet gas mixture is composed of 85 % hydrogen and 15 % silane, that is $X_{\text{H}_2} = 85$ % and $X_{\text{SiH}_4} = 15$ %. The pressure is set at $p_0 = 2.28$ Torr, the heavy-species temperature is taken equal to $T_h = 500$ K. We first present results for symmetric radio-frequency waveforms. Then, a self-consistent computation of the DC bias is implemented and the effect of asymmetric waveforms is studied.

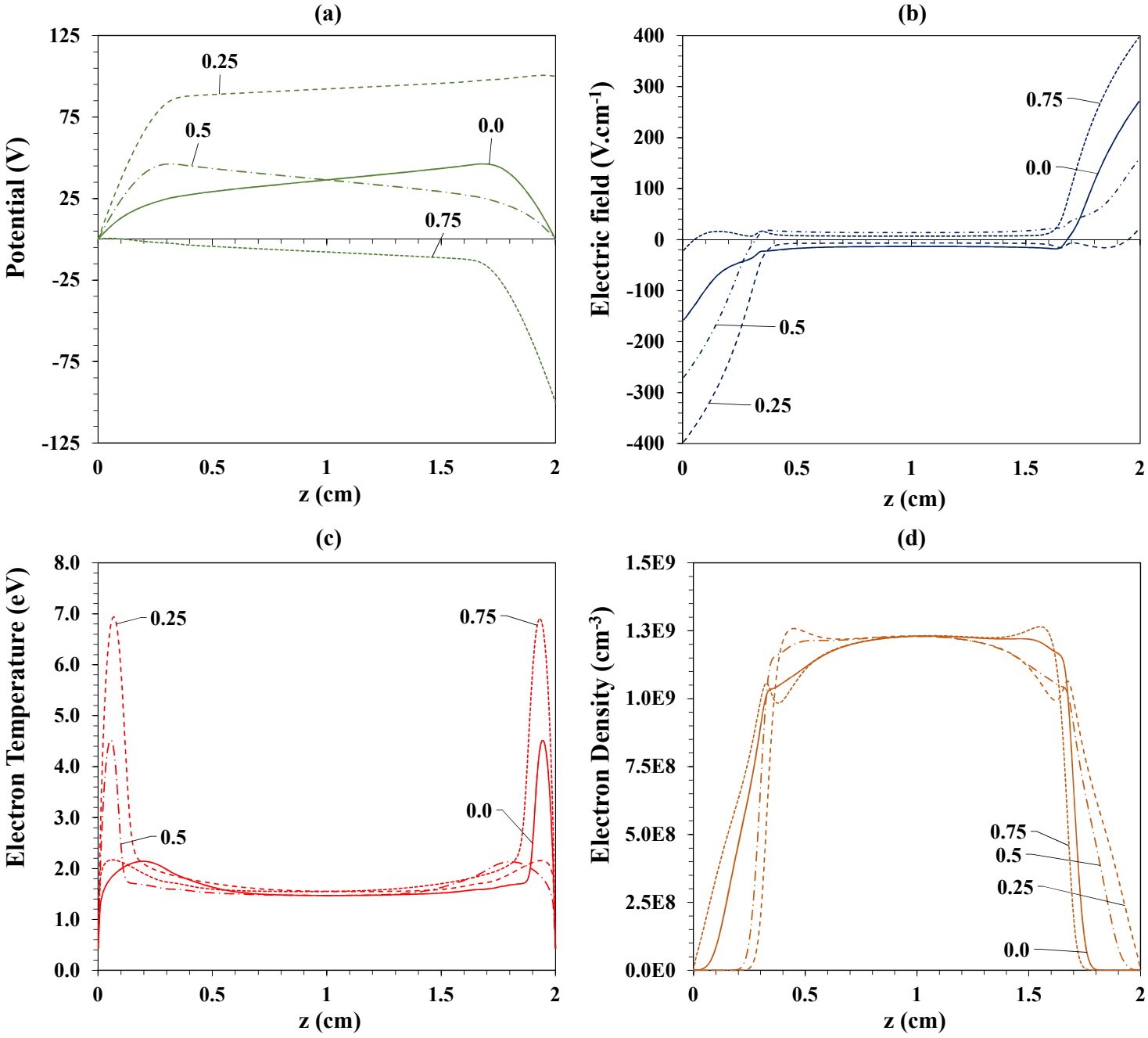

Figure 4.7 – Pseudo-steady-state electric potential (a), electric field (b), electron temperature (c) and electron density (d) profiles along the axis of symmetry of the reactor at several instants of the radio-frequency cycle, namely $ft = 0.0$, 0.25, 0.5, and 0.75.

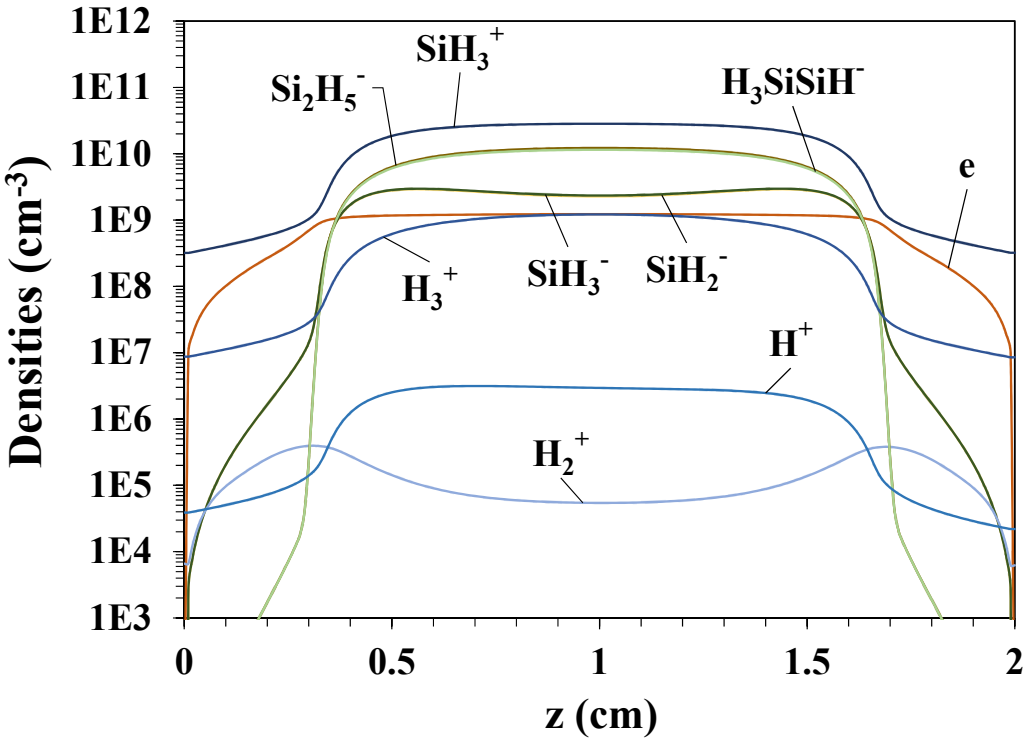

Figure 4.8 – Charged species density profiles along the axis of symmetry of the reactor, averaged over an RF period.

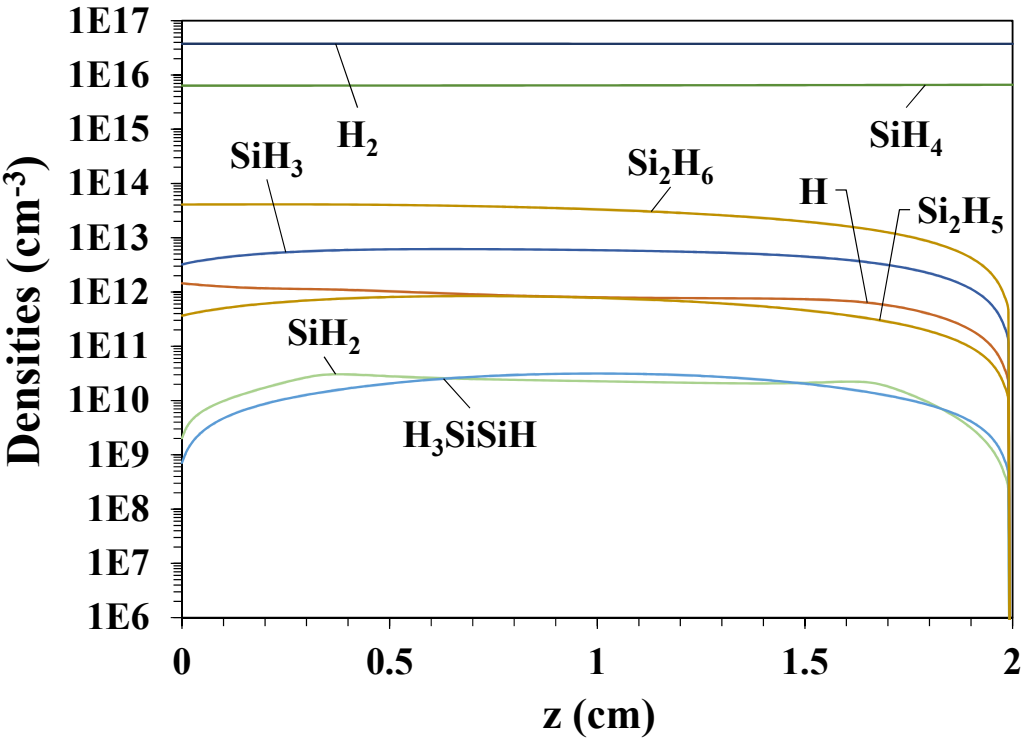

Figure 4.9 – Neutral species density profiles along the axis of symmetry of the reactor, averaged over an RF period.

4.11.1 Symmetric Discharge

Figures 4.5 and 4.6 depict the ARCAM reactor used in PICM for several decades. This reactor, as most research reactors, is actually geometrically asymmetric due to the relatively small surface area of the electrodes. In particular, the reactor walls are grounded, so that the grounded area is larger than the powered area. This induces an asymmetry in the current flowing into the discharge, which in turn translates into a DC bias at the powered electrode, due to the accumulation of charge between the blocking capacitor, illustrated in Figure 4.2, and the reactor. In standard industrial processes, however, the reactors used have much larger lateral dimensions, and the DC bias induced by the geometrical asymmetry is generally negligible. This justifies the use of a symmetric one-dimensional geometry.

The frequency is set at $f = 13.56$ MHz, and the applied potential amplitude is $\varphi_{\text{RF}} = 100$ V. For those "base case" conditions, the power dissipated in the discharge is equal to 5 W. The initial profiles are uniform over the reactor length. Time iterations are performed with timesteps bounded by 0.1 ns, until a pseudo-steady-state is reached, where the relative changes in the main plasma properties do not exceed 10^{-5} between two cycles. The electron temperature and electric potential reach a pseudo-steady-state after a few thousand cycles. The charged species densities reach a pseudo-periodic state after approximately 20,000 cycles, while some of the neutral species densities require up to 100,000 cycles to reach a pseudo-steady-state.

The pseudo-steady-state electric potential, electric field, electron temperature, and electron density profiles along the axis of symmetry of the reactor are shown in Figure 4.7, at four different instants of the radio-frequency cycle, namely $ft = 0.0$, $ft = 0.25$, $ft = 0.5$ and $ft = 0.75$. As can be seen on these figures, the imposed potential induces an oscillating electric field accross the reactor. The quasi-neutrality is generally ensured in the center of the discharge, called the "bulk" plasma, so that the electric field is significant mostly in the vicinity of the electrode surfaces, in the region referred to as the "plasma sheaths". Also, the potential is quasi-concave because electrons are more mobile and less easily trapped in the plasma bulk, so that the net charge density is essentially positive accross the reactor. The electron temperature is in the range $1 - 2$ eV in the plasma bulk, and oscillates between $1-2$ eV and $6-7$ eV in the sheaths. The pseudo-steady-state electron density is of the order of 10^9 cm^{-3}, which is relatively low compared to commonly observed radio-frequency plasma discharges. This is due to the presence of negative ions in silane plasma discharges, which are the dominant negatively charged species.

The pseudo-steady-state density profiles, averaged over an RF cycle, are shown in Figures 4.8 and 4.9, respectively for charged species and neutrals. The main positive ion is the SiH_3^+ ion, and the ionization ratio of silane is equal to

$$\frac{X_{\text{SiH}_3^+}}{X_{\text{SiH}_4}} = 3.0 \times 10^{-6}, \tag{4.11.1}$$

at the center of the discharge. This result is comparable to the value obtained by Salabas et al. in [SGA02]. The silane depletion rate accross the reactor length is equal to 4 %.

The main negatively charged species are the negative ions $Si_2H_5^-$ and H_3SiSiH^-. These species are produced from the clustering reactions between the smaller negative ions SiH_2^- and SiH_3^- and silane, namely reactions 19 and 20 of Table 4.3. These species are known to be the main precursors of the nanoparticle nucleation in silane plasma discharges [BSGK00]. The electron density is of the order of 10^9 cm^{-3}, that is one order of magnitude lower than the overall negative ion density.

As expected, H_3^+ ion is dominant over $H2^+$ and H^+ ions, but its density is one order of magnitude lower than that of silicon containing ions. The hydrogen ionization ratio is equal to

$$\frac{X_{\text{H}_3^+}}{X_{\text{H}_2}} = 1.7 \times 10^{-8} \tag{4.11.2}$$

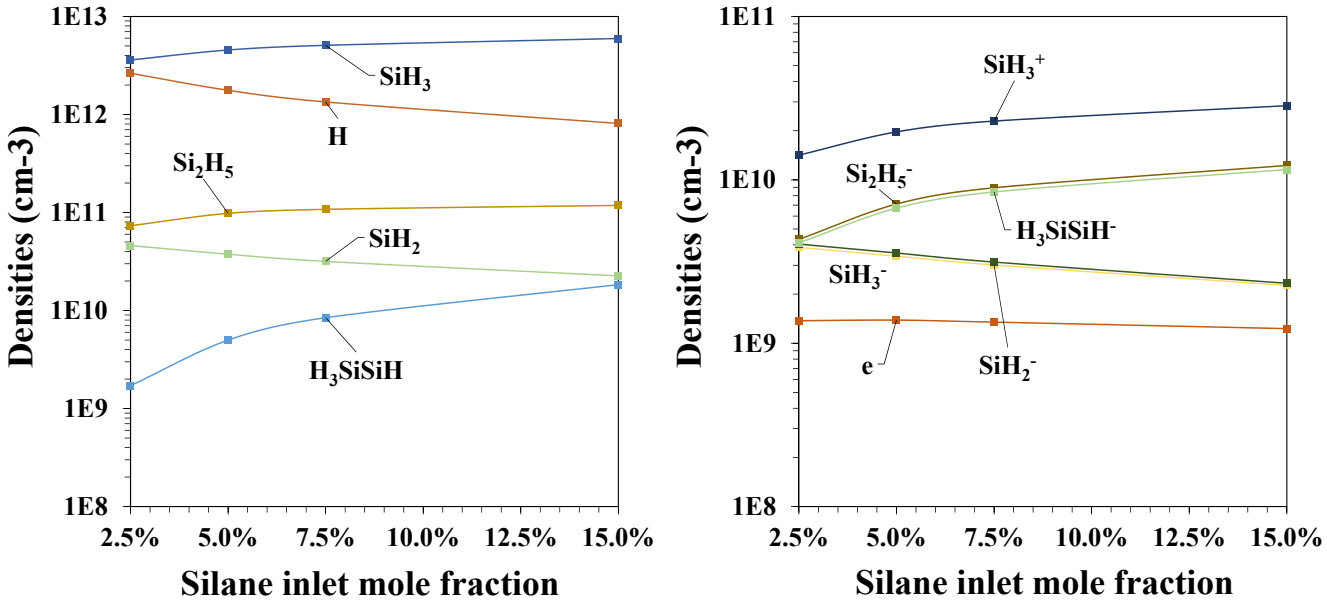

Figure 4.10 – Main radicals (Left) and ion (Right) densities at the center of the reactor as a function of the silane dilution ratio.

at the center of the discharge. For comparison in [DCL05] Diomede et al. obtained a ratio of the order of 10^{-7} for a pure H_2 discharge, and Salabas et al. obtained a ratio of roughly $7 \cdot 10^{-8}$ in for a 7 %-93 % SiH_4-H_2 discharge [SGA02]. A possible explanation for this relatively low ionization ratio of hydrogen is the presence of silane, which is more easy to ionize than hydrogen, since its ionization energy is significantly lower. Results are also in good agreement with experimental results of [HDD+94].

The SiH_3 radical produced by the dissociation of silane is the dominant radical, and Si_2H_6 is the second most abundant neutral spcies. Atomic hydrogen is also abundantly present in the reactor, and the dissociation degree of molecular hydrogen is equal to

$$\frac{X_{\mathrm{H}}}{X_{\mathrm{H_2}}} = 2.7 \times 10^{-5}, \tag{4.11.3}$$

at the center of the discharge.

The influence of the silane dilution in H_2 is investigated in Figure 4.10. The pressure and applied potential have been kept equal to 2.28 Torr and 100 V, respectively, as in the base case. As can be seen on this Figure, increasing the dilution ratio tends to hinder the rate of clustering reactions leading to the formation of $Si_2H_x^-$ ions, and also decrease the density of SiH_3^+ ion. Also, the electronegativity decreases as the electron density does not decrease substantially when the dilution ratio is varied from 15 % to 2.5 %. It is well known that at high H_2 dilution ratio, the films produced tend to be microcrystalline (μc-Si), while at high silane flow rate the films are generally hydrogenated amorphous silicon a-Si:H. The significant increase in hydrogen atom density as the dilution is increased could explain the transition to microcrystalline deposition, as H atoms, which are very reactive, have been shown to enhance crystallization of silicon nanoparticles [VB05] and are also expected to enhance crystallization within the deposited layer. Interestingly, Si_2H_x silicon radical densities decrease as the dilution ratio is increased, following the trend of $Si_2H_x^-$ ions, while SiH_2 density increases, following the trend of SiH_x^- ions.

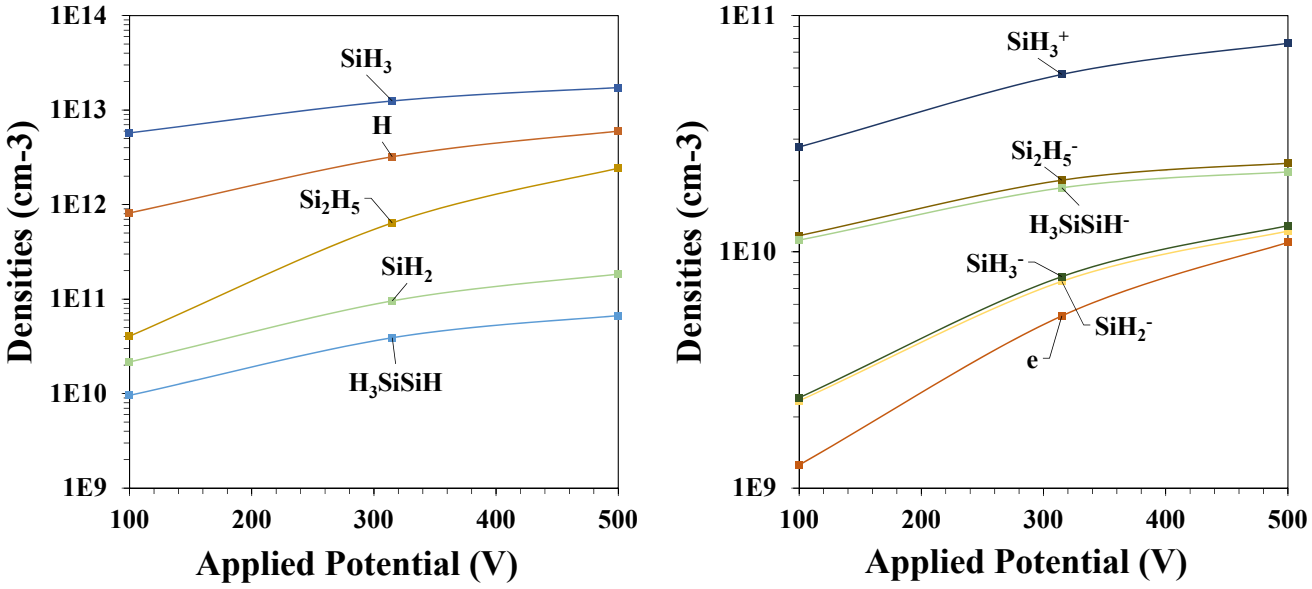

Figure 4.11 – Main radicals (Left) and ion (Right) densities at the center of the reactor as a function of the RF voltage.

Finally, the influence of the radio-frequency power is investigated in Figure 4.11. The pressure and silane inlet mole fraction have been kept equal to 2.28 Torr and 15 %, respectively, as in the base case. As expected, increasing the power increases the ionization rate as well as the silicon clustering reaction rates. Also, the plasma tends to become less electronegative, which is consistent with the increase in the DC bias observed when increasing RF power in an asymmetric discharge setup under similar conditions [Kim12]. However, from a practical viewpoint, increasing the RF power also increases ion flux and energy, as well as dust formation, and thus induce impurities in the deposited layers [Kim12].

4.11.2 Asymmetric Excitation

As mentioned in the preceding subsection, industrial reactors are generally geometrically symmetric. However, the use of asymmetric excitation waveforms is now seen as an interesting tool to control independently the ion flux and ion energy in a capacitively coupled radio-frequency discharge [DSHC09] [SSC09] [LDJB12]. This kind of waveform generally induce a nonnegligible DC bias even in a geometrically symmetric discharge, due to the temporal asymmetry of the applied potential. Additionally, in research reactors the evolution of the DC bias is strongly related to the formation of nanoparticles and powders [BBH96] [WB12] [Kim12], and is often used as a tool for controlling the discharge conditions and deposition process. This is a stong motivation for implementing a self-consistent calculation of the DC bias in the plasma fluid model, as described in section 4.9. In a one-dimensional formulation, no geometrical asymmetry will be observed, so in the following we will consider "tailored voltage waveforms".

We first consider a two-frequency waveform that is the sum of a fundamental frequency and its first harmonic [HCBM08]

$$\varphi_{\mathrm{AP}}(t) = \varphi_{\mathrm{RF}}\big[\cos(\omega t + \psi_0) + \cos(2(\omega t + \psi_0))\big], \tag{4.11.4}$$

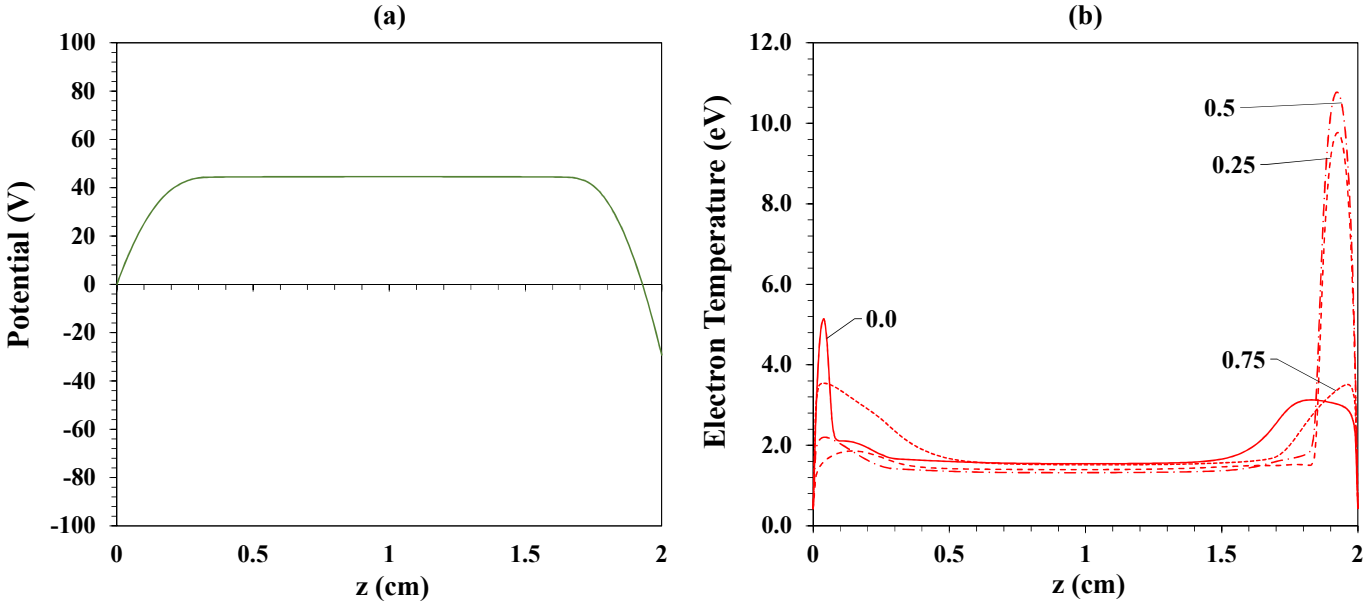

Figure 4.12 – Electric potential profile averaged over a radio-frequency cycle (a) and electron temperature profiles at four different instants of the radio-frequency cycle (b) under a two-frequency waveform excitation. The fundamental frequency is $f = 13.56$ MHz and the applied potential amplitude is $\varphi_{\mathrm{RF}} = 100$ V. Other parameters are those of the base case.

where $\omega = 2\pi f$ is the RF pulsation and $f = 13.56$ MHz. The pressure is set at $p = 2.28$ Torr, and the silane inlet mole fraction is kept at $X^{\mathrm{in}}_{\mathrm{SiH_4}} = 15$ %. Simulation results are shown in Figure 4.12. Under such conditions, the average electric potential is clearly asymmetric, and a DC bias potential of $\varphi_{\mathrm{DC}} = -29$ V has appeared. This in line with the analytical expression of the DC bias derived in [DSHC09], in the form

$$\varphi_{\mathrm{DC}} = -\frac{\varphi_{\max} + \epsilon\varphi_{\min}}{1+\epsilon}, \tag{4.11.5}$$

where ϵ is a geometrical asymmetry parameter. For $\epsilon = 1$, that is if all the asymmetry could be attributed to the amplitude asymmetry of the applied signal, the DC bias observed would be of -25 V [DSHC09] [Bru15]. However, the asymmetry of the signal induces additional asymmetry between the two electrodes, which explains the difference with this theoretical value. The electron temperature profile is also strongly asymmetric, with a higher excitation peak occuring in the vicinity of the powered electrode during the sheath contraction period. This is consistent with the results of Donkó et al. [DSHC09].

Another type of waveforms has recently been considered, whose asymmetry is not an amplitude asymmetry, as in the preceding example, but a slope asymmetry. Sawtooth-like waveforms are obtained by truncating the Fourier series of a "sawtooth" function [BGO+15]

$$\varphi_{\mathrm{AP}}(t) = \varphi_{\mathrm{RF}} \sum_{k=1}^{N_{\mathrm{RF}}} \frac{1}{k} \sin(k\omega t). \tag{4.11.6}$$

This kind of waveform also induces a DC bias on the powered electrode, which has revealed sensitive to the chemistry employed. In particular, when an electronegative gas is used such as CF_4, the sign of the DC bias is reversed compared to the argon case. When H_2 is used as a gas precursor, an intermediate behavior is observed with a less pronounced asymmetry effect, attributed to the lower

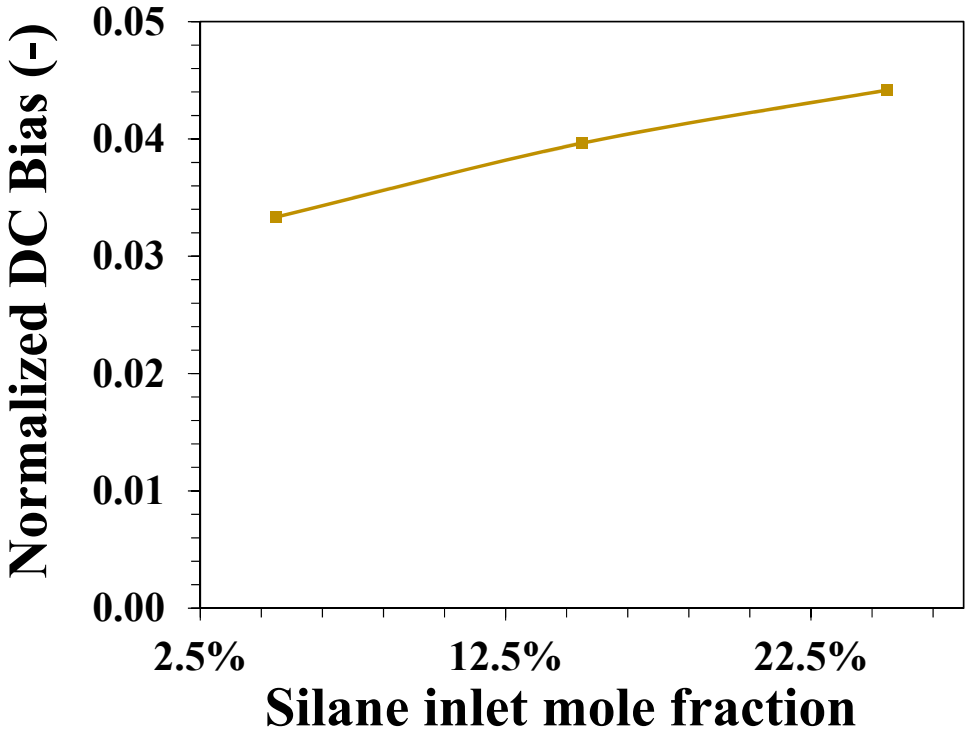

Figure 4.13 – Normalized DC bias as a function of the silane dilution ratio, for a geometrically symmetric discharge excited with sawtooth waveforms. The DC bias has been normalized by the peak to peak voltage.

mass of hydrogen [BLG$^+$16]. Therefore, an investigation of the effect of sawtooth-like waveform on a silane-hydrogen plasma is desirable, since silane and hydrogen respond differently to such waveforms.

Simulations have been run for a silane-hydrogen discharge excited with sawtooth waveforms (4.11.6), in a perfectly symmetric reactor with an interelectrode distance of 2.5 cm, a potential amplitude of $\varphi_{\text{RF}} = 200$ V, and at a pressure of 900 mTorr. Those conditions are close to the conditions used in [BLG$^+$16]. Figure 4.13 shows the values of the normalized DC bias as a function of the SiH_4 dilution ratio. The DC bias is positive, as was the case with CF_4. This can be explained by the electronegativity of silane. Given the very low densities of H_x^+ positive ions compared to silicon hydride ions, hydrogen ions do not play a significant role on the bias formation. However, silane is less electronegative than CF_4, and the electron density remains comparable to the main negative ion densities under the conditions considered. This can explain the relatively low values of DC bias obtained, compared to CF_4 chemistry, although further investigation should be carried out.

4.12 Conclusion

The chemical vapor deposition software developed in Chapter 3 has been extended in order to model self-consistently a radio-frequency discharge in silane-hydrogen. The Poisson's equation for the electric potential and the evolution equation for the electron temperature have been incorporated and coupled to the existing set of equations. The convection velocity has been neglected, and the expressions for transport fluxes have been simplified using approximations routinely employed in the modeling of non-thermal plasmas. The self similar formulation in axisymmetric coordinates has been conserved. A complete chemistry mechanism has been incorporated, taking into account electron collisions depending on the electron temperature T_e, and heavy-species reactions depending on the heavy-species temperature T_h. A surface chemistry mechanism has also been used for modeling the interaction of the neutral species with the substrate.

Simulations have been performed under typical conditions for plasma-enhanced low-temperature epitaxy of silicon. The numerical method used in Chapter 3 for chemical vapor deposition has been conserved. The problem is fully non-stationary, and the plasma parameters are shown to reach a pseudo-steady-state, in which the discharge properties are quasi-perodic, after a few tens of thousands of RF cycles. The plasma is electronegative, with a majority of SiH_3^+ positive ions and $Si_2H_x^-$ negative ions. The results obtained are in agreement with previous studies under similar conditions. A study of the influence of silane dilution ratio and RF power was carried out. The results are in good qualitative agreement with previous experimental studies under conditions for deposition of amorphous silicon.

Finally, a self-consistent calculation of the DC bias potential was implemented, by taking into account the blocking capacitor in the external circuit. This allowed for the study of excitation by asymmetric waveforms. The effect of amplitude asymmetry was first considered by using a two-frequency waveform. In this case, the value of the bias potential depends essentially on the amplitude ratio of the applied signal, and the bias obtained was found to be close to theoretical predictions and previous results in argon discharges. The effect of a new kind of waveforms, called "sawtooth" waveforms, was also investigated. The DC bias was found to be of the same sign as for CF_4 chemistry, which can be attributed to the electronegativity of silane. However, the value of the DC bias is much lower than was observed for CF_4 in similar conditions. A possible explanation is the lower electronegativity of silane. Under the conditions considered, the influence of hydrogen ions was found to be negligible.

The plasma model will be enriched in Chapter 5 with a sectional model for nanoparticles. The negative ions containing two silicon atoms $Si_2H_x^-$ are known to be the main precursors of nanoparticle nucleation [BSGK00], and their rate of clustering with silane molecules will be used as the nucleation rate for nanoparticles. The incorporation of nanoparticles will induce additional complexity, since the characteristic time governing the nanoparticle evolution, typically of the order of the μs, far exceeds the plasma properties characteristic times, of the order of the RF period $T_{\text{RF}} = 1/f = 7.37 \times 10^{-8}$ s.

Bibliography

[Aga12] P. Agarwal. *Numerical Modeling of Plasmas in which Nanoparticles Nucleate and Grow*. PhD thesis, University of Minnesota, 2012. 113, 140, 145, 151, 153, 154

[BB90] Ph. Belenguer and J.-P. Boeuf. Transition between different regimes of rf glow discharges. *Physical Review A*, 41(8):4447, 1990. 117

[BBH96] L. Boufendi, A. Bouchoule, and T. Hbid. Electrical characterization and modeling of a dust forming plasma in a radio frequency discharge. *Journal of Vacuum Science and Technology A*, 14(2):572–576, 1996. 2, 129, 156

[BGCR87] J. Berkowitz, J. P. Greene, H. Cho, and Ruščić. Photoionization mass spectrometric studies of SiH n (n=1–4). *The Journal of Chemical Physics*, 86:1235, 1987. 117

[BGO+15] B. Bruneau, T. Gans, D. O'Connell, A. Greb, E. V. Johnson, and J.-P. Booth. Strong ionization asymmetry in a geometrically symmetric radio frequency capacitively coupled plasma induced by sawtooth voltage waveforms. *Physical Review Letters*, 114:125002, 2015. 130

[Bha03] U. Bhandarkar. *Study of particle nucleation and growth in low pressure silane plasmas*. PhD thesis, University of Minnesota, 2003. 113, 116, 139

[BL04] C. K. Birdsall and A. B. Langdon. *Plasma Physics via Computer Simulation*. Series in Plasma Physics. CRC Press, 2004. 103

[BLG+16] B. Bruneau, T. Lafleur, T. Gans, D. O'Connell, A. Greb, I. Korolov, A. Derzsi, Z. Donkó, S. Brandt, E. Schüngel, J. Schulze, P. Diomede, D. J. Economou, S. Longo, E. Johnson, and J.-P Booth. Effect of gas properties on the dynamics of the electrical slope asymmetry effect in capacitive plasmas: comparison of Ar, H_2 and CF_4. *Plasma Sources Sci. Technol.*, 25:01LT02, 2016. 131

[Boe87] J.-P. Boeuf. Numerical model of rf glow discharges. *Physical Review A*, 36(6):2782–2792, 1987. 103, 123

[Bru15] B. Bruneau. *Control of radio frequency capacitively coupled plasma asymmetries using Tailored Voltage Waveforms*. PhD thesis, Ecole Polytechnique, 2015. 130

[BSGK00] U. V. Bhandarkar, M. T. Swihart, S. L. Girshick, and U. R. Kortshagen. Modelling of silicon hydride clustering in a low-pressure silane plasma. *J. Phys. D: Appl. Phys.*, 33:2731–2746, 2000. 113, 114, 115, 127, 132, 139

[CB11] P. Chabert and N. St. J. Braithwaite. *Physics of Radio-Frequency Plasmas*. Cambridge University Press, 2011. 106

[CC70] S. Chapman and T. G. Cowling. *The Mathematical Theory of Non-Uniform Gases*. Cambridge University Press, Cambridge, 1970. 5, 11, 12, 14, 18, 20, 21, 32, 33, 47, 82, 88, 111, 118, 145, 153

[CH88] P. C. Cosby and H. Helm. Experimental determination of the H_3^+ bond dissociation energy. *Chemical Physics Letters*, 152(1):71–74, 1988. 117

[CKE89] M. E. Coltrin, R. J. Kee, and G. H. Evans. A mathematical model of the fluid mechanics and gas-phase chemistry in a rotating disk chemical vapor deposition. *J. Electrochem. Soc.*, 136(3):819–829, 1989. 81, 119

[CKM86] M. E. Coltrin, R. J. Kee, and J. A. Miller. A mathematical model of silicon chemical vapor deposition. *J. Electrochem. Soc.*, 133(6):1206–1213, 1986. 93, 94, 119

[dB06] K. de Bleecker. *Modeling of the formation and behavior of nanoparticles in dusty plasmas*. PhD thesis, Universiteit Antwerpen, 2006. 113, 116, 119, 139, 145, 147, 151, 153, 154

[dBGG04] K. de Bleecker, A. Bogaerts, R. Gijbels, and W. Goedheer. Numerical investigation of particle formation mechanisms in silane discharges. *Physical Review E*, 69:056409, 2004. 5, 104, 117, 139

[DCL05] P. Diomede, M. Capitelli, and S. Longo. Effect of discharge voltage on capacitively coupled, parallel plate rf hydrogen plasmas. *Plasma Sources Science and Technology*, 14:459–466, 2005. 5, 116, 128

[DEL+14] P. Diomede, D. J. Economou, T. Lafleur, J.-P. Booth, and S. Longo. Radio-frequency capacitively coupled plasmas in hydrogen excited by tailored voltage waveforms: comparison of simulations with experiments. *Plasma Sources Sci. Technol.*, 23:065049, 2014. 104

[DSHC09] Z. Donkó, J. Schulze, B. G. Heil, and U. Czarnetzki. PIC simulations of the separate control of ion flux and energy in CCRF discharges via the electrical asymmetry effect. *J. Phys. D: Appl. Phys.*, 42:025205, 2009. 129, 130

[EG94] A. Ern and V. Giovangigli. *Multicomponent Transport Algorithms*, volume m24 of *Lecture Notes in Physics Monographs*. Springer-Verlag, Berlin, 1994. 11, 17, 19, 69, 75, 79, 80, 82, 83, 88, 89, 90, 91, 110

[FK72] J. H. Ferziger and H. G. Kaper. *Mathematical Theory of Transport Processes in Gases*. North-Holland Publishing Company, 1972. 11, 12, 14, 18, 20, 21, 32, 33, 47, 59, 82, 88, 118, 153

[GCC+92] C. Gorse, R. Celiberto, M. Cacciatore, A. Laganà, and M. Capitelli. From dynamics to modeling of plasma complex systems: negative ion (h^-) sources. *Chemical Physics*, 161:211–227, 1992. 5, 104

[Gio90] V. Giovangigli. Mass conservation and singular multicomponent diffusion algorithms. *IMPACT Comput. Sci. Eng.*, 2(1):73–97, 1990. 90, 110

[Gio99] V. Giovangigli. *Multicomponent Flow Modeling*. MESST Series. Birkhauser, Boston, 1999. 5, 6, 13, 14, 15, 17, 18, 20, 32, 33, 47, 59, 73, 75, 76, 77, 79, 80, 82, 84, 85, 88, 89, 90, 92, 110, 111

[GJ86] D. B. Graves and K. F. Jensen. A continuum model of DC and RF discharges. *IEEE Transactions on Plasma Science*, 14(2):78–91, 1986. 103

[Hag16] G. J. M. Hagelaar. *Documentation of BOLSIG+*. Laboratoire Plasma et Conversion d'Energie (LAPLACE), Université Paul Sabatier, March 2016. 52, 111, 112

[HC49] J. O. Hirschfelder and C. F. Curtiss. Flame propagation in explosive gas mixtures. In *Third International Symposium on Combustion*, pages 121–127. Reinhold, 1949. 110, 111

[HCBM08] B. G. Heil, U. Czarnetzki1, R. P. Brinkmann, and T. Mussenbrock. On the possibility of making a geometrically symmetric RF-CCP discharge electrically asymmetric. *J. Phys. D: Appl. Phys.*, 41:165202, 2008. 129

[HDD+94] Ch. Hollenstein, J.-L. Dorier, J. Dutta, L. Sansonnens, and A. A. Howling. Diagnostics of particle genesis and growth in RF silane plasmas by ion mass spectrometry and light scattering. *Plasma Sources Sci. Technol.*, 3:278–285, 1994. 128, 139, 158

[HGG99] K. Hassouni, T. A. Grotjohn, and A. Gicquel. Self-consistent microwave field and plasma discharge simulations for a moderate pressure hydrogen discharge reactor. *Journal of Applied Physics*, 86(1):134–151, 1999. 5, 104

[HP05] G. J. M. Hagelaar and L. C. Pitchford. Solving the boltzmann equation to obtain electron transport coefficients and rate coefficients for fluid models. *Plasma Sources Science and Technology*, 14:722–733, 2005. 111, 112

[IST] IST-Lisbon database. http://www.lxcat.net, retrieved on December 20, 2016. 112

[JLEP87] R. K. Janev, W. D. Langer, K. Evans, Jr., and D. E. Post, Jr. *Elementary Processes in Hydrogen-Helium Plasmas*. Springer-Verlag, 1987. 117

[KCG03] R. J. Kee, M. E. Coltrin, and P. Glarborg. *Chemically Reacting Flow: Theory and Practice*. Wiley, 2003. 73, 87, 92, 94, 119

[KDLW+86] R. J. Kee, G. Dixon-Lewis, J. Warnatz, M. E. Coltrin, and J. A. Miller. A FORTRAN computer code package for the evaluation of gas-phase multicomponent transport properties. Technical Report SAND86–8246, SANDIA National Laboratories, 1986. 88, 111

[Kim12] K.-H. Kim. *Hydrogenated polymorphous silicon: establishing the link between hydrogen microstructure and irreversible solar cell kinetics during light soaking*. PhD thesis, Ecole Polytechnique, 2012. 129

[KNF+04] B. Kalache, T. Novikova, A. Fontcuberta i Morral, P. Roca i Cabarrocas, W. Morscheidt, and K. Hassouni. Investigation of coupling between chemistry and discharge dynamics in radio frequency hydrogen plasmas in the Torr regime. *Journal of Physics D: Applied Physics*, 37:1765–1773, 2004. 52, 114, 115, 116, 119

[LAM06] B. Lyka, E. Amanatides, and D. Mataras. Simulation of the electrical properties of sih_4/h_2 discharges. *Japanese Journal of Applied Physics*, 45(10B):8172–8176, 2006. 5, 104

[LDJB12] T. Lafleur, P.-A. Delattre, E. V. Johnson, and J.-P. Booth. Separate control of the ion flux and ion energy in capacitively coupled radio-frequency discharges using voltage waveform tailoring. *Applied Physics Letters*, 101:124104, 2012. 129

[LE93] D. P. Lymberopoulos and D. J. Economou. Fluid simulations of glow discharges: Effect of metastable atoms in argon. *Journal of Applied Physics*, 73:3668–3679, 1993. 116

[LE95] D. P. Lymberopoulos and D. J. Economou. Two-dimensional self-consistent radio frequency plasma simulations relevant to the gaseous electronics conference rf reference cell. *Journal of Research of the National Institute of Standards and Technology*, 100:473–494, 1995. 116

[Lor05] H. A. Lorentz. The motion of electrons in metallic bodies. In *Proc. Roy. Acad. Amsterdam*, volume 7, pages 438–453, 585–593, 684–691, 1905. 12, 111

[McD64] E. W. McDaniel. *Collision Phenomena in Ionized Gases*. Wiley, 1964. 93, 118

[MJA07] L. Marques, L. Jolly, and L. L. Alves. Capacitively coupled radio-frequency hydrogen discharges: The role of kinetics. *Journal of Applied Physics*, 102:063305, 2007. 116

[MW60] H. Motz and H. Wise. Diffusion and heterogeneous reaction. III. Atom recombination at a catalytic boundary. *J. Chem. Phys.*, 32(6):1893–1894, 1960. 93, 94, 118, 119

[Nie98] J. Nienhuis. *Plasma Models for Silicon Deposition*. PhD thesis, FOM Institute for Plasma Physics Rijnhuizen, 1998. 52, 104, 116

[OB81] E. S. Oran and J. P. Boris. Detailed modelling of combustion systems. *Progress in Energy and Combustion Science*, 7(1):1–72, 1981. 110, 111

[Pat80] S. V. Patankar. *Numerical Heat Transfer and Fluid Flow*. Series in Computational Methods in Mechanics and Thermal Sciences. McGraw-Hill, 1980. 94, 123, 124

[PBEL94] J. Perrin, C. Böhm, R. Etemadi, and A. Lloret. Possible routes for cluster growth and particle formation in RF silane discharges. *Plasma Sources Sci. Technol.*, 3:252–261, 1994. 2, 116, 139, 156

[PE90] S.-K. Park and D. J. Economou. Analysis of low pressure rf glow discharges using a continuum model. *J. Appl. Phys.*, 68(8):3904–3915, 1990. 103

[PLB96] J. Perrin, O. Leroy, and M.-C. Bordage. Cross-sections, rate constants and transport coefficients in silane plasma chemistry. *Contribution to Plasma Physics*, 36(1):3–49, 1996. 111, 117, 119, 120

[PSd+82] J. Perrin, J.P.M. Schmitt, G. de Rosny, B. Drevillon, J. Huc, and A. Lloret. Dissociation crodd sections of silane and disilane by electron impact. *Chemical Physics*, 73:383–.94, 1982. 117

[Qui05] G. Quinio. *Modélisation numérique de la génération d'un plasma d'air dans un écoulement aérodynamique*. PhD thesis, UniversitÃl' Paul Sabatier, 2005. 121

[RCL12] Pere Roca i Cabarrocas, Romain Cariou, and Martin Labrune. Low temperature plasma deposition of silicon thin films. *J. Non Cryst. Solids*, 358:2000–2003, 2012. 3, 104, 124, 139, 140, 151

[RiCNTD+07] P. Roca i Cabarrocas, Th. Nguyen-Tran, Y. Djeridane, A. Abramov, E. Johnson, and G. Patriarche. Synthesis of silicon nanocrystals in silane plasmas for nanoelectronics and large area electronic devices. *J. Phys. D.: Appl. Phys.*, 40:2258–2266, 2007. 2, 3, 103, 141

[RTS87] A. D. Richards, B. E. Thompson, and H. H. Sawin. Continuum modeling of argon radio frequency glow discharges. *Applied Physics Letter*, 50:492–494, 1987. 103

[SFG+96] C. D. Scott, S. Farhat, A. Gicquel, K. Hassouni, and M. Lefebvre. Determining electron temperature and density in a hydrogen microwave plasma. *Journal of Thermophysics and Heat Transfer*, 10(3):426–435, 1996. 114, 115

[SG69] D. L. Scharfetter and H. K. Gummel. Large-signal analysis of a silicon read diode oscillator. *IEEE Transactions on Electron Devices*, 16(1):64–77, 1969. 123, 124

[SG91] M. Surendra and D. B. Graves. Particle simulations of radio-frequency glow discharges. *IEEE Trans. Plasmma Sci.*, 19:144–157, 1991. 117

[SGA02] A. Salabas, G. Gousset, and L. L. Alves. Two-dimensional fluid modelling of charged particle transport in radio-frequency capacitively coupled discharges. *Plasma Sources Sci. Technol.*, 11:448–465, 2002. 5, 127, 128

[SIG] SIGLO database. http://www.lxcat.net, retrieved on December 20, 2016. 112

[SSC09] J. Schulze, E. Schüngel, and U. Czarnetzki. The electrical asymmetry effect in capacitively coupled radio frequency discharges – measurements of dc self bias, ion energy and ion flux. *J. Phys. D: Appl. Phys.*, 42:092005, 2009. 129

[Tol38] R. C. Tolman. *The Principles of Statistical Mechanics*. Oxford University Press, 1938. 81, 113

[VB05] H. Vach and Q. Brulin. Controlled growth of silicon nanocrystals in a plasma reactor. *Physical Review Letters*, 95:165502, 2005. 128, 158

[WB12] G. Wattieaux and L. Boufendi. Discharge impedance evolution, stray capacitance effect, and correlation with the particles size in a dusty plasma. *Physics of Plasmas*, 19:033701, 2012. 129, 153

[WG07] S. Warthesen and S. Girshick. Numerical simulation of the spatiotemporal evolution of a nanoparticle-plasma system. *Plasma Chemistry and Plasma Processing*, 27(3):292–310, 2007. 5, 6, 117, 140, 141, 142, 145

Chapter 5

Nanoparticle Formation in a Silane-Hydrogen Plasma Discharge

5.1 Introduction

The presence of nanoparticles, microparticles, and possibly powder is an important feature of silane-hydrogen plasmas, which has a significant impact on silicon thin-film deposition process. If the deposition of amorphous silicon (a-Si:H) at low pressure and RF power is generally explained by the contribution of SiH_3 radicals [Str05], most models fail at explaining deposition rates and material properties under conditions where particle nucleation occurs [RiCHS$^+$98]. In particular, the deposition of so-called "polymorphous silicon" (pm-Si:H), as well as low-temperature plasma enhanced silicon epitaxy are obtained under conditions close to powder formation [RiCHS$^+$98] [RCL12].

The formation and behavior of nanoparticles and microparticles in silane plasma discharges has been studied extensively over the last decades, both from the experimental and numerical viewpoints. A more detailed presentation of the historical developments may be found in [Bou99]. We only mention the pioneering experimental works of Watanabe and coworkers [WSK$^+$96], and Boufendi, Bouchoule and coworkers [BB94], which led to the identification of the four distinct phases of particle formation, illustrated in Figure 5.1. J. Perrin and coworkers [PBEL94], following Hollenstein and coworkers [HDD$^+$94], also accomplished a tremendous experimental work on the study of silane plasma discharge chemistry, which contributed to identify the main clustering reactions leading to the nucleation of nanoparticles.

From the numerical point of view, Girshick, Swihart and coworkers developed for the first time a kinetic model for silicon hydride clustering in low-temperature silane plasma [BSGK00]. Their model used a group additivity scheme to predict the thermochemical properties of large silicon hydride clusters, and data from ab initio calculations. Reaction rate constants were estimated from available experimental data and cross-sections. Clustering was principally due to reactions between negative ions and neutral species, in accordance with experimental results of Hollenstien [HDD$^+$94]. Bhandarkar, Kortshagen and Girshick coupled this kinetic model to a sectional model for nanoparticles in a quasi-one-dimensional formulation for low pressure argon-silane plasmas [BKG03] [Bha03].

Akdim and Goedheer developed a self-consistent model for the transport of dusts in silane-hydrogen plasma [AG03], accounting for electric drift, diffusion, ion drag and thermophoresis. Dusts were assumed to be monodispersed with prescribed radius and corresponding equilibrium charge, and coupled to a one-dimensional plasma fluid model. Nucleation was not taken into account self-consistently and the total dust density was taken as an input parameter. They also introduced a "time splitting" procedure to speed up the convergence towards a quasi-steady state solution [AG03].

Bogaerts, de Bleecker, and Goedheer investigated the nucleation of nanoparticles in silane discharges [dBBGG04] [dBGG04] [dB06]. Their one-dimensional plasma fluid model accounted for the

chemical kinetics of silicon hydrides containing up to 12 silicon atoms, following the work of Girshick et al.. According to their model, over 90 % of the dust formation was initiated by the clustering reaction between SiH_3^- and SiH_4. They also observed a delay in nucleation when gas temperature is increased, in agreement with experimental observations. Their model was then coupled to a sectional model accounting for nucleation, coagulation, and transport of nanoparticles. The clustering reaction rate of the largest silicon anions was taken as a source term for nucleation of nanoparticles [dBG06]. The charge of a nanoparticle of a given size was taken equal to its equilibrium value, and surface growth of nanoparticles was not taken into account. They obtained quasi-steady-state nanoparticle density profiles and charge distributions in a pure silane discharge. They also investigated the effects of different forces on nanoparticles [dBBG04] [dBBG05].

In the meantime, Warthesen and Girshick implemented a self-consistent one-dimensional plasma fluid model, coupled to a sectional model for nanoparticles accounting for nucleation, coagulation, and surface growth [WG07] [War06]. The nanoparticles were sorted out in sections of given size and charge, so that the charging dynamics was modeled self-consistently. They obtained results for a silane plasma discharge diluted in argon at 100 mTorr. Their model did not consider the complete chemical kinetics of clustering but imposed a fixed nucleation rate over a short period of time at the beginning of the simulations, and a fixed surface growth rate. Their results evidenced four distinct phases of nanoparticle growth, namely a charge-limited phase, a charge accumulation phase, an early ion drag phase, and a sheath interaction phase. They also showed a qualitative agreement with laser light scattering experiments by Rózsa et al. [RBG01], although the influence of coagulation was found to be underestimated. Finally, Agarwal and Girshick [AG11] [AG12] [Aga12] modified the coagulation rates in order to take into account the image potential between neutral and charge particles, which can strongly enhance the coagulation [RG09]. They also investigated the effect of gravity, thermophoresis, and neutral drag. They further incorporated a gas phase chemical mechanism allowing for a self-consistent evaluation of nucleation and nanoparticle surface growth rates. Pulsed radio-frequency discharges were also investigated as a way of controlling the nanoparticle nucleation [LAG17].

More recently, Michau and Hassouni have developed a self-consistent model for carbonaceous particle formation in an argon graphite cathode dc discharge used for simulating parasitic discharges expected under tokamak divertor domes [MH10] [MAL+16]. Their model coupled a DC discharge module base on hybrid Monte Carlo analytic simulations, a cluster module describing the kinetics of particle formation, and a particle module including nucleation, transport, coagulation, and particle surface growth, and a self-consistent calculation of average mass and average charge.

The regime of main interest for photovoltaic applications corresponds to the intermediate regime where the plasma experiences the $\alpha \rightarrow \gamma'$ transition, as depicted in Figure 5.1. Indeed, this regime corresponds to improved deposition rate and material quality, and both the deposition of so-called "polymorphous" silicon and the low-temperature plasma enhanced epitaxy of crystalline silicon are obtained under such conditions [RiCHS+98] [RCL12]. In this regime, the nanoparticle size remains generally below 10 nm, which is beyond the current resolution of most experimental techniques. In particular, it is currently not possible to measure directly the density nor the size distribution of such a nanoparticle cloud. Furthermore, due to the high surface reactivity of silicon radicals and clusters, traditional plasma probe measurements are not straightforward in silane-hydrogen discharges. As a consequence, there is a lack of experimental data on the nanoparticle early coagulation phase, and previous numerical studies have generally focused on the latest phase of particle cloud formation, where coagulation is dominant, and where dust particle radius ranges up to $10 - 250$ nm, and possibly higher. In particular, the argon-silane chemistry considered by Girshick and coworkers is known to enhance powder formation compared to silane or silane-hydrogen chemistry. As well, de Bleecker and coworkers considered pressures in the range $100 - 300$ mTorr, an interelectrode distance of 3 cm, a frequency of 50 MHz, and a power of 5 Watts.

In this Chapter, a fully coupled numerical model for nanodusty silane-hydrogen plasma discharge

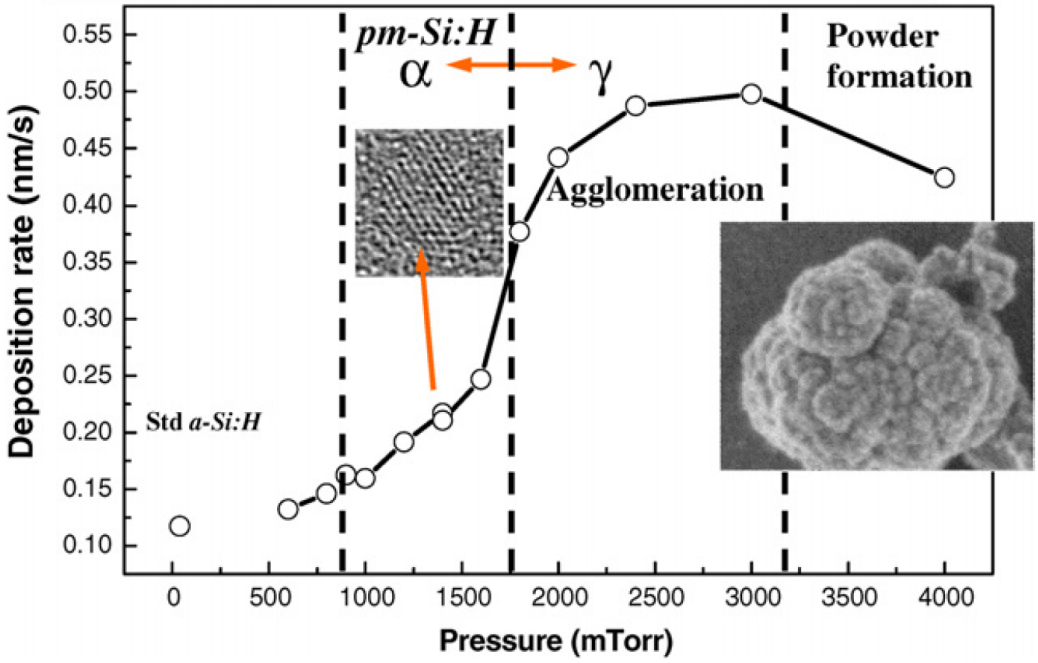

Figure 5.1 – Schematic representation of powder formation in silane plasmas. Results from [RiCNTD+07].

is implemented, and a numerical investigation of the early phase of particle growth is carried out. The pristine plasma software presented in Chapter 4 has been extended to account for nucleation, coagulation, surface growth, and transport of nanoparticles. A sectional model with sections of given size and charge has been used, following the method of Girshick and coworkers [WG07] [AG12]. The enhancement due to electrostatic interaction between charged particles and the influence of image potential are taken into account for coagulation. The model is fully coupled and fully non-stationary.

In section 5.2, the sectional model is described and the general sectional equation is stated. In section 5.3, the computation of the nucleation rate from the gas phase chemical kinetics is described, and the expression for the coagulation rate is derived in section 5.4. The nanoparticle surface growth rate due to deposition of plasma species or radicals on nanoparticles is expressed in section 5.5, and the charging rates due to collection of electrons or ions in section 5.6. The nanoparticle transport fluxes is given in 5.7, and the self-consistent plasma-nanoparticle equations are summarized in section 5.8. Results are presented and discussed in section 5.9.

5.2 Sectional Model

We denote by $n_c(t, \boldsymbol{x}, \mathfrak{v})$ the continuous distribution function for aerosol particles of a given charge number c. The continuous distribution depends on the volume of the particle $\mathfrak{v}$, and is a solution to the general dynamic equation [Fri00]

$$\frac{\partial n_c}{\partial t} + \boldsymbol{\partial}_{\boldsymbol{x}} \cdot (n_c \boldsymbol{\mathcal{V}}_c) + \frac{\partial}{\partial \mathfrak{v}} \big(n_c(t, \mathfrak{v}) I_c(t, \mathfrak{v}) \big) = \left[\frac{\partial n_c}{\partial t} \right]_{\text{nuc}} + \left[\frac{\partial n_c}{\partial t} \right]_{\text{coag}} + \left[\frac{\partial n_c}{\partial t} \right]_{\text{charge}}, \tag{5.2.1}$$

where $\boldsymbol{\mathcal{V}}_c$ is the diffusion velocity of aerosol particles with charge number c, I_c is the particle current associated with nanoparticle surface growth, $[\frac{\partial n_c}{\partial t}]_{\text{nuc}}$ is the nanoparticle nucleation source term due to the cluster growth of plasma species, $[\frac{\partial n_c}{\partial t}]_{\text{coag}}$ is the coagulation source term, and $[\frac{\partial n_c}{\partial t}]_{\text{charge}}$ is the nanoparticle source term due to charging through ion or electron capture.

The sectional model consists in sorting the nanoparticles into a finite number of discrete bins of a given size $p = 1, \ldots, N_p$ and charge $c = -K_-, \ldots, K_+$, over which the particle volume density is assumed to be constant:

$$\mathfrak{v} n_c(t, \boldsymbol{x}, \mathfrak{v}) = \mathfrak{y}_{pc}(t, \boldsymbol{x}), \quad \mathfrak{v} \in]\mathfrak{v}_{p-1}, \mathfrak{v}_p[, \tag{5.2.2}$$

and solving the evolution equations for the densities in each section

$$N_{pc}(t, \boldsymbol{x}) = \int_{\mathfrak{v}_{p-1}}^{\mathfrak{v}_p} n_c(t, \boldsymbol{x}, \mathfrak{v})\, d\mathfrak{v} = \mathfrak{y}_{pc}(t, \boldsymbol{x}) \ln\left(\frac{\mathfrak{v}_p}{\mathfrak{v}_{p-1}}\right), \quad 1 \leq p \leq N_p,\ -K_- \leq c \leq K_+, \tag{5.2.3}$$

The sectional model is thus equivalent to approximating the continuous density by

$$n_c(t, \boldsymbol{x}, \mathfrak{v}) = \sum_{p=1}^{N_p} \mathbb{1}_{]\mathfrak{v}_{p-1}, \mathfrak{v}_p[}(\mathfrak{v}) \frac{N_{pc}(t, \boldsymbol{x})}{\mathfrak{v} \ln\left(\frac{\mathfrak{v}_p}{\mathfrak{v}_{p-1}}\right)}, \quad -K_- \leq c \leq K_+, \tag{5.2.4}$$

for almost every $\mathfrak{v} \in \mathbb{R}$.

Upon introducing the volume contained in each section

$$V_{pc}(t, \boldsymbol{x}) = \int_{\mathfrak{v}_{p-1}}^{\mathfrak{v}_p} \mathfrak{v} n_c(t, \boldsymbol{x}, \mathfrak{v})\, d\mathfrak{v} = \mathfrak{y}_{pc}(t, \boldsymbol{x})(\mathfrak{v}_p - \mathfrak{v}_{p-1}), \quad 1 \leq p \leq N_p,\ -K_- \leq c \leq K_+. \tag{5.2.5}$$

the sectional density can be expressed as

$$N_{pc}(t, \boldsymbol{x}) = \frac{V_{pc}(t, \boldsymbol{x})}{\overline{\mathfrak{v}}_p}, \quad 1 \leq p \leq N_p,\ -K_- \leq c \leq K_+, \tag{5.2.6}$$

where $\overline{\mathfrak{v}}_p$ is the average volume in size section p

$$\overline{\mathfrak{v}}_p = \frac{\mathfrak{v}_p - \mathfrak{v}_{p-1}}{\ln\left(\frac{\mathfrak{v}_p}{\mathfrak{v}_{p-1}}\right)}, \quad 1 \leq p \leq N_p. \tag{5.2.7}$$

The equations for the sectional volumes V_{pc}, $1 \leq p \leq N_p$, $-K_- \leq c \leq K_+$, are generally obtained by multiplying the general dynamic equation (5.2.1) by $\mathfrak{v}$, and integrating over the volume $\mathfrak{v}$:

$$\frac{\partial V_{pc}}{\partial t} + \boldsymbol{\partial}_{\boldsymbol{x}} \cdot (V_{pc} \boldsymbol{\mathcal{V}}_{pc}) = \left[\frac{\partial V_{pc}}{\partial t}\right]_{\text{nuc}} + \left[\frac{\partial V_{pc}}{\partial t}\right]_{\text{growth}} + \left[\frac{\partial V_{pc}}{\partial t}\right]_{\text{coag}} + \left[\frac{\partial V_{pc}}{\partial t}\right]_{\text{charge}}, \tag{5.2.8}$$

where $\boldsymbol{\mathcal{V}}_{pc}$ is the average diffusion velocity of nanoparticles in section (p, c), and the terms on the right hand side are the respective source terms associated with nucleation, nanoparticle surface growth or condensation, coagulation, and charge fluctuations. The equations for the densities N_{pc}, N_{pc}, $1 \leq p \leq N_p$, $-K_- \leq c \leq K_+$, are then deduced dividing equation (5.2.8) by $\overline{\mathfrak{v}}_p$, and read [GTS80] [WG07]

$$\frac{\partial N_{pc}}{\partial t} + \boldsymbol{\partial}_{\boldsymbol{x}} \cdot (N_{pc} \boldsymbol{\mathcal{V}}_{pc}) = \left[\frac{\partial N_{pc}}{\partial t}\right]_{\text{nuc}} + \left[\frac{\partial N_{pc}}{\partial t}\right]_{\text{growth}} + \left[\frac{\partial N_{pc}}{\partial t}\right]_{\text{coag}} + \left[\frac{\partial N_{pc}}{\partial t}\right]_{\text{charge}}. \tag{5.2.9}$$

5.3 Nucleation

The nucleation rate is taken equal to the production rate of $Si_3H_x^-$ negative ions induced by the clustering reactions

$$H_3SiSiH^- + SiH_4 \rightharpoonup Si_3H_6^- + H_2 \tag{5.3.1}$$

$$Si_2H_5^- + SiH_4 \rightharpoonup Si_3H_7^- + H_2, \tag{5.3.2}$$

that is

$$\left[\frac{\partial N_{pc}}{\partial t}\right]_{\text{nuc}} = \delta_{p1}\delta_{c(-1)}(k_{\text{nuc}} n_{\text{H}_3\text{SiSiH}^-} n_{\text{SiH}_4} + k_{\text{nuc}} n_{\text{Si}_2\text{H}_5^-} n_{\text{SiH}_4}), \tag{5.3.3}$$

where k_{nuc} is the reaction rate constant [dBG06]

$$k_{\text{nuc}} = 1.0 \times 10^{-12}\ \text{cm}^3.\text{s}^{-1}. \tag{5.3.4}$$

The freshly nucleated particles are added to section of size $p = 1$ and charge $c = -1$.

5.4 Coagulation

The coagulation term appearing in the general dynamic equation (5.2.1) reads [GTS80]

$$\left[\frac{\partial n_c}{\partial t}\right]_{\text{coag}} = \frac{1}{2}\sum_{a+b=c}\int_0^{\mathfrak{v}} \beta_{ab}(\tilde{\mathfrak{v}}, \mathfrak{v}-\tilde{\mathfrak{v}}) n_a(\tilde{\mathfrak{v}}) n_b(\mathfrak{v}-\tilde{\mathfrak{v}})\, d\tilde{\mathfrak{v}} - \sum_a \int_0^{\mathfrak{v}} \beta_{ca}(\mathfrak{v}, \tilde{\mathfrak{v}}) n_c(\mathfrak{v}) n_a(\tilde{\mathfrak{v}})\, d\tilde{\mathfrak{v}}, \tag{5.4.1}$$

where $\beta_{ab}(\mathfrak{v}, \tilde{\mathfrak{v}})$ is the coagulation coefficient of aerosol particles of charge a and volume $\mathfrak{v}$ with aerosol particles of charge b and volume $\tilde{\mathfrak{v}}$, and where for the sake of simplicity the dependance on t and $\boldsymbol{x}$ has been dropped. The term $\beta_{ab}(t, \boldsymbol{x}, \mathfrak{v}, \tilde{\mathfrak{v}}) n_a(t, \boldsymbol{x}, \mathfrak{v}) n_b(t, \boldsymbol{x}, \tilde{\mathfrak{v}})\, d\mathfrak{v} d\tilde{\mathfrak{v}}$ represents the number of particles of size $\mathfrak{v} + \tilde{\mathfrak{v}}$ arising from coagulation of a particle of size $\mathfrak{v}$ with a particle of size $\tilde{\mathfrak{v}}$, at time t and position $\boldsymbol{x}$.

In order to compute the net coagulation rate $[\frac{\partial V_{pc}}{\partial t}]_{\text{coag}}$ into section (p, c), one has to distinguish between several subcases, as follows.

1. The mass flux into section (p, c) due to coagulation between particles from sections of size strictly lower than p reads, when $p \geq 2$

$$\sum_{c_1+c_2=c} \frac{1}{2}\int_{\mathfrak{v}_0}^{\mathfrak{v}_{p-1}} \int_{\mathfrak{v}_0}^{\mathfrak{v}_{p-1}} \delta(\mathfrak{v}_{p-1} < \mathfrak{u}+\mathfrak{v} < \mathfrak{v}_p)(\mathfrak{u}+\mathfrak{v}) \beta_{c_1,c_2}(\mathfrak{u}, \mathfrak{v}) n_{c_1}(\mathfrak{u}) n_{c_2}(\mathfrak{v})\, \mathrm{d}\mathfrak{u}\mathrm{d}\mathfrak{v}. \tag{5.4.2}$$

2. The mass flux into section (p, c) due to coagulation between a particle of size strictly lower than p and a particle of size p reads, when $p \geq 2$

$$\sum_{c_1+c_2=c} \int_{\mathfrak{v}_0}^{\mathfrak{v}_{p-1}} \int_{\mathfrak{v}_{p-1}}^{\mathfrak{v}_p} \delta(\mathfrak{u}+\mathfrak{v} < \mathfrak{v}_p)(\mathfrak{u}+\mathfrak{v}) \beta_{c_1,c_2}(\mathfrak{u}, \mathfrak{v}) n_{c_1}(\mathfrak{u}) n_{c_2}(\mathfrak{v})\, \mathrm{d}\mathfrak{v}\mathrm{d}\mathfrak{u}. \tag{5.4.3}$$

3. The mass flux outwards section (p, c) due to coagulation with a particle of size strictly lower than p, growing into a particle of size p, reads, for any $p \in \{1, \ldots, N_p\}$

$$\sum_{c_2} \int_{\mathfrak{v}_0}^{\mathfrak{v}_{p-1}} \int_{\mathfrak{v}_{p-1}}^{\mathfrak{v}_p} \delta(\mathfrak{u}+\mathfrak{v} < \mathfrak{v}_p)\mathfrak{u} \beta_{c,c_2}(\mathfrak{u}, \mathfrak{v}) n_c(\mathfrak{u}) n_{c_2}(\mathfrak{v})\, \mathrm{d}\mathfrak{u}\mathrm{d}\mathfrak{v}. \tag{5.4.4}$$

4. The mass flux outwards section (p, c) due to coagulation with a particle of size strictly lower than p, growing into a particle of size strictly larger than p, reads, when $2 \leq p \leq N_p - 1$

$$\sum_{c_2} \int_{\mathfrak{v}_0}^{\mathfrak{v}_{p-1}} \int_{\mathfrak{v}_{p-1}}^{\mathfrak{v}_p} \delta(\mathfrak{u}+\mathfrak{v} > \mathfrak{v}_p)\mathfrak{u} \beta_{c,c_2}(\mathfrak{u}, \mathfrak{v}) n_c(\mathfrak{u}) n_{c_2}(\mathfrak{v})\, \mathrm{d}\mathfrak{u}\mathrm{d}\mathfrak{v}. \tag{5.4.5}$$

5. The mass flux into section (p, c) due to coagulation between particles from sections of size p reads, when $p \geq 2$

$$\sum_{c_1+c_2=c} \frac{1}{2}\int_{\mathfrak{v}_{p-1}}^{\mathfrak{v}_p} \int_{\mathfrak{v}_{p-1}}^{\mathfrak{v}_p} \delta(\mathfrak{u}+\mathfrak{v} < \mathfrak{v}_p)(\mathfrak{u}+\mathfrak{v}) \beta_{c_1,c_2}(\mathfrak{u}, \mathfrak{v}) n_{c_1}(\mathfrak{u}) n_{c_2}(\mathfrak{v})\, \mathrm{d}\mathfrak{u}\mathrm{d}\mathfrak{v}. \tag{5.4.6}$$

6. The mass flux outwards section (p, c) due to coagulation with a particle of the same size p and of a different charge, growing into a particle of size p, reads, for any $p \in \{1, \dots, N_p\}$

$$\sum_{c_2 \neq c} \int_{\mathfrak{v}_{p-1}}^{\mathfrak{v}_p} \int_{\mathfrak{v}_{p-1}}^{\mathfrak{v}_p} \delta(\mathfrak{u} + \mathfrak{v} < \mathfrak{v}_p) \mathfrak{u} \beta_{c,c_2}(\mathfrak{u}, \mathfrak{v}) n_c(\mathfrak{u}) n_{c_2}(\mathfrak{v}) \, \mathrm{d}\mathfrak{u}\mathrm{d}\mathfrak{v}. \tag{5.4.7}$$

7. The mass flux outwards section (p, c) due to coagulation with a particle of the same size p and charge c, growing into a particle of size p, reads, for any $p \in \{1, \dots, N_p\}$

$$\frac{1}{2} \int_{\mathfrak{v}_{p-1}}^{\mathfrak{v}_p} \int_{\mathfrak{v}_{p-1}}^{\mathfrak{v}_p} \delta(\mathfrak{u} + \mathfrak{v} < \mathfrak{v}_p)(\mathfrak{u} + \mathfrak{v}) \beta_{c,c}(\mathfrak{u}, \mathfrak{v}) n_c(\mathfrak{u}) n_c(\mathfrak{v}) \, \mathrm{d}\mathfrak{u}\mathrm{d}\mathfrak{v}. \tag{5.4.8}$$

8. The mass flux outwards section (p, c) due to coagulation with a particle of the same size p and of a different charge, growing into a particle of size strictly larger than p, reads, when $p \leq N_p - 1$

$$\sum_{c_2 \neq c} \int_{\mathfrak{v}_{p-1}}^{\mathfrak{v}_p} \int_{\mathfrak{v}_{p-1}}^{\mathfrak{v}_p} \delta(\mathfrak{u} + \mathfrak{v} > \mathfrak{v}_p) \mathfrak{u} \beta_{c,c_2}(\mathfrak{u}, \mathfrak{v}) n_c(\mathfrak{u}) n_{c_2}(\mathfrak{v}) \, \mathrm{d}\mathfrak{u}\mathrm{d}\mathfrak{v}. \tag{5.4.9}$$

9. The mass flux outwards section (p, c) due to coagulation with a particle of the same size p and charge c, growing into a particle of size strictly larger than p, reads, when $p \leq N_p - 1$

$$\frac{1}{2} \int_{\mathfrak{v}_{p-1}}^{\mathfrak{v}_p} \int_{\mathfrak{v}_{p-1}}^{\mathfrak{v}_p} \delta(\mathfrak{u} + \mathfrak{v} > \mathfrak{v}_p)(\mathfrak{u} + \mathfrak{v}) \beta_{c,c_2}(\mathfrak{u}, \mathfrak{v}) n_c(\mathfrak{u}) n_{c_2}(\mathfrak{v}) \, \mathrm{d}\mathfrak{u}\mathrm{d}\mathfrak{v}. \tag{5.4.10}$$

10. The mass flux outwards section (p, c) due to coagulation with a particle of size strictly larger than p reads, when $p \leq N_p - 1$

$$\sum_{c_2} \int_{\mathfrak{v}_p}^{\mathfrak{v}_{N_p}} \int_{\mathfrak{v}_{p-1}}^{\mathfrak{v}_p} \mathfrak{u} \beta_{c,c_2}(\mathfrak{u}, \mathfrak{v}) n_c(\mathfrak{u}) n_{c_2}(\mathfrak{v}) \, \mathrm{d}\mathfrak{u}\mathrm{d}\mathfrak{v}. \tag{5.4.11}$$

From the preceding results, the net coagulation rate into section (p, c) reads

$$\begin{aligned} \left[\frac{\partial V_{pc}}{\partial t}\right]_{\text{coag}} = & \qquad (5.4.12) \\ \frac{1}{2} \sum_{p_1=1}^{N_p} \sum_{p_2=1}^{N_p} \sum_{c_1+c_2=c} & \int_{\mathfrak{v}_{p_1-1}}^{\mathfrak{v}_{p_1}} \int_{\mathfrak{v}_{p_2-1}}^{\mathfrak{v}_{p_2}} \delta(\mathfrak{v}_{p-1} < \mathfrak{u} + \mathfrak{v} < \mathfrak{v}_p)(\mathfrak{u} + \mathfrak{v}) \beta_{c_1,c_2}(\mathfrak{u}, \mathfrak{v}) n_{c_1}(\mathfrak{u}) n_{c_2}(\mathfrak{v}) \, \mathrm{d}\mathfrak{u}\mathrm{d}\mathfrak{v} \\ & - \sum_{(p_2,c_2) \neq (p,c)} \int_{\mathfrak{v}_{p_2-1}}^{\mathfrak{v}_{p_2}} \int_{\mathfrak{v}_{p-1}}^{\mathfrak{v}_p} \mathfrak{u} \beta_{c,c_2}(\mathfrak{u}, \mathfrak{v}) n_c(\mathfrak{u}) n_{c_2}(\mathfrak{v}) \, \mathrm{d}\mathfrak{u}\mathrm{d}\mathfrak{v} \\ & - \frac{1}{2} \int_{\mathfrak{v}_{p-1}}^{\mathfrak{v}_p} \int_{\mathfrak{v}_{p-1}}^{\mathfrak{v}_p} (\mathfrak{u} + \mathfrak{v}) \beta_{c,c}(\mathfrak{u}, \mathfrak{v}) n_c(\mathfrak{u}) n_c(\mathfrak{v}) \, \mathrm{d}\mathfrak{u}\mathrm{d}\mathfrak{v}, \end{aligned}$$

which can be rewritten in the form

$$\begin{aligned} \left[\frac{\partial V_{pc}}{\partial t}\right]_{\text{coag}} = & \sum_{p_1 < p_2} \sum_{c_1+c_2=c} \beta^{pc}_{p_1c_1p_2c_2} V_{p_1c_1} V_{p_1c_2} + \sum_{p_1} \sum_{\substack{c_1 \leq c_2 \\ c_1+c_2=c}} \beta^{pc}_{p_1c_1p_1c_2} V_{p_1c_1} V_{p_1c_2} \\ & - \sum_{p_2} \sum_{c_2} \beta_{pcp_2c_2} V_{pc} V_{p_2c_2}, \end{aligned}$$

where

$$\beta^{pc}_{p_1c_1p_2c_2} = \tag{5.4.13}$$
$$\begin{cases} \displaystyle\int_{\mathfrak{v}_{p_1-1}}^{\mathfrak{v}_{p_1}}\int_{\mathfrak{v}_{p_2-1}}^{\mathfrak{v}_{p_2}} \frac{\delta(\mathfrak{v}_{p-1}<\mathfrak{u}+\mathfrak{v}<\mathfrak{v}_p)(\mathfrak{u}+\mathfrak{v})\beta_{c_1,c_2}(\mathfrak{u},\mathfrak{v})}{\mathfrak{u}\mathfrak{v}(\mathfrak{v}_{p_2}-\mathfrak{v}_{p_2-1})(\mathfrak{v}_{p_1}-\mathfrak{v}_{p_1-1})}\,\mathrm{d}\mathfrak{u}\mathrm{d}\mathfrak{v}, & (p_2,c_2)\neq(p_1,c_1),\\ \dfrac{1}{2}\displaystyle\int_{\mathfrak{v}_{p_1-1}}^{\mathfrak{v}_{p_1}}\int_{\mathfrak{v}_{p_2-1}}^{\mathfrak{v}_{p_2}} \frac{\delta(\mathfrak{v}_{p-1}<\mathfrak{u}+\mathfrak{v}<\mathfrak{v}_p)(\mathfrak{u}+\mathfrak{v})\beta_{c_1,c_2}(\mathfrak{u},\mathfrak{v})}{\mathfrak{u}\mathfrak{v}(\mathfrak{v}_{p_2}-\mathfrak{v}_{p_2-1})(\mathfrak{v}_{p_1}-\mathfrak{v}_{p_1-1})}\,\mathrm{d}\mathfrak{u}\mathrm{d}\mathfrak{v}, & (p_2,c_2)=(p_1,c_1), \end{cases}$$

and

$$\beta_{pcp_2c_2} = \int_{\mathfrak{v}_{p_2-1}}^{\mathfrak{v}_{p_2}}\int_{\mathfrak{v}_{p-1}}^{\mathfrak{v}_{p}} \frac{\mathfrak{u}\beta_{c,c_2}(\mathfrak{u},\mathfrak{v})}{\mathfrak{u}\mathfrak{v}(\mathfrak{v}_{p_2}-\mathfrak{v}_{p_2-1})(\mathfrak{v}_{p}-\mathfrak{v}_{p-1})}\,\mathrm{d}\mathfrak{u}\mathrm{d}\mathfrak{v} \tag{5.4.14}$$

are the sectional coagulation coefficients.

The coagulation kernel is expressed as [WG07]

$$\beta_{cd}(\mathfrak{u},\mathfrak{v}) = f(q_c,q_d,r(\mathfrak{u}),r(\mathfrak{v}))\beta(\mathfrak{u},\mathfrak{v}), \tag{5.4.15}$$

where $r(\mathfrak{v})$ is the radius of a ball of volume $\mathfrak{v}$

$$r(\mathfrak{v}) = \Big(\frac{3\mathfrak{v}}{4\pi}\Big)^{\frac{1}{3}}, \tag{5.4.16}$$

and $\beta(\mathfrak{u},\mathfrak{v})$ is the coagulation kernel between neutral particles in the "free molecular regime", i.e., when the particle diameter d_{P} is negligible compared to the particle mean free path l_{P} [Fri00]

$$\beta(\mathfrak{u},\mathfrak{v}) = \Big(\frac{3}{4\pi}\Big)^{\frac{1}{6}}\Big(\frac{6k_{\text{B}}T_h}{\rho_{\text{P}}}\Big)^{\frac{1}{2}}\Big(\frac{1}{\mathfrak{u}}+\frac{1}{\mathfrak{v}}\Big)^{\frac{1}{2}}\Big(\mathfrak{u}^{\frac{1}{3}}+\mathfrak{v}^{\frac{1}{3}}\Big)^2. \tag{5.4.17}$$

The neutral coagulation kernel depends on the gas temperature T_h and the particle volume density ρ_{P}. For silicon nanoparticles, the volume density is taken equal to [dB06]

$$\rho_{\text{P}} = 2.3\text{kg.m}^{-3}. \tag{5.4.18}$$

Equation (5.4.17) can be obtained from the kinetic theory of gases for rigid spherical molecules [CC70] [Fri00]. The factor $f(q_c,q_d,r(\mathfrak{u}),r(\mathfrak{v}))$ in (5.4.15) is the enhancement factor due to the respective charges q_c and q_d carried by the coalescing particles, and reads [KB99] [AG12]

$$f(q_1,q_2,r_1,r_2) = \begin{cases} 1, & q_1=q_2=0,\\ 1-\dfrac{q_1q_2}{4\pi\varepsilon_0(r_1+r_2)k_{\text{B}}T_h}, & q_1q_2<0,\\ \exp\Big(-\dfrac{q_1q_2}{4\pi\varepsilon_0(r_1+r_2)k_{\text{B}}T_h}\Big), & q_1q_2>0,\\ \mathscr{E}(q_1,r_1,r_2), & q_2=0, q_1\neq 0, \end{cases} \tag{5.4.19}$$

where $\mathscr{E}(q_1,r_1,r_2)$ denotes the image potential for an interaction between a neutral an a charged particle.

Generally, the charge enhancement factor is taken constant over each nanoparticle size section [Aga12]

$$f(q_c,q_d,r(\mathfrak{u}),r(\mathfrak{v})) = f(q_c,q_d,\overline{r}_p,\overline{r}_q), \quad \mathfrak{u}\in]\mathfrak{v}_{p-1},\mathfrak{v}_p[,\ \mathfrak{v}\in]\mathfrak{v}_{q-1},\mathfrak{v}_q[. \tag{5.4.20}$$

5.5 Nanoparticle Surface Growth

5.5.1 Sectional growth rate

The expression of the sectional growth rate is a critical issue. In the present study, the "orbital motion limited" theory will be used for the description of charged species interactions with nanoparticles [All92].

The continuous nanoparticle surface growth rate $I_c(t,\mathfrak{v})$ is given by [Fri00]

$$I_c(t,\mathfrak{v}) = \Big(\sum_{l\in\mathfrak{S}} \widehat{\omega}^l_{pc} \mathrm{V}^{\mathrm{Si}}_{\mathrm{m}} \nu^l_{\mathrm{Si}}\Big) s(\mathfrak{v}) \tag{5.5.1}$$

where $\widehat{\omega}^l_{pc}$ is the average molar surface flux of the l^{th} gaseous species on a nanoparticle of size p and charge c, ν^l_{Si} is the average number of Si atoms in a molecule of the l^{th} species depositing on the surface of a nanoparticle upon collision, $\mathrm{V}^{\mathrm{Si}}_{\mathrm{m}}$ is the molar volume of silicon, and $s(\mathfrak{v})$ is the surface of a sphere of volume $\mathfrak{v}$

$$s(\mathfrak{v}) = \pi^{\frac{1}{3}} 6^{\frac{2}{3}} \mathfrak{v}^{\frac{2}{3}}. \tag{5.5.2}$$

The sectional nanoparticle surface growth term is obtained from integration of the particle current $\mathfrak{v}\frac{\partial}{\partial\mathfrak{v}}[n(t,\mathfrak{v})I_c(t,\mathfrak{v})]$ over $\mathfrak{v}$, which yields integrating by part

$$\begin{aligned}\left[\frac{\partial V_{pc}}{\partial t}\right]_{\text{growth}} &= -\int_{v_{p-1}}^{v_p} \mathfrak{v}\frac{\partial}{\partial\mathfrak{v}}\big(n_c(t,\mathfrak{v})I_c(t,\mathfrak{v})\big)\mathrm{d}\mathfrak{v},\\ &= \overline{H}_{pc}(t)V_{pc} + I_{p-1c}(t) - I_{pc}(t),\end{aligned}$$

where

$$I_{pc}(t) = \mathfrak{v}_p n_c(t,\mathfrak{v}_p) I_c(t,\mathfrak{v}_p) \tag{5.5.3}$$

is the intersectional growth rate and $\overline{H}_{pc}(t)$ is the intrasectional growth rate, which reads

$$\overline{H}_{pc}(t) = \Big(\sum_{l\in\mathfrak{S}} \widehat{\omega}^l_{pc} \mathrm{V}^{\mathrm{Si}}_{\mathrm{m}} \nu^l_{\mathrm{Si}}\Big) \frac{\overline{s}_p}{\overline{v}_p}, \tag{5.5.4}$$

where $\overline{s}_p$ is the average surface of particles of size p

$$\overline{s}_p = \frac{\int_{v_{p-1}}^{v_p} n_c(t,\boldsymbol{x},\mathfrak{v}) s(\mathfrak{v})\,\mathrm{d}\mathfrak{v}}{\int_{v_{p-1}}^{v_p} n_c(t,\boldsymbol{x},\mathfrak{v})\,\mathrm{d}\mathfrak{v}} = \frac{3}{2}\pi^{1/3}6^{2/3}\frac{v_p^{2/3} - v_{p-1}^{2/3}}{\ln\left(\frac{v_p}{v_{p-1}}\right)}. \tag{5.5.5}$$

The density at the interface between section p and $p+1$, $n_c(t,\mathfrak{v}_p)$, was left undefined in expression (5.2.4) and can be chosen arbitrarily, and so is the intersectional growth rate (5.5.3). For the sake of numerical stability, it is desirable that the total number density be conserved during surface growth [WS85], namely

$$\overline{H}_{pc}\frac{V_{pc}}{\overline{\mathfrak{v}}_p} = \frac{I_{pc}}{\overline{\mathfrak{v}}_p} - \frac{I_{pc}}{\overline{\mathfrak{v}}_{p+1}}, \quad 1 \le p \le N_p - 1,\ -K_- \le c \le K_+, \tag{5.5.6}$$

from which the intersectional growth rate reads [WS85]

$$I_{pc} = \frac{\overline{\mathfrak{v}}_{p+1}}{\overline{\mathfrak{v}}_{p+1} - \overline{\mathfrak{v}}_p}\overline{H}_{pc}V_{pc}, \quad 1 \le p \le N_p - 1,\ -K_- \le c \le K_+. \tag{5.5.7}$$

Also, the growth rate into the smallest section must be zero

$$I_{0c} = 0, \quad -K_- \le c \le K_+, \tag{5.5.8}$$

and the growth rate out of the largest section is traditionally taken equal to zero

$$I_{N_{pc}} = 0, \quad -K_- \leq c \leq K_+, \tag{5.5.9}$$

which is valid provided that the mass flux into the largest section is negligible in the timescale considered.

The nanoparticle surface growth term can then be rewritten in terms of the sectional densities N_{pc}, $1 \leq p \leq N_p - 1$, $-K_- \leq c \leq K_+$. This yields

$$\left[\frac{\partial N_{pc}}{\partial t}\right]_{\text{growth}} = \frac{\overline{v}_{p-1}}{\overline{v}_p - \overline{v}_{p-1}} \overline{H}_{p-1c} N_{p-1c} - \frac{\overline{v}_p}{\overline{v}_{p+1} - \overline{v}_p} \overline{H}_{pc} N_{pc}. \tag{5.5.10}$$

5.5.2 Average surface flux

The average molar surface flux $\widehat{\omega}^l_{pc}$ of molecules of the l^{th} species onto particles in section (p, c), where $1 \leq p \leq N_p - 1$, $-K_- \leq c \leq K_+$, depends on the respective charges q_c and q_l.

Surface flux of a neutral species onto a neutral particle When $q_c = 0$ and $q_l = 0$, the surface flux is equal to the thermal flux [Fri00]

$$\widehat{\omega}^l_{pc} = \frac{1}{4} s^l_{pc} \gamma_l v_{\text{th},l}, \tag{5.5.11}$$

where $\gamma_l = n_l / \mathcal{N}_{\text{A}}$ is the molar concentration of the l^{th} species, s^l_{pc} is the accomodation coefficient of the l^{th} species on a particle of section (p, c), and $v_{\text{th},l}$ is the thermal velocity of the l^{th} species

$$v_{\text{th},l} = \Big(\frac{8 k_{\text{B}} T_l}{\pi \mathfrak{m}_l}\Big)^{\frac{1}{2}}, \quad l \in \mathfrak{S}. \tag{5.5.12}$$

Surface flux of a charged species onto a charged particle with opposite signs When $q_c q_l < 0$, the surface flux is equal to

$$\widehat{\omega}^l_{pc} = \frac{1}{4} \gamma_l \overline{v}_l \Big(1 - 2 \frac{q_p q_c}{4\pi\varepsilon_0 \overline{r}_p \mathfrak{m}_l \overline{v}_l^2}\Big), \tag{5.5.13}$$

where $\gamma_l = n_l / \mathcal{N}_{\text{A}}$ is the molar concentration of the l^{th} species, and where $\overline{v}_l$ is an average macroscopic velocity of the l^{th} species, given by [dB06]

$$\overline{v}_l = \big(v_l^2 + (2 v_{\text{th},l})^2\big)^{\frac{1}{2}}. \tag{5.5.14}$$

Surface flux of a charged species onto a charged particle with the same sign When $q_c q_l > 0$, the surface flux is equal to

$$\widehat{\omega}^l_{pc} = \frac{1}{4} \gamma_l \overline{v}_l \exp\Big(-2 \frac{q_p q_c}{4\pi\varepsilon_0 \overline{r}_p \mathfrak{m}_l \overline{v}_l^2}\Big). \tag{5.5.15}$$

Surface flux of a neutral species onto a charged particle When $q_c \neq 0$ and $q_l = 0$, the surface flux is taken in the form (5.5.11)

$$\widehat{\omega}^l_{pc} = \frac{1}{4} \tilde{s}^l_{pc} \gamma_l v_{\text{th},l}. \tag{5.5.16}$$

where $\tilde{s}^l_{pc}$ is an effective accomodation coefficient. In practice most of the surface growth can be attributed to SiH_4, and the corresponding accomodation coefficient is independent of (p, c)

$$\tilde{s}^{\text{SiH}_4}_{pc} = \tilde{s}_{\text{SiH}_4}. \tag{5.5.17}$$

Surface flux of an ion onto a neutral particle When $q_c = 0$ and $q_l \neq 0$, the surface flux is taken according to the Orbital Motion Limited, or "OML" theory, as

$$\widehat{\omega}^l_{pc} = \frac{1}{4}\gamma_l \overline{v}_l. \tag{5.5.18}$$

In a future study, we intend on considering the effect of the image potential on the surface flux of ions onto neutral nanoparticles.

5.6 Charge fluctuations rate

The source term for charge fluctuations can then be written in the form

$$\left[\frac{\partial N_{pc}}{\partial t}\right]_{\text{charge}} = \nu^e_{p,c+1} N_{p,c+1} + \sum_{l\in\mathfrak{I}^-} \nu^l_{p,c+1} N_{p,c+1} + \sum_{l\in\mathfrak{I}^+} \nu^l_{p,c-1} N_{p,c-1} \tag{5.6.1}$$

$$- \nu^e_{pc} N_{pc} - \sum_{l\in\mathfrak{I}^-} \nu^l_{pc} N_{pc} - \sum_{l\in\mathfrak{I}^+} \nu^l_{pc} N_{pc}, \tag{5.6.2}$$

where $\mathfrak{I}^-$ and $\mathfrak{I}^+$ denote the sets of negative ions and positive ions, respectively, and ν^l_{pc} is the collection frequency of molecules from the l^{th} species by particles in section (p, c)

$$\nu^l_{pc} = 4\pi \overline{r}^2_p \mathcal{N}_{\text{A}} \widehat{\omega}^l_{pc}. \tag{5.6.3}$$

5.7 Nanoparticle Transport

Nanoparticle transport is governed by a classical drift-diffusion equation [Fri00]. The sectional drift-diffusion velocity is taken in the form [Cha43] [Fri00] [AG03]

$$N_{pc}\boldsymbol{\mathcal{V}}_{pc} = \frac{1}{f_{pc}} \boldsymbol{F}^{\text{ext}}_{pc} - D_{pc}\boldsymbol{\partial}_{\boldsymbol{x}} N_{pc}, \tag{5.7.1}$$

where f_{pc} is the friction coefficient of particles in section (p, c), $\boldsymbol{F}^{\text{ext}}_{pc}$ is the sum of external forces acting on particles in section (p, c), and D_{pc} is the diffusion coefficient of particles in section (p, c), given by the Stokes-Einstein expression [Fri00]

$$D_{pc} = \frac{k_{\text{B}} T_h}{f_{pc}}. \tag{5.7.2}$$

In the free molecule range, that is when the particle diameter is negligible compared to the particle mean free path $d_p \ll l_p$, the friction coefficient follows the Epstein's law [Eps24] [Fri00]

$$f_{pc} = \frac{4}{3}\pi \overline{r}^2_p n \sqrt{\frac{8 k_{\text{B}} T \overline{\mathfrak{m}}}{\pi}} \Big(1 + \frac{\pi\alpha}{8}\Big), \tag{5.7.3}$$

where n and T are the density and temperature of the background gas, respectively, $\overline{r}_p$ is the average radius of particles of size p, $\overline{\mathfrak{m}}$ is the mean mass of the mixture

$$\frac{1}{\overline{\mathfrak{m}}} = \sum_{l\in\mathfrak{S}} \frac{Y_l}{\mathfrak{m}_l}, \tag{5.7.4}$$

and α is an accomodation coefficient representing the fraction of the gas molecules that leave the surface in equilibrium with the surface, the remaining fraction $1 - \alpha$ being specularly reflected.

Finally, external forces comprise gravity, ion drag, and electric drift

$$\boldsymbol{F}_{pc}^{\text{ext}} = \boldsymbol{F}_{pc}^{\text{grav}} + \boldsymbol{F}_{pc}^{\text{ion}} + \boldsymbol{F}_{pc}^{\text{drift}}. \tag{5.7.5}$$

No neutral drage is considered, since the mixture convection velocity is neglected. The effect of neutral drag is not significant for the sizes of nanoparticles considered in the following. The gravity field reads

$$\boldsymbol{F}_{pc}^{\text{grav}} = \frac{4}{3}\pi \overline{r}_p^3 \rho_{\text{P}} \mathbf{g}, \tag{5.7.6}$$

where ρ_{P} is the volume density of silicon nanoparticles, and $\mathbf{g}$ is the gravity vector. The electric drift force reads classically

$$\boldsymbol{F}_{pc}^{\text{drift}} = q_c \mathbf{E}. \tag{5.7.7}$$

The ion drag force is decomposed according to the Orbital Motion Limited, or "OML" theory into a collection force and an orbital force

$$\boldsymbol{F}_{pc}^{\text{ion}} = \boldsymbol{F}_{pc}^{\text{coll}} + \boldsymbol{F}_{pc}^{\text{orb}}. \tag{5.7.8}$$

The collection force is the momentum transfer due to collection of ions by nanoparticles in section (p, c), and reads [BKF+92]

$$\boldsymbol{F}_{pc}^{\text{coll}} = \sum_{l \in \mathfrak{I}} \pi b_{\text{c}}^2 \overline{v}_l n_l \mathfrak{m}_l \boldsymbol{v}_l, \tag{5.7.9}$$

where b_{c} is the collection parameter, given by

$$b_{\text{c}}^2 = \begin{cases} \overline{r}_p^2 \Big[1 - \dfrac{2 q_c q_l}{4\pi\varepsilon_0 \overline{r}_p \mathfrak{m}_l \overline{v}_l^2} \Big], & q_c q_l < 0, \\ \overline{r}_p^2 \exp\Big[- \dfrac{2 q_c q_l}{4\pi\varepsilon_0 \overline{r}_p \mathfrak{m}_l \overline{v}_l^2} \Big], & q_c q_l > 0, \\ \overline{r}_p^2, & q_c = 0. \end{cases} \tag{5.7.10}$$

The orbital force is due to the deflection of a nanoparticle induced by ions approaching its surface without being collecting, and reads [BKF+92]

$$\boldsymbol{F}_{pc}^{\text{orb}} = \sum_{l \in \mathfrak{I}} 4\pi b_{\pi/2}^2 \Gamma_{\text{G}} \overline{v}_l n_l \mathfrak{m}_l \boldsymbol{v}_l, \tag{5.7.11}$$

where $b_{\pi/2}$ is the effective impact parameter

$$b_{\pi/2} = \overline{r}_p \Big(- \frac{q_c q_l}{4\pi\varepsilon_0 \overline{r}_p \mathfrak{m}_l \overline{v}_l^2} \Big), \tag{5.7.12}$$

Γ_{G} is the integral of the Coulomb logarithm from b_{c} to λ_{D}

$$\Gamma_{\text{G}} = \frac{1}{2} \ln \Big(\frac{\lambda_{\text{D}}^2 + b_{\pi/2}^2}{b_{\text{c}}^2 + b_{\pi/2}^2} \Big) \tag{5.7.13}$$

where λ_{D} is the linearized Debye length

$$\frac{1}{\lambda_{\text{D}}^2} = \frac{1}{\lambda_e^2} + \frac{1}{\lambda_l^2}, \tag{5.7.14}$$

which depends on the respective electron and l^{th} ion Debye lengths

$$\lambda_e = \Big(\frac{\varepsilon_0 k_{\text{B}} T_e}{n_e q_e^2} \Big)^{\frac{1}{2}}, \tag{5.7.15}$$

$$\lambda_l = \Big(\frac{\varepsilon_0 \mathfrak{m}_l \overline{v}_l^2}{n_l q_l^2} \Big)^{\frac{1}{2}}, \; l \in \mathfrak{I}. \tag{5.7.16}$$

5.8 Plasma-Nanoparticle Model

The plasma-nanoparticle model describing the coupled evolution of electron temperature, electric potential, plasma species densities, and nanoparticle densities, is now summarized. The plasma equations (4.4.3)-(4.4.5) are modified accordingly and solved consistently with equation (5.2.9). The fully-coupled equations then read

$$\partial_t(\rho Y_k) + \boldsymbol{\partial_x} \cdot (\rho Y_k \boldsymbol{\mathcal{V}}_k) = m_k \omega_k - \sum_{p=1}^{N_p} \sum_{c=-K_-}^{K_+} m_k \mathfrak{L}_{pc}^k, \quad k \in \mathfrak{S},\, k \neq \mathrm{H}_2, \tag{5.8.1}$$

$$Y_{\mathrm{H}_2} = 1 - \sum_{k \neq \mathrm{H}_2} Y_k, \tag{5.8.2}$$

$$\partial_{\boldsymbol{x}}^2 \varphi = -\frac{nq}{\varepsilon_0} - \sum_{p=1}^{N_p} \sum_{c=-K_-}^{K_+} \frac{N_{pc} q_c}{\varepsilon_0}, \tag{5.8.3}$$

$$\partial_t\Big(\frac{3}{2} n_e k_{\mathrm{B}} T_e\Big) + \boldsymbol{\partial_x} \cdot \boldsymbol{\mathcal{Q}}_e = \boldsymbol{J}_e \cdot \mathbf{E} + \Delta E_{eh} - \sum_{p=1}^{N_p} \sum_{c=-K_-}^{K_+} \Delta E_{pc}^e, \tag{5.8.4}$$

$$\frac{\partial N_{pc}}{\partial t} + \boldsymbol{\partial_x} \cdot (N_{pc} \boldsymbol{\mathcal{V}}_{pc}) = \left[\frac{\partial N_{pc}}{\partial t}\right]_{\mathrm{nuc}} + \left[\frac{\partial N_{pc}}{\partial t}\right]_{\mathrm{growth}} + \left[\frac{\partial N_{pc}}{\partial t}\right]_{\mathrm{coag}} + \left[\frac{\partial N_{pc}}{\partial t}\right]_{\mathrm{charge}}, \tag{5.8.5}$$

where $\mathfrak{L}_{pc}^k$ is the loss term for the k^{th} species due to deposition onto particles of section (p, c) [War06]

$$\mathfrak{L}_{pc}^k = \nu_{pc}^k N_{pc}, \quad k \in \mathfrak{S},\, 1 \leq p \leq N_p,\, -K_- \leq c \leq K_+, \tag{5.8.6}$$

and ΔE_{pc}^e is the electron energy loss term due to collisions with nanoparticles of section (p, c) [War06]

$$\Delta E_{pc}^e = -\frac{q_c q_e}{4\pi\varepsilon_0 \overline{r}_p} \mathfrak{L}_{pc}^e. \tag{5.8.7}$$

The boundary conditions for the plasma variables, namely the electron temperature, electric potential and plasma species mass fractions, have been given in section 4.8. For the nanoparticles, the boundary conditions depend on the charge of the section considered. The densities of negative particles are assumed to vanish at both electrodes

$$N_{pc}|_{t,0} = 0, \quad 1 \leq p \leq N_p,\, -K_- \leq c \leq -1, \tag{5.8.8}$$

$$N_{pc}|_{t,L} = 0, \quad 1 \leq p \leq N_p,\, -K_- \leq c \leq -1, \tag{5.8.9}$$

while for positive and neutral particles the density gradients vanish at both electrodes

$$(\boldsymbol{\partial_x} N_{pc} \cdot \boldsymbol{n})|_{t,0} = 0, \quad 1 \leq p \leq N_p,\, 0 \leq c \leq K_+, \tag{5.8.10}$$

$$(\boldsymbol{\partial_x} N_{pc} \cdot \boldsymbol{n})|_{t,L} = 0, \quad 1 \leq p \leq N_p,\, 0 \leq c \leq K_+, \tag{5.8.11}$$

where $\boldsymbol{n}$ denotes the unit vector normal to the surface.

5.9 Results and Discussion

The non-stationary plasma-nanoparticle model has been incorporated into the plasma software described in Chapter 4. Equations (5.8.1)-(5.8.5) are solved iteratively over a specified number of radio-frequency cycles. Time iterations are performed with time steps bounded by 2.5×10^{-10} s. Unlike for the pristine plasma, the nanoparticle characteristic time scales being much longer than the plasma characteristic time scales, no pseudo-steady-state is reached, and transient profiles must be considered. We consider in particular the early stage of nanoparticle formation, which is believed to play a crucial role in the silicon deposition process.

5.9.1 Parameters

The conditions considered in Chapter 4, which are typical conditions for silicon epitaxy [RCL12], have been conserved. The inlet gas mixture contains 85 % hydrogen and 15 % silane, that is $X_{\mathrm{H_2}} = 85$ % and $X_{\mathrm{SiH_4}} = 15$ %. The pressure is set at $p_0 = 2.28$ Torr, the heavy-species temperature is taken equal to $T_h = 500$ K. The frequency is set at $f = 13.56$ MHz, and the applied potential amplitude is $\varphi_{\mathrm{RF}} = 100$ V. The initial particle profiles are uniform over the reactor length. The cycle-averaged pseudo-steady-state profiles obtained from the pristine plasma model of Chapter 4 are taken as initial profiles for electron temperature, electric potential and plasma species mass fractions. The corresponding density profiles were plotted in Figures 4.8 and 4.9. We adopt logarithmic spacing for section volumes, namely

$$\mathfrak{v}_{p+1} = \gamma \mathfrak{v}_p, \quad 1 \leq p \leq N_p. \tag{5.9.1}$$

The logarithmic spacing factor is taken equal to $\gamma = 2.85$. Since we are interested in the early stages of nanoparticles growth, the absolute charge carried by a nanoparticle does not exceed a few elementary charges [dB06] [Aga12].

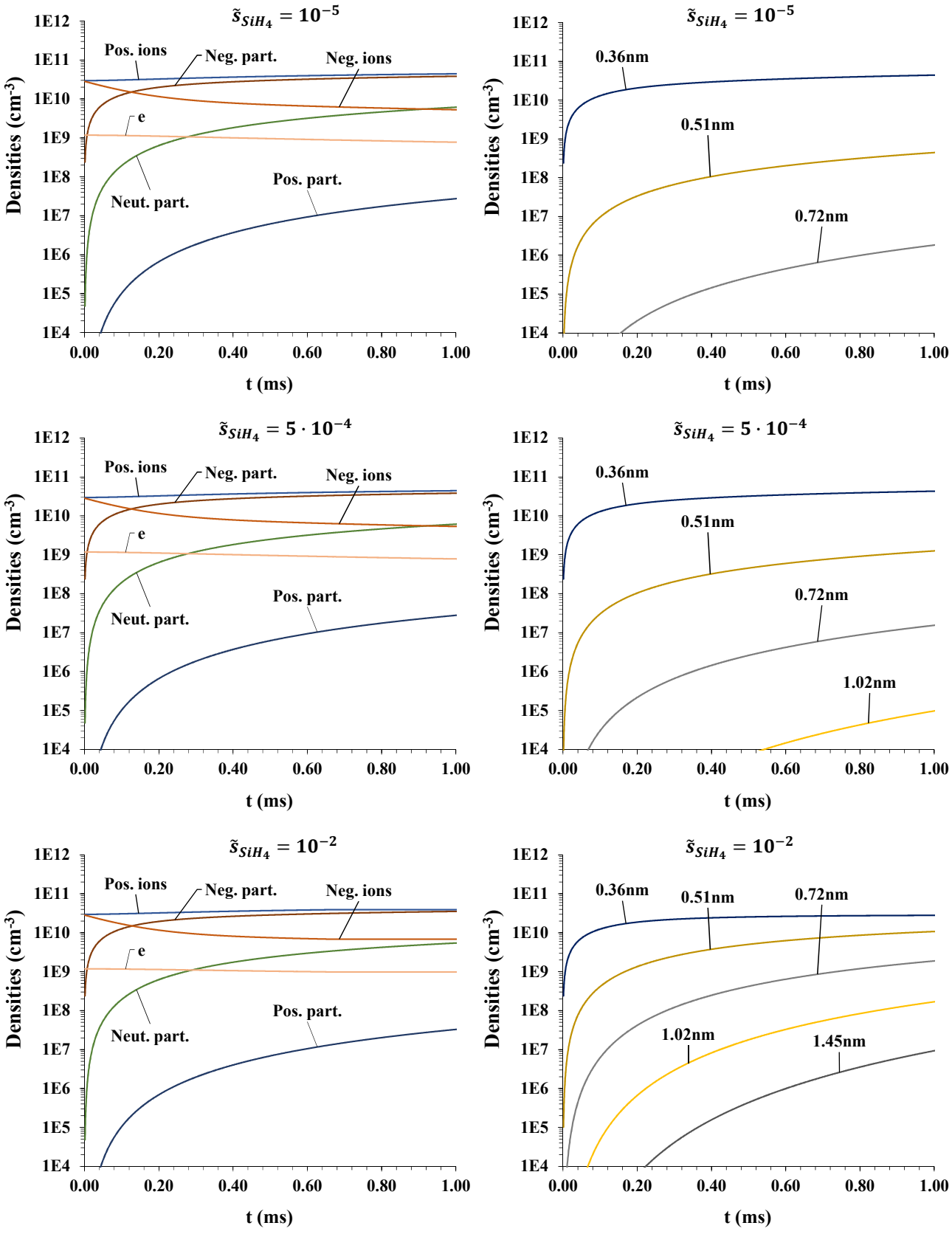

Figure 5.2 – Temporal evolution of the time-averaged densities of electrons, ions, and nanoparticles of each charge at the center of the discharge (left) and density profiles of nanoparticles of each size at the center of the discharge (right), for different values of $\tilde{s}_{\mathrm{SiH_4}}$.

5.9.2 Investigation of nanoparticle surface growth rate

We first consider the influence of the accomodation coefficient $\tilde{s}^{\mathrm{SiH_4}}$ of silane on charged nanoparticles. Indeed, this is the main parameter driving the nanoparticle growth rate at early stages, and the values found in the literature may vary significantly. In [War06], a uniform surface growth rate of 12 nm.s^{-1} is applied, while in [Aga12], the surface growth rate is computed from the collision frequency according to the kinetic theory of rigid elastic spherical molecules [CC70] [FK72], multiplied by the surface sticking coefficient of the molecule considered, with a sticking coefficient of 10^{-5} for SiH_4. Finally, in [dB06] the nanoparticle surface growth is not taken into account. In order to shed light on nanoparticle surface growth, the coagulation is turned off, and we consider only five sections of size, and three sections of charges, namely

$$q_c = -1, 0, +1. \tag{5.9.2}$$

Figure 5.2 shows the temporal evolution of the main species densities at the center of the discharge during the early stage of particle growth. The accomodation coefficient has been varied between $\tilde{s}_{\mathrm{SiH_4}} = 1 \times 10^{-5}$ (above), $\tilde{s}_{\mathrm{SiH_4}} = 5 \times 10^{-4}$ (middle), and $\tilde{s}_{\mathrm{SiH_4}} = 1 \times 10^{-2}$ (below). The densities of negative, neutral, and positive nanoparticles, negative and positive ions, and electrons, are represented on the left of the figure, while the size distribution of nanoparticles is shown on the right.

One can see a rapid increase in the density of negative nanoparticles, which tend to replace negative ions as the main negatively charged species within the plasma. As expected, neutral and positive nanoparticle densities remain low compared to negative nanoparticle density, since the latter remain trapped inside the plasma due to the potential barrier. In the meantime, the electron density slightly decreases, while the positive ions density remains stable or slightly increases, which is coherent with experimental observations for this phase of particle growth [WB12].

Table 5.1 – Reaction rate constant computed for a molecule of radius 2 Å, and a gas temperature of 500 K.

$\tilde{\boldsymbol{s}}_{\mathbf{SiH_4}}$	1×10^{-5}	5×10^{-4}	1×10^{-2}	2.5×10^{-2}
k (cm^3.s^{-1})	4.3×10^{-16}	2.2×10^{-14}	4.3×10^{-13}	1.1×10^{-12}

As can be seen in Figure 5.2, the evolution of the main species densities are not affected drastically by the value of the accomodation coefficient of silane, while the growth rate is very sensitive to $\tilde{s}_{\mathrm{SiH_4}}$. It is readily seen from (5.5.16) that a constant accomodation coefficient induces a constant radial growth rate $\widehat{\omega}_{pc}^{l} V_{\mathrm{m}}^{\mathrm{Si}}$, with values of 2 Å.s^{-1}, 95 Å.s^{-1}, 1900 Å.s^{-1}, respectively for the three cases. Radial growth rate in the range of 1000 Å.s^{-1} has been achieved experimentally under similar conditions [NTRiCP07], so that an accomodation coefficient around 1×10^{-2} seems to be the most appropriate choice for silicon epitaxy conditions. Another confirmation is obtained from the comparison of the reaction rate constants obtained for the different values of accomodation coefficient with the rate constants associated with the clustering reactions of the smallest negative ions, namely

$$\mathrm{Si}_n\mathrm{H}_{2n}^- + \mathrm{SiH_4} \longrightarrow \mathrm{Si}_{n+1}\mathrm{H}_{2n+2}^- + \mathrm{H_2}, \tag{5.9.3}$$

$$\mathrm{Si}_n\mathrm{H}_{2n+1}^- + \mathrm{SiH_4} \longrightarrow \mathrm{Si}_{n+1}\mathrm{H}_{2n+3}^- + \mathrm{H_2}, \tag{5.9.4}$$

which has been taken equal to $k_{\mathrm{nuc}} = 1.0 \times 10^{-12}$ cm^3.s^{-1} according to (5.3.4). The reaction rate constant computed for a molecule of radius 2 Å, and a gas temperature of 500 K, are presented

in Table 5.1. The rate constant computed is closest to the nucleation rate for an accomodation coefficient value of $\tilde{s}_{SiH_4} = 2.5 \times 10^{-2}$, which is consistent with the results above. Therefore, we will keep in the following the value of

$$\tilde{s}_{SiH_4} = 2.5 \times 10^{-2}. \tag{5.9.5}$$

5.9.3 Study of a silane-hydrogen discharge during the early stages of nanoparticle formation

We now apply the fully consistent software, including coagulation and influence of the image potential. We consider ten sections of size, as listed in Table 5.2, and five sections of charges, namely

$$q_c = -3, -2, -1, 0, +1. \tag{5.9.6}$$

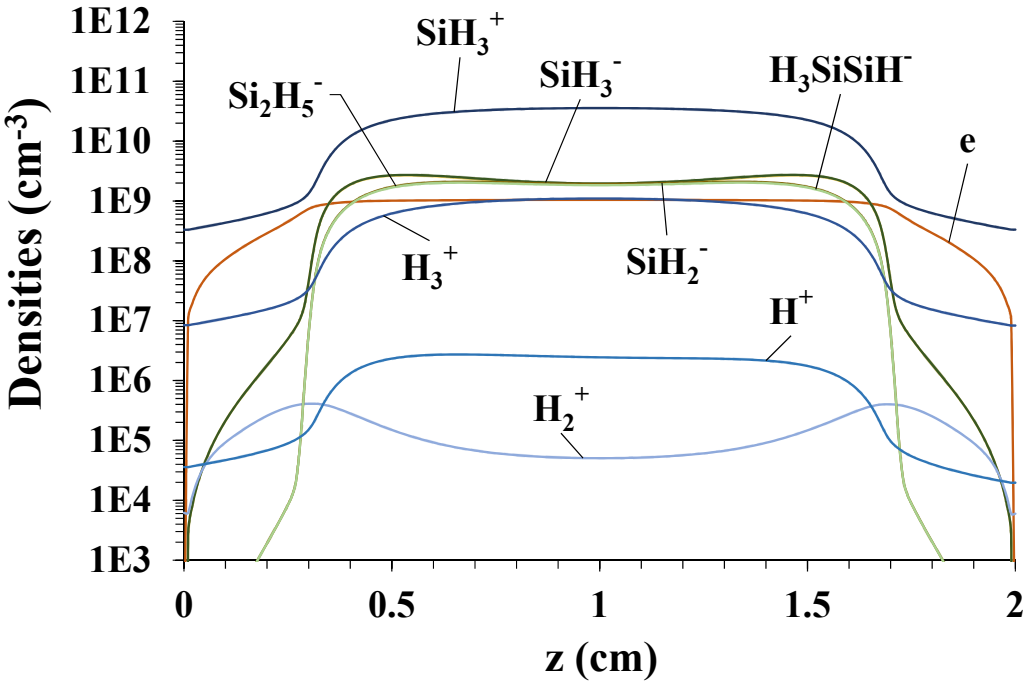

Figure 5.3 – Density profiles of charged plasma species.

Figure 5.3 shows density profiles for charged plasma species, and Figure 5.5 shows the nanoparticle density profiles, as obtained after 6,000 radio-frequency cycles. At this stage, nanoparticles with one negative elementary charge are dominant, and the first two sections of size are dominant, so that for the time considered the nanoparticles observed are essentially "large" negative ions or clusters containing at most a few thousands of silicon atoms.

Due to the strong potential barrier, the negatively charged nanoparticles are trapped at the center of the discharge, in agreement with previous results [dB06] [Aga12]. The trapped negative particles have therefore a longer residence time than neutral or positive particles, and continue to grow and accumulate charge. The density of neutral nanoparticles, which appear mainly due to neutralization of negative nanoparticles by positive ions, is one or two orders of magnitude lower than negative nanoparticle density. Positive nanoparticle density is about five orders of magnitude lower than negative nanoparticle density. Compared to the SiH_3^+ ion profile in Figure 5.3, positive nanoparticles have a negligible density, at least for the time considered. It should be noted that

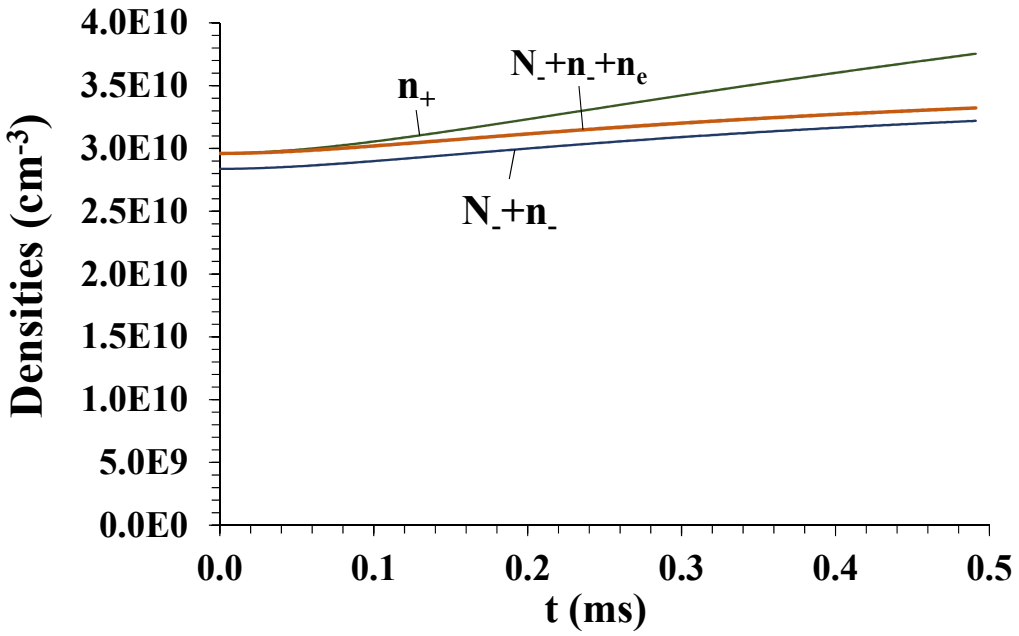

Figure 5.4 – Temporal evolution of the positive ion density n_+, the sum of negative nanoparticle density and negative ion density $n_- + N_-$, and the sum of all negative species densities $n_- + N_- + n_e$, at the center of the reactor.

Table 5.2 – List of sections considered with corresponding average radius and number of silicon atoms.

Section	Average radius (nm)	Number of Si atoms
1	0.36	10
2	0.51	28
3	0.72	81
4	1.02	231
5	1.45	659
6	2.06	1,878
7	2.92	5,353
8	4.13	15,256
9	5.86	43,478
10	8.31	123,914

the OML theory describing the charging mechanism still needs to be assessed, as far as nanometric or subnanometric particles are concerned. Charge fluctuations of such silicon clusters are indeed very frequent, possibly increasing the number of positive nanoparticles under some specific discharge conditions. Taking into account UV photodetachment could also modify the charge distribution. However, a significant density of neutral nanoparticles is observed, which are not trapped in the plasma and can therefore contribute atively to the deposition process.

The temporal evolution of the main negative species and positive ions densities at the center

of the reactor are given in Figure 5.4. It is readily seen that the positive ion density increases as nanoparticles nucleate and grow. This increase is associated with an increase in the density of negative nanoparticles and ions, a slight decrease in electron density, and an increase in the number of charges carried on average by a nanoparticle, which explains the difference observed between the positive ion density and the total negative species density. Nanoparticles with a radius below one nanometer are so small that they can actually stand a limited number of charges. Calculations with a charge limit of 1 have been carried out, and the increase in positive ion and negative nanoparticle densities are also observed under such conditions. The evaluation of the charge limit is discussed in [Gal00] [LG16]. Since the number of charges considered here remains limited, the charge limit was discarded so that the charge of the smallest nanoparticles might be overestimated. In experimental conditions, the charge accumulation may thus be slightly delayed compared to the present results.

The decrease in electron density and increase in electron bulk temperature are notoriously observed in silane-hydrogen plasmas during the nanoparticle nucleation. This change in the plasma properties may be associated with the beginning of an $\alpha \rightarrow \gamma'$ transition [BB93] [PBEL94] [BBH96]. Precisely, epitaxy of silicon and deposition of polymorphous silicon thin films occur under conditions where the discharge is maintained on the verge of nanoparticle agglomeration [SRiC06]. Similarly, the rapid increase in positive ion density induces an increase in ion fluxes on the substrate, which in turn induces a dramatic increase in deposition rate. This result is consistent with previous experimental observations, which have pointed out the dominant contribution of ions to the deposition of polymorphous silicon [HFiMNB00] [NTRiCP07] [KJK$^+$17].

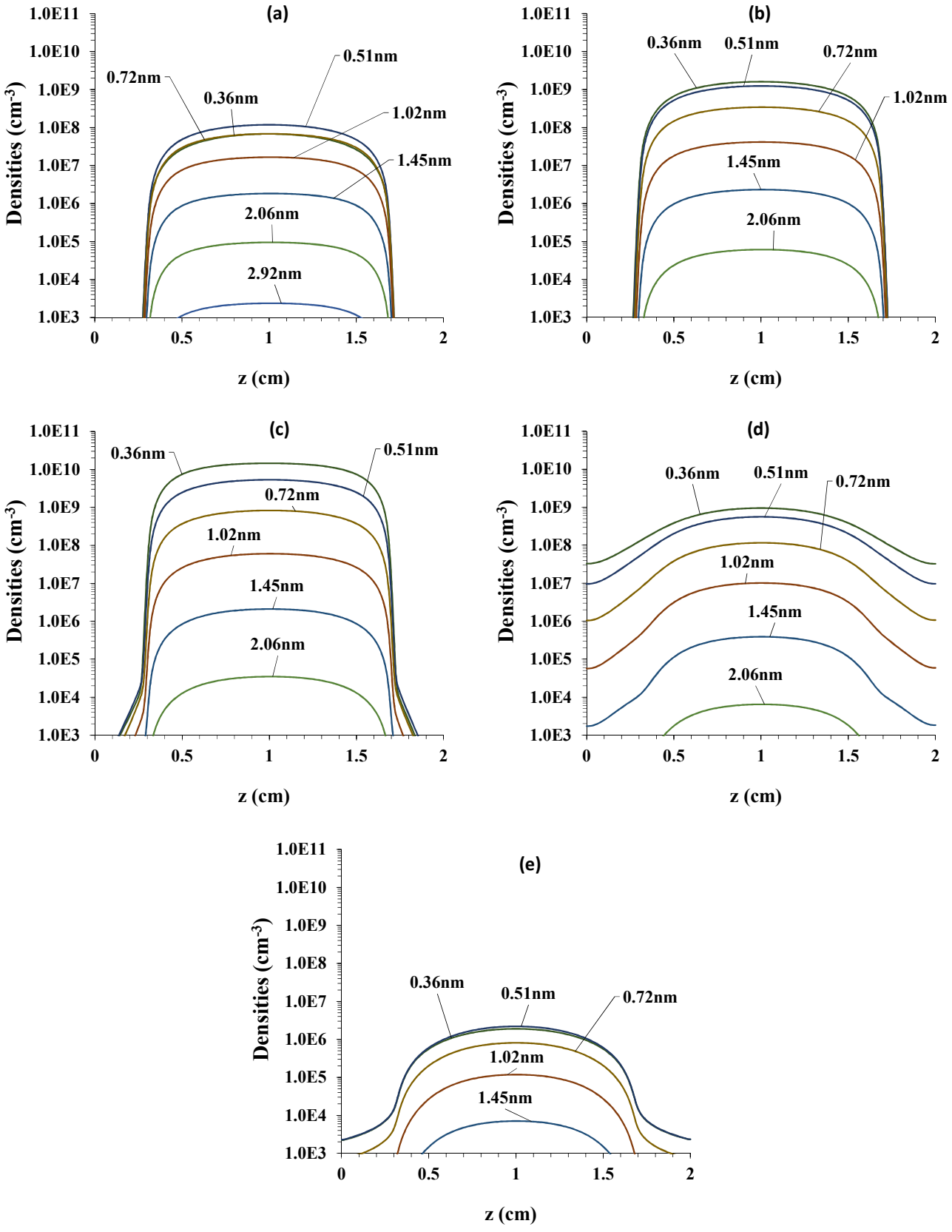

Figure 5.5 – Transient profiles of nanoparticles as obtained after 6,000 radio-frequency cycles, that is after 0.5 ms. (a) Density profiles of negative nanoparticles with three elementary charges $c = -3$. (b) Density profiles of negative nanoparticles with two elementary charges $c = -2$. (c) Density profiles of negative nanoparticles with one elementary charge $c = -1$. (d) Density profiles of neutral nanoparticles $c = 0$. (c) Density profiles of positive nanoparticles with one elementary charge $c = +1$.

5.10 Conclusion

We have implemented a self-consistent and fully coupled numerical model for nanoparticle formation in silane-hydrogen plasma discharge. The model includes a complete chemistry mechanism for nucleation of nanoparticles, effect of charge enhancement on coagulation, and transport of nanoparticles. In turn, the influence of the nanoparticles on electric potential, plasma species densities and electron temperature is accounted for. The model is fully non-stationary, and has been used to investigate the early phase of nanoparticle formation, where particles' radii remain below ten nanometers, under industrial conditions typical of silicon thin-film deposition.

The surface flux of silane on clustering particles has been treated by means of an effective accomodation coefficient $\tilde{s}_{SiH_4}$. Different values of the accomodation coefficient have been tested, and $\tilde{s}_{SiH_4}$ was found to be in the range $1 - 2.5 \times 10^{-2}$. The strong interaction of silane with clusters can be explained by several reasons. The surface growth rate on particles could be strongly enhanced by an increased nanoparticle temperature. As supported by molecular dynamics simulations [VB05], the nanoparticles can be strongly heated due to to hydrogen interaction with nanoparticle surface, which can adsorb on an existing dangling bond or recombine with an H atom on the cluster surface. Experimental observations confirm that it is possible to grow crystalline nanoparticles when a high hydrogen dilution is used [NTRiCP07], although other heating mechanisms could play a role as well. In turn, an increase in the cluster temperature will enhance drastically the surface accomodation coefficient of silicon containing species. Additionnally, the polarizability of SiH_4 induces a dipole interaction which can influence the surface flux on charged silicon clusters of a given size. Finally, the surface flux of silane in general depends on the size and charge of the nanoparticle. It is expected to decrease rapidly when nanoparticles reach a critical size, and become equal to the standard accomodation coefficient on the walls, leading to amorphous growth of large nanoparticles once nucleation has been quenched by coagulation [HDD$^+$94].

The instantaneous nanoparticle density profiles presented are in qualitative agreement with previous results obtained for different conditions [dBG06] [AG12]. Although the density of neutral nanoparticles was found to be nonnegligible compared to that of negative particles, positive nanoparticle densities are several orders of magnitude below, so that positive nanoparticles are not expected to play a significant role in the deposition process. However, a rapid increase in positive ion density has been observed, and the subsequent increase in positive ion flux may have a significant impact on silicon thin-film deposition.

Given the very small time scale associated with the radio-frequency excitation, namely $T_{RF} = \frac{1}{13.56\times10^6} = 7.37\times10^{-8}$ s, time iterations are time consuming. In a future study, we intend on applying the "time splitting" procedure of Akdim and Goedheer [AG03], where seperated time integrations are carried out for "fast" variables, namely the electric potential, the electron temperature and the charged species densities, and "slow" variables, namely the nanoparticles and most of the neutral species [dBG06] [War06] [AG12]. The results obtained will be validated by comparison with the fully coupled method applied in the present version of the software.

Bibliography

[AG03] M. R. Akdim and W. J. Goedheer. Modeling of dust in a silane/hydrogen plasma. *Journal of Applied Physics*, 94:104–109, 2003. 139, 148, 158

[AG11] P. Agarwal and S. L. Girshick. Numerical simulations of nanodusty RF plasmas. *IEEE Transactions on Plasma Science*, 39(11):2760–2761, 2011. 140

[AG12] P. Agarwal and S. L. Girshick. Sectional modeling of nanoparticle size and charge distributions in dusty plasmas. *Plasma Sources Sci. Technol.*, 21:055023, 2012. 5, 6, 140, 141, 145, 158

[Aga12] P. Agarwal. *Numerical Modeling of Plasmas in which Nanoparticles Nucleate and Grow*. PhD thesis, University of Minnesota, 2012. 113, 140, 145, 151, 153, 154

[All92] J. E. Allen. Probe theory -the orbital motion approach. *Physica Scripta*, 45:497–503, 1992. 146

[BB93] A. Bouchoule and L. Boufendi. Particulate formation and dusty plasma behaviour in argon-silane RF discharge. *Plasma Sources Sci. Technol.*, 2:204–213, 1993. 2, 156

[BB94] L. Boufendi and A. Bouchoule. Particle nucleation and growth in a low-pressure argon-silane discharge. *Plasma Sources Sci. Technol.*, 3:262–267, 1994. 139

[BBH96] L. Boufendi, A. Bouchoule, and T. Hbid. Electrical characterization and modeling of a dust forming plasma in a radio frequency discharge. *Journal of Vacuum Science and Technology A*, 14(2):572–576, 1996. 2, 129, 156

[Bha03] U. Bhandarkar. *Study of particle nucleation and growth in low pressure silane plasmas*. PhD thesis, University of Minnesota, 2003. 113, 116, 139

[BKF+92] M. S. Barnes, J. H. Keller, J. C. Forster, J. A. O'Neill, and D. Keith Coultas. Transport of dust particles in glow-discharge plasmas. *Physical Review Letters*, 68(3):313–316, 1992. 149

[BKG03] U. Bhandarkar, U. Kortshagen, and S. L. Girshick. Numerical study of the effect of gas temperature on the time for onset of particle nucleation in argon-silane low-pressure plasmas. *J. Phys. D: Appl. Phys.*, 36:1399–1408, 2003. 5, 139

[Bou99] A. Bouchoule, editor. *Dusty Plasmas: Physics, Chemistry and Technological Impacts in Plasma Processing*. Wiley, 1999. 2, 139

[BSGK00] U. V. Bhandarkar, M. T. Swihart, S. L. Girshick, and U. R. Kortshagen. Modelling of silicon hydride clustering in a low-pressure silane plasma. *J. Phys. D: Appl. Phys.*, 33:2731–2746, 2000. 113, 114, 115, 127, 132, 139

[CC70] S. Chapman and T. G. Cowling. *The Mathematical Theory of Non-Uniform Gases*. Cambridge University Press, Cambridge, 1970. 5, 11, 12, 14, 18, 20, 21, 32, 33, 47, 82, 88, 111, 118, 145, 153

[Cha43] S. Chandrasekhar. Stochastic problems in physics and astronomy. *Reviews of Modern Physics*, 15(1), 1943. 148

[dB06] K. de Bleecker. *Modeling of the formation and behavior of nanoparticles in dusty plasmas*. PhD thesis, Universiteit Antwerpen, 2006. 113, 116, 119, 139, 145, 147, 151, 153, 154

[dBBG04] K. de Bleecker, A. Bogaerts, and W. Goedheer. Modeling of the formation and transport of nanoparticles in silane plasmas. *Physical Review E*, 70:056407, 2004. 140

[dBBG05] K. de Bleecker, A. Bogaerts, and W. Goedheer. Role of the thermophoretic force on the transport of nanoparticles in dusty silane plasmas. *Physical Review E*, 71:066405, 2005. 140

[dBBGG04] K. de Bleecker, A. Bogaerts, W. Goedheer, and R. Gijbels. Investigation of growth mechanisms of clusters in a silane discharge with the use of a fluid model. *IEEE Transactions on Plasma Science*, 32(2):691–698, 2004. 139

[dBG06] K. de Bleecker, A. Bogaerts, and W. Goedheer. Modelling of nanoparticle coagulation and transport dynamics in dusty silane discharges. *New Journal of Physics*, 8:178, 2006. 5, 140, 143, 158

[dBGG04] K. de Bleecker, A. Bogaerts, R. Gijbels, and W. Goedheer. Numerical investigation of particle formation mechanisms in silane discharges. *Physical Review E*, 69:056409, 2004. 5, 104, 117, 139

[Eps24] P. S. Epstein. On the resistance experienced by spheres in their motion through gases. *Physical Review*, 23:710–733, 1924. 148

[FK72] J. H. Ferziger and H. G. Kaper. *Mathematical Theory of Transport Processes in Gases*. North-Holland Publishing Company, 1972. 11, 12, 14, 18, 20, 21, 32, 33, 47, 59, 82, 88, 118, 153

[Fri00] S. K. Friedlander. *Smoke, Dust, and Haze: Fundamentals of Aerosol Dynamics*. Oxford University Press, 2000. 141, 145, 146, 147, 148

[Gal00] A. Gallagher. Model of particle growth in silane discharges. *Physical Review E*, 62(2):2690–2706, 2000. 156

[GTS80] F. Gelbard, Y. Tambour, and J. H. Seinfeld. Sectional representations for simulating aerosol dynamics. *Journal of Colloid and Interface Science*, 76(2):541–556, 1980. 142, 143

[HDD+94] Ch. Hollenstein, J.-L. Dorier, J. Dutta, L. Sansonnens, and A. A. Howling. Diagnostics of particle genesis and growth in RF silane plasmas by ion mass spectrometry and light scattering. *Plasma Sources Sci. Technol.*, 3:278–285, 1994. 128, 139, 158

[HFiMNB00] E. A. G. Hamers, A. Fontcuberta i Morral, C. Niikura, and R. Brenot. Contribution of ions to the growth of amorphous, polymorphous, and microcrystalline silicon thin films. *Journal of Applied Physics*, 88(6):3674–3688, 2000. 156

[KB99] U. Kortshagen and U. Bhandarkar. Modeling of particulate coagulation in low pressure plasmas. *Physical Review E*, 60(1):887–898, 1999. 145

[KJK+17] Ka-Hyun Kim, E. V. Johnson, A. G. Kazanskii, M. V. Khenkin, and P. Roca i Cabarrocas. Unravelling a simple method for the low temperature synthesis of silicon nanocrystals and monolithic nanocrystalline thin films. *Nature Scientific Reports*, 7:40553, 2017. 156

[LAG17] C. Larriba-Andaluz and S. L. Girshick. Controlled fluxes of silicon nanoparticles to a substrate in pulsed radio-frequency argonâĂŞsilane plasmas. *Plasma Chem. Plasma Process.*, 37:43–58, 2017. 140

[LG16] R. Le Picard and S. L. Girshick. The effect of single-particle charge limits on charge distributions in dusty plasmas. *Journal of Physycs D: Applied Physics*, 49:095201, 2016. 156

[MAL+16] A. Michau, C. Arnas, G. Lombardi, X. Bonnin, and K. Hassouni. Nanoparticle formation and dusty plasma effects in dc sputtering discharge with graphite cathode. *Plasma Sources Sci. Technol.*, 25:015019, 2016. 140

[MH10] A. Michau and K. Hassouni. Modelling of dust grain formation in a low-temperature plasma reactor used for simulating parasitic discharges expected under tokamak divertor domes. *Plasma Sources Sci. Technol.*, 19:034023, 2010. 140

[NTRiCP07] Th. Nguyen-Tran, P. Roca i Cabarrocas, and G. Patriarche. Study of radial growth rate and size control of silicon nanocrystals in square-wave-modulated silane plasmas. *Appl. Phys. Lett.*, 91:111501, 2007. 153, 156, 158

[PBEL94] J. Perrin, C. Böhm, R. Etemadi, and A. Lloret. Possible routes for cluster growth and particle formation in RF silane discharges. *Plasma Sources Sci. Technol.*, 3:252–261, 1994. 2, 116, 139, 156

[RBG01] K. Rózsa, G. Banó, and A. Gallagher. The location of very small particles in silane RF discharge. *IEEE Transactions on Plasma Science*, 29(2):256–260, 2001. 140

[RCL12] Pere Roca i Cabarrocas, Romain Cariou, and Martin Labrune. Low temperature plasma deposition of silicon thin films. *J. Non Cryst. Solids*, 358:2000–2003, 2012. 3, 104, 124, 139, 140, 151

[RG09] L. Ravi and S. L. Girshick. Coagulation of nanoparticles in a plasma. *Physical Review E*, 79:026408, 2009. 140

[RiCHS+98] P. Roca i Cabarrocas, S. Hamma, S. N. Sharma, G. Viera, and E. Bertran. Nanoparticle formation in low-pressure silane plasmas: bridging the gap between a-Si:H and μc-Si films. *Journal of Non-Crystalline Solids*, 227–230:871–875, 1998. 3, 139, 140

[RiCNTD+07] P. Roca i Cabarrocas, Th. Nguyen-Tran, Y. Djeridane, A. Abramov, E. Johnson, and G. Patriarche. Synthesis of silicon nanocrystals in silane plasmas for nanoelectronics and large area electronic devices. *J. Phys. D.: Appl. Phys.*, 40:2258–2266, 2007. 2, 3, 103, 141

[SRiC06] V. Suendo and P. Roca i Cabarrocas. Plasma diagnostics in silane-methane-hydrogen plasmas under pm-$Si_{1-x}C_x$:H deposition conditions: Correlation with film properties. *Journal of Non-Crystalline Solids*, 352:959–963, 2006. 156

[Str05] R. A. Street. *Hydrogenated Amorphous Silicon.* Cambridge University Press, 2005. 139

[VB05] H. Vach and Q. Brulin. Controlled growth of silicon nanocrystals in a plasma reactor. *Physical Review Letters*, 95:165502, 2005. 128, 158

[War06] S. J. Warthesen. *Numerical Investigations of Nanodusty Plasmas.* PhD thesis, University of Minnesota, 2006. 140, 150, 153, 158

[WB12] G. Wattieaux and L. Boufendi. Discharge impedance evolution, stray capacitance effect, and correlation with the particles size in a dusty plasma. *Physics of Plasmas*, 19:033701, 2012. 129, 153

[WG07] S. Warthesen and S. Girshick. Numerical simulation of the spatiotemporal evolution of a nanoparticle-plasma system. *Plasma Chemistry and Plasma Processing*, 27(3):292–310, 2007. 5, 6, 117, 140, 141, 142, 145

[WS85] D. R. Warren and J. H. Seinfeld. Simulation of aerosol size distribution evolution in systems with simultaneous nucleation, condensation, and coagulation. *Aerosol and Science Technology*, 4(1):31–43, 1985. 146

[WSK+96] Y. Watanabe, M. Shiratani, H. Kawasaki, S. Singh, T. Fukuzawa, Y. Ueda, and H. Ohkura. Growth processes of particles in high frequency silane plasmas. *J. Vac. Sci. Technol. A*, 14:540–545, 1996. 139

Chapter 6

Conclusion and Perspectives

In this thesis, a fully coupled, fully consistent, and fully non-stationary plasma-nanoparticle model has been developed and implemented numerically.

A plasma fluid model for a multicomponent reactive two-temperature polyatomic plasma has been derived from the kinetic theory of gases. For the first time, the internal energy levels of the heavy plasma species were taken into account, yielding additional terms in the expression for transport fluxes. This derivation has set a sound basis for the modeling of non-thermal plasmas accomplished in the remaining of the thesis, and opens new perspectives of applications in the field.

In the limiting case of a neutral mixture, classical models for multicomponent reactive gas flows have been retrieved. A numerical model for thermal chemical vapor deposition (CVD) of crystalline silicon was then implemented numerically. A software has been written in FORTRAN and validated against a benchmark model from the literature. The results are fully consistent with the benchmark within a few percents accuracy.

The fluid model derived from the kinetic theory has then been simplified to describe a radio-frequency plasma discharge reactor. The software for CVD modeling has been enriched and adapted to the modeling of PECVD, including thermal non-equilibrium, a two-temperature chemistry, and self-consistent calculation of charged species transport and electric potential. Numerical results are presented in conditions typical of polymorphous silicon deposition, and influence of silane dilution ratio as well as RF power is studied. A simplified gas phase chemical mechanism was shown sufficient to reproduce the main plasma properties. A self-consistent calculation of the DC bias was also incorporated. This allowed to assess the influence of asymmetric waveform excitation on discharge chemistry and electrical properties in silane-hydrogen.

Finally, a sectional model for nanoparticles with respect to size and charge was derived, and implemented in the software. The surface growth rate of nanoparticles was investigated, and compared to experimental results from LPICM. The nanoparticle and plasma species transient density profiles have been studied. Although positive nanoparticle densities remain several orders of magnitude below the positive ion density, a non-negligible fraction of nanoparticles are neutral and can thus reach the substrate without beinng trapped in the plasma. Besides, under the conditions considered, the early phase of nanoparticle is associated with a significant increase in the positive ion density and subsequent ion flux, which is a possible explanation for the apparition of embedded crystalline structure in the deposited layers.

Several perspectives of research can be drawn. From a theoretical viewpoint, the derivation from the kinetic theory will be completed and extended in a future work. In particular, the sign of the entropy production rate will be asserted, since a positive entropy structure is required for the sake of numerical stability. In addition, the effect of "strong" magnetic field will be included, and a scaling where some of the heavy species internal energy modes thermalize at T_e while the others thermalize at T_h will be considered. The complete model derived in Chapter 2 still needs to be implemented and validated against kinetic models and when possible against experimental

data. For practical applications, the knowledge of transport parameters and thermochemical data is required, in particular for the computation of collision integrals. If electron collision cross-sections are generally well referenced for the most current discharge chemistries, transport data for positive and negative ions in silane discharges is currently scarcely available. As well, existing chemical reaction rates between silicon hydrides and other plasma species can be improved. The use of molecular dynamic simulations could be useful as well as new experimental measurements under a wide range of discharge conditions. However, the model derived from the kinetic theory is general and can also be applied to different chemistries and processes.

The description of surface processes as well can be improved. In particular, a self-consistent description of surface kinetics should account for hydrogen surface coverage, and for the impact energy of ions bombarding the substrate. The derivation of a self-consistent reaction mechanism and associated reaction rates is a tremendous task, especially in plasma discharges where ion bombarding energy play an important role in the surface processes. A better description of the nanoparticle surface growth process is also desirable. Indeed, the description by means of an effective accomodation coefficient has proved to be efficient in explaining the observed nanoparticle radial growth rate under polymorphous silicon deposition conditions, but does not describe self-consistently the surface growth kinetics. In particular, H surface coverage and ion impact energies should be accounted for, while additional complexity could arise from the actual geometry of nanoparticles, the variation of their surface temperature, as well as polarizability effects and influence of image potential on surface fluxes. In turn, a better knowledge of reaction rates between clusters and plasma species would provide a more accurate description of nanoparticle charging. Finally, in this work the full charge distribution was accounted for by means of a sectional model with sections of size and charge. The charge distribution of "small" nanometer-sized nanoparticles is particularly narrow, so it would be interesting to compare the average charge computed from this model to results of models where only the average charge on each particle of a given size is computed.

Comparison with experiments are also expected. The computation of the DC bias will be validated against existing results from experiments and kinetic modeling of hydrogen discharges. Experimental measurements of the DC bias in silane-hydrogen discharges will then be carried out at LPICM for comparison with simulations under conditions where nanoparticles are absent and in the presence of nanoparticles. Comparison of deposition rates obtained from simulations and from experiments is also envisioned. This requires to estimate the contribution of silicon nanoparticles to growth. As a first approximation, sticking coefficients can be used, until a more precise description is available. Finally, experimental measurement of positive, neutral and negative cluster densities under polymorphous deposition conditions, whenever possible, would of great interest.

From a numerical viewpoint, several improvements are possible to accelerate the computations. The use of the time splitting procedure of Akdim and Goedheer would allow to use much larger time steps and thus simulate the discharge over a longer period of time. Parallelization of numerical algorithms would also accelerate considerably the computations. Currently, most of the computational cost arises from the evaluation of the numerical Jacobian, which requires $3n^c + 1$ evaluations of the function F_Z, as explained in Chapter 3. Parallelization of those function evaluations, which are completely independant from each others, would significantly lower the time required for the Jacobian evaluation. In a second time, parallelization could be applied to accelerate the evaluation of F_Z itself. The gain in computation rate could be used to enrich the discharge chemistry, or could as well permit to develop a two-dimensional axisymmetric model.

université PARIS-SACLAY
ÉCOLE DOCTORALE
INTERFACES
Approches Interdisciplinaires : Fondements, Applications et Innovation

Titre : Modélisation d'un plasma de silane avec dynamique de nanoparticules pour applications photovoltaïques

Mots clefs : plasmas froids, modélisation, nanoparticules, silane, théorie cinétique, épitaxie

Résumé : Cette thèse porte sur la modélisation des plasmas de silane à couplage capacitif pour applications photovoltaïques.
Une dérivation complète des équations fluides pour un plasma bi-température poly-atomique a été effectuée dans le cadre de la théorie cinétique des gaz. La méthode de Chapman-Enskog a permis d'obtenir les équations du régime Euler à l'ordre zéro et les équations de type "Navier-Stokes-Fourier" à l'ordre un. La méthode fournit également une expression des flux de transport et des coefficients de transport associés.
Le modèle ainsi dérivé a été implémenté numériquement en vue de décrire un processus de dépôt chimique en phase vapeur assisté par plasma. Un logiciel a été écrit en FORTRAN et validé numériquement à l'aide d'un cas test issu de la littérature. Le modèle de plasma a été couplé à un modèle sectionnel en taille et en charges pour les nanoparticules. Le logiciel a ensuite été mis en oeuvre dans les conditions de l'épitaxie. Les densités des principales espèces du plasma sont en accord avec la littérature. L'influence de la chimie du silane sur la tension d'auto-polarisation a également été étudiée, grâce à l'utilisation de formes d'ondes asymétriques sur mesure. Enfin, la comparaison avec les taux de croissance expérimentaux a permis d'étudier l'influence du coefficient d'accommodation du silane sur les nanoparticules.
Le modèle développé dans cette thèse ouvre ainsi la voie à une étude systématique de l'évolution du plasma en fonction des conditions de dépôt et de l'influence des nanoparticules sur les propriétés physico-chimiques du plasma.

Title : Modeling of Silane Plasma Discharges Including Nanoparticle Dynamics for Photovoltaic Applications

Keywords : cold plasmas, modeling, nanoparticles, silane, kinetic theory, epitaxy

Abstract : This thesis addresses the modeling of radio-frequency capacitively-coupled silane plasma discharges for photovoltaic applications.
A complete derivation of fluid equations for a two-temperature polyatomic plasma has been achieved in the framework of the kinetic theory of gases. The Chapman-Enskog method was applied to derive the zeroth-order Euler-type equations and the first-order Navier-Stokes-Fourier-type equations. Expressions for transport fluxes and associated transport coefficients have also been obtained.
The model thus derived has been implemented numerically in order to describe a plasma enhanced chemical vapor deposition process. A software has been written in FORTRAN and validated against a benchmark model from the literature. The plasma model has been coupled with a sectional model accounting for size and charge of nanoparticles.
The software has then been applied to silicon epitaxy conditions. The main plasma species densities are in agreement with experimental data. The influence of silane plasma chemistry on the DC bias voltage has also been investigated using tailored voltage asymmetric waveforms. Finally, a comparison with experimental growth rates allowed to study the influence of the accommodation coefficient of silane on nanoparticles.
The model implemented in this work opens the path for a systematic study of the evolution of the plasma properties as a function of the process conditions and of the influence of nanoparticles on the plasma physicochemical properties.

Université Paris-Saclay
Espace Technologique / Immeuble Discovery
Route de l'Orme aux Merisiers RD 128 / 91190 Saint-Aubin, France